FOSSIL ENERGY

DOE/BC/14850-5
(OSTI ID: 750251)

FRACTURED PETROLEUM RESERVOIRS

Final Report
June 11, 1999

By
Dr. Abbas Firoozabadi

Work Performed Under Contract No. DE-FG22-96BC14850

Reservoir Engineering Research Institute
Palo Alto, California

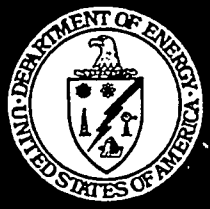

National Petroleum Technology Office
U. S. DEPARTMENT OF ENERGY
Tulsa, Oklahoma

DISCLAIMER

DISCLAIMER

Portions of this document may be illegible in electronic image products. Images are produced from the best available original document.

DOE/BC/14850-5
Distribution Category UC-122

Fractured Petroleum Reservoirs

By
Dr. Abbas Firozabadi

January 2000

Work Performed Under Contract No. DE-FG22-96BC14850

Prepared for
U.S. Department of Energy
Assistant Secretary for Fossil Energy

Robert E. Lemmon Program Manager
National Petroleum Technology Office
P.O. Box 3628
Tulsa, OK 74101

Reservoir Engineering Research Institute
385 Sherman Avenue, Suite 2B
Palo Alto, CA 94306

Table of Contents

List of Tables

Chapter I

Part I

Part II

Chapter II

Chapter III

Part II

Chapter IV

Part I

Part III

Part IV

Part V

List of Figures

Chapter I

Part I

Part II

Chapter II

Chapter III

Part I

Part II

Chapter IV

Part I

Part II

Part III

Part IV

Part V

Acknowledgements

The findings presented in the final report prepared for the US DOE for grant DE-FG22-96BC14850 in the period of March 1996 to March 1999 are based on the work of a number of highly dedicated and talented post doctorals, research engineers, and visiting scientists at RERI: Dr. Mehran Pooladi-Darvish, Dr. Ivan Terez, Dr. Kewen Li, Dr. Kassem Ghorayeb, and Dr. Keshawa Shukla. Unique features of the work at RERI is high productivity of some of researchers. The five-part work in Chapter IV is based on 16 months work of Dr. Ghorayeb. Dr. Pooladi-Darvish's work include two parts encompassing experimental work and theoretical research and another piece of work which was carried out in a period of about 20 months.

In addition to the above colleagues, Dr. Mike Riley did an outstanding job on convection and diffusion in fractured porous media in 1996 which was published in the AIChE Journal (February 1998). This work is not reported in this report for brevity and in order to keep the final report in a reasonable size. Dr. Riley's work at RERI laid down the foundation for our work on diffusion and convection in porous media.

As principal investigator of the projects, I have learned from my colleagues and the learning experience has been the most rewarding part of the work.

The research work on fractured petroleum reservoirs at RERI in the 1996-1998 period was supported by grant DE-FG22-96BC14850 from the US DOE and the following companies: Abu Dhabi National Oil Company (ADNOC) (UAE), ARCO Exploration and Production Technology (USA), BP Amoco (UK), Chevron Petroleum Technology Company (USA), Elf Aquitaine Production (France), Exxon Production Research Company (USA), Intevep (Venezuela), Maersk Oil and Gas (Denmark), Marathon Oil Company (USA), Mobil Technology Corporation (USA), Norsk Hydro Production, A. S. (Norway), Petrobras, S. A. (Brazil), Petrofina, S. A. (Belgium), Petronas Research and Scientific Services SDN BHD (Malaysia), Phillips Petroleum Company (USA), SAGA Petroleum A/S (Norway), Shell Exploration and Production Company (USA), Statoil, A/S (Norway), Texaco, Inc. (USA), Total (France).

The DOE support has been an important source of funding for our research work and has allowed us to continue the research work on fractured reservoirs. As a result of DOE's continued support and support from nearly all the major oil companies, RERI has evolved as a world leader in the area of fractured reservoirs. During the 1996-1998 period, our project managers with DOE were Dr. Bob Lemmon and Mr. Bob Harris. They kindled an atmosphere that we can focus on the various research tasks of our research program.

Summary

The four chapters that are described in this report cover a variety of subjects that not only give insight into the understanding of multiphase flow in fractured porous media, but they provide also major contribution towards the understanding of flow processes with in-situ phase formation. In the following, a summary of all the chapters will be provided.

Chapter I addresses issues related to water injection in water-wet fractured porous media. There are two parts in this chapter. Part I covers extensive set of measurements for water injection in water-wet fractured porous media. Both single matrix block and multiple matrix blocks tests are covered. There are two major findings from these experiments: 1) co-current imbibition can be more efficient than counter-current imbibition due to lower residual oil saturation and higher oil mobility, and 2) tight fractured porous media can be more efficient than a permeable porous media when subjected to water injection. These findings are directly related to the type of tests one can perform in the laboratory and to decide on the fate of water injection in fractured reservoirs.

Part II of Chapter I presents modelling of water injection in water-wet fractured media by modifying the Buckley-Leverett Theory. A major element of the new model is the multiplication of the transfer flux by the fractured saturation with a power of ½. This simple model can account for both co-current and counter-current imbibition and computationally it is very efficient. It can be orders of magnitude faster than a conventional dual-porosity model. Part II also presents the results of water injection tests in very tight rocks of some 0.01 md permeability. Oil recovery from water imbibition tests from such at tight rock can be as high as 25 percent.

Chapter II discusses solution gas-drive for cold production from heavy-oil reservoirs. The impetus for this work is the study of new gas phase formation from in-situ process which can be significantly different from that of gas displacement processes. The work is of experimental nature and clarifies several misconceptions in the literature. Based on experimental results, it is established that the main reason for high efficiency of solution gas drive from heavy oil reservoirs is due to low gas mobility.

Chapter III presents the concept of the alteration of porous media wettability from liquid-wetting to intermediate gas-wetting. The idea is novel and has not been introduced in the petroleum literature before. There are significant implications from such as proposal. The most direct application of intermediate gas wetting is wettability alteration around the wellbore. Such an alteration can significantly improve well deliverability in gas condensate reservoirs where gas well deliverability decreases below dewpoint pressure. Part I of Chapter III studies the effect of gravity, viscous forces, interfacial tension, and wettability on the critical condensate saturation and relative permeability of gas condensate systems. A simple phenomenological network model is used for this study. The theoretical results reveal that wettability significantly affects both the critical gas saturation and gas relative permeability. Gas relative permeability may increase ten times as contact angle is altered from 0° (strongly liquid wet) to 85° (intermediate gas-wetting). The results from the theoretical study motivated the experimental investigation described in Part II. In Part II we demonstrate

that the wettability of porous media can be altered from liquid-wetting to gas-wetting. This part describes our attempt to find appropriate chemicals for wettability alteration of various substrates including rock matrix.

Chapter IV provides a comprehensive treatment of molecular, pressure, and thermal diffusion and convection in porous media. Basic theoretical analysis is presented using irreversible thermodynamics. The developments presented in Part I are used to estimate thermal diffusion factors and to calculate compositional variation in hydrocarbon reservoirs, both fractured and unfractured media. The ultimate goal is to characterize fractured reservoirs through analysis of PVT data.

Part II uses the concepts presented in Part I to estimate thermal diffusion factors – a key parameter for the calculation of compositional variation in hydrocarbon reservoirs. For the first time, we present a model for the estimation of thermal diffusion coefficients in a ternary and higher component mixtures. We were pleasantly surprised that the estimated coefficients describe measured data well.

Part III presents features of convection and diffusion in porous media for a binary mixture. It is interesting to note that permeability affects the composition variation in different ways.

Part IV studies the compositional variation in a rectangular two-dimensional (x,z) fractured porous medium. The work examines the effects of various fracture parameters: fracture permeability, fracture aperture, fracture intensity, and connectivity. Numerical results show that due to high fracture permeability, a pronounced convection motion within the fracture network takes place. As a result, composition in the entire media can be very uniform above a certain permeability.

Part V is the study of compositional variation in porous media for a multicomponent mixture. Both binary and multicomponent mixtures are considered. The results include compositional variation calculation in a field in Colombia which is in good agreement with data. Various cross effects are rigorously accounted for in our multicomponent study.

Chapter I – Water Injection in Fractured Porous Media

Part I – Experimental Study of Water Injection in Water-Wet Fractured Porous Media

MEHRAN POOLADI-DARVISH AND ABBAS FIROOZABADI

Summary

For predicting the performance of water injection in naturally fractured reservoirs, scale-up of the recovery data from immersing an oil-saturated core into water is commonly used. Oil recovery from some of the naturally fractured reservoirs of the North Sea has been better than what is predicted using the immersion laboratory experiments. In the field, the matrix blocks do not become surrounded by water at once; they experience an advancing fracture-water level (FWL).

In this paper, the results of experiments of water injection in fractured porous media comprising a number of water-wet matrix blocks are reported for the first time. The blocks experienced an advancing fracture-water level (FWL). Immersion-type experiments were performed for comparison; the dominant recovery mechanism changed from co-current to counter-current imbibition when the boundary conditions changed from advancing FWL to immersion-type. We performed single block experiments of co-current and counter-current imbibition and found that co-current imbibition leads to more efficient recovery.

Kansas chalk and Berea sandstone were investigated. A column of three blocks of Berea sandstone (ϕ =0.22, k=0.62 μm^2, pore volume (PV)=8800×10^{-6} m^3) and a stack of 12 blocks (4 rows and 3 columns) of an outcrop Kansas chalk (ϕ =0.30, k=0.002-0.005 μm^2, PV=13,900×10^{-6} m^3) were used. Breakthrough recoveries were 0.2-0.4 for the Berea and 0.2-0.6 of PV for the chalk experiments. Corresponding ultimate recoveries were around 0.5 and 0.65 of PV; oil recovery from low permeability chalk was better than that of high permeability Berea. Fracture apertures in all the above experiments were in the range of 150-200 μm.

An approximate mathematical model was developed for counter-current imbibition. It was found that the late-time matrix-fracture transfer function simplifies to an exponential function. Hence, the physical significance of the empirical transfer function of Aronofsky et al. was demonstrated. The exponential transfer function was incorporated in a model, which was used to match the water injection experiments performed on a stack of very low permeability Austin chalk (ϕ =0.05, k=0.00001–0.00005 μm^2, PV=287×10^{-6} m^3). These experiments were dominated by counter-current imbibition.

Introduction

Water injection is known as an important method for oil recovery from some fractured reservoirs. In water-wet fractured reservoirs, the capillary pressure contrast between the fracture and the matrix media provides the main driving force for water imbibition, which can be an efficient recovery mechanism[1]. Field application of water injection in fractured reservoirs has been implemented since the early fifties[2]. Many issues, however, remain unresolved in the understanding of this process. Since the early studies, it was

understood that recovery behaviour from a block totally covered by water is different than the same block in contact with water from some faces and with oil from other faces[2]. However, the majority of studies have centred on immersion-type boundary conditions[3]. Intuitively, if a block is surrounded by water, oil is forced to flow in the opposite direction of water flow, hence by counter-current imbibition. If the block is partially covered by water, water is imbibed into the rock and oil can flow downstream of the water-front and through the faces which are in contact with oil. In the latter case, water and oil might flow in the same direction and the process is called co-current imbibition. Experimental[4,5] and modelling studies[6] have indicated that boundary conditions other than immersion change the dominant flow mechanism from counter-current to co-current imbibition, and that the latter mechanism can be more efficient than the former. In a detailed experimental study, Bourbiaux and Kalaydjian[5] reported that the half recovery time for co-current imbibition was 7.1 hr., and that for counter-current imbibition was 22.2 hr. for one set of experiments. In the modelling studies of Pooladi-Darvish and Firoozabadi[6] it was found that recovery by co-current imbibition was 4 to 8 times faster than that by counter-current imbibition.

In a fractured reservoir subjected to water injection, the fracture network does not become flooded at once – the fracture-water level has an advancing behaviour. Some of the early studies have examined the recovery performance of a matrix block under advancing fracture-water level[7-9]. Differences were observed between rising water level and immersion experiments. These studies do not use a stack of blocks. Despite the differences observed between behaviour of the imbibition process with advancing fracture-water level (FWL) and those with immersion boundary conditions, recent studies have focused on the latter process. We are unaware of any experimental study of water imbibition in a stack of matrix blocks with advancing FWL.

In this work, the results of water injection in an aggregate of matrix blocks are reported. Berea sandstone and Kansas chalk outcrops were used. In these laboratory experiments, the fracture-water level is advancing and the matrix blocks experience the two types of boundary conditions mentioned earlier, i.e., partially covered and immersion type. By increasing the injection rate, the velocity of the FWL is increased and the effect of changing the contribution of each boundary condition is examined. Immersion-type tests are performed and the results are compared with advancing FWL experiments.

The paper is presented along the following sequence. The experimental apparatus and procedure are first described. Experimental results and their interpretation follow. Development of a mathematical model for counter-current imbibition is then presented, and a set of experimental data dominated by this process is modelled. A physical and mathematical basis for the empirical model of Aronofsky *et al.*[10], i.e. exponential transfer function is also presented.

Apparatus

Figure 1 shows the schematic diagram of the apparatus. The central part is the visual core-holder that houses the matrix blocks. Its body is made of 12-mm thick clear polycarbonate sheet that is pushed against the rocks using an external frame. The rocks and the polycarbonate sheets are sandwiched between two 25-mm thick aluminium caps. The inlet and outlet, as well as vacuum and fluid charge fittings are mounted on the two caps. The application of clear polycarbonate sheets permits measurement of fracture-water level data, and identification of the active imbibition mechanisms, discussed later.

In addition to the multi-block apparatus, which was used for advancing FWL experiments, two single-block apparatuses were built to study the differences between immersion-type boundary condition and advancing FWL. The roughness of the rock surface created a small gap of 150-200 μm between the rock surface and

the body of core-holder and/or another rock surface that it came in contact with. These gaps act as fractures. Hence, the column of Berea sandstones had four vertical and four horizontal fractures, and the multi-block chalk column had six vertical and five horizontal fractures. For the immersion tests, spacers were used to allow a larger fracture width and to assure complete coverage of the matrix block by water (see Figure 1b).

A unique feature of the apparatus used in our advancing FWL experiments was small fracture width; the fracture PV was around 0.5% of the total fracture and matrix PV. The importance of small fracture volume can be understood by realising that under a constant rate of water injection, the rate of FWL advance is determined by the rate of water imbibition inside the matrix. The smaller the fracture width the more pronounced the change in FWL, when the imbibition rate in the matrix changes. In our experiments, measurement of the FWL provides the rate of water imbibition in the matrix block. This was not possible in the previous studies,[7,8] where fracture width was very large.

Rock and Fluid Data

Three matrix-fracture assemblies were made, one comprising three blocks of Berea sandstone, another twelve blocks of Kansas chalk, and the other a single block of Kansas chalk. The Kansas chalk blocks are from the Upper Cretaceous Niobrara Formation, northern Ellis County, west-central Kansas. The chalk sample is white and appears homogeneous, lacking evidence of stratification. Analysis of the samples indicate 99% calcite and 1% quartz, which resembles that of "clean" North Sea chalks, which lacks significant chert and clay minerals. Kansas chalk shows close similarities with reservoir chalk from some of the North Sea reservoirs with regards to capillary pressure behaviour. The main difference between the two rock-types is that the Kansas chalk does not show evidence of tectonic structures such as fractures.

Figure 2 shows the rock assemblies and the dimensions of the blocks. The permeability and porosity of the Berea sandstone blocks were approximately 0.620 μm^2 and 22 percent[11]. The chalk permeability is in the 0.002-0.005 μm^2 range with porosity close to 30 percent.

In order to estimate the properties of vertical fractures, the total permeability of the fracture-matrix media was calculated by measuring the single-phase flow rate of normal decane (nC_{10}) under gravity force. The fracture permeability and aperture were calculated knowing the matrix and total system permeability. All fractures were assumed to be of equal aperture, and the cubic law was assumed valid[12]. Fracture apertures were in the range of 150-200 μm.

The total volume of the horizontal and vertical fractures including the dead volumes was estimated after each test by measuring the volume of liquid drained from the system during a short period of time. Table 1 gives the rock and fracture data.

Deareated solution of 1 w% NaCl in distilled water and normal decane were the aqueous and oleic phases, respectively. In this paper, the term water is used to refer to the brine solution.

Test Procedure

We first removed the in-situ fluid and the adsorbed material on the pore surface by exerting a high vacuum for one to two weeks. The matrix-fracture system was then saturated with normal decane, and a period of two days was allowed for saturation at atmospheric pressure. The volume of nC_{10} was recorded for pore volume measurement. In the advancing FWL experiments, gravity driven single-phase flow of nC_{10} was performed for permeability measurement.

Each test started by injection of the brine solution using a constant flow rate pump, and the mass of the produced oil was measured and was continuously recorded. The outlet valve was at the same level as the top of the blocks and was opened to the atmosphere. In our tests, the compressibility effect is negligible and the oil production rate before breakthrough is equal to the injection rate. Before water breakthrough, the data of primary importance are the fracture-water levels. A fine interface curvature was detected at the water-oil contact in the four edge fractures, which was recorded as the fracture-water level.

As the test progressed, the FWL rose to the top of the column. Breakthrough was detected when water appeared in the outlet tubing at the top of the column. The produced fluid was then directed to a separator and the water-oil interface in the separator was recorded by a video camera. Brine injection was continued until production rate dropped to very low values. The injection was then stopped, and was started after a period of 24 to 48 hrs, to measure the oil produced, if any. The collected data were FWL before breakthrough and oil production data at all times.

For the immersion-type tests, spacers were used to increase the fracture aperture to about 0.01 m, ensuring complete coverage of the block by water. After complete saturation of the matrix-fracture system with nC_{10}, water was flowed through the system, and the oil in the fracture was displaced upward. Water flow was continued until all the oil around the block was displaced and the water-oil interface rose to the top of a graduated cylinder which was connected to the top of the core-holder using an acrylic pipe with large diameter (see Figure 1b). At this time water flow was stopped. The total time required for displacing the oil in the fractures by water was approximately four minutes. As soon as water came in contact with the block, the imbibition process became active. However, almost all of the oil that was expelled during this early time remained attached to the rock surface. The total volume of oil separated from the rock before oil production rate could be measured, is estimated to be less than 0.1% of matrix pore volume and is neglected.

Oil production was measured by monitoring the oil-water interface in the graduated cylinder. The large diameter of the connecting pipe permitted free flow of produced oil blobs from the top of the core-holder into the graduated cylinder. At the end of the test when oil production rate had reduced to nearly zero, air was flowed through the fracture spacing to remove the oil blobs remaining on the surface of the block.

Scope of Experimental Study

The objective of the experimental study is the examination of the effectiveness of oil recovery by water injection in water-wet fractured porous media. A stack of multiple blocks with small fracture width is used to represent realistic conditions. Berea sandstone (k = 0.620 μm^2) and a Kansas chalk (k = 0.002-0.005 μm^2) are employed. Water injection rate is changed from one run to the next. When the injection rate increases, the FWL rises faster. This in turn creates a larger surface area between the matrix and the water in the fracture, and the rate of matrix oil production increases. As injection rate is increased further, there will be little time for imbibition before the blocks are covered by water. After blocks are covered, oil production is through the two–phase region by counter-current imbibition. In our tests, this is confirmed by visual observation. An infinitely high injection rate is equivalent to immersing a block in water. Immersion

experiments are performed on the single block set-up. In one test, by tilting the column of twelve chalk blocks to an angle of 60 degrees from the vertical axis, the gravity effects were evaluated.

In the following, first the test results performed on Berea are presented. Then, the single-block and multi-block chalk tests follow.

Experimental Result and Analysis

a- Berea Experiments (3 Blocks)

Test 1 – Injection rate = 190×10^{-6} m^3/hr (0.022 PV/hr) A low flow rate was chosen for the first test. Upon injection, oil production started from the top of the column, and water started to rise in the fractures. The rate of FWL rise was high for about half of the height of the first block. Once enough exchange area between the matrix and the water in the fracture was established, the rate of FWL advance declined. Figure 3 shows the FWL for Test 1 (as well as Tests 2 to 4). The horizontal lines show the location of the horizontal fractures. The data for each test include multiple readings from different fractures around the column. Figure 3 indicates that the FWL along the four edges of the column are nearly the same. Careful study of Figure 3 suggests that the velocity of FWL seems to increase after the level passes a horizontal fracture. (For example, see the change in the slope at 1.215 m.) When this happens and water covers the lower block, water will be imbibed into the rock from all the faces and oil is produced through the two-phase region by counter-current imbibition. At an earlier time some of the boundaries of the block are in contact with the oil, and the oil production can be through the single-phase region, by co-current imbibition. One explanation for the increase of the rate of FWL rise after it passes a horizontal fracture is that oil production by counter-current imbibition is slower than that by co-current imbibition, leaving more water to rise in the fracture. This is in line with the modelling studies of Pooladi-Darvish and Firoozabadi[6].

Water breakthrough in Test 1 occurred at about 0.38 PV water injected at $t \approx 17.5$ hrs, corresponding to an average velocity of FWL 2.5 m/day. Figure 4 shows the recovery data of Tests 1 to 4. Ultimate recovery after 66 hours was about 50%.

Test 2 and 4 – Injection rate = 380×10^{-6} m^3/hr (0.043 PV/hr) Tests 2 and 4 were duplicates and were performed at the same injection rate. Figures 3 and 4 indicate that the two tests are in agreement.

At this flow rate, as the FWL was rising, small blobs of oil, comparable to the grain size, could be observed below the FWL on the rock surface. This oil flowed opposite to the direction of water flow into the matrix. Visual observation indicated that the contribution of this amount of oil to the total production was negligible.

Figure 3 shows that similar to Test 1, a fast rise was followed by a slower period; although in Tests 2 (and 4) the injection rate was double of that in Test 1, little difference between the recovery behaviour vs. PV injected was observed (see Figure 3, also Figure 4). Recovery at breakthrough was roughly the same for the three tests while FWL velocity doubles from Test 1 to Tests 2 (and 4). For the injection range of 190×10^{-6} – 380×10^{-6} m^3/hr, the imbibition rate is high and the performance is not sensitive to the injection rate. Note that about 20% of the recoverable oil for both injection rates is recovered after water breakthrough. Hence, these two tests are performed above the critical rate of Kleppe and Morse[8]. The recovery performance is not, however, adversely affected by increasing the injection rate from 190×10^{-6} to 380×10^{-6} m^3/hr.

Test 3 – Injection rate = 840×10^{-6} m^3/hr (0.095 PV/hr) The high injection rate resulted in a high velocity of the fracture-water level, and little time for oil production from the blocks before they were immersed in water. Extensive flow of discontinuous oil blobs was observed below the FWL. This was significant before breakthrough and remained active afterward. Oil recovery at breakthrough is only half of the other runs. It is interesting to note that even at a high velocity of FWL of about 22 m/day imbibition is very efficient, and oil recovery at 1 PV injection is 45%. The high recovery is believed to be related to blocks with a small width. The recovery at the end of all the tests was around 0.5 of PV (see Figure 4).

b- Chalk Experiments (Single Block)

A single block of Kansas chalk was placed in a visual core-holder. The block was surrounded by top, bottom, and four side-fractures. Five tests were performed. In three of the tests the injection rate was varied and the last two tests were immersion experiments. The same core was used for all the tests, but the core-holder for the immersion tests had a much larger fracture width. The results are presented next.

Test 5 – Injection rate = 22×10^{-6} m^3/hr (0.021 PV/hr) In the first test on the single chalk block, water was injected at a low rate of 22×10^{-6} m^3/hr. Figure 5 shows the plot of oil recovery vs. PV of injected water. Before breakthrough, nC_{10} production and water injection rates are the same. Oil recovery at breakthrough is 60 percent. Very little oil was produced after water breakthrough.

Figure 6 depicts the FWL in the vertical fractures between the chalk blocks and the polycarbonate sheets. As the figure shows, the FWL moves faster initially in two of the fractures. For PV of injected water > 0.15, the FWL in all four fractures advances with the same speed. FWL reaches the top at PV ≈ 0.6 at an average velocity of 0.24 m/day, and afterwards only water is produced. Before breakthrough, except in the beginning of the test, water was observed to be moving on the surface of the matrix about 0.005 m (0.5 cm) above of the FWL. Before and after breakthrough, we did not observe any oil production below the FWL. Both observations imply that the imbibition is co-current.

Test 6 – Injection Rate = 140×10^{-6} m^3/hr (0.13 PV/hr) In Test 6, the rate of injection was increased to 140×10^{-6} m^3/hr, which resulted in an average FWL velocity of 2.4 m/day. Figure 5 depicts the recovery data; breakthrough occurred at 0.39 PV injection. Oil production rate decreased continuously after breakthrough and recovery at 1 PV injection was close to 60 percent. The FWL data are shown in Figure 6, which shows that similar to the previous tests, FWL moves fast initially and rises slowly afterwards.

In this test, while the FWL was rising, very small droplets of oil were visible forming on the matrix surface, and then flowing towards the water-oil contact in the fracture.

Test 7 – Injection Rate = 276×10^{-6} m^3/hr (0.26 PV/hr) The injection rate in this test was set at twice the rate in Test 6, which roughly quartopled the average rate of FWL. Figure 5 shows the recovery data. The breakthrough occurred at 0.20 PV injection. Oil production rate decreased continuously after breakthrough. The ultimate recovery is 60 percent – very similar to the previous two tests. Recovery is over 50% at 1 PV injection.

Figure 6 shows the FWL vs. PV injected. Initially the FWL moves very fast; the level moves to 0.15 m height at 0.04 PV injection. The FWL then moves at a lower speed. At this high injection rate, very small droplets of oil were visible, forming on the rock surface. We also observed oil production in the form of small droplets underneath the block flowing to the FWL. When the injection rate is increased the FWL rises fast and water covers a large portion of the block surface before much of the oil is produced. As time

passes, water-front moves inward and displaces the oil. When the level is already high in the fracture, before being able to displace the oil in the inner-lower parts of the block, the capillary pressure driving force may not be enough to push the oil to be produced above the FWL. In turn, oil may be produced below the FWL in the opposite direction of water flow. This explains why in all of our tests with increased injection rate, more oil was produced below the FWL. Detailed discussion and modelling of this phenomenon is given elsewhere[6].

Tests 8 and 9 – Immersed Block In these duplicate tests, the block was immersed in water in a short time. Water was imbibed into the rock and oil was expelled from all the surfaces. Oil blobs formed and grew on the rock surface. The process was very similar to sweating. Once the blobs were large enough they detached from the surface and moved towards the oil-water contact. Figure 7 shows the oil recovery vs. time for Tests 6 to 9. The initial rate of imbibition for the immersion tests is very high. This is due to the large contact area between the block and the fracture water. Later on, however, the production rates for Tests 8 and 9 is much slower than those of Tests 6 and 7 (see Figure 7). Immersion leads to counter-current imbibition, whereas oil production under rising FWL is dominated by co-current imbibition. The low production rate by counter-current imbibition as evidenced by Figure 7 is an experimental verification of our previous modelling study[6], and is in line with experimental data of Bourbiaux and Kalaydjian[5].

Note that if the data of Test 5 were plotted in Figure 7, they would fall below the recovery data of the other tests; always a low enough injection rate can be chosen such that the oil recovery rate from co-current imbibition is less than counter-current imbibition. Of course, such an injection rate will not be operationally attractive.

c- Chalk Experiments (12-Blocks)

We conducted five tests on a stack of 12 matrix blocks, which were placed in four rows and three columns (see Figure 2 and Table 1). The blocks were the same size and type as that in single-block tests. In the first four tests the column was vertical and water was injected from the bottom. Water injection rate was varied by more than one orer of magnitude from 0.011 to 0.16 PV/hr. In the last test, water was injected at the high rate of 0.16 PV/hr and the column was at 60 degrees angle from the vertical axis. In the following, Tests 10 to 13 are presented collectively, and then Test 14 is discussed.

Tests 10 – 13 – Injection rates 151×10^{-6} – 2200×10^{-6} m^3/hr (0.011 – 0.16 PV/hr) Test 10 was performed at a low injection rate of 151×10^{-6} m^3/hr. The advance of FWL was very uniform in all the fractures at a velocity of 0.49 m/day as depicted in Figure 8. Before breakthrough, the rock surface was wet 0.005 to 0.025 m (0.5 – 2.5 cm) above the FWL. The oil displaced by water is produced above the water level in the fracture, i.e., by co-current imbibition. Furthermore, it was observed that the distance between the FWL and the water-front on the block surface reduced to about zero, when the water level approached the top of each block. In other words, flow of water from one block to the one above the horizontal fractures was limited during the time available.

At this low injection rate, the blocks had enough time for imbibition and after FWL reached the top of the block at about 64% recovery (matrix recovery ≈ 60%), there was no more oil production (see Figure 9).

For Test 11 the injection rate was increased to 445×10^{-6} m^3/hr, which resulted in an average FWL velocity of 1.5 m/day. Similar to what was observed in Tests 1 and 2, increasing the injection rate had little effect on the recovery behaviour in the range of 151×10^{-6}– 2200×10^{-6} m^3/hr.

In the stacked blocks, there are three blocks in each row; each block will see one third of the total injection rate, in average. This is nearly equal to the condition of Test 6 on the single block (Injection rate = 150×10^{-6} m^3/hr) which resulted in about 40% oil recovery at breakthrough.

Figure 8 indicates that FWL reached the top of the first row of blocks at about 0.12 of total PV injection. Accounting for the dead volume at the inlet, and the fracture volume, matrix recovery at this time is about 40%, equal to that of Test 6. Figures 8 and 9 indicate that by the time of water breakthrough at the top of the column, oil recovery is 0.63 (average matrix recovery of 0.6). This indicates that before water breakthrough, oil recovery behind the FWL increases with injected pore volume. It is interesting to note that this behaviour is different than what is experienced in the Buckley-Leverett solution of oil displacement in a homogeneous medium, where average water saturation behind the front is independent of injection time. In water injection in fractured porous media, however, the rock left behind the FWL may continue to imbibe water and to enhance recovery. This of course does not happen if the water injection rate has been slow enough that ultimate recovery is achieved as the FWL advances (Test 10).

In Test 11, some oil flow in the form of droplets patched between the rock surface and the body of the core-holder below the FWL was observed. Contribution of this oil to the total produced oil was very small. Oil production after breakthrough was less than 2% of total recovery.

In Tests 12 and 13, the water injection rate was increased to 1114×10^{-6} and 2200×10^{-6} m^3/hr (0.08 and 0.16 PV/hr), respectively. Figure 8 shows the FWL advanced fast initially and slowed down subsequently. Figure 9 indicates that breakthrough recovery for Tests 13 and 14 was 0.55 and 0.45 at average FWL velocity of 4.4 m/day and 11 mm/day, respectively. Ultimate recovery for all the tests at 1.5 PV injected and beyond was around 0.64.

Test 14 – Injection rate = 2200×10^{-6} m^3/hr, tilted In Test 14 the stacked-block system was tilted 60 degrees from the vertical axis; the effect of the gravity was reduced by half. The tilt was such that one of the edges of the column was closest to the ground, two of the edges were at the same height from the ground and the last edge was at the highest point. The outlet at the top of the column was close to the highest edge such that the volume of the rock at the very top corner of the column, which was not contacted by water at the end of the test, was very small. The water injection rate in this test was equal to that of Test 13. Figure 8 shows very similar recovery behaviour between Tests 13 and 14. Breakthrough recovery was 0.43 (breakthrough recovery of Test 13 was 0.44).

Figure 10 depicts the FWL of Tests 13 and 14. For Test 14, the distance of oil-water contact in four edges from the base is plotted. The behaviour of FWL in the middle edges is very similar to that of Test 13. FWL in the lower edge showed a faster advance and that in the high edge showed a slower advance. The recovery and the FWL data clearly indicate that gravity effects are not important.

Summary of Experimental Results

The experimental results reveal that oil recovery by water injection in the Berea and chalk tests reported in this paper was governed by very efficient capillary-dominated flow, and the effects of gravity and viscous forces during the course of the tests were minimal. The negligible effect of viscous forces can be demonstrated by calculating the pressure drop across the blocks knowing the permeability of the vertical fractures and the velocity of the FWL.

The tests showed that depending on the injection rate, both mechanisms of co-current and counter-current imbibition could be active. However before a block is fully covered by water, the dominant recovery mechanism is co-current imbibition. As the injection rate increases, the rate of matrix oil recovery increases due to increased contact area between the matrix and the water in the fracture. With further increase in injection rate, water breakthrough occurs earlier, and the portion of oil to be recovered by counter-current imbibition increases. Tests 8 and 9 showed that when injection rate approaches infinity, (immersion case) oil recovery is dominated by counter-current imbibition and this is slower than oil recovery from Tests 6 and 7 which are dominated by co-current imbibition. The fact that Tests 6 and 7, in which contact area between the rock and the water was less than (or equal to) the contact area of Tests 8 and 9, resulted in a more efficient recovery, suggests that for equal area of water contact, co-current imbibition is more efficient than counter-current imbibition, provided everything else is the same. Another interesting feature of the tests is the high recovery efficiency of low permeability chalk compared with the high permeability Berea sandstone. This is believed to be due to high imbibition capillary pressure of the outcrop chalk. The results of the tests also show that in contrast with the Buckley-Leverett displacement in homogeneous porous media, where oil recovery behind the front is independent of the injected PV, in fractured porous media, oil recovery behind the front increases with the injected PV.

Mathematical Modelling

Recently, Terez and Firoozabadi[25] presented a mathematical model that was based on an extension of the Buckley-Leverret solution for two-phase flow in fractured porous media. A source term was incorporated in the model to account for fluid transfer between the matrix and the fracture. Based on the experimental results presented in this paper and fine grid simulation, the authors included two transfer functions to account for co-current and counter-current imbibition. The transfer terms were in the form of exponential function[10]. The solution was based on the method of characteristics, and the model solved for fracture water saturation.

In the following, the physical significance of the exponential transfer function is demonstrated in terms of late-time solution of the counter-current imbibition. The function is then incorporated in a simple mathematical model to calculate the fracture-water level and the imbibition rate. The model is then used to match a set of experimental data of water injection in fractured porous media, which were dominated by counter-current imbibition.

Formulation and Approximate Solution

Counter-current imbibition can be described by a nonlinear diffusion equation[13], given in Appendix A. The Heat Integral Method (HIM)[14] is used to find an approximate solution for saturation (see Equations A-10 to A-12.) The solution is obtained for a constant diffusion coefficient, i.e. the diffusion equation was assumed linear. Later, it is shown that the results for the linear problem may apply for the nonlinear problem.

Using the saturation profiles of Equations A-10 to A-12, one can calculate water imbibition rate,

$$q_D(t_D)_{early} = \sqrt{\frac{3}{8t_D}} \qquad t_D \le \frac{1}{24} \qquad (1)$$

$$q_D(t_D)_{late} = A_1 e^{-\lambda_{D1} t_D} + A_2 e^{-\lambda_{D2} t_D} \qquad t_D \ge \frac{1}{24} \qquad (2)$$

where,

$$q_D(t_D) = -\frac{\partial S_D}{\partial x_D}\Big|_{x_D=0} = \frac{Lq(t)}{\phi AD(1-S_{or}-S_{wc})} \qquad (3)$$

In the above equations, q_D and t_D are dimensionless production rate and dimensionless time, respectively. Parameters A_1, A_2, λ_{D1} and λ_{D2} are defined in appendix A.

The early-time production rate in the above finite system is similar to that in a semi-infinite medium. The difference between the exact solution for the semi-infinite problem for all times, $1/\sqrt{\pi t_D}$, and Equation 1 is 8.3%. Using Equations 1 and 2 the dimensionless cumulative volume of water imbibed can be calculated as,

$$Q_D(t_D)_{early} = \sqrt{\frac{3t_D}{2}} \qquad t_D \le \frac{1}{24} \qquad (4)$$

$$Q_D(t_D)_{late} = 1 - \frac{A_1}{\lambda_{D1}} e^{-\lambda_{D1} t_D} - \frac{A_2}{\lambda_{D2}} e^{-\lambda_{D2} t_D} \qquad t_D \ge \frac{1}{24} \qquad (5)$$

where,

$$Q_D(t_D) = \int_0^{t_D} q_D(\tau)\, d\tau = \frac{Q}{\phi LA(1-S_{or}-S_{wc})} \qquad (6)$$

The definition of Q_D is the same as recovery with respect to total recoverable oil in place, $R(t_D)$. By writing the R.H.S. of Equation 4 in conventional units one obtains,

$$R(t)_{early} = \sqrt{\frac{3D}{2}\frac{t}{L^2}} \qquad t \le \frac{L^2}{24D} \qquad (7)$$

Equation 7 implies that recovery during the early-time is proportional to the square root of time, and is inversely proportional to the length. In other words, the time corresponding to a specific recovery is proportional to the square of the length, which is in line with the results from the previous scaling studies.[19,20,22]

At the beginning of the late-time regime, the ratio of the first exponential function to the second exponential term in the R.H.S. of Equation 5 is only 1/20, and decreases very rapidly with time. Upon neglecting the first exponential function one obtains,

$$R(t_D)_{late} = 1 - \frac{A_2}{\lambda_{D2}} e^{-\lambda_{D2} t_D} \qquad t_D \ge \frac{1}{24} \qquad (8)$$

where for a linear problem A_2 and λ_{D2} are constant and do not depend on the length of the system. Equation 8 has the same form as Aronofsky *et al.*'s[10] exponential function. One can readily show from

Equation 8 and definition of t_D that, similar to the early-time behaviour, the time corresponding to a specific recovery is proportional to square of the length.

Figure 11 shows a comparison between the exact and the HIM solutions of the linear diffusion problem. Recoveries based on the one-term and two-term exponential functions, Equations 5 and 8, are shown. Figure 11 indicates that the HIM solution is in agreement with the exact solution, and that the one-term exponential function is a good approximate solution.

Equations A-10 to A-12 were obtained for a constant diffusion coefficient. When the HIM is used to solve the nonlinear problem, a similar solution can be obtained, where parameters A_1, A_2, λ_{D1}, λ_{D2} are a function of the shape of the diffusion coefficient with respect to saturation. Of course, the solutions are approximate and account, only partially, for saturation dependency of the diffusion coefficient. However, if we do not derive the solution but assume that the <u>form</u> of the solutions does not change, the following hold for the nonlinear case.

1. The plot of recovery vs. $\sqrt{t/L^2}$ during the early-time is a straight line, passing through the origin (see Equation 7).
2. The recovery at which the data deviate from straight line is independent of length.
3. The plot of (1- R(t_D)) at the late-time vs, t/L^2 on a semi-log scale is a straight line with a negative slope, which will not necessarily pass through the point $t = 0$, R = 0 (see Equation 8).

Model Verification

The exponential function proposed by Aronofsky *et al.* has been widely accepted as an empirical equation, which approximates the oil production due to spontaneous imbibition with a step change in the boundary condition reasonably well. Some authors attribute a physical meaning to the solution and others do not[23]. In light of the discussion presented in the above section, here the physical significance of the exponential function is discussed as the late-time solution of the nonlinear 1-D counter-current imbibition, and its validity for experimental data is presented. This is done by verifying the three conclusions we inferred from our approximate solution.

A one-dimensional matrix block with absolute permeability of 0.020 μm^2 and length of 0.20 m is considered. Oil and water viscosity are assumed to be 1 mPas. The relative permeability and the imbibition capillary pressure functions are expressed as

$$k_{ro} = A_o(1-S_D)^{no}, \qquad k_{rw} = A_w S_D^{nw} \tag{9}$$

$$P_c(S_D) = -C\ln(S_D) \tag{10}$$

where S_D is defined by Equation A-7. The parameters A_o, A_w, n_o, n_w, and C are constant. Table 2 gives the values considered in this study. The detailed method of solution of the above problem is presented in reference 6. Here, we present the results.

Figures 12 and 13 depict the behaviour of the numerical solution of the counter-current problem at the early- and late-times. Figure 12 indicates that the early-time recovery is proportional to $\sqrt{t/L^2}$, and Figure 13 shows that the late-time recovery may be approximated by an exponential function, especially that of Equation 8 with $A_2/\lambda_{D2} \neq 1$.

This shows that items 1 and 3 suggested above, based on the HIM solution of the linear problem, might apply to the nonlinear problem of counter-current imbibition. In Figures 12 and 13 the behaviour of the exponential function of Aronofsky *et al.*[10] is also shown, where an exponent of $\lambda_D = 0.01$ was chosen. It can be observed that Aronofsky's solution, if selected to match the overall behaviour, under- and over-predicts the early- and late-time solutions, respectively.

Next, we use the counter-current data from references 20 and 21 to examine the validity of items 1 to 3 above. Figure 14 shows of the early-time solution. The experimental data follow a straight line, and deviate from the straight line, independent of core length, at around 0.8 recoverable oil. The physical properties of the rock and fluids used in references 20 and 21 are different, leading to two distinct lines in Figures 14 and 15. These properties are given in Table 3. The last recovery data point reported in references 20 and 21 was considered as the ultimate recovery. In Figure 14 the data corresponding to the 0.0248-m sample[21] is not in agreement with the rest. This could be due to the error in the oil production data of a very small sample.

Figure 15 shows the plot of the above imbibition data on a semi-log scale. It can be noted at late time, each data-set can be approximated by a single straight line. Note that the straight line passing through the late-time data of Figures 15, if extrapolated to zero time, predicts a non-zero recovery. If an exponential solution similar to that of Aronofsky *et al.*[10] is chosen such that it predicts a zero recovery at the initial time, a behaviour similar to that in Figures 12 and 13 will be observed; an exponent larger than that obtained from the slope of the semi-log straight line will be needed to predict the overall behaviour of the system. The latter solution, then would under- and over-predict the early- and late-time behaviour, respectively. Ma *et al.*[22] also observed the same behaviour when they used an exponential function to match experimental data of counter-current imbibition (see Figure 9 of Ref. 22).

Modelling of Rising FWL of Counter-Current Imbibition

In the previous section, oil production due to counter-current imbibition with a step change in boundary conditions was considered. It was found that the late-time recovery could be approximated by an exponential function. In this section we use the following exponential function, to find oil production for rising fracture-water level.

$$R'(t) = R'_\infty(1-e^{-\lambda t}) \qquad (11)$$

where[23],

$$R'_\infty = \phi(1-S_{or}-S_{wc}) \qquad (12)$$

and

$$R'(t) = \phi(S_w(t)-S_{wc}) \qquad (13)$$

Parameter λ is a constant that determines the rate at which the recovery approaches its maximum value. Similar to Parsons and Chaney[7] one can account for the effect of the rising water level in a fracture adjacent to a single matrix block,

$$Q(t) = R'_\infty A_{ma}\left[\int_0^{t_{BT}} e^{-\lambda(t-\tau)}\frac{\partial \hat{Z}_f}{\partial \tau}d\tau\right] \qquad (14)$$

where $Q(t)$ is the cumulative oil produced at time t, A_{ma} is the cross-sectional area of the matrix perpendicular to the direction of water level rise, and $\hat{Z}_f$ is the location of the water oil contact in the fracture, FWL. Equation 14 assumes that imbibition occurs transverse to the direction of water-level rise in the fracture. Hence, the effect of horizontal fractures is neglected and a stack of matrix blocks is assumed to behave similar to a tall matrix of equivalent height.

References 10 and 24 are based on the assumption that $\hat{Z}_f$ is known in Equation 14. Often instead of $\hat{Z}_f$, the injection rate is known. In Appendix B, the material balance equation for the fracture water is combined with Equation 14, and the solution for the oil production rate and the water level in the fracture are obtained for a known injection rate, Equations B-6 and B-4, respectively. The above model, developed for counter-current imbibition, cannot be used for our experimental data, mainly because co-current imbibition had a large contribution. Instead, we use our simple model to match the experimental data recently presented in reference 25, where oil recovery was dominated by counter-current imbibition. Very tight Austin chalk blocks were used. The cylindrical blocks stacked on top of each other had a permeability of 0.00001 – 0.00005 μm^2 (0.01 – 0.05 md) and porosity of about 5%. The total PV was about 290×10^{-6} m^3. As a result of imbibition, about 20 to 25 percent of the oil was produced over a period of two to four and half months. Figure 16 shows the cumulative oil production as a function of time for one of the tests in reference 25. After breakthrough, water injection was stopped several times while imbibition proceeded. When water injection was resumed, the oil in the fracture was produced first, until the next breakthrough occurred. The experimental data show that the first breakthrough occurred after a very short time. Beyond this point, the blocks are covered by water and oil production is due to counter-current imbibition. We used the rising fracture-water level model with the counter-current transfer function developed above to match the oil recovery data. Figure 16 shows the comparison between the experimental data and the model for Test "a" of Terez and Firoozabadi[25]. Parameter λ was used as a matching parameter and was found to be 0.053 day^{-1}. Maximum oil recovery was set equal to 23%. We did not try to use different λ for different blocks. After breakthrough all the matrix blocks contribute to oil production, and an average λ was used to match the tests.

In summary, Figures 13 and 15 show that the late time recovery data by counter-current imbibition can be represented by an exponential function. In Figure 16, the exponential function was successfully used to match the experimental results of water injection in a stack of matrix blocks, where recovery was dominated by counter-current imbibition. The importance of such a model is that once parameter λ is estimated by matching the experimental data on small samples, λ can be estimated for larger blocks. Comparison of Equations 8 and 11 suggests that $\lambda \propto 1/L^2$, which is in line with previous scaling studies.[19]

Conclusions

We performed water injection experiments in fractured porous media composed of a stack of water-wet chalk and Berea matrix blocks, where the matrix blocks were subjected to rising fracture-water level (FWL). Single block tests of immersion-type and rising FWL were performed for comparison. The unique features of the experiments, in addition to implementation of a stack of blocks were: low fracture pore volume, quantitative data on FWL prior to water breakthrough, and visual observations enhancing the identification of the active imbibition mechanism. Based on the results of these tests, the following conclusions can be made.

1. Water injection in water-wet fractured porous media can be a very efficient recovery mechanism.

2. Depending on the injection rate, both mechanisms of co-current and counter-current imbibition can contribute to recovery.
3. Before a block is fully covered by water, the dominant recovery mechanism can be co-current imbibition; this mechanism often leads to more efficient oil recovery compared with counter-current imbibition.

An approximate analytical model was also developed for counter-current imbibition, which showed the physical significance of the exponential transfer function. The model was successfully used to match the experimental results of water injection in a stack of low permeability Austin chalk.

Nomenclature

Latin Letters

A	Cross Sectional Area, m^2
A	Constant (see Equations 9, A-18 and A-19)
B	Constant, s^{-1} (see Equation B-5)
C	Constant, kPa (see Equation 10 and Table 2)
D	Diffusion Coefficient, m^2/s
L	Half Length, m
P	Pressure, N/m^2
q	Production Rate, m^3/s
Q	Cumulative Production, m^3
R	Recovery w.r.t. Maximum Recoverable Oil (R_{max}=1)
R'	Recovery w.r.t. Total Volume, ($R'_{max}=\phi(1-S_{or}-S_{wc})$)
S	Saturation
$\hat{Z}$	Height of Water Level, m
k	Permeability, μm^2
t	time, s

Greek Letters

ϕ	Porosity
λ	Exponent, s^{-1}
μ	Viscosity, Pas
τ	Variable of Integration

Subscripts

BT	Breakthrough
c	Capillary
D	Dimensionless
f	Fracture
early	Early-Time
i	Injection
late	Late-Time
ma	Matrix
o	Oil
or	Residual Oil
r	Relative
w	Water

wc Connate Water

Symbols

∞ Infinite Time

References

1. Oen, P.M., Engell-Jensen, M. and Barendregt, A.A.: "Skjold Field, Danish North Sea: Early Evaluations of Oil Recovery Through Water Imbibition in a Fractured Reservoir", *SPE Resevoir Engineering* (Feb. 1988) 17-22.
2. Brownscombe, E.R. and Dyes, A.B.: "Water-Imbibition Displacement: A Possibility for the Spraberry", *Drilling and Production Practice API*, (1952) 383-390.
3. Zhang, X., Morrow, N.R., and Ma, S.: "Experimental Verification of Modified Scaling Group for Spontaneous Imbibition", *SPE Resevoir Engineering* (Nov. 1996) 280-285.
4. Iffly, R., Rousselet, D.C., and Vermeulen, J.L.: "Fundamental Study of Imbibition in Fissured Oil Fields", paper SPE 4102 presented at the 1972 Annual Fall Meeting, San Antonio, TX, Oct 8-11.
5. Bourbiaux, B. and Kalaydjian, F.: "Experimental Study of Cocurrent and Countercurrent Flow in Natural Porous Media", *SPE Resevoir Engineering* (Aug. 1990) 361-368, *Trans.* AIME, **289**.
6. Pooladi-Darvish, M. and Firoozabadi, A.: "Co-Current and Counter-Current Imbibition in a Water-Wet Matrix Block", *SPE Journal*, (to be published).
7. Parsons, R.W. and Chaney, R.R.: "Imbibition Model Studies on Water-Wet Carbonate Rocks", *SPE Journal* (March 1966) 26-34, *Trans.* AIME **237**.
8. Kleppe, J. and Morse, R.A.: "Oil Production from Fractured Reservoirs by Water Displacement", paper SPE 5084 presented at the 1974 Annual Fall Meeting, Houston, TX, Oct. 6-9.
9. Kazemi, H. and Merrill, L.S.: "Numerical Simulation of Water Imbibition in Fracture Cores", *SPE Journal* (June 1979) 175-182.
10. Aronofsky, J.S., Masse, L., and Natanson, S.G.: "A Model for the Mechanism of Oil Recovery from Porous Matrix Due to Water Invasion in Fractured Reservoirs", *Trans.* AIME (1958) **213**, 17-19.
11. Firoozabadi, A. and Markeset, T.: "Fracture-Liquid Transmissibility in Fractured Porous Media," *SPE Resevoir Engineering* (Aug. 1994) 201-207.
12. Witherspoon, P.A., Wang, J.S.Y., Iwai, J., and Gale, J.E.: "Validity of Cubic Law for Fluid Flow in a Deformable Rock Fracture", *Water Resources Research*, (1980), **16**, No. 6, 1016-1024.
13. Marle, C.M.: *Multiphase Flow in Porous Media*, Gulf Pub. Co. Editions Technip, Paris 1981.
14. Goodman, T.R.: "Application of Integral Methods to Transient Nonlinear Heat Transfer", In *Advances in Heat Transfer* ed. Irvine, T.F., and Hartnett, J.P., Academic Press, N.Y., N.Y. (1964) 51-121.
15. Carslaw, H.S. and Jaeger, J.C.: *Conduction of Heat in Solids*, 2nd ed. Oxford University Press, London (1959).
16. Finlayson, B.A.: *Method of Weighted Residuals*, Academic Press, N.Y., N.Y. (1972) P. 44-48.
17. Pooladi-Darvish, M., Tortike, W.S., and Farouq Ali, S.M.: "Steam Heating of Fractured Formations – Basic Premises and A Single Block Analytical Model", paper SPE 28642 presented at the 1994 SPE Annual Technical Conference and Exhibition, New Orleans, TX, Sept. 25-28.
18. Barenblatt, G.I., Entev, V.M., and Ryshik, V.M.: *Theory of Fluid Flows Through Natural Rocks*, Kulwar Academic Publishers (1990) Chapter 5.
19. Mattax, C.C. and Kyte, J.R.: "Imbibition Oil Recovery From Fractured Water Drive Reservoirs", *SPE Journal* (June 1962) 177-184, *Trans.* AIME (1962) **225**.
20. Hamon, G. and Vidal, J.: "Scaling-up the Capillary Imbibition Process from Laboratory Experiments on Homogeneous Samples", paper SPE 15852 presented at the 1986 SPE European Petroleum Conference, London, Oct. 22-25.

21. Graham, J.W. and Richardson, J.G. in Collins, R.E.: *Flow of Fluids through Porous Materials*, Reinhold Pub. Co. N.Y., N.Y. (1961).
22. Ma, S., Morrow, N.R., and Zhang, X.: "Generalised Scaling of Spontaneous Imbibition Data for Strongly Water-Wet Systems", paper CIM 95-138 presented at the 1995 South Saskatchewan Conference, Regina, SK, Oct. 16-18.
23. Kazemi, H., Gilman, J.R., and Elsharkawy, A.M.: "Analytical and Numerical Solution of Oil Recovery From Fractured Reservoirs with Empirical Transfer Functions", *SPE Resevoir Engineering* (May 1992),219-227.
24. Freeman, H.A. and Natanson, S.G.: "Recovery Problems in a Fracture Pore System – Kirkuk Field", Section II, paper 24, *Proc.* 5th Petroleum Congress (1959) 297-317.
25. Terez, I.E. and Firoozabadi, A.: "Water Injection in Water-Wet Fractured Porous Media: Experiments and a New Model Using Modified Buckley-Leverett Theory," *SPE Journal* (to be published).

Appendix A: Approximate Solution of 1-D Counter-Current Imbibition Problem

In an incompressible one-dimensional system with negligible gravity force, counter-current imbibition can be described by the following nonlinear diffusion equation[13],

$$\frac{\partial}{\partial x}\left(D(S_w)\frac{\partial S_w}{\partial x}\right)=\frac{\partial S_w}{\partial t} \tag{A-1}$$

where,

$$D(S_w)=\frac{1}{1+\frac{k_{ro}}{\mu_o}\frac{\mu_w}{k_{rw}}}\frac{k_{ro}}{\mu_o}\frac{k}{\phi}\frac{dP_c}{dS_w} \tag{A-2}$$

Consider a water-wet core of length L initially at connate water saturation, coated by an impermeable material such that only one face of the core is open to flow. When the open face is contacted with water, continuity of capillary pressure requires $P_c = 0$ at the inlet (see footnote[1]). The other end is closed; $q_w = 0$ at $x = L$. The initial and boundary conditions can be expressed as,

$$S_w = S_{wc} \qquad 0 \le x \le L \qquad t = 0 \tag{A-3}$$

$$S_w = 1 - S_{or} \qquad x = 0 \qquad t \ge 0 \tag{A-4}$$

$$\frac{\partial S_w}{\partial x} = 0 \qquad x = L \qquad t \ge 0 \tag{A-5}$$

The diffusion coefficient defined by Equation A-2 is a strong function of saturation. However, if temporarily we assume a constant diffusion coefficient, Equation A-1 with the initial and boundary conditions A-3 to A-5 can be solved analytically[15],

$$S_D = 1-\frac{4}{\pi}\sum_{n=1}^{\infty}\frac{\sin\left(\frac{2n-1}{2}\right)x_D}{2n-1}\exp\left[-\left(\frac{2n-1}{2}\right)^2\pi^2 t_D\right] \tag{A-6}$$

where,

$$S_D = \frac{S_w - S_{wc}}{1-S_{or}-S_{wc}} \tag{A-7}$$

$$x_D = \frac{x}{L} \tag{A-8}$$

$$t_D = \frac{Dt}{L^2} \tag{A-9}$$

We use the Heat Integral Method (HIM)[14] to provide an appropriate solution to the above linear diffusion problem. The advantage of using the HIM is that its application can be extended to solve nonlinear problems. The Heat Integral Method, one of the variations of the Method of Weighted Residuals[16], was previously used to solve diffusion-dominated problems in thermal recovery processes[17]. In this method, a

[1] In simple experiments, we examined oil expulsion from rock, in counter-current imbibition by visual observations. The diameter of the produced oil blobs on the rock surface was much larger than the pore diameter. This observation justifies the boundary condition of $P_c = 0$[18].

trial function is assumed, which in addition to satisfying the initial and boundary conditions, is forced to satisfy the integrated form of the original differential equation. Hence, the method is an appropriate choice for studying the problem of interest, since the total water imbibed into the system, which is an integral characteristic of the system, is obtained with high accuracy. For increased accuracy of the solution at early time, the concept of penetration depth is introduced which corresponds to the extent of the medium beyond which there is no effect of the diffusion process. For a linear diffusion problem, any change at the boundary is instantaneously transferred through the whole domain, where the effect is negligible beyond a certain limit. The penetration depth is analogous to the radius of investigation in well-testing. Barenblatt et al.[18] showed that for the initial condition of Equation A-3, the saturation at the front drops to connate water saturation and there is no effect of saturation change downstream of the front. This further justifies using the concept of penetration depth.

Pooladi-Darvish et al.[17] solved Equation A-1 approximately with the initial and boundary conditions given by Equations A-3 to A-5 using HIM, where the diffusion coefficient was assumed constant, and found the following solution,

$$S_D = \left(1 - \frac{x_D}{\sqrt{24 t_D}}\right)^3 \qquad t_D \le \tfrac{1}{24} \qquad \text{(A-10)}$$

$$S_D = 1 + b(t_D) x_D + c(t_D) x_D^2 \qquad 0 \le x_D \le \tfrac{1}{2} \qquad t_D \ge \tfrac{1}{24} \qquad \text{(A-11)}$$

$$S_D = 1 + b(t_D)\left(-\tfrac{1}{4} + 2x_D - x_D^2\right) + c(t_D)\left(-\tfrac{1}{2} + 2x_D - x_D^2\right) \qquad \tfrac{1}{2} \le x_D \le 1 \qquad t_D \ge \tfrac{1}{24} \qquad \text{(A-12)}$$

where,

$$b(t_D) = -A_1 e^{-\lambda_{D1} t_D} - A_2 e^{-\lambda_{D2} t_D} \qquad \text{(A-13)}$$

$$c(t_D) = \left(1 + \frac{\sqrt{2}}{2}\right) A_1 e^{-\lambda_{D1} t_D} + \left(1 - \frac{\sqrt{2}}{2}\right) A_2 e^{-\lambda_{D2} t_D} \qquad \text{(A-14)}$$

$$\lambda_{D1} = \frac{24}{7}\left(5 + 3\sqrt{2}\right) \qquad \text{(A-15)}$$

$$\lambda_{D2} = \frac{24}{7}\left(5 - 3\sqrt{2}\right) \qquad \text{(A-16)}$$

$$A_1 = \frac{6 - \sqrt{2}}{4} e^{\frac{5+3\sqrt{2}}{7}} \qquad \text{(A-17)}$$

$$A_2 = \frac{6 + \sqrt{2}}{4} e^{\frac{5-3\sqrt{2}}{7}} \qquad \text{(A-18)}$$

Equations A-10 to A-12 are used in the text to study imbibition.

Appendix B: Solution to Rising FWL Problem

By writing the material balance equation for water in the fracture, one obtains,

$$\int_0^t q_i(\tau)d\tau = A_f\hat{Z}_f + R'_\infty A_{ma}\left(\hat{Z}_f - \int_0^t e^{-\lambda(t-\tau)}\frac{\partial\hat{Z}_f}{\partial\tau}d\tau\right) \qquad \text{(B-1)}$$

where the left side is the total volume of water injected, and the right side represents the volume of water in the fracture, and the volume of water imbibed into the matrix represented by Equation 14 of the text. The water flow in the fracture is assumed to follow piston-like displacement with zero residual saturation, and the intrinsic fracture porosity is assumed to be one. If λ is known, $\hat{Z}_f(t)$ is the only unknown in Equation B-1, and can be solved for using a proper initial condition.

Differentiating Equation B-1 with respect to t results in

$$q_i(t) = A_f\frac{\partial\hat{Z}_f}{\partial t} + \lambda R'_\infty A_{ma}\int_0^t e^{-\lambda(t-\tau)}\frac{\partial\hat{Z}_f}{\partial\tau}d\tau \qquad \text{(B-2)}$$

By eliminating the right integral from Equations B-1 and B-2, one obtains,

$$\frac{\partial\hat{Z}_f}{\partial t} + \lambda\left(1+\frac{R'_\infty A_{ma}}{A_f}\right)\hat{Z}_f = \frac{q_i(t)}{A_f} + \frac{\lambda}{A_f}\int_0^t q_i(\tau)d\tau \qquad \text{(B-3)}$$

For a constant injection rate and initial condition of $\hat{Z}_f(t=0)=0$, Equation B-3 can be integrated to obtain a simple closed-form solution for the fracture-water level,

$$\hat{Z}_f(t) = \frac{q_i}{BA_f}\left[\left(1-\frac{\lambda}{B}\right)\left(1-e^{Bt}\right)+\lambda t\right] \qquad \text{(B-4)}$$

where,

$$B = \left(1+\frac{R'_\infty A_{ma}}{A_f}\right)\lambda \qquad \text{(B-5)}$$

Equation B-4 is valid before breakthrough. During this interval, oil production rate is equal to injection rate. After breakthrough, the water level stays at the top of the block, and the oil production rate can be expressed as,

$$q_o = \lambda R'_\infty A_{ma}\left[\int_0^{t_{BT}} e^{-\lambda(t_{BT}-\tau)}\frac{\partial\hat{Z}_f}{\partial\tau}d\tau\right]e^{-\lambda(t-t_{BT})} \qquad \text{(B-6)}$$

where t_{BT} is the breakthrough time. For a variable injection rate, Equation B-2 can be solved numerically, similar to that proposed in reference 23. Alternatively, Equation B-3 can be solved numerically, for example using the Runge-Kutta method. Note that Equations B-2 and B-3 are valid when injection rate is more than the imbibition rate, i.e. water level is rising, and also when the injection rate is less than imbibition rate, i.e.

water level is dropping. The above solutions are used in the text to model water injection in a stack of Austin chalk matrix blocks.

Table 1: Rock and Fracture Data for Advancing FWL Tests			
	Berea Sandstone	**Chalk (12 blocks)**	**Chalk (single block)**
Total Pore Volume×10^6 (m^3)	8800	13900	1050
Total Fracture PV×10^6, (m^3) Including dead volumes	250	700	40
Fracture aperture (μm)	155	190	170
Effective Permeability ((μm^2)	9.5	17	16
Matrix Permeability (μm^2)	0.620	0.002-0.005	0.002-0.005
Matrix Porosity (percent)	22	29.6	29
Matrix dimensions (m)	0.1471×0.1471×0.6047	0.635×0.1875×0.3048	0.635×0.1875×0.3048

Table 2: Rock and Fluid Data for the Counter-Current Study			
L	0.20 m	S_{Di}	0.01
k	0.020 μm^2	n_o	4.0
μ_o	1 mPas	n_w	4.0
μ_w	1 mPas	A_o	0.75
ϕ	0.3	A_w	0.2
C	10 kPa		

Table 3: Counter-Current Imbibition Data		
Reference	**Length, m**	**Permeability, μm^2**
Graham and Richardson (G-R)[21]	0.125	0.236[a]
Graham and Richardson[21]	0.1008	0.236
Graham and Richardson[21]	0.0756	0.236
Graham and Richardson[21]	0.0502	0.236
Graham and Richardson[21]	0.0248	0.236
Hamon and Vidal (H-V)[20]	0.852	4.070
Hamon and Vidal[20]	0.40	4.400
Hamon and Vidal[20]	0.198	3.200

a- Permeability was assumed constant

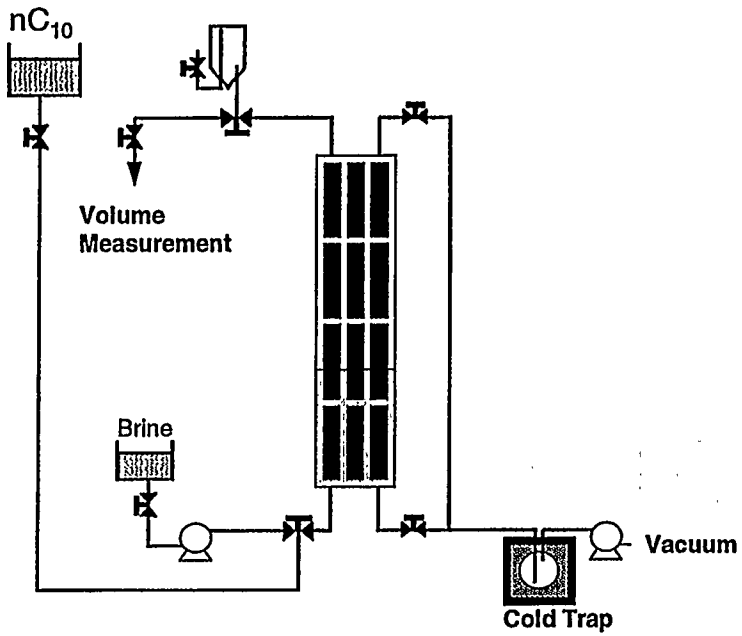

Figure 1. Schematic digram of the apparatus

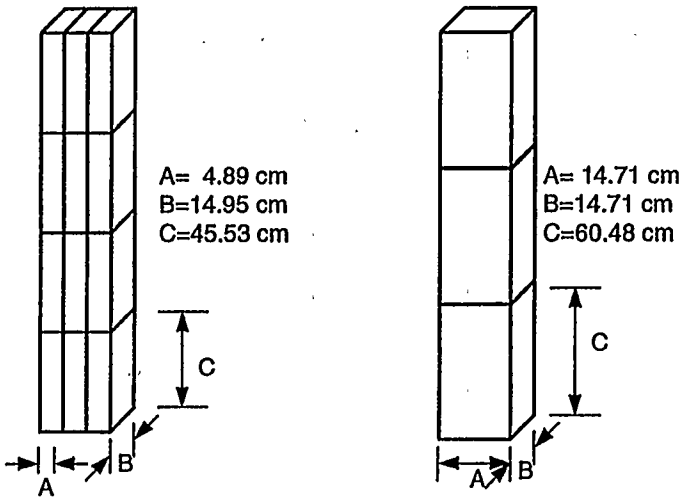

Figure 2. The rock assembly for SB and SS tests

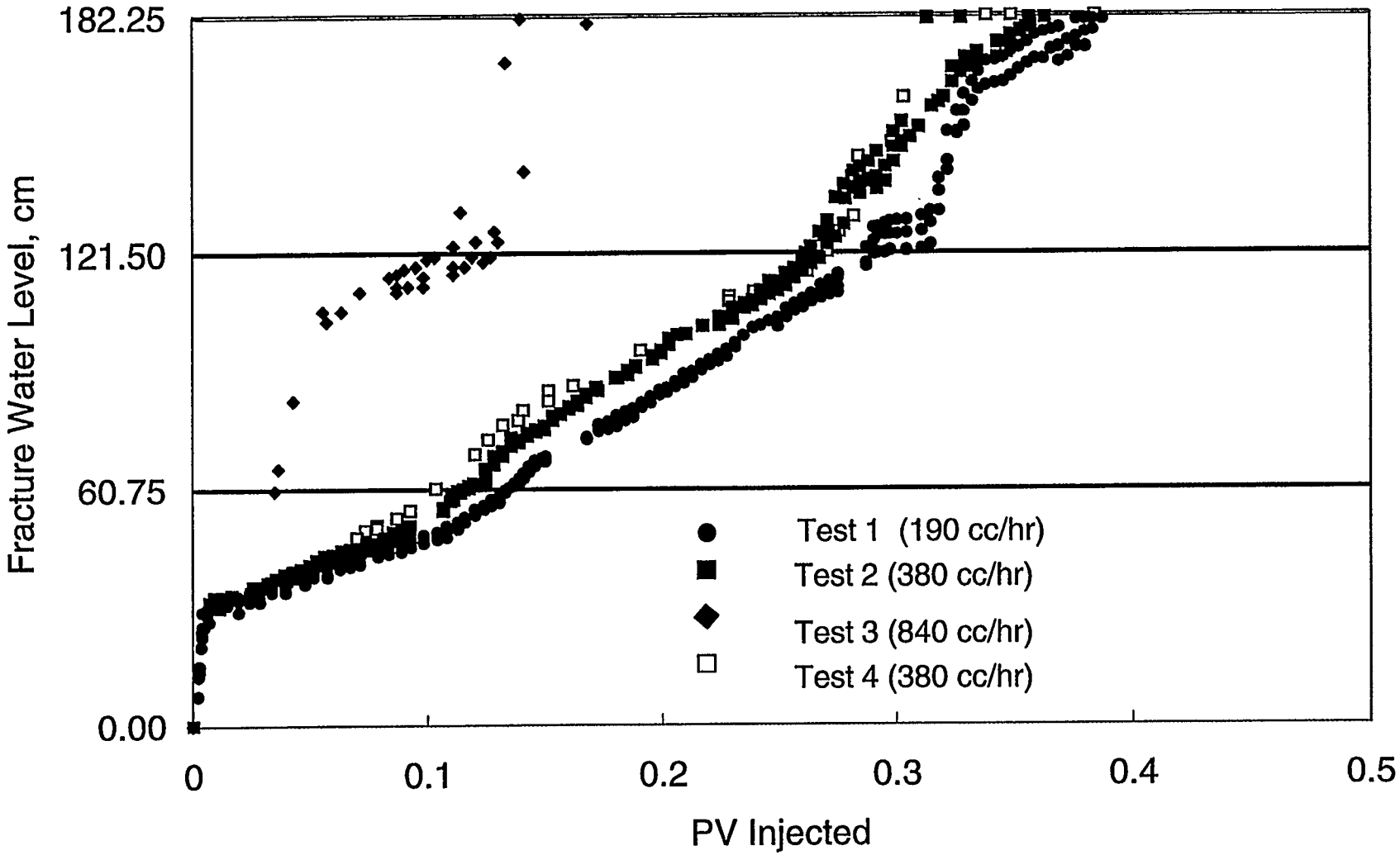

Figure 3. Fracture water level for tests 1 to 4

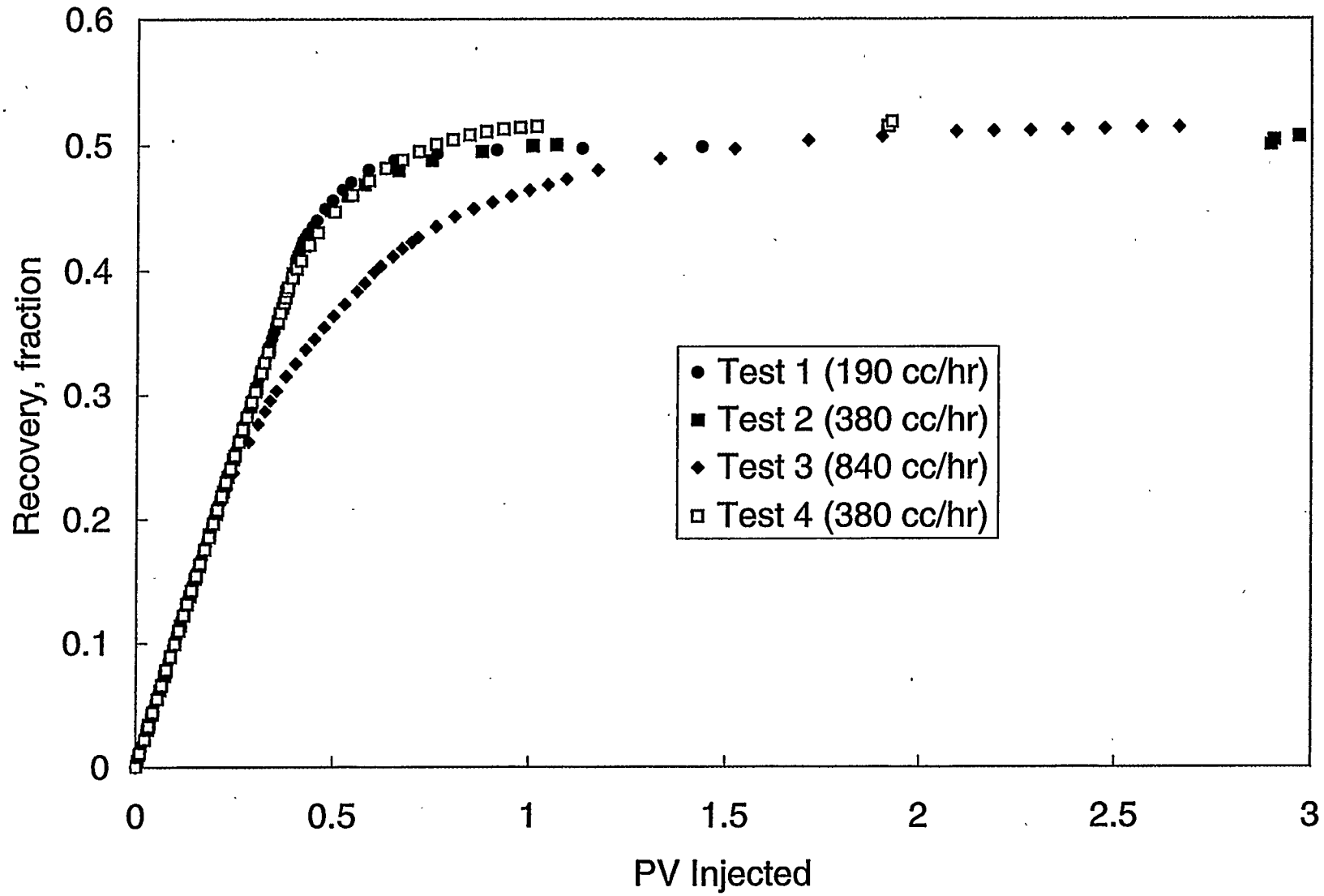

Figure 4. Recovery for tests 1 to 4

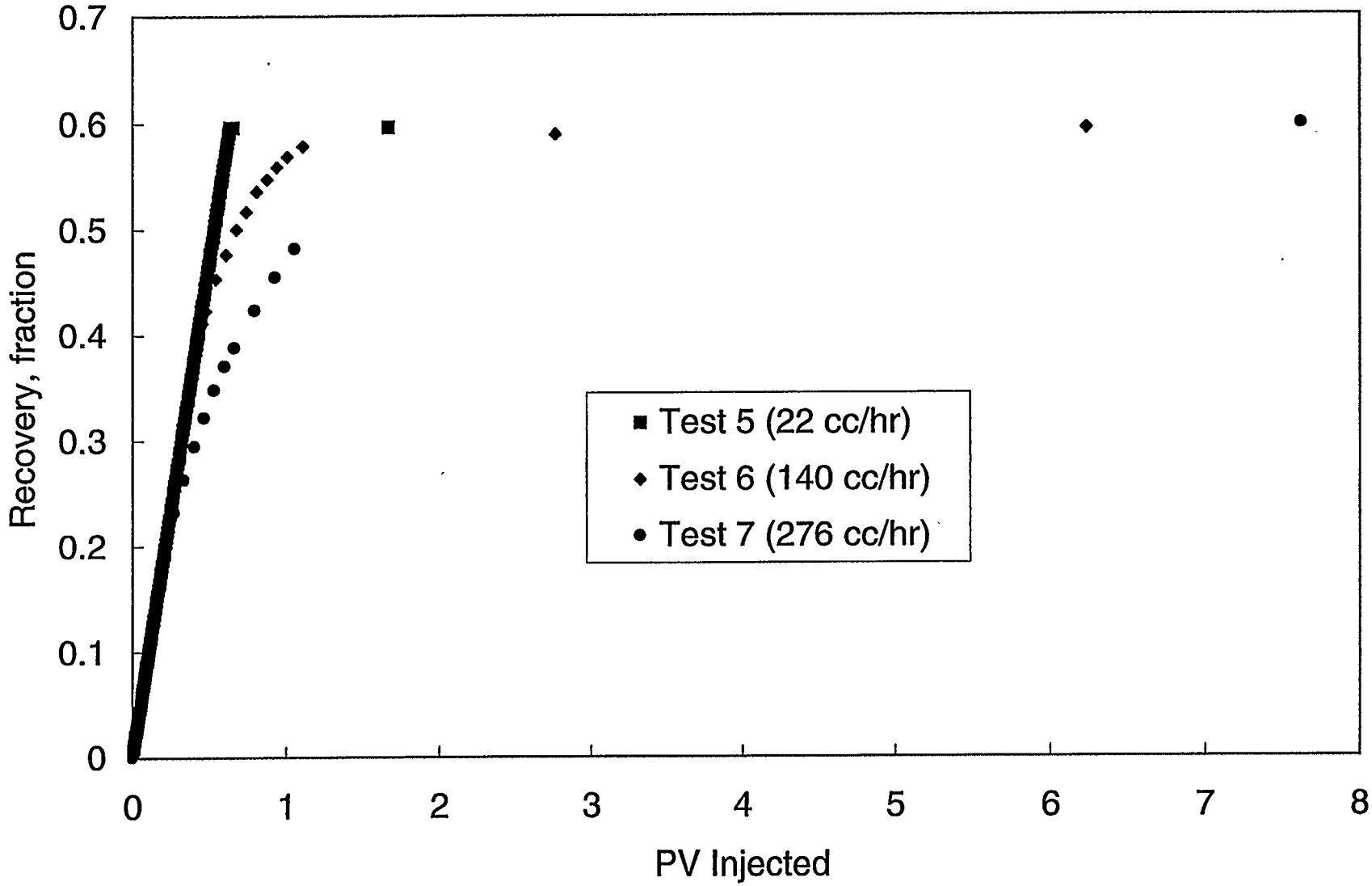

Figure 5. Recovery for tests 5 to 7

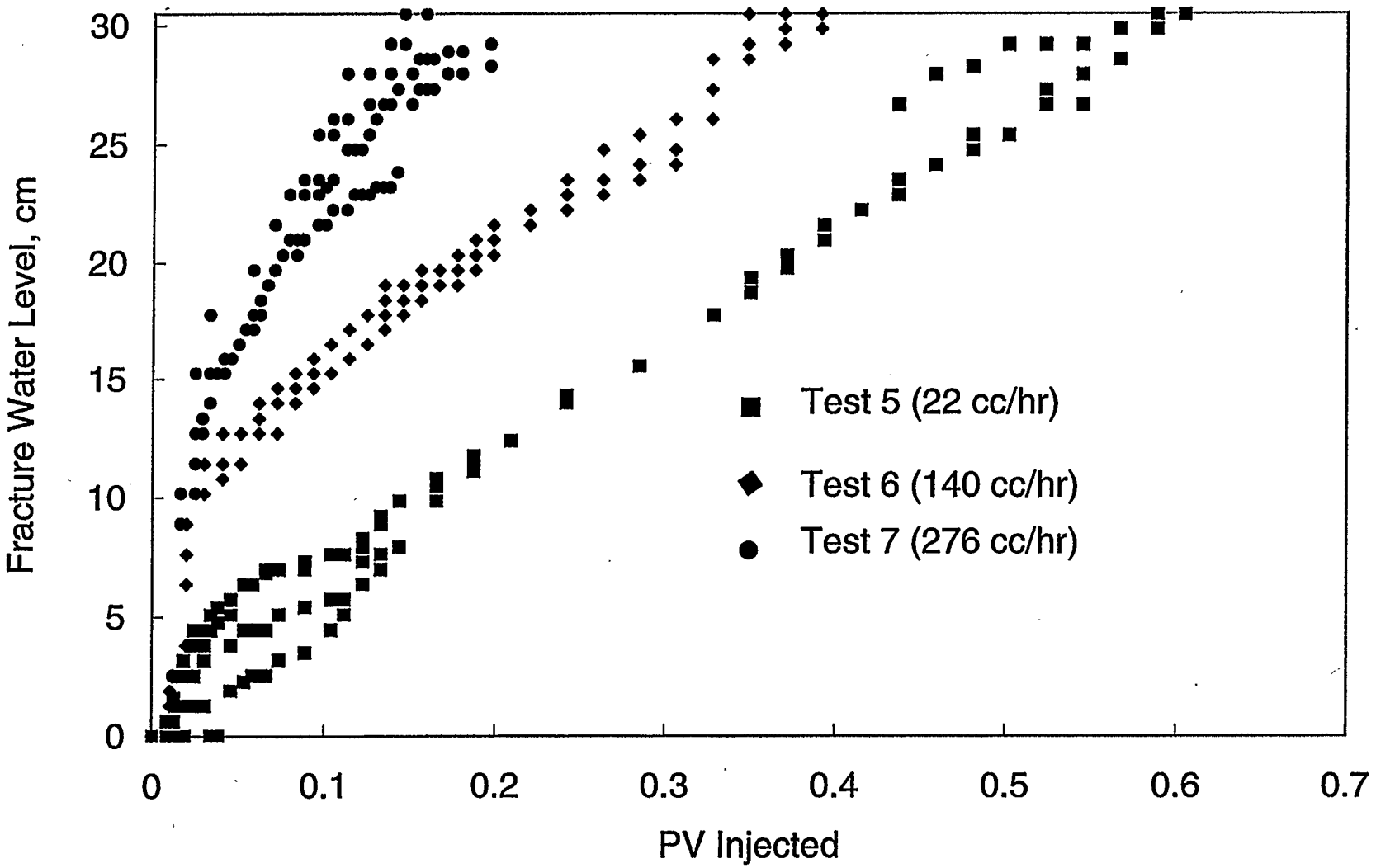

Figure 6. FWL for tests 5 to 7

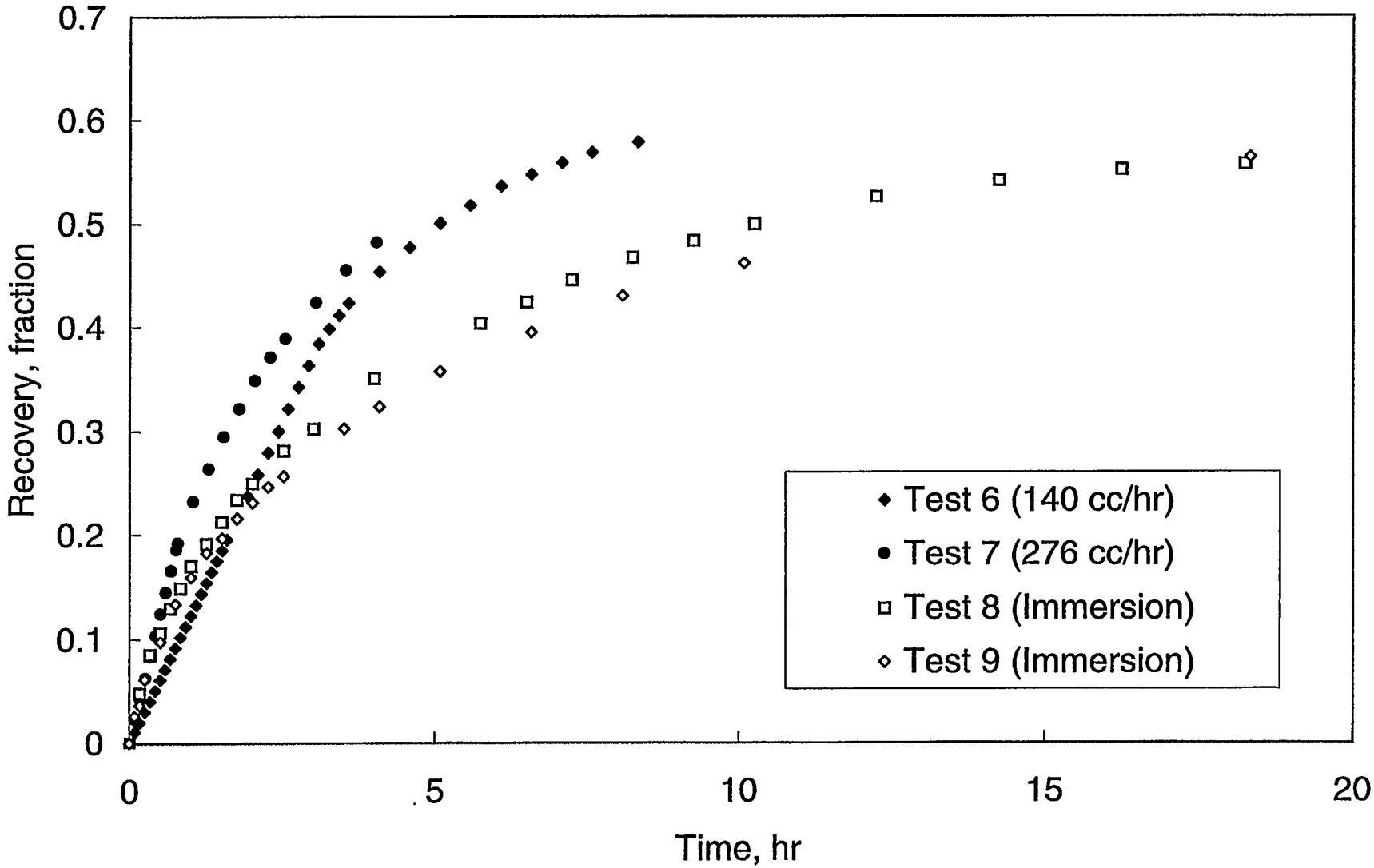

Figure 7. Recovery for tests 6 to 9

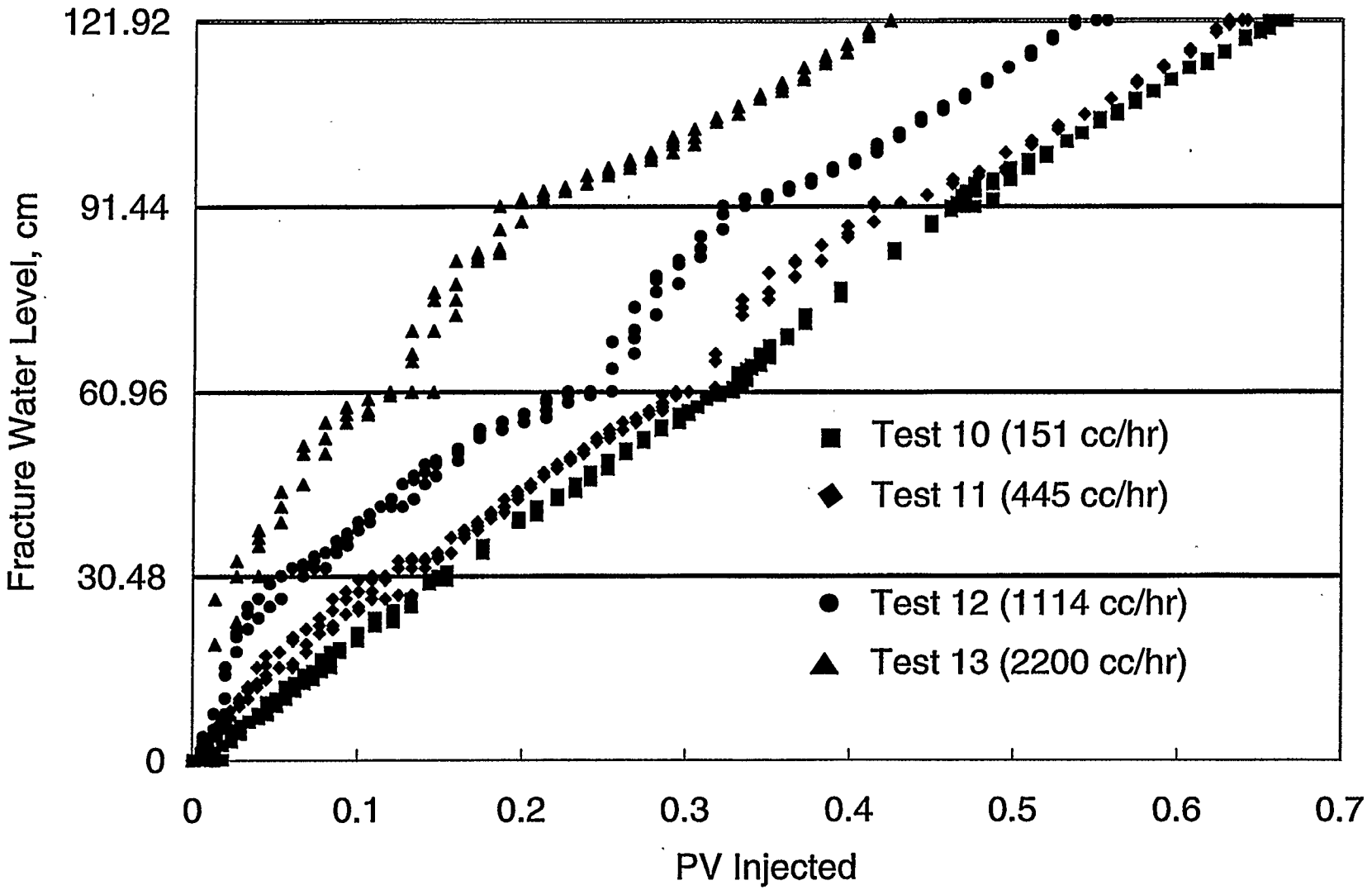

Figure 8. FWL for tests 10 to 13

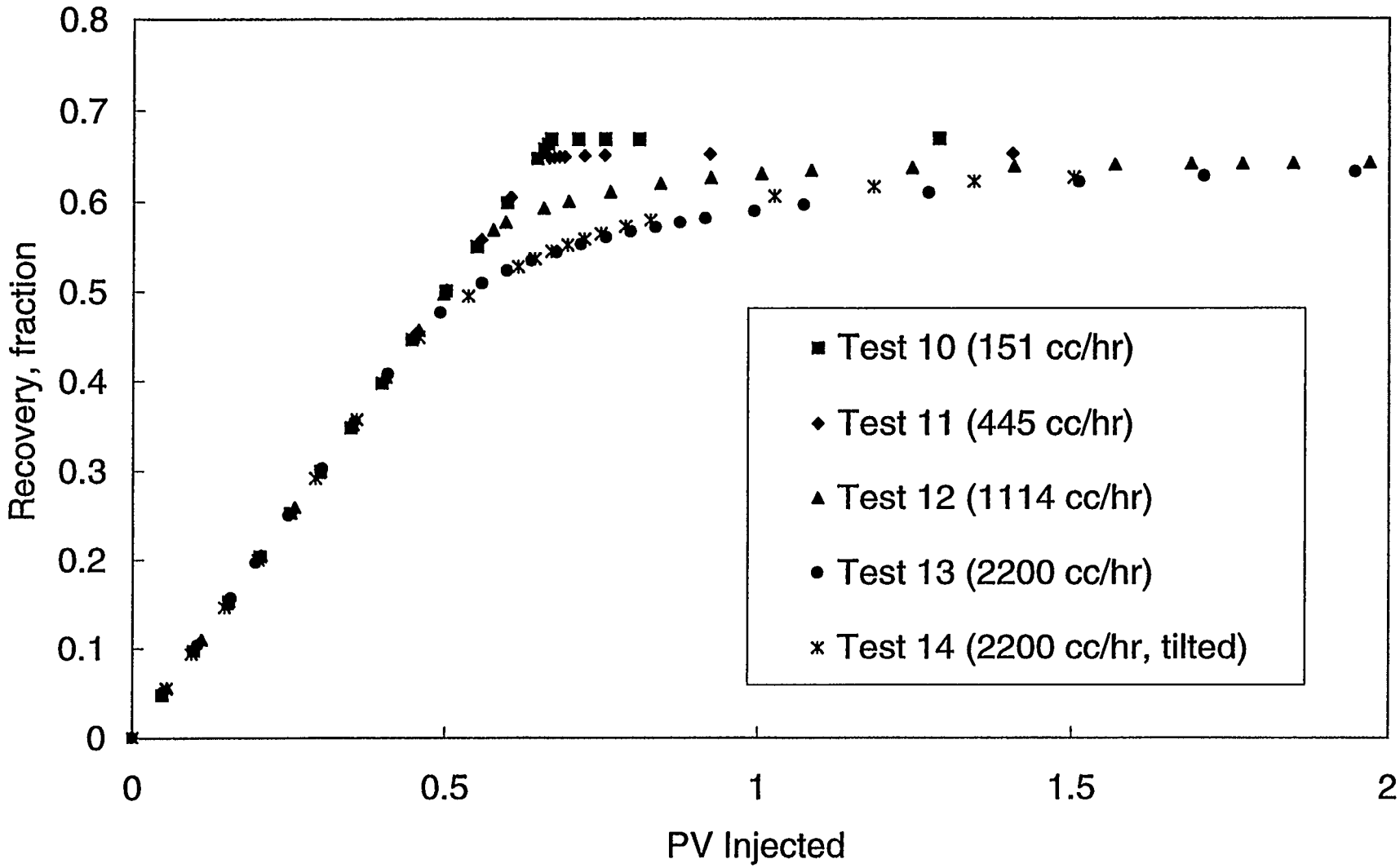

Figure 9. Recovery for tests 10 to 14

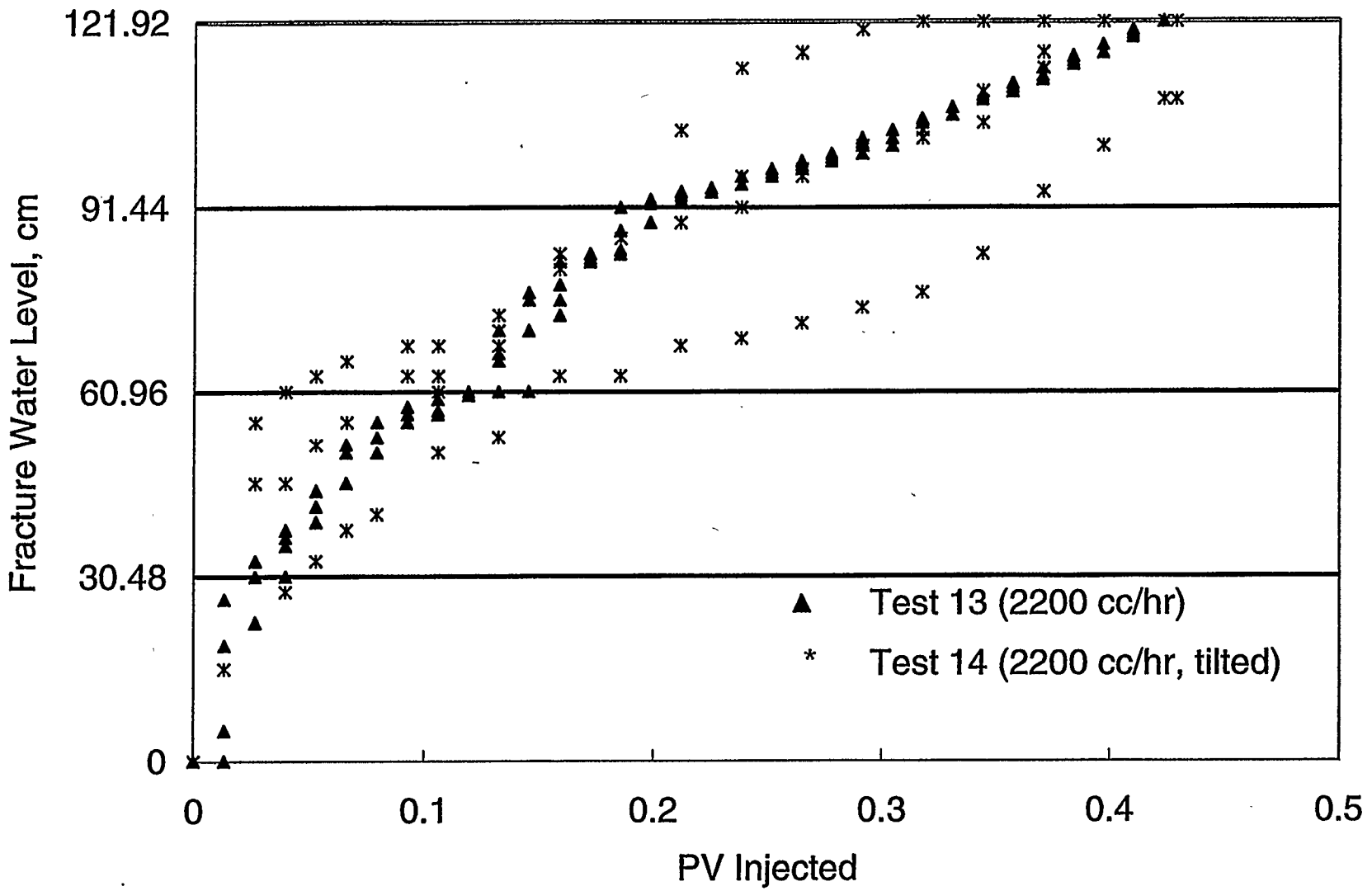

Figure 10. FWL for tests 13 and 14

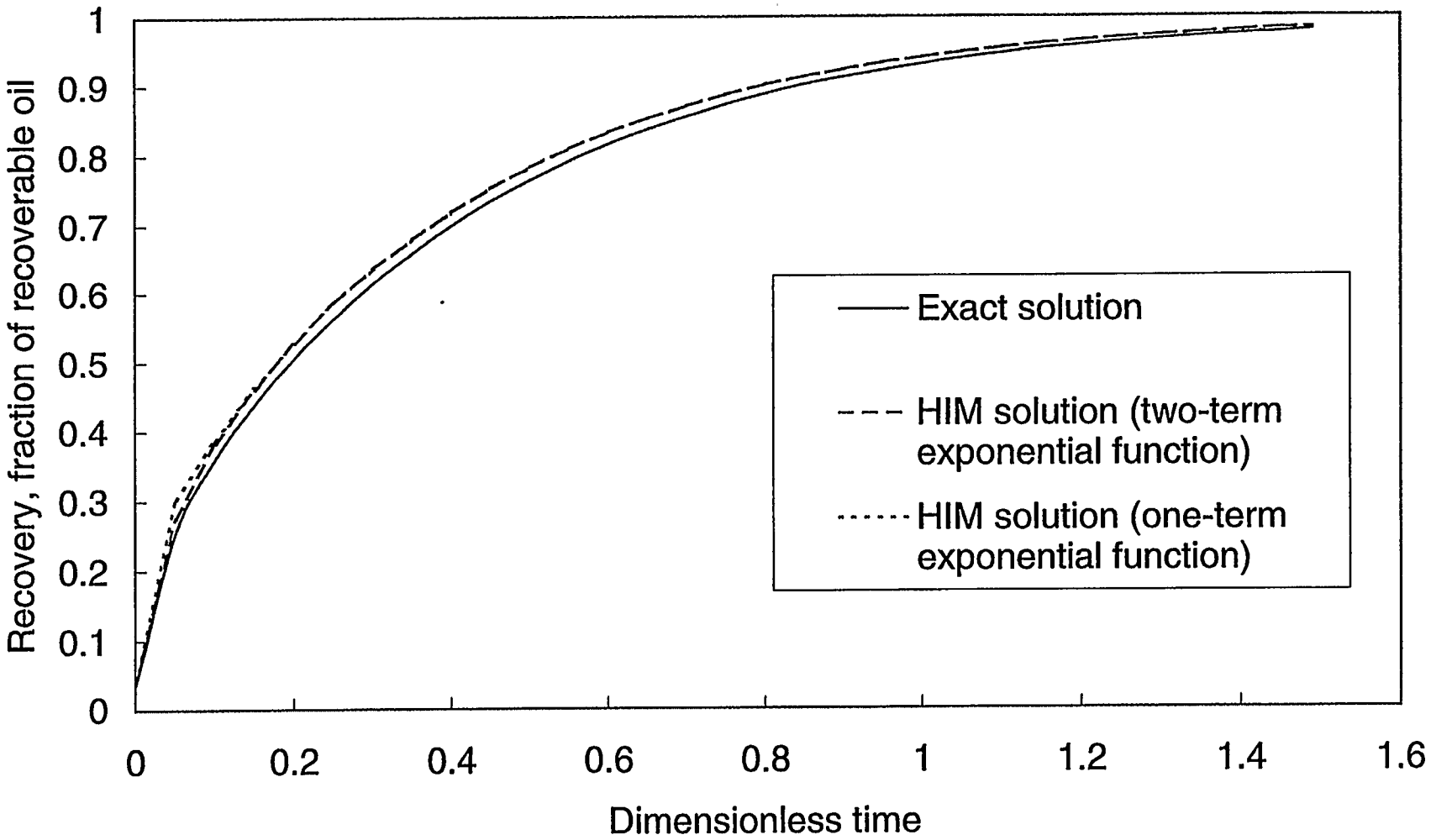

Figure 11. Solution to the linear diffusion equation

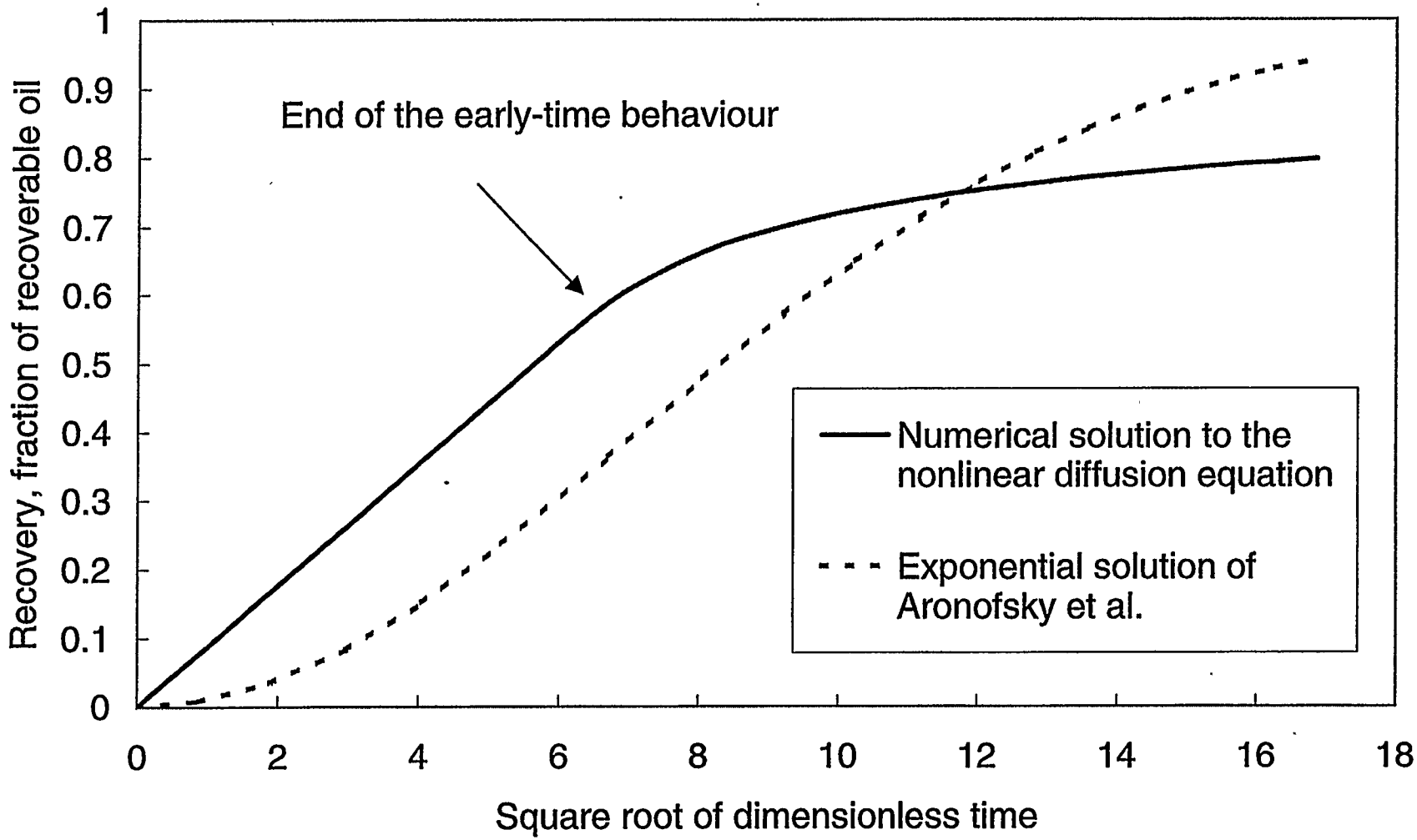

Figure 12. Early time behaviour of counter-current imbibition

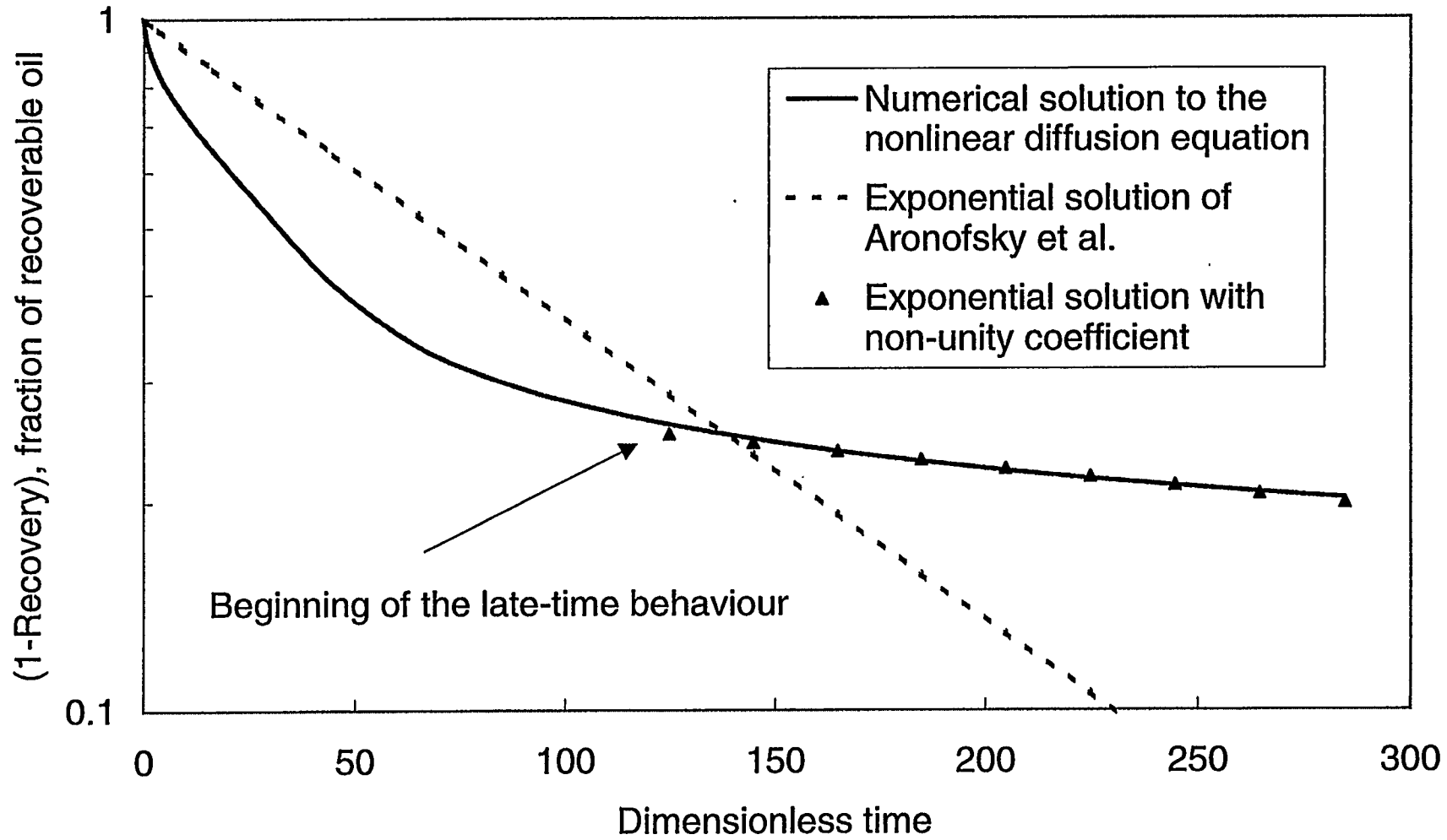

Figure 13. Late-time behaviour of counter-current imbibition

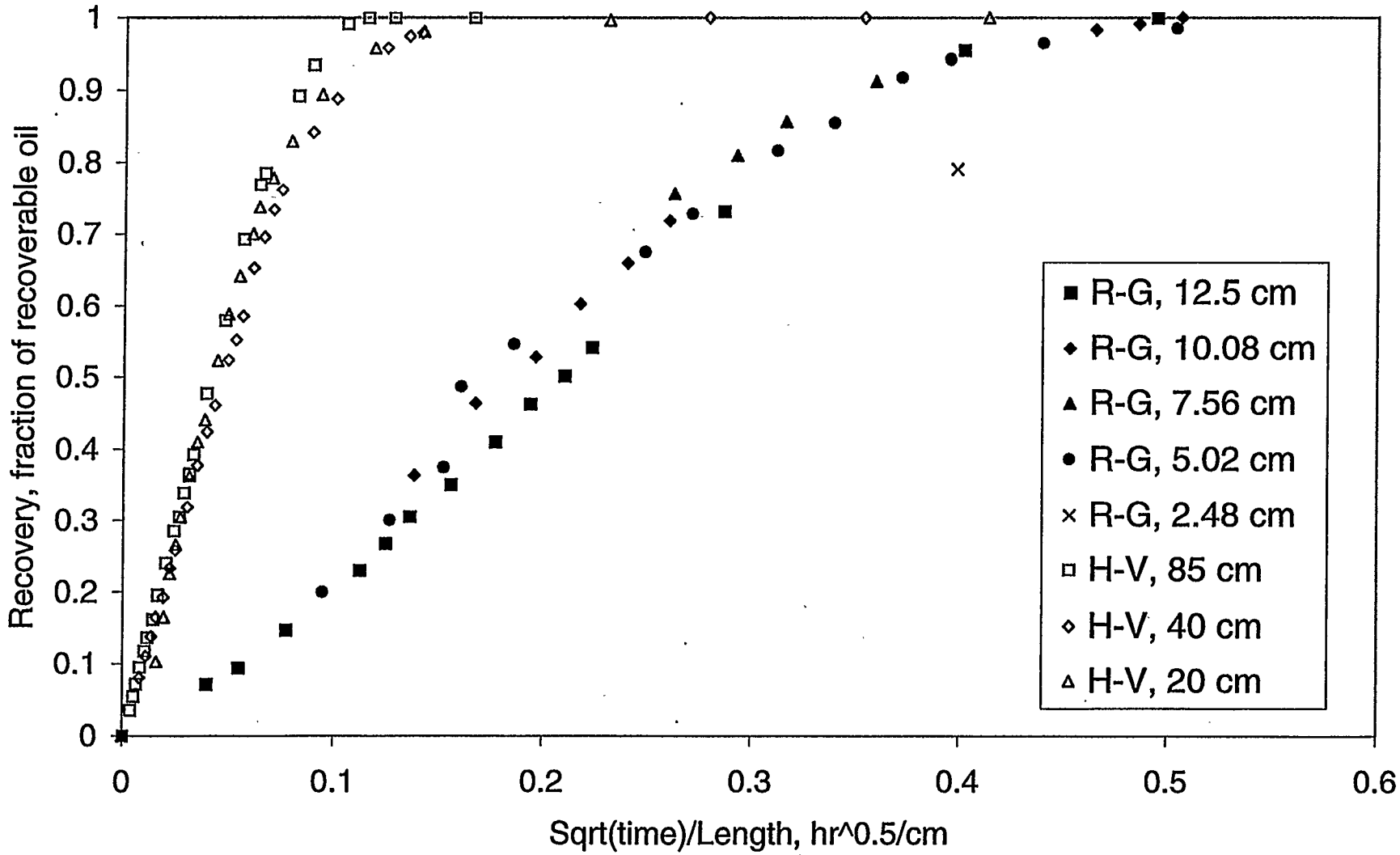

Figure 14. Early-time behaviour of counter-current imbibition tests

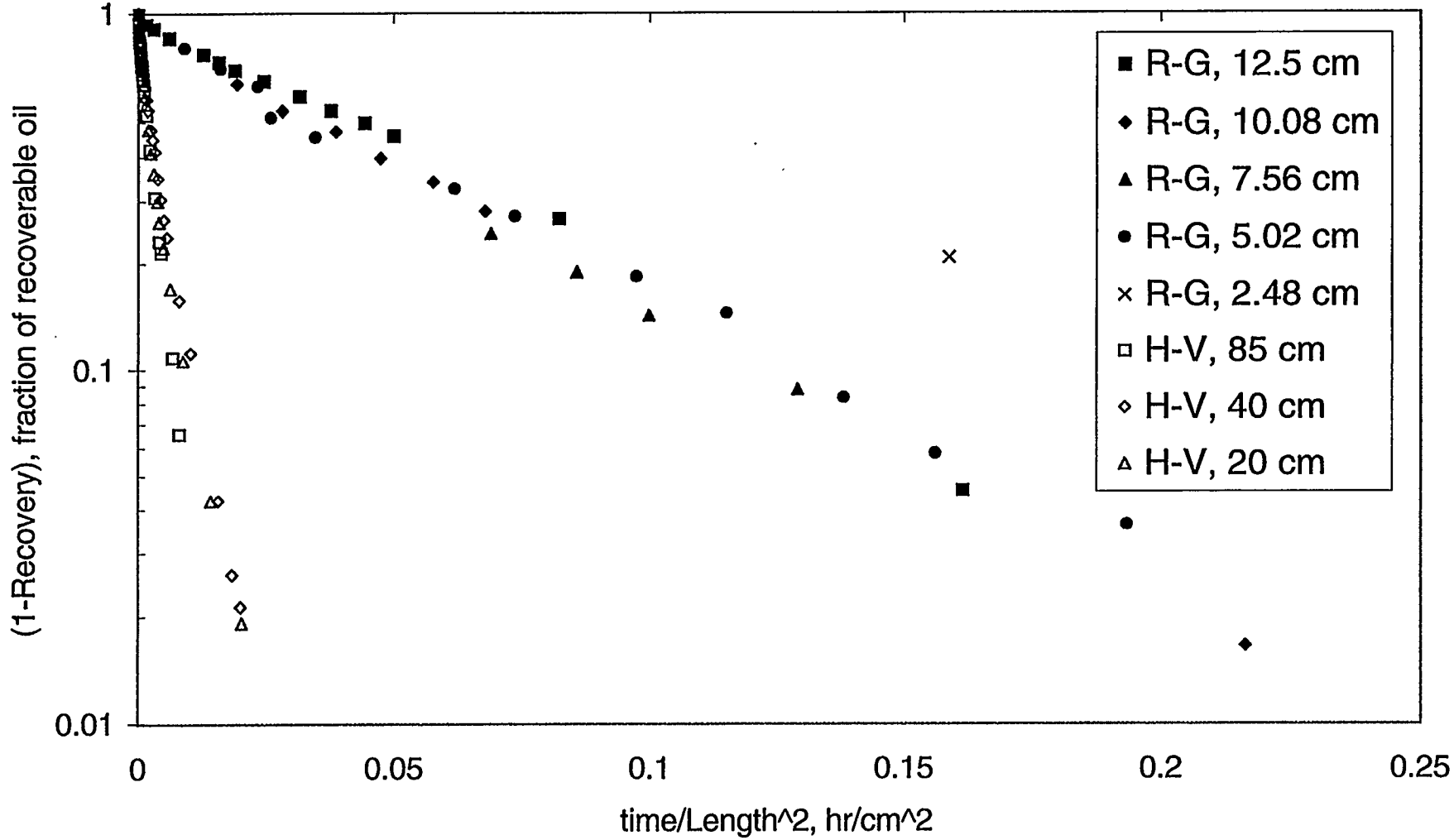

Figure 15. Late-time behaviour of counter-current imbibition tests

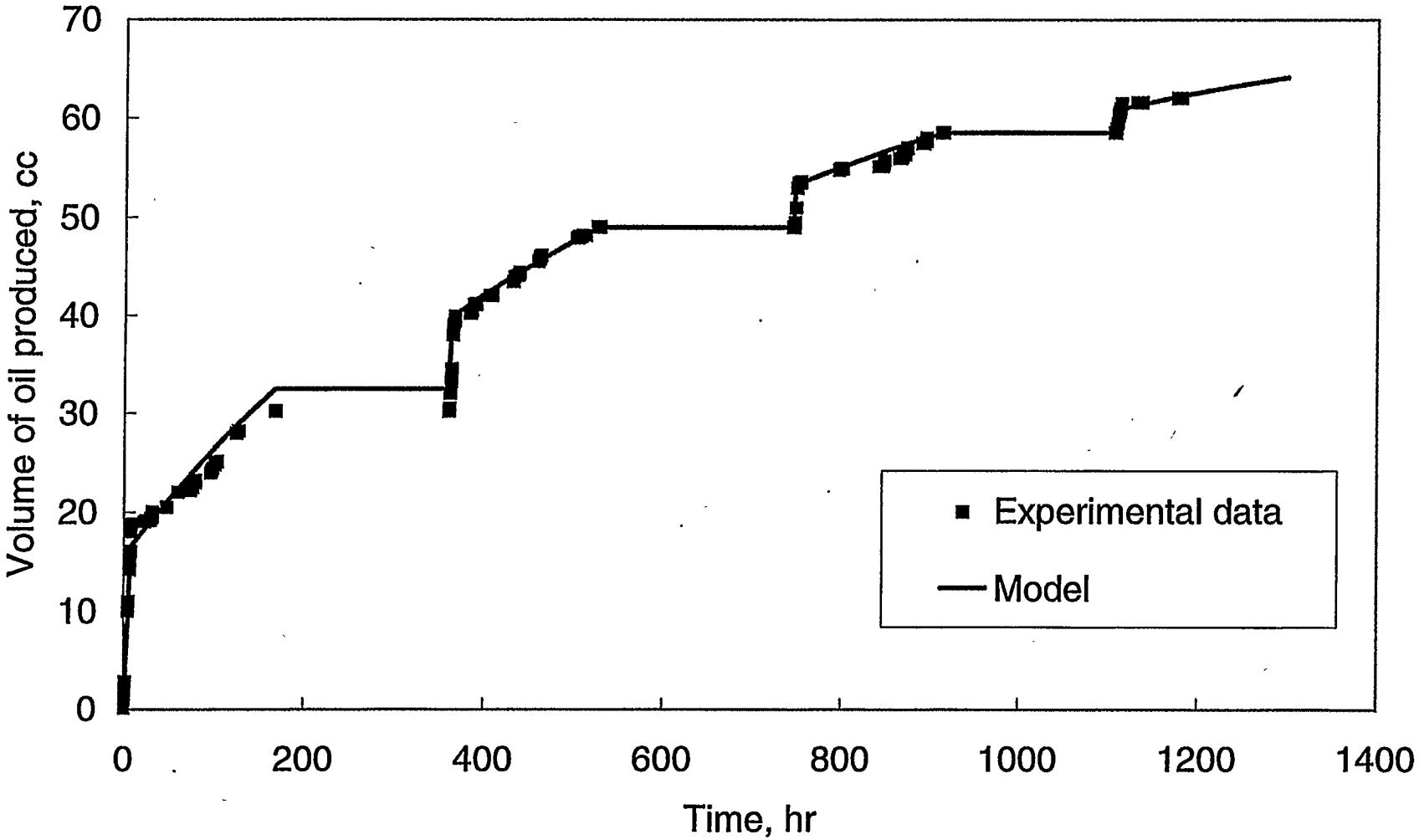

Figure 16. Modelling of the Austin chalk test

Part II – Water Injection in Water-Wet Fractured Porous Media: Further Experiments and a New Model for Water Injection in Water-Wet Fractured Porous Media

IVAN E. TEREZ AND ABBAS FIROOZABADI

Summary

This study examines water injection in water-wet fractured porous media and its modeling using the Buckley-Leverett theory. New experimental data on water injection in Berea and Austin chalk matrix block(s) are presented. Water injection in Austin chalk with a permeability of 0.01-0.04 md and porosity of 5% results in about 20% recovery from the rock matrix.

In the second part of the paper, we use the Buckley-Leverett displacement in a dual-porosity model to simulate the literature data as well as experimental data from this work. A new model is devised for the simulation of water injection in fractured porous media. A major element of the new model is the multiplication of the transfer flux by the fracture saturation with a power of 1/2. This simple model can account for both co-current and counter-current imbibition and computationally it is very efficient. The results of the proposed model and the fine-grid simulation are in good agreement with the experimental data.

Introduction

Water injection has been an efficient recovery process in some naturally fractured hydrocarbon reservoirs. Despite the success, the understanding of the true mechanisms and the numerical simulation have to be advanced further. In fact, accurate simulation of water injection in fractured porous media is a real challenge. Fine-grid simulation can provide proper results when fracture capillary pressure and relative permeability are appropriately described; computationally, however, it is very expensive. Dual-porosity models have the advantage of computational efficiency but may be less accurate. A third alternative which can be extremely efficient is the use of the Buckley-Leverett displacement theory[1] in a dual-porosity model. Here, matrix blocks feed into the fracture network through a transfer term; flow in the fractured media is represented by the Buckley-Leverett displacement. In an early paper, de Swaan[2] modeled water displacement in fractured porous media on the basis of the Buckley-Leverett displacement theory. De Swaan's work is based on certain assumptions; these include: 1) the fracture fractional flow function is equal to the fracture saturation (i.e., $f_w^f = S_w^f$, see the Nomenclature), and 2) the effect of gravity is negligible. The assumption of $f_w^f = S_w^f$ is valid only when oil and water phases have equal viscosities and the fracture relative permeability is equal to saturation. Later, Chen and Liu[3] relaxed the assumption of $f_w^f = S_w^f$. Kazemi, Gillman and Elsharkawy[4] gave examples for the Buckley-Leverett flow in a 1D fractured porous media using a model similar to de Swaan's. These authors reported good agreement with experimental data using an empirical transfer term between the fracture and the matrix. Kazemi *et al.*, however, changed the oil viscosity from 4.6 to 0.25 cp to match the laboratory data. The λ parameter of the empirical transfer term was based on the general imbibition recovery data (see Fig. 1 of Ref. 4).

The basic idea behind the transfer term in the literature is the use of counter-current imbibition data for a single matrix block. Pooladi-Darvish and Firoozabadi[5,6] have shown that counter-current imbibition may not

describe recovery from a matrix block when the water level advances in the fracture. The source term in the flow equations in the Buckley-Leverett expression for a dual-porosity model is in fact based on a moving fracture water level with saturation change (we will discuss the equations shortly). The moving water level may imply that co-current imbibition should also be considered.

The major goal of this study is to model water injection in water-wet fractured porous media considering both co-current and counter-current imbibition in the Buckley-Leverett flow. The model will be used to analyze the laboratory data. (A large portion of some fractured reservoirs in the North Sea are strongly water-wet and, therefore, water injection in water-wet fractured media is of practical interest.)

In this work, we first report experimental data on water injection in matrix blocks. Two types of rock were used in the experiments: 1) Berea sandstone, and 2) Austin chalk. In the second part, we present mathematical formulation for flow in fractured porous media; water imbibition in a single matrix block for various injection rates is also examined. Using the transfer term from a single block, water imbibition in an aggregate of several matrix blocks is then predicted.

Experimental Results

An extensive set of data on water injection in Berea sandstone and Kansas outcrop chalk for an aggregate of matrix blocks is presented in Ref. 5. The rock assemblies used in those experiments are shown in Figs. 1a, 1b and 1c. In addition to the stacked block experiments, Ref. 5 also provides experimental data on imbibition performance of a single matrix block of the Kansas outcrop chalk shown in the right side of Fig. 1a. In this work, we have performed water injection experiments on 1) a single Berea slab (see Fig. 1b, the right side), 2) a single Berea block (see Fig. 1c, the right side), and 3) a stack of Austin chalk blocks (see Fig. 1d). The experimental setup is similar to the one used by Pooladi-Darvish and Firoozabadi[5]. The purpose of water injection tests in a single slab or a block is to further improve the understanding of co-current and counter-current imbibition. For the tight Austin chalk of about 0.01 md permeability, the goal is to find out if any oil can be recovered from a very tight rock.

In all the experiments, 1% brine was used as the injection water, and the porous media was saturated with normal decane (Austin chalk was saturated with normal hexane), and the water was injected from the bottom. We did not establish initial water saturation in our experiments. The effect of the initial water saturation (S_{wi}) is, in general, as increase in the imbibition rate for a water-wet porous medium at early time, followed by a decrease in recovery at late stages. Extensive set of tests show that the variation of initial water saturation in the range of 0 to 40 percent does not have a significant effect on the imbibition performance of strongly water-wet Berea (The results will be published later). *Viskund et al.*[7], also report a small variation in the oil recovery with change in initial water saturation for Berea. For chalk, these authors report an overall tendency for imbibition rate to first increase with increase in S_{wi} and then decrease slightly with increase in S_{wi} of about 34 percent. In view of the fact that in some of the water-wet fractured reservoirs with a tight rock matrix, the initial water saturation is low, around 5 to 10 percent[8], we have conducted all of our experiments without initial water saturation. In the following, we present the results.

Berea sandstone. Two tests were conducted using the single Berea slab (dimensions are given in Fig. 1b): 1) an immersion test, and 2) an injection test at a rate of 2.7 PV/day. The porosity of the matrix was 22%, and the matrix PV was 684 cm^3. The average vertical and horizontal permeabilities for the slab were 630 and 730 md, respectively. These values are based on minipermeability measurements. In the setup used for the single matrix slab, the fracture aperture surrounding the slab was 4.7 *mm*, and the corresponding fracture PV was

880 cm^3. The imbibition results are presented in Fig. 2. Note that the data in the figure are based on the matrix PV. Also note that the last data point in Fig. 2b and some other plots shows final recovery beyond the time scale of the plot.

Two tests were also conducted using the single Berea block (dimensions shown in Fig. 1c): 1) an immersion test, and 2) an injection test at a rate of 0.75 PV/day. The porosity of the matrix rock was 22%, and the matrix PV was 2860 cm^3. The average permeability for the block was 650 md. In the setup used for the single matrix block, the fracture aperture surrounding the slab was 130 μm and corresponding fracture PV was 46 cm^3. Fig. 3 shows the oil recovery (*i.e.*, normal decane recovery) in terms of PV of the matrix vs. time. For all four tests, we performed duplicate runs with excellent reproducibility. Unique features of the immersion and injection tests are: 1) the residual oil saturation is higher for the immersion tests (*i.e.*, counter-current imbibition), and 2) unlike the results from the Kansas chalk (see Ref. 5), the rate of imbibition is slower for water injection tests than for that of the immersion tests. The rate is related to the surface area of the flooded matrix, and in the immersion test, the whole block is flooded instantaneously. The imbibition in the immersion test is only due to counter-current while in the injection test both co-current and counter-current contribute to imbibition. Residual oil saturations for the immersion tests were higher than that from the injection tests. Ref. 5 also reports higher residual oil saturation for the immersion test for the Kansas chalk.

Austin chalk. The setup used to perform water injection on the Austin chalk is shown in Fig. 1d. Three water injection tests were carried out on the assembly of six cylindrical cores. The length, permeability, porosity, and PV of the cores are shown in Table 1. The diameter of each core was 8.54 *cm*. The total PV of the matrix was around 287 cm^3. The space between the core and the coreholder provided the vertical fracture. Special design allowed a hydraulic aperture of 38 μm. The fracture PV around the matrix was estimated as 4 cm^3, and the effective permeability of the combined matrix/fracture system was measured as 150 md using liquid nC_6 . Water injection recoveries are presented in Fig. 4. In the first two tests, the cores were saturated with nC_6 and then water was injected. In the third test, about 1 weight percent of a 35 API crude was added to nC_6, and the cores were saturated with the mixture. When a small amount of a crude is diluted into normal alkanes such as nC_6 and nC_7, the waterflood performance may become essentially the same as that of the original reservoir crude (see Ref. 9). In all three tests, the imbibition rate was so slow that water injection was stopped several times in order to allow water imbibition into the tight matrix blocks. The injection rates of 0.17 and 0.25 PV/day for the three test are close; therefore, the effect of rate on recovery performance cannot be studied. Fig. 4 shows that water injection in the tight Austin chalk results in 19-23 % recovery.

Model Formulation

In the following, we will present expressions for water displacement in fractured porous media using the Buckley-Leverett flow. Similar expressions have been derived by Chen and Liu[3].

Modified Buckley-Leverett Model (BLM). We consider one-dimensional flow with the vertical upward direction z. Darcy's law for water and oil phases in the fracture medium is:

$$u_w = -\frac{k^f k_{rw}^f}{\mu_w}\left(\frac{\partial p}{\partial z} + \rho_w g\right) \quad \text{.....(1)}$$

$$u_o = -\frac{k^f k_{ro}^f}{\mu_o}\left(\frac{\partial p}{\partial z} + \rho_o g\right) \quad \text{.....(2)}$$

where u_w is the velocity of water phase, ρ_w is water density, μ_w is water viscosity, k_{rw}^f is water relative permeability in the fracture, u_o is the velocity of oil phase, ρ_o is oil density, μ_o is oil viscosity, k_{ro}^f is oil relative

permeability in the fracture, p is the pressure in the fracture medium, and g is the acceleration of gravity. Note that the fracture capillary pressure is assumed zero.

Continuity equation for water phase is:

$$\frac{\partial u_w}{\partial z} + q_w = -\phi_e^f \frac{\partial S_w^f}{\partial t} \quad \text{.....(3)}$$

where q_w is the transfer term representing the fluid exchange rate per unit matrix pore volume, and ϕ_e^f is the effective fracture porosity. The effective fracture porosity is defined as the fracture volume divided by the bulk volume of the total matrix and fracture.

The fluids are assumed incompressible, therefore:

$$u_w + u_o = i_n(t) \quad \text{.....(4)}$$

where $i_n(t) = i(t)/A$ is the injection rate $i(t)$ normalized by the cross-sectional area A of the matrix and fracture media.

Combining Eqs. 1 to 4, one obtains:

$$[i_n(t) f'(S_w^f) - (\rho_w - \rho_o) g F'(S_w^f)] \frac{\partial S_w^f}{\partial z} + \phi_e^f \frac{\partial S_w^f}{\partial t} + q_w = 0 \quad \text{.....(5)}$$

where

$$F(S_w^f) = f(S_w^f) k^f \frac{k_{ro}^f}{\mu_o} \quad \text{.....(6)}$$

and

$$f(S_w^f) = 1/(1 + \frac{\mu_w}{\mu_o} \frac{k_{ro}^f}{k_{rw}^f}) \quad \text{.....(7)}$$

In Eq. 5, the symbol " ' " represents derivative with respect to S_w^f.

Next we discuss how to obtain the transfer term q_w. Aronofsky *et. al.*[10] have shown that the cumulative production per unit pore volume of the matrix block for counter-current imbibition can be expressed by $W_p(t) = N_{pa}(1 - e^{-\lambda t})$, where N_{pa} is the ultimate cumulative production per unit pore volume, and λ is an imbibition parameter. In general, prior to the time that a block is immersed in water, the oil recovery is a result of both co-current and counter-current imbibition[6]. After a block is completely immersed in water, counter-current imbibition is the only imbibition process. We may, therefore, need to modify the expression for the cumulative imbibition to $W_p(t) = N_{pa} - R_1 e^{-\lambda_1 t} - R_2 e^{-\lambda_2 t}$ (*i.e.*, $N_{pa} = R_1 + R_2$). The first exponential term may represent co-current imbibition and the second one can account for counter-current imbibition. This expression with three empirical parameters also provides a better representation of the counter-current imbibition and is similar to that of Civan[11] except for the coefficients of the exponential terms. (In the work of Civan, the coefficients of the exponential terms are related to λ_1 and λ_2.) The transfer rate is given by $q_w = dW_p/dt$, when the water saturation is kept at $S_w^f = 1$. However, with a constant saturation less than unity, q_w is assumed to be $(S_w^f)^m dW_p/dt$. In previous models[2,3,4], it has been assumed that the transfer term is proportional to the fracture saturation (*i.e.* m=1); the reasoning is that for a partially saturated gridblock only the portion that water has invaded can only contribute to imbibition (*i.e.*, counter-current

imbibition). As we will see later, the oil production from a matrix block can be from co-current imbibition; there is no need for water to be in contact with oil in the matrix for oil production from the block. We performed various sensitivity calculations by assigning different values to *m* in the range of 0 to 1. These calculations revealed that *m*=0.5 may appropriately describe the transfer term. This particular choice of *m* will be discussed shortly. Let us write the expression for the transfer term $q_w(z,t)$ for the variable fracture saturation using Duhamel's principle:

$$
\begin{aligned}
&q_w(z,t)=[S_w(z,t_o)]^m R_1\lambda_1 e^{-\lambda_1(t-t_o)}+([S_w(z,t_1)]^m-[S_w(z,t_o)]^m)R_1\lambda_1 e^{-\lambda_1(t-t_1)}+\ldots\\
&\ldots+([S_w(z,t_{n-1})]^m-[S_w(z,t_{n-2})]^m)R_1\lambda_1 e^{-\lambda_1(t-t_{n-1})}+\\
&[S_w(z,t_o)]^m R_2\lambda_2 e^{-\lambda_2(t-t_o)}+([S_w(z,t_1)]^m-[S_w(z,t_o)]^m)R_2\lambda_2 e^{-\lambda_2(t-t_1)}+\ldots\\
&\ldots+([S_w(z,t_{n-1})]^m-[S_w(z,t_{n-2})]^m)R_2\lambda_2 e^{-\lambda_2(t-t_{n-1})} \quad \ldots\ldots\ldots\ldots\ldots\ldots\ldots\ldots\ldots\ldots \text{(8)}
\end{aligned}
$$

In the above and subsequent equations, the superscript *f* is dropped for the sake of brevity. The time period from t_o to t_n is divided into *n* parts. Letting $n \rightarrow \infty$ and using the definition of an integral and integrating by parts, one obtains:

$$
\begin{aligned}
&q_w=R_1\lambda_1([S_w(z,t)]^m-\lambda_1\int_0^t[S_w(z,\tau)]^m\cdot e^{-\lambda_1(t-\tau)}d\tau)+\\
&R_2\lambda_2([S_w(z,t)]^m-\lambda_2\int_0^t[S_w(z,\tau)]^m\cdot e^{-\lambda_2(t-\tau)}d\tau) \quad \ldots\ldots\ldots\ldots\ldots\ldots\ldots\ldots\ldots\ldots \text{(9)}
\end{aligned}
$$

The substitution of Eq. (9) into Eq. (5) completes the problem formulation. Eq. (5) is a quasi-linear hyperbolic equation with a source function given by Eq. (9). It can be solved using the method of characteristics. The system of characteristic equations are:

$$
\begin{cases}
\left.\dfrac{dz}{dt}\right|_{S_w}=[i_n(t)f'_w\,(S_w)-(\rho_w-\rho_o)gF'(S_w)]/\phi_e \\
\dfrac{dS_w}{dt}=-\dfrac{q_w}{\phi_e}
\end{cases}
\quad \ldots\ldots\ldots\ldots\ldots\ldots\ldots\ldots\ldots\ldots \text{(10)}
$$

The boundary and initial conditions are:

$$S_w(t,z=0)=S_w^o=1$$

$$S_w(t=0,z)=S_{wi}=0 \quad \ldots\ldots\ldots\ldots\ldots\ldots\ldots\ldots\ldots\ldots\ldots\ldots\ldots\ldots\ldots \text{(11)}$$

Fracture relative permeabilities for water and oil phases are given by:

$$k_{rw}=k_{rw}^o S_w^n \ldots\ldots\ldots\ldots\ldots\ldots\ldots\ldots\ldots\ldots\ldots\ldots\ldots\ldots\ldots \text{(12)}$$

$$k_{ro}=k_{ro}^o(1-S_w)^n \ldots\ldots\ldots\ldots\ldots\ldots\ldots\ldots\ldots\ldots\ldots\ldots\ldots\ldots \text{(13)}$$

Model Results

In the following, we will use fine-grid simulation to study imbibition in a single block and to obtain matrix relative permeabilities. The fine-grid simulation is also used to study counter-current and co-current

imbibition. The BLM is then used in order to examine the features of imbibition in a single block and to predict water injection in the multiblock systems. In all fine-grid simulations, we use the Eclipse simulator[12] with the implicit option.

Kansas outcrop chalk. First we perform fine-grid simulation of water injection in the single block of the Kansas outcrop chalk. The recovery data for the three injection tests (at the injection rates of 0.5, 3.2 and 6.3 PV/day) and the immersion test are provided in Ref. 5. The permeability and porosity of the Kansas outcrop chalk are 2.5 md and 29%, respectively. Other relevent data are also provided in Ref. 5. We use 51 unequal gridblocks in the vertical direction and 3 gridblocks in x and y directions (Δz=3$\times$ 0.0022, 3 $\times$ 0.08, 3 $\times$ 0.1667, 3 $\times$ 0.3333, 27 $\times$ 1.0, 3 $\times$ 0.3333, 3 $\times$ 0.1667, 3 $\times$ 0.08, 3 $\times$ 0.0022 *cm*, Δy=9.0, 0.25, 0.125 *cm*, Δx=3.0, 0.137, 0.037 *cm*) to simulate one half of the single block. Finer grids gave essentially the same results. The following expressions are used for the matrix capillary pressure and relative permeabilities:

$$P_c(S_w) = -B\ln(S_w) \quad \text{.....(14)}$$

$$k_{rw} = k_{rw}^o S_w^{nw} \quad \text{..... (15)}$$

$$k_{ro} = k_{ro}^o (1 - S_w)^{no} \quad \text{.....(16)}$$

The parameter of the matrix capillary pressure B =1.76 *atm* is estimated from the measured data on the chalk from Ref. 13. The recovery of the single block was matched using *nw=4, no=2,* k_{rw}^o =0.1 and k_{ro}^o=1.0 for all three injection rates. For the immersion test, the recovery was matched using *nw=3, no=3,* k_{rw}^o =0.08 and k_{ro}^o=0.8. The oil relative permeability for counter-current imbibition is less favorable for recovery perfomance than that for co-current imbibition. The difference in matrix relative permeablities for counter-current and co-current imbibition has been observed by other authors[13]. The fracture relative permeabilities are assumed to be proportional to saturation, and the fracture capillary pressure P_c is assumed zero. The intrinsic fracture porosity is assumed to be one. These assumptions continue throughout this study. The empirical transfer function with two exponential terms described earlier was used to match recovery. The match was performed manually using the exponential parameters R_1 and λ_1 for the first part of the recovery curve, and then the tail portion was matched by varying parameter λ_2 (note that $R_2 = N_{pa} - R_1$). Other procedures such as regression-based methods may also be used. We examined transfer fluxes of individual gridblocks in the z direction using the fine-grid simulation. The transfer fluxes are nearly the same for all the gridblocks. The parameters R_1, R_2, λ_1 and λ_2 in the empirical transfer function are: R_1 =0.57, R_2 =0.06, and λ_2^{-1}=11 hr which are independent of the injection rate. Only λ_1 varies with the rate (see Table 2). Note that the immersion test is also described by the two exponents. The parameters λ_1 and λ_2 represent the imbibition rate of the matrix blocks. These parameters can be estimated using fine grid-simulation of a single field-size block, and then perform a field study.

Single Block. Let us now compare the fine-grid simulation and the BLM results for the single block, and examine the contribution of co-current and counter-current imbibition. In the fine-grid simulation, we use λ_1^{-1}=2.4 hr for all the tests; this value represents an average. The recovery results (not shown) from the BLM and the fine-grid simulation show good agreement with the experimental data, as expected. The calculated fracture saturation profiles, and water and oil fluxes from the fine-grid simulation are shown in Fig. 5 at an injection rate of 0.5 PV/day. This figure shows that at both 0.1 and 0.3 PV injection, most of the oil is produced by co-current imbibition. In previous studies[2,3,4] the transfer term has been assumed to be proportional to the fracture saturation, i.e. m=1 in expressing the transfer flux (see Eq.(9)). Using m=1 in the BLM, the fracture saturation profiles are diffused at the low injection rate of 0.5 PV/day (see Fig. 6a). We

carried out several calculations with different values of m parameter in the range of 0.1 to 1.0. Using m=0.5 in the BLM, we obtain fracture saturation profiles shown in Fig. 6b. (Note that in the BLM, the oil flux is not calculated). At the low injection rate (W=0.5 PV/day), the BLM model provides fluid segregation close to the fine-grid simulation. The water transfer flux also has the same features as in the fine-grid simulation. At the injection rate of 3.2 and 6.3 PV/day (experimental results available in Ref. 5) and using m=1, the BLM produces an unrealistically high saturation front speed. Using m=1, the breakthrough times were orders of magnitude less than those measured in the experiments and in the fine-grid simulation. Using m=0.5, the position of the saturation front is in good agreement with the fine-grid simulation. The shapes of the fracture saturation profiles and water fluxes are, however, different from that of the fine-grid simulation. (The results at 3.2 and 6.3 PV/day are not shown.)

Stack of Blocks. The Buckley-Leverett model and the fine-grid simulation are used to predict the recovery performance of the Kansas chalk multiblock experiments (reported in Ref. 5). The single block transfer functions obtained in the previous section are used to predict the results. Fig. 7 (left panel) presents the predicted recovery performance at different injection rates; the predicted recovery performance from the Buckley-Leverett model is in good agreement with the experimental data and the fine-grid simulation. The computation for the BLM is orders of magnitude faster than the fine-grid simulation. Here parameter R_1 was adjusted to match the predicted ultimate oil recovery with the experiments. In the experiments (see Ref. 5), the ultimate oil recovery varied from 67% to 63% depending on the water injection rate. Fig. 7 (right panel) shows the predicted fracture water-oil contact position vs. PV injected. There is good agreement between the experimental data and the predicted results using the modified Buckley-Leverett model.

Berea sandstone. Similar to the Kansas chalk block, we use 51 unequal gridblocks in the vertical direction and 3 gridblocks in each of the horizontal directions (Δz = 3× 0.0133, 3 × 0.0332, 3 × 0.133, 3 × 0.929, 27 × 1.99, 3 × 0.929, 3 × 0.1329, 3 × 0.0332, 3 × 0.0133 *cm*, Δy=7.0, 0.45, 0.025 *cm*, Δx=7.0, 0.45, 0.025 *cm* for the single slab and Δz=3 × 0.0133, 3 × 0.025, 3 × 0.1, 3 × 0.7, 27 × 1.6, 3 × 0.7, 3 × 0.1, 3 × 0.025, 3 × 0.0133 *cm*, Δy=7.0, 0.45, 0.025 *cm*, Δx=2.0, 0.4, 0.045 *cm* for the single block) to simulate one half of the single block and slab. Eqs. 14 to 16 were used to represent the matrix capillary pressure and relative permeabilities. The parameter of the matrix capillary pressure B =0.098 *atm* is estimated from the measured data of Berea from Ref. 14. The recovery of the single slab was matched using *nw=4, no=2,* k^o_{rw}=0.19 and k^o_{ro}=0.85 both for the immersion and the injection test at a 2.7 PV/day rate (see Figs. 2a and 2b). The simulated recovery of the single block for the injection test was also matched with the experimental data using the above parameters of the relative permeabilities. The immersion test for the Berea single block was matched using *nw=4, no=2,* k^o_{rw}=0.15 and k^o_{ro}=0.6 (see Fig 3a). Therefore, the difference between the counter-current and co-current imbibition relative permeabilities for Berea is insignificant. The parameters of the transfer function are: R_1 = 0.47, R_2 = 0.08, λ^{-1}_1 = 5.0 hr, λ^{-1}_2 = 23.0 hr for the single slab and R_1 = 0.53, R_2 = 0.08, λ^{-1}_1 = 4.5 hr, λ^{-1}_2 = 17.0 hr for the single block. These values are for the injection tests.

Single Slab and Block. The recovery performance data and the calculated results of the single slab and the single block of Berea are shown in Figs. 2b and 3b, respectively. Results from the Buckley-Leverett model and the fine-grid simulation are in good agreement with the experimental data due to the history match.

Stack of Slabs. The BLM is used to predict the recovery performance of the Berea multislab system reported in Ref. 5, using the transfer function from the single slab. Fig. 8 (left panel) presents the recovery performance results at two injection rates. The predicted recovery performance from the BLM is in good agreement with the experimental data for the intermediate injection rate of 1.0 PV/day. Fig. 8 (right panel) shows the fracture water-oil contact position at the intermediate (1.0 PV/day) and high (2.3 PV/day)

injection rates. There is good agreement between the calculated results and the experimental data at the injection rate of 1.0 PV/day. At the high injection rate of 2.3 PV/day, the model overestimates breakthrough time and recovery performance; an appropriate λ_1 can improve predictions.

Stack of Blocks. We use the transfer function for the single block discussed earlier to predict the imbibition performance of the multiblock system of Ref. 5. Fig. 9 presents the recovery performance at three injection rates. The predicted recovery performance from the BLM shows good agreement with the experimental data for 0.5 and 1.0 PV/day injection rates. Fig. 9 shows (the right panel) the fracture water-oil contact position at three injection rates. There is good agreement between the calculated results and the experimental data at the low (0.5 PV/day) and intermediate (1.0 PV/day) injection rates. Similar to the stack of slabs, the model overestimates breakthrough time and recovery at the high injection rate of 2.3 PV/day.

Discussion and Conclusions

We can now compare water injection performance between the same size stacked blocks of Berea and Kansas outcrop chalk using the BLM. Let us choose the aggregate size corresponding to the setup in Fig. 1b with corresponding porosity, permeability, capillary pressure and relative permeabilities of Berea and Kansas chalk. Fig. 10 shows the recovery vs. the injected PV using the BLM at an injection rate of 2.3 PV/day. The breakthrough recoveries are 22 and 45% for Berea and Kansas chalk, respectively. As Fig. 10 shows, the recovery performance of Kansas outcrop chalk is very efficient. Kansas outcrop chalk is more than 2 orders of magnitude less permeable than Berea. The efficient imbibition in Kansas chalk fractured media makes it an ideal candidate for water injection. The main reason for the high imbibition efficiency in Kansas chalk is the strong capillarity and favorable oil relative permeability. Gravity has a negligible effect. We have simulated the case corresponding to an injection rate of 3.8 PV/day in the stacked block system of Fig. 1a with 1) normal gravity, 2) no gravity, and 3) an exaggerated gravity term with the density difference between the oil and water increased by a factor of 5. There is no difference between the normal and no gravity cases. Recovery performance is slightly better in the exaggerated gravity case but the difference is very small. These results are in agreement with the experimental data for the tilted stacked blocks reported in Ref. 5. There is a substantial difference between co-current and counter-current imbibition performance of Kansas chalk, when co-current imbibition is more efficient. For Berea, the data on the single slab and block shows the converse. However, simulation results of a large Berea matrix block showed that the difference between the immersion and injection processes becomes small as the matrix size increases.

The main conclusions of this study are:

1. The experimental data on Berea reconfirm that the residual oil saturations from the counter-current and co-current imbibition are not the same. The residual oil saturation is higher for counter-current imbibition.
2. Water injection in very tight fractured media of Austin chalk with a permeability of 0.01 md and porosity of 5% may result in about 20% recovery.
3. Water injection in fractured porous media is governed by both co-current and counter-current imbibition. The Buckley-Leverett displacement model can account for both processes. A major element of the BLM for application to water injection in fractured porous media is the exchange term. The multiplication of this term by fracture saturation with a power of 1/2 drastically improves the predictions. The computational time from the BLM is orders of magnitude less than that of the fine-grid simulation.

Nomenclature

A = cross-sectional area of the matrix block
f = fractional flow
g = gravity component
i = injection rate
i_n = injection rate normalized by A
k = permeability, md
k_r = relative permeability
N_{po} = ultimate oil recovery
p = pressure
P_c = capillary pressure
q_w = transfer term
q_o = oil production rate
R = recovery parameter
S = saturation
t = time, hours
u = velocity
W_p = cumulative water produced
x = coordinate, cm
λ = imbibition parameter, hour^{-1}
μ = viscosity, cp
ρ = density
σ = matrix block scaling parameter
ϕ = porosity

Subscripts
e = effective
m = matrix
o = oil
w = water
r = residual

Superscripts
f = fracture
o = endpoint value
i = initial

References

1. Buckley, S.E. and Leverett, M.: "Mechanism of Fluid Displacement in Sands," (1942); *Trans.*, AIME, 107-116.
2. de Swaan, A.: "Theory of Waterflooding in Fractured Reservoirs," *SPEJ* (April 1978) 117-22; *Trans.*, AIME, 265.

3. Chen, Z. and Liu, C.: "Theory of Fluid Displacement in a Medium with Double Porosity," *Energy Sources* (1982) 6, No. 3, 193-214.
4. Kazemi, H., Gillman, J.R., Elsharkawy, A.M.: "Analytical and Numerical Solution of Oil Recovery from Fractured Reservoirs with Empirical Transfer Functions," *SPERE* (May 1992) 219-227.
5. Pooladi-Darvish, M. and Firoozabadi, A. "Experimental Study of Water Injection in Water-Wet Fractured Porous Media," Chapter I, Part I.
6. Pooladi-Darvish, M. and Firoozabadi, A. "Co-Current and Counter-Current Imbibition in a Water-Wet Matrix Block," (to be published).
7. Viskund, B.G., Morrow, N.R., Ma, S., Wang, W., and Graue, A.: "Initial Water Saturation and Oil Recovery from Chalk and Sandstone by Spontaneous Imbibition," Proceedings of the 1998 International Symposium of the Society of Core Analysis, the Hague, Netherlands, Sept. 14-16.
8. Spinler, E.A., and Hedges, J.H.: "Variation of the Electrical Behavior of the Ekofisk Field in the North Sea," Proceedings of the 1993 International Symposium of the Society of Core Analysis, San Francisco, 1993.
9. Salathiel, R.A.: "Oil Recovery by Surface Film Drainage in Mixed-Wettability Rocks," *JPT* (1973) 1216-1224.
10. Aronofsky, J.S., Masse, L., Natanson, S.G.: "A Model for the Mechanism of Oil Recovery from Porous Media Due to Water Invasion in Fractured Reservoirs," ; *Trans.*, AIME (1958), 213, 17-19.
11. Civan, F.: "Quadrature Solution for Waterflooding of Naturally Fractured Reservoirs," *SPERE* (April 1998) 141-147.
12. ECLIPSE 100, Reference Manual (1996), Schlumberger GeoQuest
13. Bourbiaux, B. and Kalaydjian, F.J.: "Experimental Study of Co-Current and Counter-Current Flows in Natural Porous Media," *SPERE* (August 1993) 361-368.
14. Kleppe, J. and Morse, R.A.: "Oil Production from Fractured Reservoirs by Water Displacement," paper *SPE* 5084 presented at the 49th Annual Fall Meeting of Petroleum Engineers of AIME in Houston, TX, Oct. 6-9.

TABLE 1 - AUSTIN CHALK CORE DATA			
core	L (cm)	k (md)	ϕ (%)
1	18.5	0.012	4.8
2	14.7	0.017	4.7
3	18.0	0.034	4.8
4	15.5	0.007	5.3
5	15.3	0.042	4.7
6	20.0	0.013	5.0

TABLE 2 - FLUX PARAMETERS FOR THE KANSAS CHALK SINGLE BLOCK		
$R_2 = 0.06$, $\lambda^{-1}_2 = 11.0$ hr		
	λ^{-1}_1 (hr)	R_1
W=0.50 PV/day	3.7	0.57
W=3.2 PV/day	2.0	0.57
W=6.3 PV/day	2.0	0.57
immersion	5.5	0.51

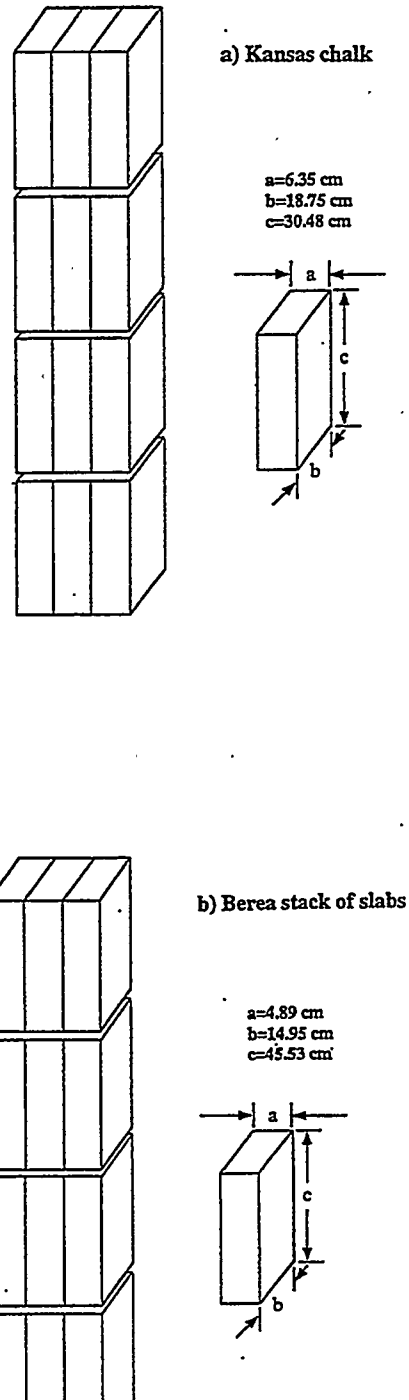

Fig. 1 - Rock assemblies for various experiments.

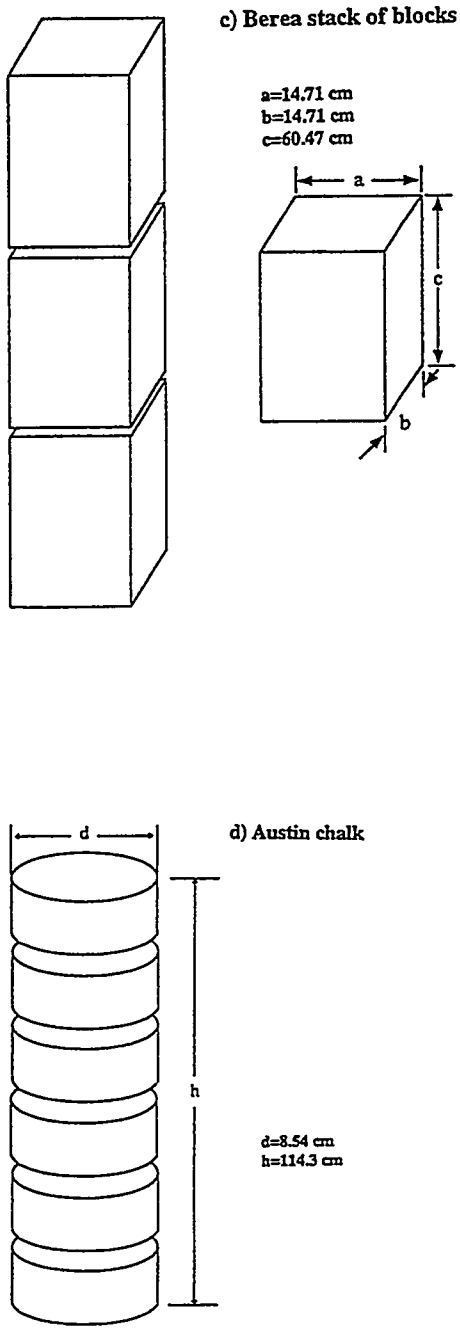

Fig. 1 - Rock assemblies for various experiments (continued).

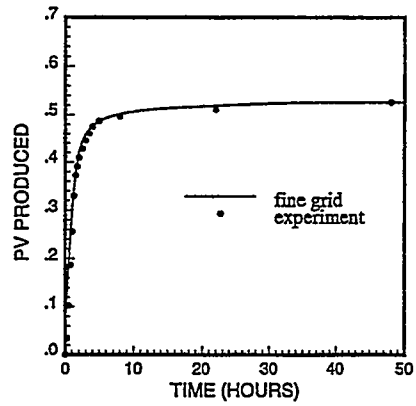

a) immersion

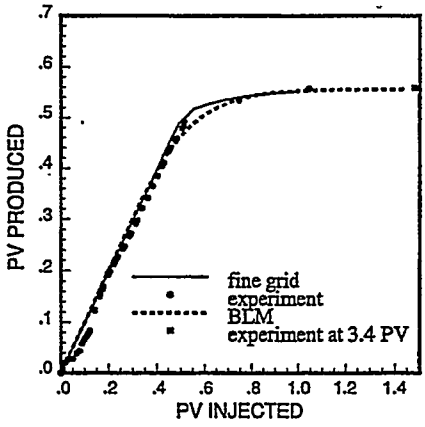

b) injection (W=2.7 PV/day)

Fig. 2 – Recovery performance of the Berea single slab.

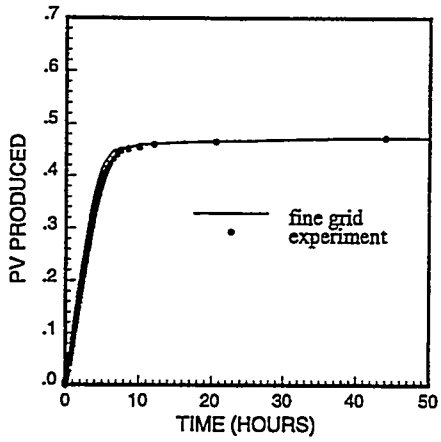

a) immersion

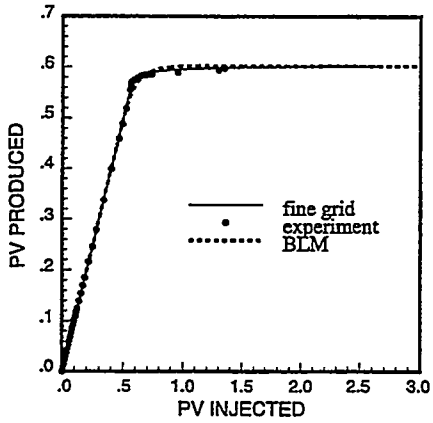

b) injection (W=0.75 PV/day)

Fig. 3 – Recovery performance of Berea single block.

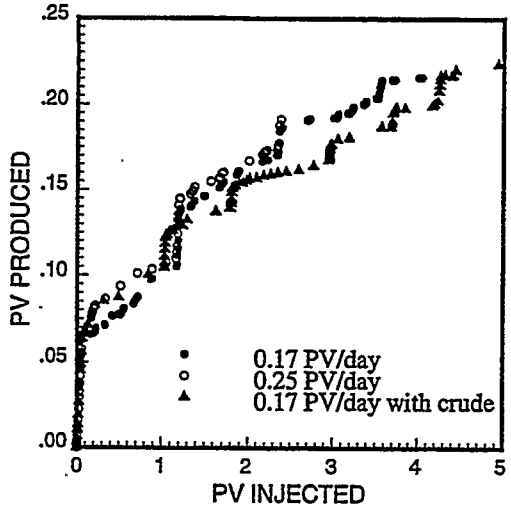

Fig. 4 – Recovery performance of Austin chalk.

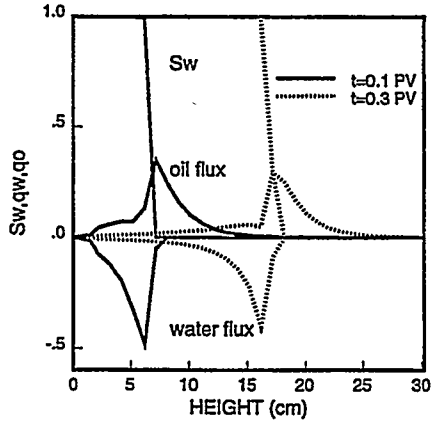

Fig. 5 – Fracture water saturation, water and oil fluxes from fine-grid simulation.

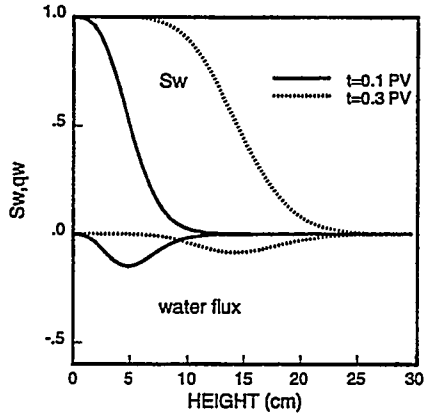

a) m=1.0

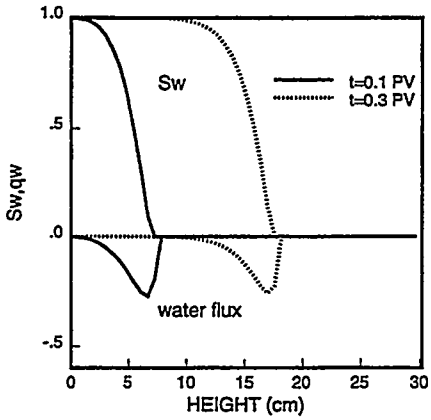

b) m=0.5

Fig. 6 – Fracture water saturation and water flux from BLM .

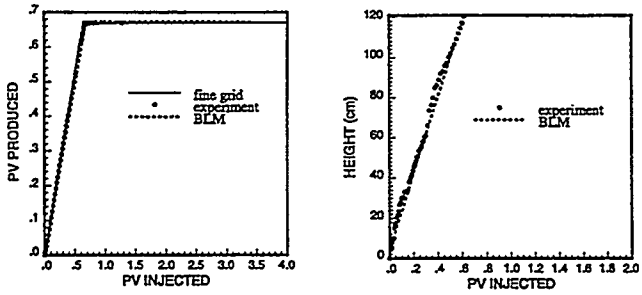

a) W=0.26 PV/day

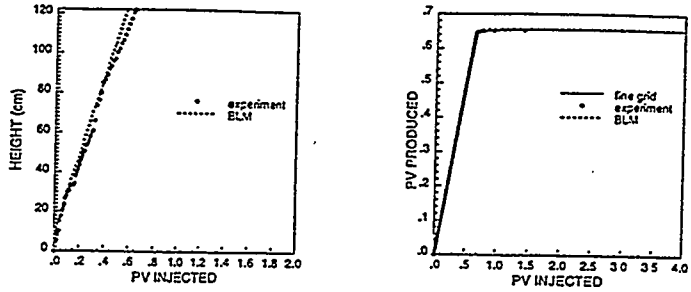

b) W=0.77 PV/day

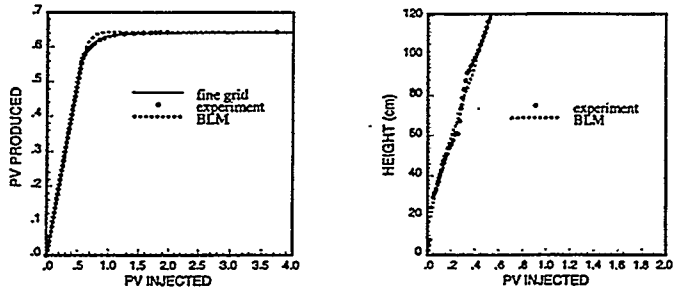

c) W=1.9 PV/day

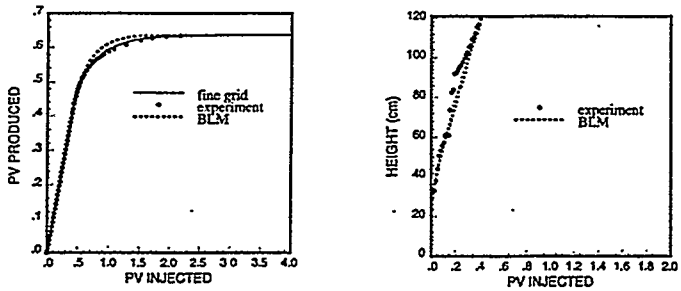

d) W=3.8 PV/day

Fig. 7 – Recovery performance of stacked blocks of the Kansas chalk: recovery (left panel), fracture water level (right panel).

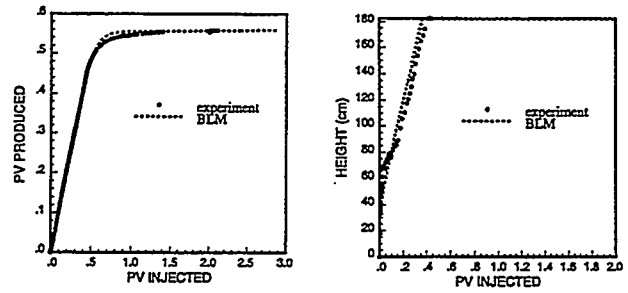

a) W=1.0 PV/day

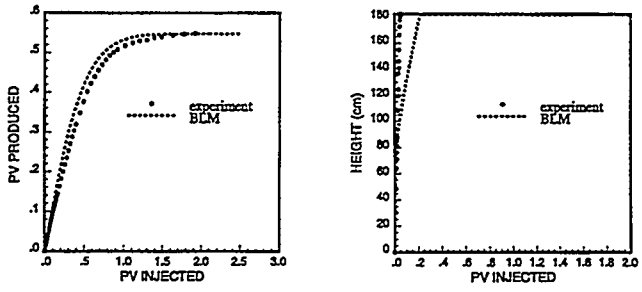

a) W=2.3 PV/day

Fig. 8 – Recovery performance of stacked slabs of the Berea: recovery (left panel), fracture water level (right panel).

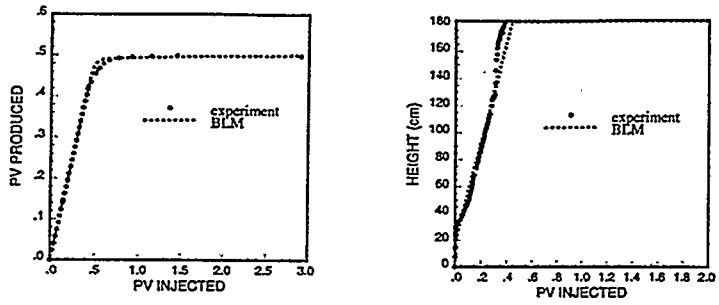

a) W=0.5 PV/day

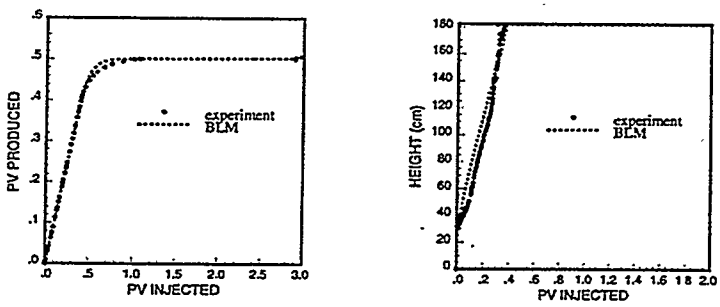

b) W=1.0 PV/day

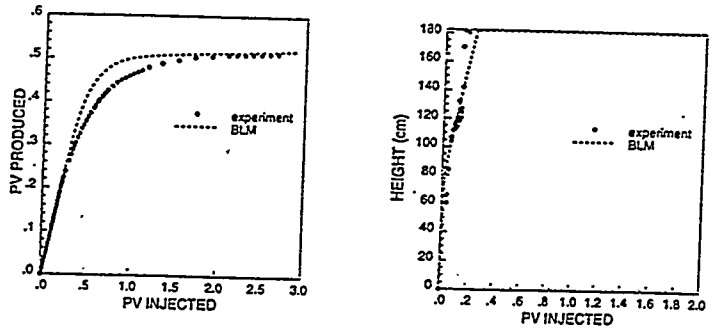

c) W=2.3 PV/day

Fig. 9 – Recovery performance of stacked blocks of the Berea: recovery (left panel), fracture water level (right panel).

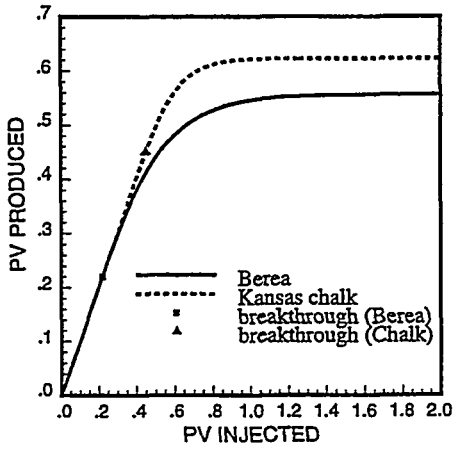

Fig. 10 – Recovery performance of stacked blocks of the Berea and Kansas chalk (W=2.3 PV/day).

Chapter II – Solution-Gas Drive in Heavy-Oil Reservoirs

MEHRAN POOLADI-DARVISH AND ABBAS FIROOZABADI

Summary

Different hypotheses have been made to explain the highly favorable behaviour of some of the heavy oil reservoirs under solution-gas drive. The main reasons however remain unclear. Using experiments in an unconsolidated sand-pack, we examined the solution-gas drive process in a light model oil and a heavy oil. Pressure and volume measurements along with visual observation of the flowing fluid at the in-situ pressure for the heavy oil system revealed that: critical gas saturation was low (5% or less), the gas phase was not made of microbubbles flowing with the oil stream, liquid mobility did not improve upon either nucleation or growth of the gas bubbles, and nonequilibrium effects were not dominant. It seems that the main reason for the desirable performance of such systems is low mobility of the gas phase in the heavy oil.

Introduction

Production from some of the heavy oil reservoirs in Canada and Venezuela has led to unexpectedly high oil rates and recoveries under solution-gas drive. In an early paper, Smith[1] reported this behaviour in the heavy oil reservoirs of the Lloydminster area, Canada. Analysis of the field data showed production rates much in excess of that predicted by the Darcy law[1]. Similarly, Loughead and Saltuklaroglu[2] and Metwally and Solanki[3] reported solution-gas drive oil recoveries as high as 14% and flow rates of one order of magnitude larger than the predictions of the Darcy radial flow. These and other authors reported coproduction of large volumes of sand and the delayed liberation of gas from the wellhead crude samples in open vessels. More recently, similar behaviour was reported in some of the heavy oil reservoirs in Venezuela. Mirabal et al.[4] presented examples of high flow rates under solution-gas drive from one of the heavy oil reservoirs of the Orinoco Belt. In addition to the unexpectedly high production rates, the reservoir pressure was nearly maintained during the 12 years of production history.

The economic advantages of the initial development of many of these reservoirs under solution-gas drive are clear; the high costs involved in the traditional thermal methods are avoided[5-7].

To explain the above behaviour, a number of mechanisms have been suggested which can be divided into two main categories; geomechanical effects such as sand dilation and development of wormholes comprise the first category. The second category, which is the subject of the current research, suggests that the special properties of the flowing fluids, the gas and the heavy oil, are the main reasons for high production performance.

The effect of many of the pressure maintenance mechanisms, such as an active aquifer and reservoir compaction, have been found small in these reservoirs[1,2,4]. Due to production, the pore pressure drops below the bubblepoint pressure to a critical supersaturation pressure, and then gas evolves in the reservoir. If the evolved gas is retained in the reservoir, two-phase compressibility will be high[1,2], and the reservoir pressure declines slowly[4]. A number of mechanisms have been proposed to explain the gas holdup in the reservoir.

Kraus, McCaffrey, and Boyd[8] proposed that below bubblepoint, the evolved gas is retained in the porous media until the pressure reduces to a lower pressure called pseudo-bubblepoint pressure. Below the pseudo-bubblepoint pressure, some of the evolved gas forms a continuous gas phase as in the conventional view of solution-gas drive. Claridge and Prats[9] in a similar analysis suggested that all of the evolved gas below the bubblepoint pressure is kept in the form of small bubbles in the porous media and does not form a continuous free gas phase. Formation of a "semi-rigid coating" of asphaltene components at the gas-oil interface was proposed to explain the discontinuity of the gas phase.

In contrast to the above reasoning in relation to the pressure-dependent properties of the oil, Sheng et al.[10] proposed a model for time-dependent physical properties of the fluids. The authors used their proposed model to match the volume behaviour of a live oil sample when its pressure was reduced from 700 psi to 350 psi. Smith[1] and other authors have reported that the volume of the produced crude in the tank at the well site reduces considerably with time. Huetra et al.[11] discussed time-dependent behaviour when they increased the volume of a live oil sample in a cylinder in discrete steps. Following each expansion, it took twenty four hours before the pressure increase became negligible. The time-dependent behaviour under field conditions with time-scales much larger than those pertaining to laboratory experiments has not been fully addressed yet. It seems unlikely, however, that time-dependent properties, with time-scales of the order of a few hours[10] to 24 hours[11] are the primary reasons for the unusual performance of heavy oil reservoirs under solution-gas drive.

Smith[1] suggested that the evolved gas below the bubblepoint pressure forms very tiny bubbles which are carried with the flowing oil phase; these bubbles do not coalesce to form a continuous gas phase. The idea of microbubble generation and flow with the oil through the pore space has been reiterated in a number of other papers on the subject. Maini, Sarma, and George[12] suggested a somewhat different mechanism to explain high gas saturation in the porous media. The authors performed steady state solution-gas drive experiments in a 1-D sandpack; the inlet pressure was kept at the bubblepoint pressure and the outlet pressure was dropped in steps of 48 psi. The authors observed production of gas-oil mixture in the form of foam at the outlet and suggested that a non-aqueous foam is generated inside the porous media, in which the oleic phase is the continuous phase. The foamy behaviour was used to explain the existence of high gas saturation in their experiments. Firoozabadi and Anderson[13] performed solution-gas drive experiments in an 8" long Berea sandstone housed in a transparent coreholder. Presence of an open window at one end of the core permitted visualization of the producing fluid at the flowing pressure. The authors observed appearance and growth of the gas bubbles on the core surface. A discrete flow of gas streams into the window, which was accompanied with large pressure fluctuations, was observed. Based on this observation, they rejected the notion of simultaneous flow of tiny gas bubbles with the oil stream. The gas saturation at which gas flow occurred, i.e., critical gas saturation was 2.5-3% for two tests on an 11-API crude. It was concluded that the critical gas saturation for heavy oil systems may be in the range of light crudes. Upon further expansion, more oil was recovered, until gas saturations as high as 10% were developed in the core. Based on this observation, the authors suggested that gas mobility may remain low in a heavy oil system. Huerta et al.[11] used a heavy-oil saturated sand-pack and performed solution-gas drive experiments at a constant production rate. The authors reported a "mobile gas saturation" of 10%, apparently inferred from the plot of GOR vs. pressure. In a recent study, Bora, Maini, and Chakma[14] reported solution-gas drive experiments in a micro-model. They did not observe simultaneous flow of a large number of microbubbles with the oil stream.

The emphasis of the majority of the above studies is on the gas phase; its behaviour and interaction with the heavy oil are used to explain the high production performance of heavy oil reservoirs under solution-gas drive. In contrast, some other authors have suggested that improved liquid phase mobility may lead to unusual performance of solution-gas drive in heavy oil reservoirs. Claridge and Prats[9] proposed that asphaltene components of the heavy oil separate from the oil and concentrate at the gas-oil interface; the asphaltenes

separation from oil leads to a much lower oil viscosity and enhanced oil mobility. Shen and Batycky[15] suggested that lubrication effects due to the presence of the nucleated gas at the pore walls enhances oil mobility. They proposed an equation for the effective viscosity of the foamy oil incorporating the lubrication effect, which was used to match the experimental data of Maini et al.[12] To address the issue of liquid mobility below bubblepoint pressure, Huerta et al.[11] used a 6 m long slim tube for solution-gas drive under constant production rate; no significant change in pressure drop was observed until the gas saturation approached the critical saturation. Close to the critical gas saturation, pressure drop increased gradually by as much as 40-70%, indicating no improvement in the oil phase mobility.

The above review indicates that there are many unresolved issues concerning the dominant mechanisms in heavy oil reservoirs under solution-gas drive. Specifically, there are different opinions on critical gas saturation, existence of microbubbles, and liquid-phase mobility improvement. In this work, we measure the critical gas saturation in an unconsolidated sandpack saturated with a light model oil and a heavy crude. We define the critical gas saturation as the minimum gas saturation at which gas flow can be sustained, which differs from the definition by Maini et al.[12] based on continuity of the gas phase. We also study gas evolution in a heavy oil-saturated unconsolidated sand and examine the nature of the flowing fluids at the experimental pressure, as they flow into a visual window at the outlet of the sandpack. Another objective of this work is to study the liquid phase mobility below the bubblepoint pressure.

Experimental

Figure 1 shows the schematic diagram of the experimental setup. The main component is the visual coreholder. An ISCO pump is used for saturating the porous medium and producing the oil during the depletion. Other components are; a high pressure cylinder used for preparation of the live oil, pressure and temperature sensors, and a video camera for detecting the onset of gas flow. All of the above components are housed in an air bath which is controlled within 0.1 F of the experimental temperature of 75 F. Acquisition of the pressure data, and control of the temperature of the bath is performed by a PC, and the video image is stored using a recorder.

The body of the coreholder is made of an acrylic tube with a wall thickness of 12 mm. The top components of the coreholder were especially designed to provide the seal while exerting pressure on the sandpack. This would ensure that the seal displaces the space from the compaction of the sand during different stages of the experiment. The top components are two stainless steel disks with a 12-mm thick rubber sandwiched between them (see the exert in Figure 1). The lower disk which sits on the sand has a stainless steel screen to avoid sand flow, and a set of groves to facilitate production of the fluids. A 6-mm OD stainless steel tubing, welded to the lower disk, passes through the rubber and the upper disks and ends in a window made inside an acrylic rod. The fluid produced from the sandpack enters the window and flows out through a 3-mm hole drilled through the acrylic rod. The window is graduated to measure the gas volume. Connections between the coreholder, the pressure transducers and the pump are made of 3-mm OD stainless steel tubing. The total dead volume at the top of the ISCO pump, in the tubings, and transducers is about 16 cm^3.

Rock and Fluid Data: Clean Ottawa sand with a grain size of 212 - 355 ?m comprised the porous medium. The top of the sandpack was covered with 6-mm layer of coarse sand grains (600 - 800 ?m). The openings of the screen at the top of the sand were 425 ?m. This configuration was used to avoid sand flow through the screen, and to prevent gas holdup below the stainless steel screen. The sandpack was prepared by pouring small batches of clean sand into the coreholder and pounding on it. The thin layer of the coarse sand was then added to the top of the pack and the components were assembled. By tightening the screws at the outlet

cap, a uniaxial pressure was exerted on the sand column. The pressure caused expansion in the rubber disk to provide the seal. Some of the relevant data are provided in Table 1.

Methane was used as the gas phase in all of the experiments. Normal decane and an 11-API crude[16] were used for the light model oil and heavy oil runs, respectively. Table 2 gives some of the physical properties of the fluids. A small amount of water was present in the heavy crude. The GOR for the light and heavy oils was 13 and 6.5 vol/vol, respectively.

Test Procedure: The live oil was prepared in a high pressure cylinder by mixing the gas and the dead oil. For the preparation of the heavy oil, heating at 120 F and mixing was applied for many days. The GOR of the live oil was used as a measure of uniformity of the fluid in the cylinder. The coreholder, which was assembled on a frame that could rotate 180 degrees, was put under vacuum. The syringe pump was then filled with the dead oil, and the entire system was saturated. The remaining oil in the pump was removed and the pump was filled with the live oil at a pressure twice of the bubblepoint pressure. The dead oil in the lines and in the core were then displaced with at least 1.5 PV of live oil. This took about five hours for the light oil and about three days for the heavy oil. The lowest pressure in the system was at least 30% above the bubblepoint pressure. The system was allowed to stabilize for at least one day before the depletion test was initiated.

Depletion started by operating the pump at a constant rate of withdrawal. The pressure decreased to below the bubblepoint pressure; at the critical supersaturation pressure gas evolved in the porous media. The onset of gas-bubble nucleation was evidenced from the pressure behaviour as will be discussed later. Expansion of the gas bubbles were observed on the surface of the sandpack. Pressure data, total production and gas production data were recorded. The gas production was read from the graduations of the window at the top of the coreholder. After the window was filled, the additional volume of the gas which had entered the pump was estimated by measuring the compressibility of the fluid mixture in the pump. It took only a few minutes to isolate the core from the pump and measure the compressibility and return the system to the conditions prior to isolation.

With the completion of one experiment, the extra gas in the pump was released, the coreholder was rotated 180 degrees and oil from the pump was injected into the core. The gas in the window, now at the bottom, was displaced into the core and was dissolved in the oil. When the single phase fluid was established in the core, the pump was filled with fresh live oil and the fluid in the core was displaced again with at least 1.5 PV of the live oil.

Results

Two light model oil runs were performed using a C_1/C_{10} mixture in which the mole fraction of C_{10} was 0.905. These tests were performed under similar conditions as duplicate runs. The coreholder was in the vertical position with the window at the top. We also performed three heavy oil runs. In two of the runs, the coreholder was in the vertical position with the window at the top. The third experiment was run in a horizontal position. In the following, the results of one of the light model oil experiments, and the horizontal heavy oil run are discussed in detail, and the differences from the other runs are pointed out.

Light-Model Oil Experiments: Figures 2 and 3 show pressure vs. expansion for the light model oil run. The pressure is from the readings of the bottom transducer. Expansion was started from an initial pressure of 302 psig. The rate of expansion was 0.432 cm^3/day, corresponding to 1% of PV every 6.25 days. The rate of pressure drop in the single phase liquid was about 48 psi/day. Due to the low viscosity of the oil, the

differential pressure transducer did not detect a pressure difference. The resolution of the differential pressure transducer was about 0.02 psi and that of the main transducers about 0.5 psi. Upon expansion, the liquid pressure decreased to a value of 272 psig at 0.28 cm^3 expansion, when the pressure trend reversed. The pressure increased to a maximum of 280 psig in about 10 hours. At this time, the pressure started to decrease at a much lower rate compared to the single phase region. The critical supersaturation pressures of the two runs were 2-3 psi apart.

During the course of the experiment, the rate of withdrawal was increased at two different times. The data with other relevant information are given in Table 3. Every time the rate of expansion increased, the P-V curve became steeper, indicating an increase of 1 to 2 psi in supersaturation. This is estimated by comparing the extrapolation of the pressure curve, for a few hours after the rate increase, with the actual pressure data. Despite this temporary increase in supersaturation, the steepness of the P-V curve has a reducing trend from the beginning to the end, suggesting a reduction in supersaturation.

Gas evolution in the pack and recovery performance: At a gas saturation of 0.1% (0.5 cm^3 expansion), two small bubbles were observed in the lower half of the core. Each bubble covered a few grains. The number and the size of the bubbles increased during the 10 days of depletion. For example, at 1.67 and 5.7 cm^3 expansion (gas saturation of 0.6 and 1.6%), 7 and 16 bubbles were visible on the core surface, respectively. Some of these bubbles may have been connected from within. By the end of the experiment 20 gas bubbles could be observed, when some of them had grown to about 3 cm in height.

At a gas saturation of 1.5%, 50 small bubbles flowed within 2 minutes into the window and occupied a volume of about 0.5 cm^3. The saturation at which gas flow occurred is considered as the critical gas saturation. At this stage, gas flow into the window continued at a frequency of 2 to 4 times per day. Hence the critical gas saturation was 1.5%. The critical gas saturation of the duplicate run was 1.3%. Figure 4 shows the increase of gas saturation in the core. With further expansion gas saturation increased to a maximum of 2.9%, when gas was the only producing fluid for three days. The maximum gas saturation for the duplicate run was 2.6%. To obtain the gas volume in the core, the gas volume in the window and pump was subtracted from the total expansion beyond bubblepoint pressure. Errors due to the expansion of the coreholder, and the effect of hydrostatic pressure are insignificant. Since the changes in formation volume factor are negligible, the gas saturation in the core is equal to oil recovery.

Although not identical, the data of the two runs and the observed behaviour are close enough to provide a basis for comparison between the light oil and heavy oil experiments, which is discussed next.

Heavy Oil Experiments: The heavy oil runs were performed at a constant expansion rate of 0.984 cm^3/day, corresponding to 1% of PV every 2.5 days. The rate of pressure drop in the single liquid phase was 130 psi/day. Figures 5 and 6 show the variation of pressure vs. volume expansion for the horizontal run. In addition to the pressure, the pressure drop across the core is also shown. At the onset, the pressure differential increased from zero to about 0.1 psi. The pressure data clearly show that the transient effects due to initiation of flow die out in a short time, and a constant differential pressure of about 0.1 psi is registered.

Critical supersaturation pressure was detected at an expansion of 1.0 cm^3 and 305 psig pressure. Subsequently, the pressure increased to 343 psig. Figure 5 shows that upon evolution of the gas phase in the porous media, the differential pressure increased slightly, and then stayed constant. In none of the runs did we observe a liquid mobility enhancement suggested in the literature by some authors[9,15].

After formation of gas in the porous media, inferred from the pressure rise, a few gas bubbles were observed on the surface of the sandpack. The size and the number of the bubbles increased with time. For example, for one of the vertical runs, at 1.9, 2.9, 3.6, and 10.6 cm^3 expansion, 1,2,6, and 40 to 50 bubbles were visible on the core surface, respectively. Generally, the bubble density for the heavy oil runs was larger than that of the light oil runs. Later in the experiment, some of the gas bubbles close to the outlet had grown in length and had many branches.

At a gas saturation of about 3.5% (9 cm^3 expansion), some pressure fluctuations were observed in the readings of the differential pressure transducer (see Figure 6). While in the two vertical runs, the pressure fluctuations corresponded to the detection of the gas in the window, the gas phase was not detectable in the window until a saturation of 4.8% was established in the core. At that time, the volume of the gas in the window was estimated 0.5 cm^3. Critical gas saturation of 4.8% is more in line with those obtained from the two vertical runs. The critical gas saturation of the two vertical runs were 4.8 and 5%.

The observations pointed out above, can be used to reject the argument of simultaneous flow of gas in the form of microbubbles with the oil through the pore space. Our observations are; an enlargement of gas bubbles in the form of patches which cover many grains on the surface of sandpack, and an accumulation of gas in the window only after gas saturation in the core had build up to 4.8 to 5%.

Another point is that the pressure drop across the core at the critical gas saturation is more than the single phase pressure drop. The data for the three runs suggest that the end-point oil relative permeability under solution-gas drive is around 0.6 to 0.8.

Upon further expansion, the gas volume increased in the window. Figure 7 shows the variation of the gas saturation in the sandpack vs. expansion. Gas saturation increased to a maximum of 6.6% at expansion of 30 cm^3. In this interval the readings of the differential pressure transducer are dominated by oscillations. Figure 8 shows the detail of the pressure fluctuations during one day of expansion. The readings decrease to a value between 0.0 and 0.10, before returning to 0.15 to 0.25 psi every one and half hours or so. The oscillations are believed to relate to the intervals of gas flow, when very small pressure drops are sufficient. Later in the experiment, the frequency of the fluctuations increased to as many as 3 to 5 cycles per hour during some intervals. The frequency of the pressure oscillations in the vertical runs was much smaller, and they were of a larger magnitude.

At the end of the experiment, the pump was stopped, and the core was isolated from the pump. The readings of the differential pressure transducer reduced from 0.1 psi to zero within about 10 minutes. In the next twenty hours, no increase was detectable in the readings of the main transducers. This indicates that by the end of experiment, the initial supersaturation had nearly vanished. In other words, in the course of one month of the experiment, with an average two-phase rate of pressure drop of 4.5 psi/day, the time-dependent behaviour had ceased. It is expected that under field conditions, with lower rates of pressure drop, the importance of nonequilibrium effects would be even smaller.

In the above experiment, some segregation on the core surface was noticed. However, this was not of importance as the results of the other two vertical experiments were nearly the same; a maximum gas saturation of 6.5 - 7% at the end of the experiment and no detectable supersaturation at 30 cm^3 expansion.

Discussion

Let us assume that we were to simulate our experiments, and were to use the same relative permeability curves and capillary pressure function (accounting for the effect of surface tension) for the heavy oil and light model oil systems. During the single phase flow period, the oil phase pressure gradient in the heavy oil experiments is four to five orders of magnitude larger than that in the light oil experiments (based on the flow rates and viscosities). If the liquid phase pressure gradient were to translate to gas phase pressure gradient using capillary pressure function, as it does in the conventional formulation of multi-phase flow, the ratio of the gas flow rate to the liquid flow rate in the heavy oil runs had to be roughly four to five orders of magnitude larger than that of the light oil experiments. The experimental observation are in clear contradiction to what the above numerical simulator would have predicted.

One flaw in the above scenario and usage of the relative permeability concept is that, at low gas saturations, the gas phase is not continuous. The experimental observations indicate that gas flow is intermittent, and during the intervals of gas flow, pressure drop across the core decreases drastically. One way to force the simulator to predict more realistic results is to reduce the gas mobility. In fact, the gas phase, when discontinuous, has a lower mobility. This behaviour is commonly seen in foam flow, where the mobility of the gas phase, which is discontinuous because of the liquid lamella, is much lower than the mobility of continuous gas phase. The mobility of the gas phase in the foam is a direct function of number of lamella per unit volume[17].

To obtain a tangible picture of the effect of the number of lamella on gas mobility, and to examine the effect of viscosity on the low mobility of gas in the heavy oil systems, tests similar to those reported by Sheng et al.[10], were performed. A silicone oil of viscosity of 30,000 cp was saturated with methane at a GOR of 6.5. Using a needle valve, about 42 g of the live oil was expanded into a graduated cylinder at atmospheric pressure. The same experiment was repeated for the heavy oil. In the silicone oil test, gas bubbles formed and coalesced very quickly, creating larger and larger bubbles which floated to the surface and broke away. Within 30 minutes virtually all of the gas had escaped the silicone oil. The behaviour of heavy oil was different. It took about two orders of magnitude longer, 50 hours, for the volume of the oleic phase (oil and the dispersed gas phase) to decrease to its final value. Figure 9 shows the apparent volume of the oleic phase for the silicone oil and the heavy oil.

Close observation of the surface of the graduated cylinder indicated that in the case of the heavy oil, the gas bubbles were very small (smaller than 1 mm), and the rate of coalescence (if any) was much smaller than the silicone oil. Gas mobility in the graduated cylinder is mainly governed by the liquid viscosity and the bubble size, and is a balance between the buoyancy and the drag forces (Stoke's law). Using this criterion, the limiting velocity of 100 ?m and 1 mm gas bubbles in a 30,000 cp liquid is 1.6 cm/day and 6.5 cm/hr, respectively.

These simple experiments showed that the gas bubbles in the heavy oil sample remained smaller, and their mobility was much lower than that in the silicone oil.

The presence of surface active material and high viscosity of the liquid are often suggested as reasons for stability of gas bubbles in heavy oil systems. The above experiments showed that, at least in the graduated cylinder, the high viscosity of the silicone oil was not enough for stability of the liquid lamella. It should be noted, that the forces acting in porous media are not limited to drag and buoyancy, and the effect of geometry-capillarity may alter the governing mechanism. Results of these experiments should be used mainly for designing more realistic experiments, similar to those presented in this paper.

Conclusions

1. In our experiments in a sandpack, many of the previously proposed mechanisms for describing cold production of heavy oil were examined and were found absent. It was found that:

- Critical gas saturation was low (5% or less)
- Oil phase mobility was not improved upon formation of the gas phase in porous media
- Gas flow was not in the form of simultaneous flow of gas microbubbles; it flowed intermittently
- Within 30 days of the experiment, time-dependent, i.e. nonequilibrium effects had nearly vanished

1. Gas mobility in the heavy oil system may remain low. This could be explained by the presence of a large number of liquid lamella per unit volume.

2. Assuming that the heavy oil viscosity did not change upon liberation of the gas phase in the porous media, oil relative permeability at critical gas saturation (end-point oil relative permeability) was in the range of 0.6 to 0.8.

Table 1. Sandpack and coreholder data

	Light oil run	Heavy oil run
Porosity, %	36	36
Diameter, cm	6.36	6.35
Height, cm	23.5	21.5
Pore Volume, cm^3	270	245
Volume of the window, cm^3	3.9	8.2

Table 2. Fluid data

	Light model oil	Heavy oil
Density at 75 F, g/cm^3	0.724	0.9854[16]
Molecular Weight	142	455 - 468[16]
Viscosity at 75 F, cp	0.9	56000[16]
GOR, vol/vol	13	6.5

Table 3. Data of the light and heavy oil experiments

	Light model oil runs	Heavy oil runs
Initial rate of expansion, cm^3 /hr	0.018	0.041
Second rate of withdrawal, cm^3 /hr	0.054 (at 0.58 cm^3)	
Third rate of withdrawal, cm^3 /hr	0.108 (at 3.22 cm^3)	
Rate of pressure drop in the single liquid phase, psi/day	50	130
Critical gas saturation, %	1.3 - 1.5	4.8-5

References

1. Smith, G.E.: "Fluid Flow and Sand Production in Heavy Oil Reservoirs under Solution Gas Dive," *SPEPE* (1988) May 169-177.

2. Loughead, D.J. and Saltuklaroglu, M.: "Lloydminster Heavy Oil Production - Why so Unusual?" paper presented at the 1992 Annual Meeting of the Canadian Heavy Oil Association, Calgary, March 11.

3. Metwally, M. and Solanki, S.C.: "Heavy Oil Reservoir Mechanisms, Lindberg and Frog Lake Fields, Alberta, Part I: Field Observations and Reservoir Simulation," paper CIM 95-63 presented at the 1995 CIM Annual Technical Meeting, Banff, AB, May 14-17.

4. Mirabal, M. de, Gordillo, R., Rojas, G., Rodriguez, H., and Huerta, M.: "Impact of Foamy Oil Mechanism on the Hamaca Oil Reserves, Orinoco Belt-Venezuela," paper SPE 36140 presented at the 1996 SPE Latin American and Caribbean Petroleum Engineering Conference, Trinidad, April 23-26.

5. Figueredo, C. and Gordillo, R.: "An Overview of Corpoven, S.A. Heavy and Extra Heavy Crude Oil Upstream Business," paper presented at the 1996 SPE Latin American and Caribbean Petroleum Engineering Conference, Trinidad, April 23-26, 791-796.

6. Huang, W.S., Marcum, B.E., Chase, M.R., and Yu, C.L.: "Cold Production of Heavy Oil from Horizontal Wells in the Frog Lake Field," paper SPE 37545 presented at the 1997 SPE Thermal Operations and Heavy Oil Symposium, Bakersfield, CA, Feb. 10-12.

7. Mirabal, M. de, Rodriguez, H., and Gordillo, R.: "Production Improvement Strategy for Foamy Hamaca Crude Oil: A Field Case," paper SPE 375554 presented at the 1997 SPE Thermal Operations and Heavy Oil Symposium, Bakersfield, CA, Feb. 10-12.

8. Kraus, W.P., McCaffrey, W.J., and Boyd, G.W.: "Pseudo-Bubble Point Model for Foamy Oil," paper CIM 93-45 presented at the 1993 CIM Annual Technical Meeting, Calgary, AB, May 9-12.

9. Claridge, E.L. and Prats, M.: "A Proposed Model and Mechanism for Anomalous Foamy Heavy Oil Behavior," paper SPE 29243 presented at the 1995 SPE International Heavy Oil Symposium, Calgary, AB, June 19-21.

10. Sheng, J.J., Maini, B.B., Hayes, R.E., and Tortike, W.S.: "A Nonequilibrium Model to Calculate Foamy Oil Properties," paper CIM 95-19 presented at the 1995 CIM Annual Technical Meeting, Banff, AB, May 14-17.

11. Huerta, M., Tico, A., Jimenez, I., Mirabal, M. de, and Rojas, G.: "Understanding Foamy Oil Mechanisms for Heavy Oil Reservoirs During Primary Production," paper SPE 36749 presented at the 1996 SPE Annual Technical Conference and Exhibition, Denver, CO, October 6-9.

12. Maini, B.B., Sarma, H.K., and George, A.E.: "Significance of Foamy-Oil Behaviour in Primary Production of Heavy Oil," *JCPT* (1993) Nov. 50-54.

13. Firoozabadi, A. and Anderson, A.: "Visualization and Measurement of Gas Evolution and Flow of Heavy and Light Oil in Porous Media," paper SPE 28930 presented at the 1994 SPE Annual Technical Conference and Exhibition, New Orleans, LA.

14. Bora, R., Maini, B.B., and Chakma, A.: "Flow Visualization Studies of Solution Gas Drive Process in Heavy Oil Reservoirs Using a Glass Micromodel," paper SPE 37519 presented at the 1997 SPE Thermal Operations and Heavy Oil Symposium, Bakersfield, CA, Feb. 10-12.

15. Shen C. and Batycky, J.: "Some Observations of Mobility Enhancement of Heavy Oil Flowing Through Sandpack under Solution Gas Drive," paper CIM 96-26 presented at the 1996 CIM Annual Technical Meeting, Calgary, AB, June 10-12.

16. Lolley, C.S. and Richardson, W.C.: "Compositional Input for Thermal Simulation of Heavy Oils with Application to the San Ardo Field," paper SPE 37538 presented at the 1997 SPE Thermal Operations and Heavy Oil Symposium, Bakersfield, CA, Feb. 10-12.

17. Falls, D.H., Hirasaki, G.J., Patzek, T.W., Gauglitz, D.A., Miller, D.D., and Ratulowski, T.: "Development of a Mechanistic Foam Simulator: The Population Balance and Generation by Snap-off," *SPERE* (1988) 884-92.

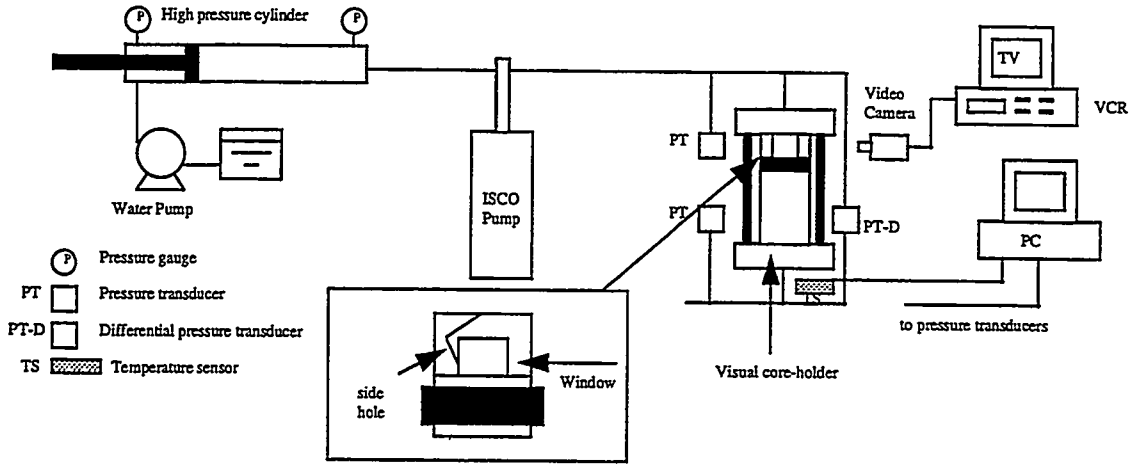

Figure 1. Schematic diagram of the setup

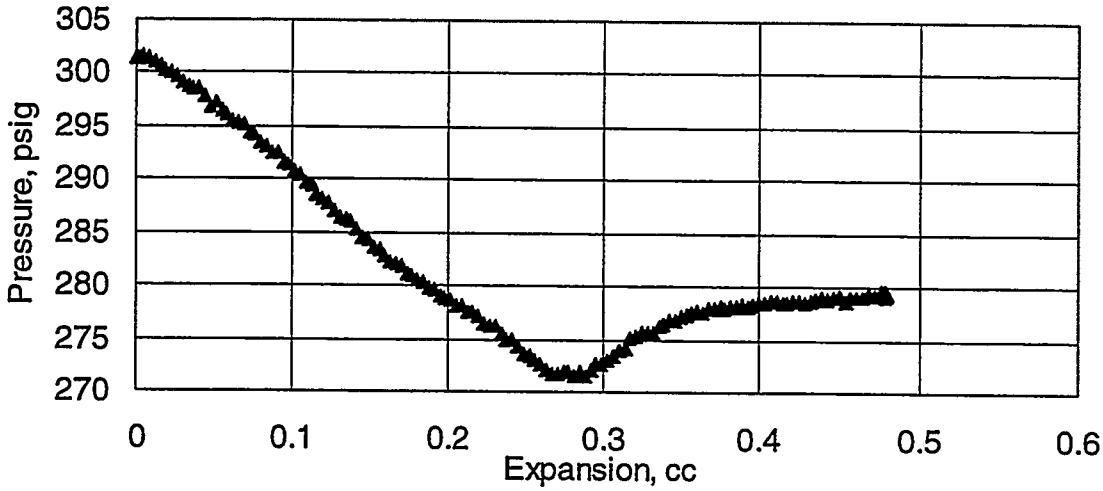

Figure 2. Pressure vs. volume expansion for the light model oil run

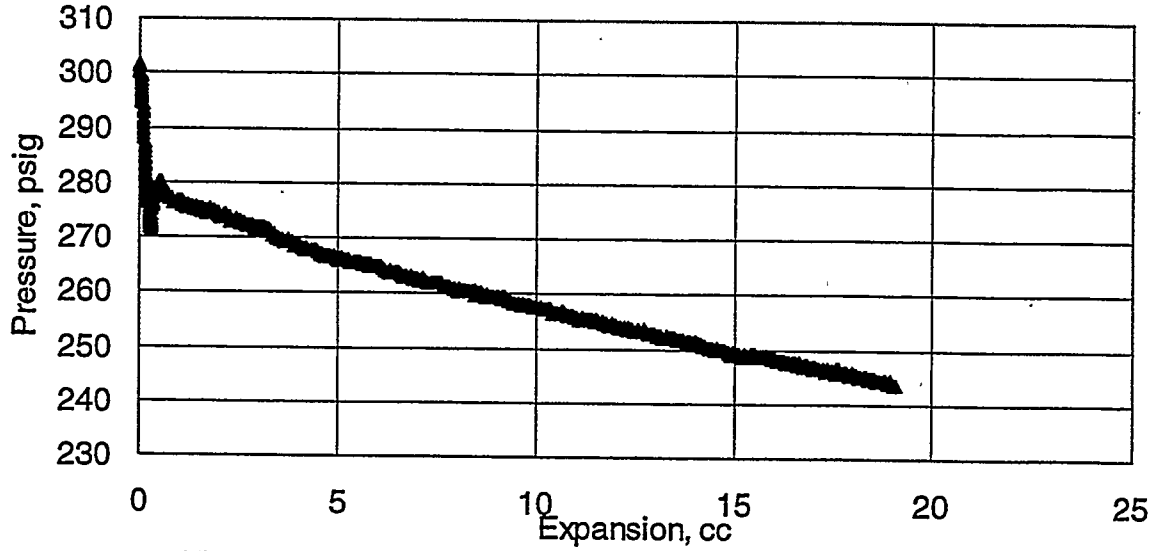

Figure 3. Pressure vs. volume expansion for the light model oil run

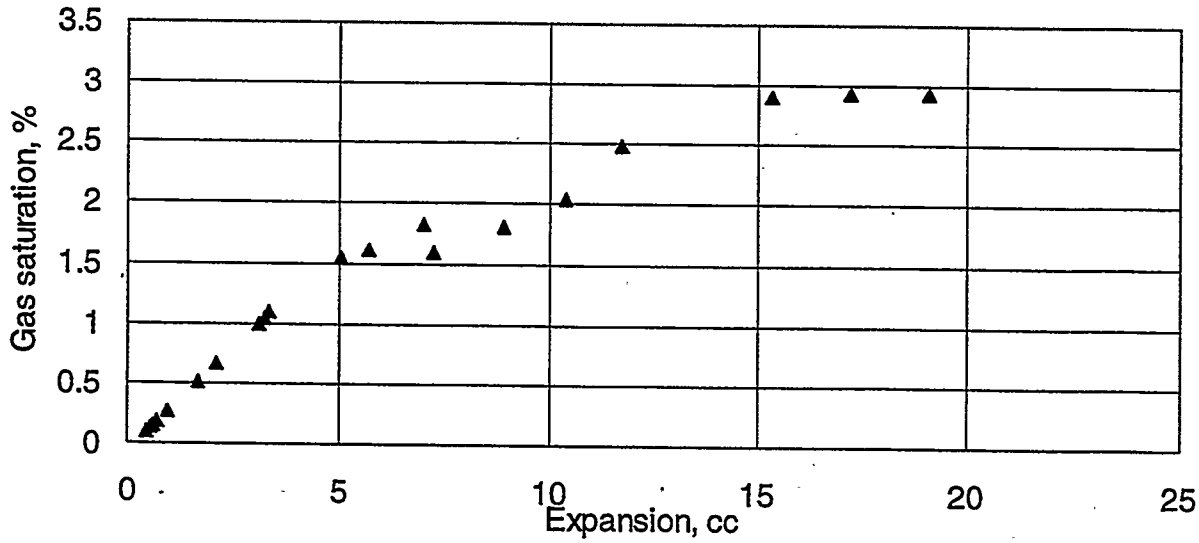

Figure 4. Gas saturation in the sand pack for the light model oil run

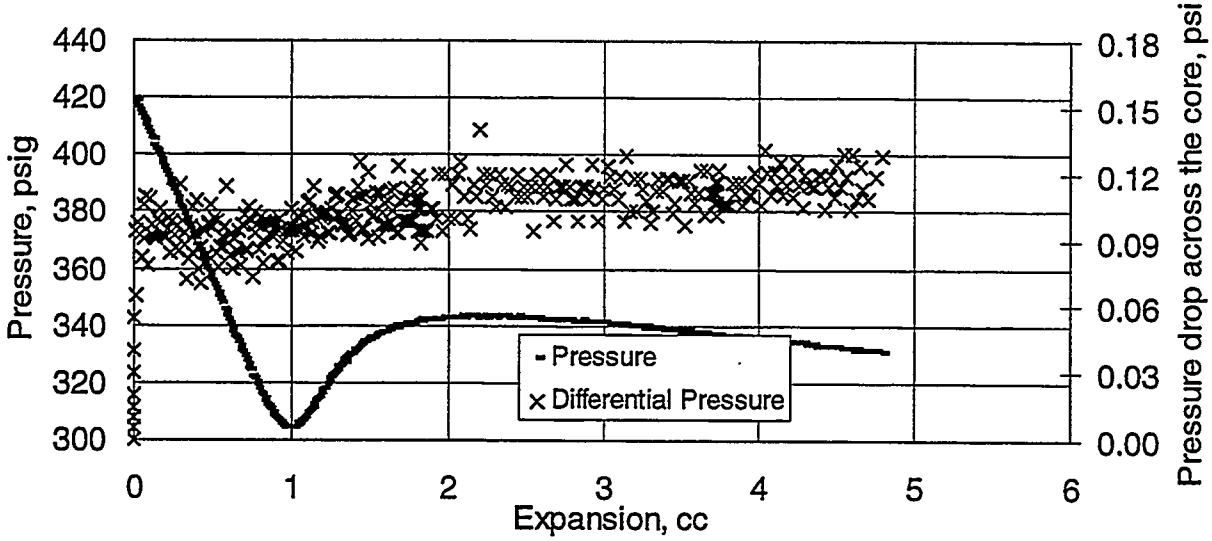

Figure 5. Pressure vs. volume expansion for the heavy oil run

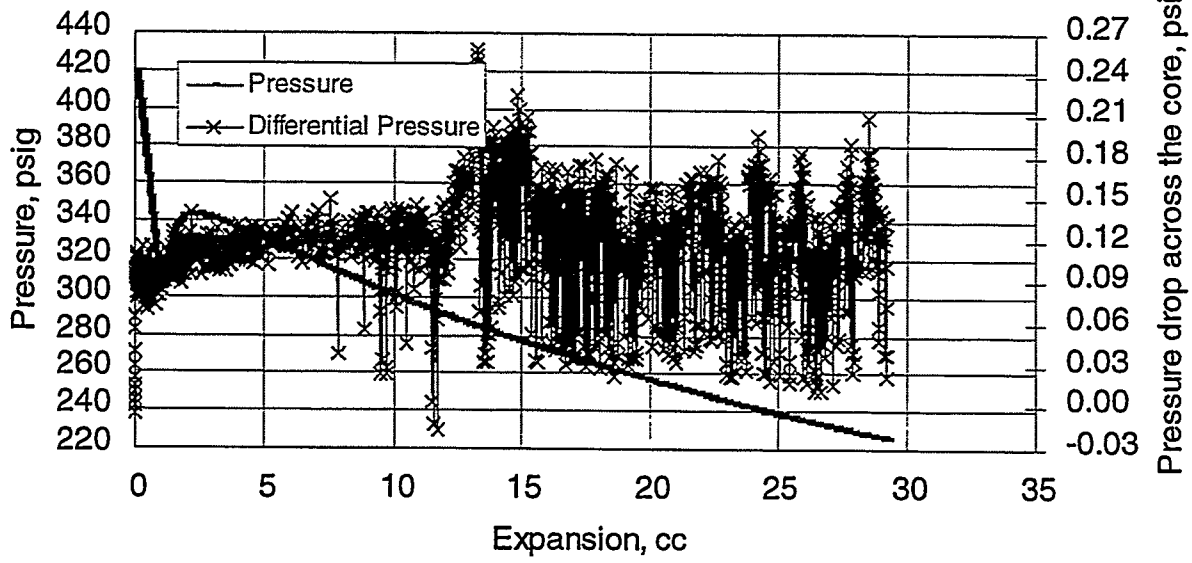

Figure 6. Pressure vs. volume expansion for the heavy oil run

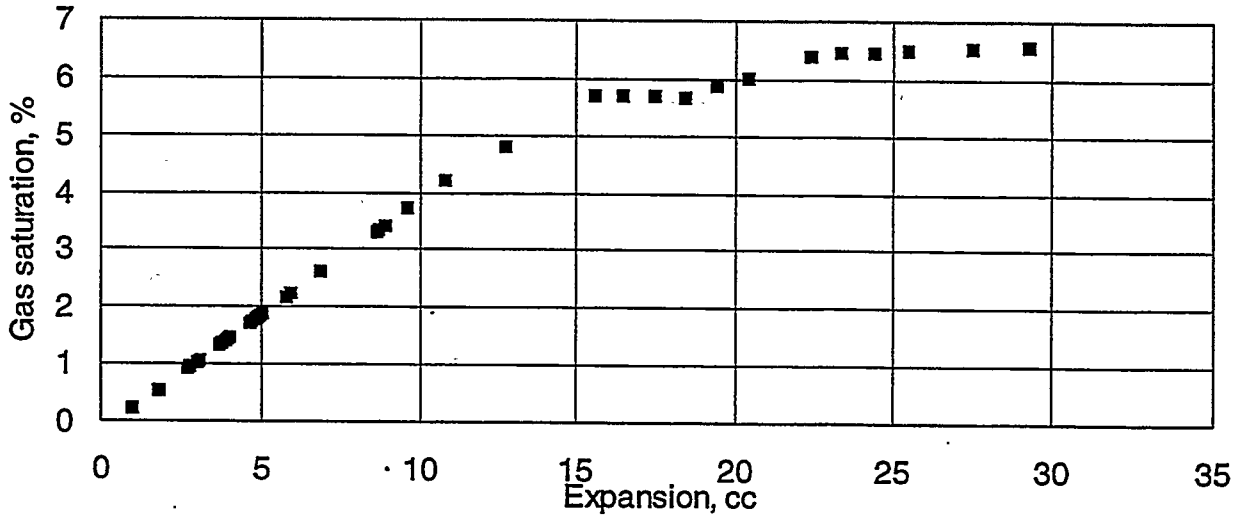

Figure 7. Gas saturation in the sand pack for the heavy oil run

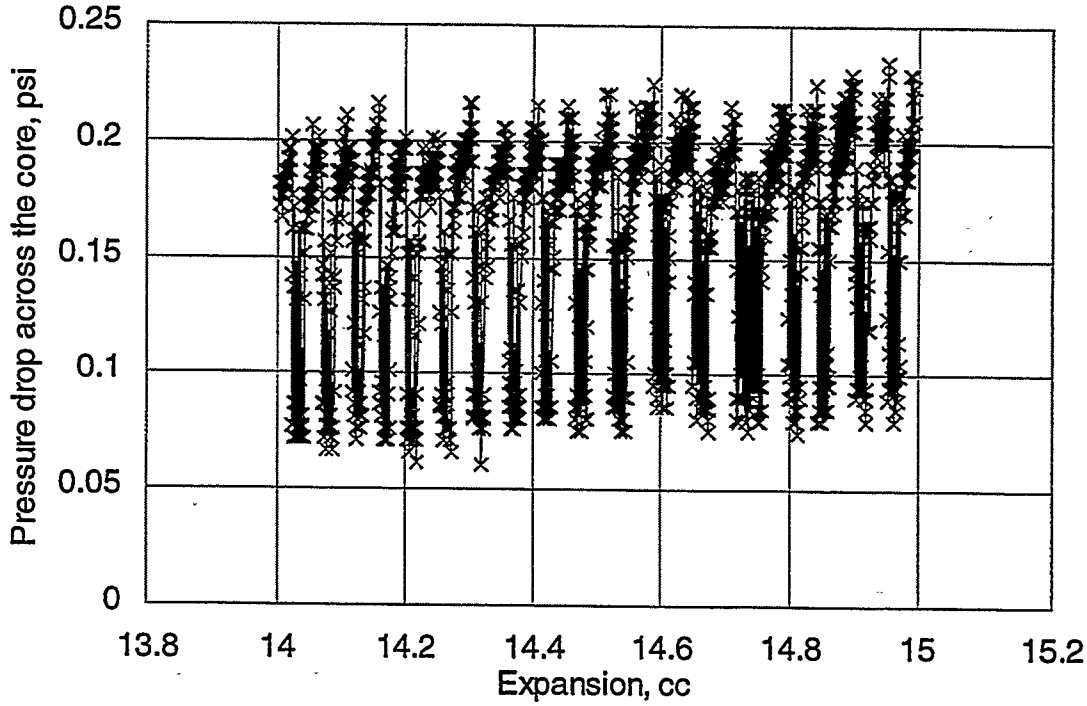

Figure 8. Pressure drop vs. volume expansion for the heavy oil run

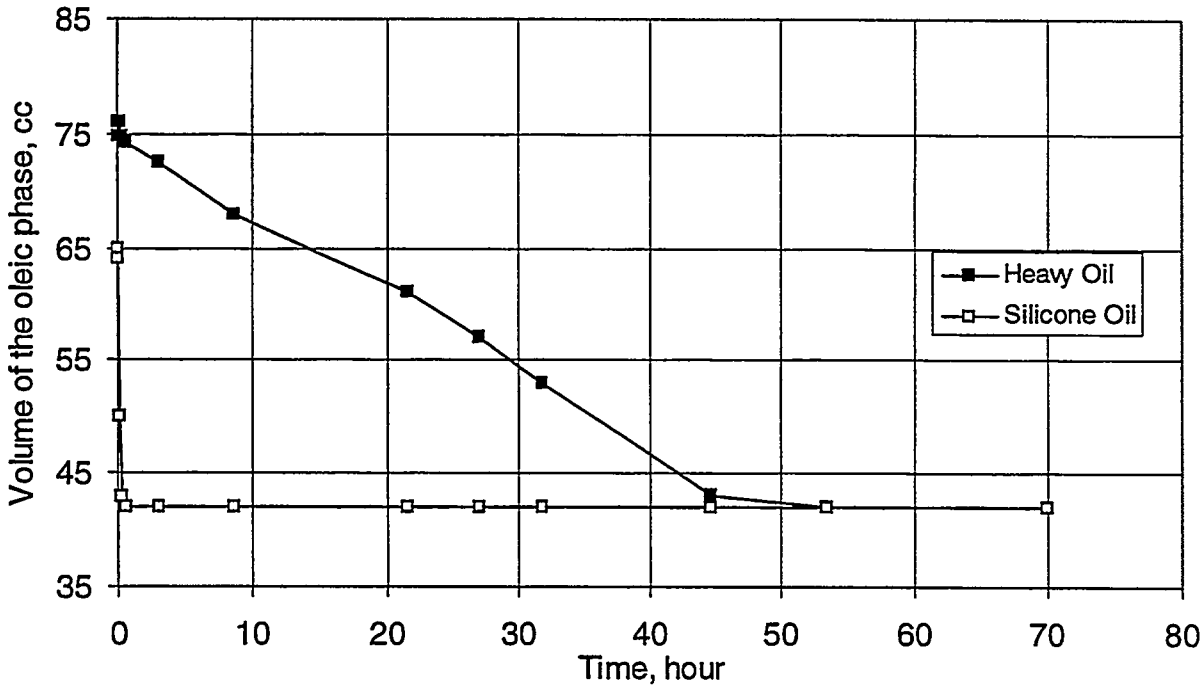

Figure 9. Volume change of the Silicone and heavy oils vs. time

Chapter III – Intermediate Gas-Wetting and Its Significance for Gas Condensate Reservoir

Part I – Phenomenological Modeling of Critical Condensate Saturation and Relative Permeabilities in Gas Condensate Systems

KEWEN LI AND ABBAS FIROOZABADI

Summary

The effects of gravity, viscous forces, interfacial tension, and wettability on the critical condensate saturation and relative permeability of gas condensate systems are studied using a phenomenological simple network model. The results from the simple model show that wettability significantly affects both critical condensate saturation and gas phase relative permeability. Gas phase relative permeability at some saturations may increase ten times as contact angle is altered from 0° (strongly liquid-wet) to 85° (intermediately gas-wet). The results suggest that gas well deliverability in condensate reservoirs can be enhanced by wettability alteration near the wellbore.

Introduction

Much attention has been paid to the study of in-situ liquid formation and fluid flow mechanisms in gas condensate systems in recent years. When gas condensate reservoirs are developed by pressure depletion, gas well deliverability is affected by the amount and the distribution of the condensate formed around the wellbore. The understanding of the parameters that affect the distribution and the amount of condensate saturation (S_o) in the wellbore and the effect of these parameters on gas and liquid flow are important towards the development of the methods for increased gas deliverability.

There are numerous field examples of gas condensate reservoirs that experience a sharp drop in gas well deliverability at high pressures due to the condensation near the wellbore.[1-3] There are examples that the condensation may even kill gas production.[2] The sharp reduction in gas deliverability may be due to the shape of gas phase relative permeability (k_{rg}); the mechanisms of gas productivity impairment are not yet clear. Two main parameters affect condensate recovery and gas well deliverability. These two parameters are: 1) critical condensate saturation (S_{oc}), and 2) gas phase relative permeability.

Various authors[4-9] have measured S_{oc} and a wide range of observations are reported. The measured values of S_{oc} are generally in the range of 10 to 50%. Gravier et al.[4] (1986) measured S_{oc} in carbonate low permeability cores with permeability in the range of 0.5 to 40 md and interfacial tension (σ) variations from 0.5 to 1.5 dynes/cm. S_{oc} varied from 24.5 to 50.5% with an average of 35.0%. These measurements were conducted in the presence of connate water. Morel et al.[9] (1992) reported a critical condensate saturation of less than 1% for σ = 0.05 dynes/cm and connate water saturation of 20%. The critical condensate saturation was

measured in a vertical dolomite core. The measured S_c is apparently related to various effects including gravity and interfacial tension.

Some authors have accounted for the effect of gravity by conducting flow experiments both in horizontal and vertical directions. Danesh et al.[10] (1991) studied the effect of gravity on S_c in water-wet micromodels and sandstone cores. They found that S_c in a vertical core was lower than that in a horizontal core; their tests showed that gravity reduced the critical condensate saturation. These authors also examined the dependence of critical condensate saturation on σ. As expected, S_c increases with an increase in σ. Ali et al.[11] (1993) observed an improved condensate recovery of 17.2% in a vertical gas injection compared with that in a horizontal injection. Their experiments were conducted with a high interfacial tension for gas condensates (σ = 0.92 dynes/cm). Sandstone cores and a synthetic six-component fluid were used by these authors. When σ was decreased to 0.04 dynes/cm, condensate recovery improved to 27.5% with vertical injection. Henderson et al.[12] (1993) also reported a significant reduction of the critical condensate saturation in long vertical core samples in comparison to those in horizontal cores. Munkerud[6] (1989), however, did not find significant difference in condensate recovery and saturation between horizontal and vertical pressure depletion. He used Berea cores and a synthetic six-component fluid.

A number of authors have studied gas phase relative permeability of gas condensate systems. Gravier et al.[4] (1986) found an abrupt decrease in k_{rg} close to S_c. Chen et al.[5] (1995) measured k_{rg} at reservoir pressures with reservoir rock and reservoir fluids from two North Sea gas condensate reservoirs. The interfacial tension σ varied from 0.01 to 0.42 dynes/cm. The results showed that k_{rg} reduced about ten-fold due to condensation when S_c reached 20% for Reservoir A core and fluid. Reduction of k_{rg} with the increase of S_c for Reservoir B core and fluid is less pronounced but an abrupt decrease of k_{rg} close to S_c was also observed. Chen et al.[5] (1995) showed that k_{rg} is rate dependent; it increases with the increase of flow rate. Henderson et al.[13] measured gas-condensate relative permeabilities using a long Berea core and a 5-component synthetic gas condensate fluid; σ varied from 0.05 to 0.40 dynes/cm. They found that the relative permeabilities of both gas and liquid phases decreased with the increase of σ and increased with the increase of flow rate. Gas relative permeability was more sensitive to σ and flow rate than liquid relative permeability. The results from the work of Munkerud[6] (1989) and Haniff et al.[14] (1990) differ from the other authors. They did not observe the abrupt decrease of k_{rg}.

The brief review above points out that there are many unresolved issues in the study of critical condensate saturation and gas-condensate relative permeability. The sharp decrease in gas relative permeability close to S_c that was observed experimentally has not yet been studied theoretically. The dependence of S_c, k_{rg}, and k_{rr} on interfacial tension, viscous force, and gravity are not clear from the experimental data. The question remains how to measure S_c, k_{rg}, and k_{rr} in the laboratory and how to scale them to field conditions. The conclusions drawn from the experimental results are sometimes not consistent. A theoretical understanding of the effect of σ, gravity, viscous force, and wettability on S_c, k_{rg}, and k_{rr} helps give insight into the recovery of liquid condensate from rich gas condensate reservoirs, and gas well deliverability from both rich and lean gas condensate reservoirs.

Theoretical work on the critical condensate saturation and relative permeabilities of gas condensate systems is very limited. Mohammadi et al.[15] found that the relative permeabilities in gas condensate systems follow the conventional displacement process. These authors used percolation theory in their work for horizontal porous media. The effect of interfacial tension, viscous force, gravity, and wettability on critical condensate saturation and gas-condensate relative permeability was not included in the work of Mohammadi et al.[15]. Fang et al.[16] (1996) developed a phenomenological network model for critical condensate saturation. The

main results from this model are that critical condensate saturation is a function of 1) interfacial tension, and 2) contact angle in gas-oil-rock systems. The model of Fang et al.[16] is based on the assumption of negligible viscous forces and limited tube length.

In this work, we first modify the S_{cc} model of Fang et al.[16] for predicting critical condensate saturation to include the effect of viscous forces and to relax the assumption of large tube length. We then develop a relative permeability model (k_r model) for gas condensate systems using a renormalization technique. Using the model, the effects of interfacial tension, flow rate, and contact angle hysteresis on the critical condensate saturation and gas or condensate relative permeabilities are investigated. The results from the modified S_{cc} model and the k_r model show that S_{cc} and k_r are significantly affected by interfacial tension, gravity, flow rate, and wettability. Wettability may have the most pronounced effect on both S_{cc} and k_{rg}.

Network Model for Condensation in Porous Media

The porous medium used in this study is represented by a simple 2D pore network with circular capillary tubes of the length L and cubic intersections of side width b; we assume b to be equal to the maximum diameter of the capillary tube in the network. There are four tubes connected to each intersection; therefore, the coordination number is four. A log-normal size distribution is assumed with a standard deviation of 5.74 and an average radius of 23 μm for the capillary tubes. The size distribution of the network with 20▶ 20 intersections is sketched in **Fig. 1**. In this sketch, the tube diameter is proportional to the thickness. The total pore volume of the network with a tube length of 6000 μm is 8.93 mm^3; the total volume of the intersections in the network is 0.03 mm^3 and the estimated permeability of the network is about 1 darcy. Note that the simple network just described is basically selected for some sensitivity studies.

Critical Liquid Height and Critical Condensate Saturation in a Single Capillary Tube

Fang et al.[16] developed a phenomenological model for the critical condensate saturation in a porous medium represented by a network. Their model is based on two assumptions: 1) viscous forces are negligible and 2) the critical liquid height (h_{cc}) from liquid formed in-situ in the capillary tubes is less than the tube length (the critical height is the maximum length before the liquid column becomes mobile). In this work, we extend the model of Fang et al.[16] to include the effect of viscous forces, and provide the option for $h_{cc} > L$. When a liquid is first formed in a capillary tube, we assume that it appears in the middle part of the tube in the form of a liquid bridge. During its growth, interfacial tension, gravity, contact angle hysteresis, viscous force and the size of capillary tubes are the main factors that affect the stability of the new liquid phase.

The critical height h_{cc} of liquid formed in-situ in a circular capillary tube of radius r is expressed as (see **Fig. 2a**):[16]

$$h_{cc} = \frac{2\sigma}{\Delta\rho g r}(\cos\theta_R - \cos\theta_A) - \frac{p_R - p_A}{\Delta\rho g} \qquad (1)$$

where p_R is the pressure at the top and p_A the pressure at the bottom of the liquid column; θ_R is the receding contact angle and θ_A the advancing contact angle; $\Delta\rho$ is the density difference between gas and liquid phase. The equation above is derived on the basis of the balance between capillary pressure, viscous force and gravity. In this study, for simplicity it is assumed that the gas density ρ_g is equal to zero (that is, $\Delta\rho = \rho_l$).

Liquid will flow downward to the bottom of the tube when the height of the liquid column exceeds h_{cr}. The advancing contact angle will then change to 90°. At this time, the critical height of the liquid column will increase and can be calculated from Eq.1. Once h_{cr} is determined, the critical condensate saturation in a single capillary tube is calculated as h_{cr}/L.

Process of Condensate Formation, Growth and Flow for $h_{cc}>L$

Liquid condensation may take place in capillary tubes of smaller diameters based on the thermodynamics of curved interfaces.[17] The condensation process in a network is represented by discrete steps.[16] When pressure decreases below dewpoint pressure, the gas in those tubes with radius $r < r_p$ is allowed to condense. The process of in-situ condensate formation, growth and flow when $h_{cr} > L$ is presented in **Fig. 3**. For the study of viscous effect, it is assumed that gas is injected from the top of the network.

As the pressure in the system decreases below the dewpoint pressure, liquid condensate is assumed to condense in the middle of tube 3 ($r_3 < r_p$) in the form of a liquid bridge as shown in step 1. The top receding contact angle θ_R (measured through the liquid phase) will be less than the bottom advancing contact angle θ_A due to gravity and viscous effects.

Continuous condensation increases the liquid height in tube 3. Assuming the critical liquid height $h_{3cr} > L$, the advancing contact angle will increase and reach 90°. This is shown in step 2. With further condensation, the advancing contact angle will exceed 90°. The receding contact angle at the top will also increase and reach 90° (see step 3).

If both the advancing and the receding contact angles reach 90° at the same time, the liquid column becomes unstable and will flow downward. The advancing contact angle will then exceed 90°. The receding and advancing contact angles will continue to increase with further condensation in tube 3 (see step 4). Given r_2 < Min (r_4, r_5, r_6), the condensate formed in-situ will contact the corner point "*A*" shown in step 5. The interface has the maximum radius, r_{max}. At this stage, the condensate becomes unstable and forms two new interfaces, one in tube 2 and another in the intersection as shown in step 6. Because the radius of the interface in tube 2 is smaller than that in the intersection, the liquid pressure in the intersection is higher than that in tube 2. The liquid will be pulled into tube 2 as a result. The new configuration is shown in step 7.

Now, the liquid interface in tube 2 serves as a new condensation site. After tube 2 is filled by the condensate, the contact angle at the left end of tube 2 will increase until it reaches 90° (i.e. flat interface); then there will be no further condensation. However, the condensation will continue at the right end of tube 2; as a result, a new liquid interface in the intersection will develop. The liquid interface will touch the corner point "*D*" with further condensation (see step 8).

The liquid interface will then break into two new liquid interfaces, one in tube 1 and another in tube 4 as shown in step 9. Given that r_1 is less than r_4, the liquid in tube 4 will be pulled into tube 1. The condensation will continue in tube 1 until it reaches the critical height (h_{13cr}). The liquid formed later in tube 1 will flow downward into tube 4. The liquid height in tube 1 remains the same. The critical height h_{13cr} is calculated from:

$$h_{13cc} = \frac{2\sigma}{\Delta\rho g}\left(\frac{\cos\theta_R}{r_1} - \frac{\cos\theta_A}{r_3}\right) - \frac{p_R - p_A}{\Delta\rho g} \qquad (2)$$

After tube 4 is filled, the contact angle at the right end of tube 4 will increase until it reaches 90° (dashed line shown in step 9). Then, the contact angle at the left end of tube 2 will start to increase. Because r_4 is larger than r_2, the condensate will flow into the intersection connecting tubes 4, 8, 9, 10 (see step 10). The contact angle at the left end of tube 2 will exceed 90° with further condensation.

When in-situ condensation continues (see step 10), if r_8 is less than r_{10}, the liquid interface in the intersection will touch the corner point *F*. The liquid interface will also break into two new interfaces, one in tube 8 and another still in the intersection after the interface contacts point *F*. The configuration of the liquid interface in the intersection near point *F* will change and adjust itself as shown in step 11. At the same time, the contact angle at the left end of tube 2 will decrease. Because the radius of the liquid interface in the intersection is larger than that in tube 8, the liquid pressure in the intersection is higher than that in tube 8, and the liquid will be pulled into tube 8. After the force balance is established between the capillary force and the gravity in the liquid column in tube 8, the liquid in tube 8 will reach critical height. With further condensation, the liquid formed in tubes 1 and 8 will flow downward and the liquid in the intersection will touch the corner point *G*.

The liquid interface in the intersection will break after it contacts the corner point *G*. If $r_9 < r_{10}$, the liquid formed in tubes 1 and 8 will be pulled into tube 9 until it is filled (see step 12). With further condensation, the liquid formed in tubes 1 and 8 will flow downward into tube 10. Assuming the critical liquid height $h_{10,cr}$ in tube 10 is less than the tube length, the liquid will flow downward when the liquid height > $h_{10,cr}$. At the same time, the liquid in tube 8 will also flow downward into tube 10. The configuration developed is shown in step 13. With further condensation, the liquid formed in tube 1 will flow downward through tube 4 to tube 10 and then to the next element. When the liquid interface in the intersection touches point *G*, the liquid will first enter tube 10, instead of tube 9 if $r_9 > r_{10}$. When the liquid height in tube 10 is equal to or larger than $h_{10,cr}$, the liquid in tube 10 flows downward (see step 14).

If $r_8 > r_{10}$, the liquid interface will form two new interfaces after contacting the corner point *G*, one in tube 10 and another in the intersection. Because the radius of the liquid interface in the intersection is larger than in tube 10, the liquid will be pulled into tube 10. The liquid formed later will also enter tube 10 instead of tube 8. Assuming $h_{10,cr} < L$, the configuration shown in step 15 is established after the liquid height in tube 10 reaches critical height. With further condensation in this element liquid will flow downward through tube 4 to tube 10 and then to the next element.

As stated previously, the process of in-situ condensate formation, growth and flow when $h_{cr} < L$ is described in Ref. 17.

Calculation of S_{cc}

The first step for the estimation of S_{cc} is to determine the differential pressure in each tube. The pressure distribution in the entire network is calculated as follows. At every intersection one can write:

$$\sum_{i=1}^{4} Q_i = 0 \qquad (3)$$

where Q_i is the flow rate of fluid in tube *i*. The flow rate in a circular capillary tube can be calculated from

$$Q_i = \frac{\pi r_i^4}{8\mu}\left(\frac{\Delta p_i}{L} + \rho g\right) \qquad (4)$$

provided that the fluid is incompressible. In the above equation, μ is fluid viscosity, ρ is fluid density, Δp_i and r_i are differential pressure (inlet-outlet) and radius of tube i, respectively.

Once the pressures at inlet and outlet sides of the network are provided, Eqs.3 and 4 can be used to obtain the pressure distribution in the network. Gauss iteration method can be used to solve the set of linear equations. Note that for every tube i with $h_c < h_{ac}$, $Q_i = 0$, as we will discuss later. S_{ac} in each tube can be calculated with the known pressure distribution according to Eqs.1 and 2. Then the value of the total S_{ac} in the network is readily calculated.

Calculation of Fluid Conductance

Consider a single-phase flow in a capillary tube of radius r_i and length L. According to Darcy's law, the flow rate across the tube is $Q_i = (k_i/\mu L)\pi r_i^2(\Delta p_i + \rho g L)$, where k_i is the permeability of tube i. An alternative form of the Darcy equation is $Q_i = G_i(\Delta p_i + \rho g L)$, where G_i is the conductance of tube i. Comparison of the Darcy equation with Eq. 4 provides the expression for the fluid conductance of tube i:

$$G_{ij} = \frac{\pi r_i^4}{8\mu_j L}, \quad (S_j = 1) \qquad (5)$$

where G_{ij} and S_j are the conductance and the saturation of fluid j in tube i, respectively; μ_j is the viscosity of phase j. Prior to S_{ac} when there is some liquid saturation in the tube, gas may not flow, and therefore, $Q_i = 0$. The effective conductance of fluid phase j in tube i, which is related to the effective permeability of phase j, can be calculated using the following equation when $S_c \le S_{ac}$:

$$G_{ij} = 0, \qquad (S_c \le S_{ac}) \qquad (6)$$

Now consider a tube with some liquid saturation S_c (see **Fig. 2b**) which is larger than S_{ac}. In this case, liquid is located at the bottom of the tube and both liquid and gas may flow. The equation for calculating the gas conductance G_{ig} of tube i is:

$$G_{ig} = \frac{\pi r_i^4}{8\mu_g L}\left[1 - S_{ic} + \frac{\mu_c}{\mu_g} S_{ic}\right]^{-1}, \quad (S_c > S_{ac}) \qquad (7)$$

where μ_g and μ_c are the gas and liquid condensate viscosity, respectively. S_{ic} is the liquid condensate saturation in tube i. Derivation of Eq.7 is provided in Appendix A. Similarly, the liquid conductance of tube i can be calculated as:

$$G_{ic} = \frac{\pi r_i^4}{8\mu_c L}\left[S_{ic} + \frac{\mu_g}{\mu_c}(1 - S_{ic})\right]^{-1}, \quad (S_c > S_{ac}) \qquad (8)$$

where G_{ic} is the conductance of the liquid phase for case $S_c > S_{cr}$.

The next step is to calculate the effective conductance of both gas and liquid phases in the entire network based on conductances of individual tubes. Once the effective conductance of both gas and liquid phases in the network is calculated, gas and condensate relative permeabilities can be readily calculated. In the following, we will use the renormalization method[18] to calculate the effective conductance of the network from conductances of individual tubes.

Renormalization Method and Relative Permeabilities

A useful technique to study transport in disordered systems is real-space renormalization group method that arises in condensed-matter physics[18]. King[19-20] (1989,1993) has applied this technique to single- and two-phase fluid flows. Filippi and Toledo[21] (1993) also used the method for heterogeneous and highly anisotropic systems. The renormalization method is accurate and computationally cost-effective in comparison with direct numerical simulation.

For a given phase and a known saturation distribution, the effective phase conductance is calculated in small regions, the so-called renormalization cells, and then in larger scales. **Fig. 4** shows the grid units with different renormalization cell number n_b for a 2D network. In this figure, renormalization cell number varies from 2 to 5. The effective conductance of one phase in the whole system can be obtained from the repeated application of the renormalization procedure.

Fig. 5 shows the renormalization procedure for $n_b = 2$. The primary network is comprised of four cell units of $n_b = 2$. After the first step of renormalization, the network reduces to one cell unit of $n_b = 2$. In the last step, the primary network is converted to two units, one in the horizontal and the other in the vertical direction. Let us consider a cell unit with eight tubes (that is, $n_b = 2$) sketched in **Fig. 6a**. The effective networks in the vertical and horizontal directions are shown in **Figs. 6b** and **6c**, respectively. The effective conductance, G_z, in the vertical direction for $n_b = 2$ is calculated from

$$G_z = \frac{G_8G_4G_6 + G_8G_4G_7 + G_8G_6G_7 + G_8G_3G_7 + G_6G_7G_3 + G_4G_6G_3 + G_4G_3G_7 + G_6G_8G_3}{G_6G_7 + G_4G_6 + G_6G_8 + G_4G_7 + G_4G_8 + G_3G_7 + G_3G_4 + G_3G_8} \tag{9}$$

The effective conductance, G_x, in horizontal direction for $n_b = 2$ can be calculated by

$$G_x = \frac{G_4G_3G_2 + G_4G_3G_1 + G_4G_2G_1 + G_4G_5G_1 + G_2G_1G_5 + G_3G_2G_5 + G_3G_5G_1 + G_2G_4G_5}{G_2G_1 + G_3G_2 + G_2G_4 + G_3G_1 + G_3G_4 + G_5G_1 + G_5G_3 + G_5G_4} \tag{10}$$

where G_1, G_2, ... , G_8 represent the phase conductance of each tube, which are shown in **Fig. 6**. Derivation of Eq.9 is provided in Appendix B. Relative permeabilities for the network presented in **Fig. 1** are calculated according to the following procedures: (1) Calculate the absolute gas conductance in the vertical direction, G_{abs} for the whole network first saturated completely with gas. This is realized by repeating the renormalization steps at different scales as shown in **Fig. 5**; (2) Calculate the effective conductance of gas G_{zg} or liquid phase, G_{zo} at a given condensate saturation S_c in the vertical direction when liquid is formed in the network due to the pressure decrease below the dewpoint pressure; (3) Calculate gas relative permeability k_{rg}

by G_{rg} / G_{abs} and liquid relative permeability k_{rc} by $(\mu_c G_{rc})/(\mu_g G_{abs})$. k_{rg} and k_{rc} data at different S_c provide relative permeabilities.

Results

The models described above are used to calculate S_{cc}, k_{rg}, and k_{rc}. The results and the sensitivity of the calculation to various parameters are described in the following.

Critical Condensate Saturation. Critical condensate saturation is calculated using the modified S_{cc} model. The results show that critical condensate saturation is a function of interfacial tension, flow rate, gravity, and contact angle hysteresis.

Effect of Interfacial Tension and Gravity. The effect of σ and gravity on S_{cc} is shown in **Fig. 7** for two different values of the viscous force, Δp, across the network. The results are based on a tube length of 6000 μm, $\theta_R = 0°$ and $0° < \theta_A \leq 90°$. **Fig. 7** shows that S_{cc} increases as σ increases ($0 < \sigma < 4.0$ dynes/cm). Fang et al.[16] (1996) made the same observation for σ in the range of 0 to 0.45 dynes/cm. The figure shows that S_{cc} decreases with an increase of $\Delta\rho$. When σ is large enough, S_{cc} reaches the same maximum value for different $\Delta\rho$ values, which implies that the effect of gravity on S_{cc} becomes negligible at high values of σ. The results in **Fig. 7** are consistent with the experimental data by Danesh et al.[10] (1991), Chen et al.[5] (1995), Ali et al.[11] (1993) and Henderson et al.[12] (1993). These authors have observed that S_{cc} increases as σ increases and the increased gravity effect lowers S_{cc}. Various calculations from the model show that as long as θ_A is not zero ($\theta_A > 0$), the critical condensate saturation is not affected by the magnitude of θ_A.

Comparison of **Figs. 7a** and **7b** reveals that S_{cc} decreases when Δp increases. The effect of gravity on S_{cc} becomes negligible at high Δp when σ varies in the range of 0 to 2 dynes/cm (see **Fig. 7b**). The results presented in **Fig. 7** demonstrate that gravity may or may not affect S_{cc}. When Δp is small (that is, at low flow rates), S_{cc} is affected by gravity whereas for high Δp, the effect of gravity is less pronounced. The results in **Fig. 7** explain the effect of gravity on S_{cc} and reveals that there may be no inconsistency in the experimental data reported by various authors. The effect of viscous forces is discussed in more detail next.

Effect of Flow Rate. The effect of viscous force (that is, flow rate) on S_{cc} is shown in **Fig. 8** for $\Delta\rho = 0.1$ and 0.5 g/ml. Other parameters are the same as those used previously. Δp varies in the range of 0.05 to 0.4 psi in **Fig. 8**. This figure shows that the critical condensate saturation decreases with the increase of the viscous force (that is increase in pressure drop). Comparison of **Figs. 8a** and **8b** reveals that the effect of Δp on S_{cc} is more pronounced at lower gravity when σ varies in the range of 0 to 2 dynes/cm (see **Fig. 8a**). The effect of Δp on S_{cc} is reduced at high σ ($\sigma > 3$ dynes/cm). The calculated results shown in **Fig. 8** are consistent with the experimental data of Chen et al.[5] who found that S_{cc} decreases as flow rate increases.

Effect of Contact Angle Hysteresis. In a gas-oil-rock system, oil phase is considered as the wetting phase and gas is the non-wetting phase. It is often assumed that the contact angle through the liquid phase is zero. The assumption of liquid-wetness in a gas-liquid system is valid but the assumption of $\theta = 0°$ may be invalid. If the wettability of the fluid-rock system in a gas condensate reservoir near wellbore could be altered to intermediate gas-wetness by some chemicals, S_{cc} and k_{rg} may also change. **Fig. 9a** presents S_{cc} vs. σ for $\theta_R = 85°$ and $85° < \theta_A \leq 90°$. Other parameters are the same as those used in **Fig. 7**. This figure shows that S_{cc}

becomes very small and variations of σ or $\Delta\rho$ have very little effect on S_{gc} when the receding contact angle increases to 85°. **Fig. 9b** shows the effect of receding contact angle; S_{gc} decreases as the receding contact angle increases from 0 to 85° at a fixed σ. This figure demonstrates that wettability alteration to the gas phase has the most pronounced effect on S_{gc}.

The observation that there may be no effect of σ on S_{gc} for intermediate gas-wettability (see **Fig. 9**) is interesting. The critical condensate saturation is sensitive to σ if the fluid-rock system is strongly liquid-wet as was shown in **Fig. 7.** However, for an intermediately gas-wet system, the critical condensate saturation becomes small and does not increase much even at very high σ as **Fig. 9** shows.

Effect of Network Size. We calculated S_{gc} with different network sizes in order to study the sensitivity of our S_{gc} model to the network size. The results showed that for σ = 0.01 dynes/cm with or without viscous force, S_{gc} becomes approximately constant when the network size is larger than 15▶ 15. This demonstrates that the network size chosen for this study, 20▶ 20, is appropriate.

Relative Permeabilities. The major theme of this work is the study of relative permeability in gas condensate systems. In the following we will present the results from the model.

Features of Gas Relative Permeability. **Fig. 10a** depicts a sketch of the measured gas-phase relative permeability curve for low permeability carbonate rocks in gas condensate systems[4]. **Fig. 10b** presents the calculated gas phase relative permeability curve from our model. This figure shows that the model results reproduce the features of the experimental data. Both the model results and experimental data show an abrupt drop in gas phase relative permeability at condensate saturation close to S_{gc}. When gas phase relative permeability decreases abruptly, the gas well deliverability reduces sharply.

Effect of Interfacial Tension. The effect of σ on gas-condensate relative permeabilities is plotted in **Fig. 11.** The saturation interval is selected to be for $S_c > S_{gc}$ to compare model results with experimental data. σ varies in the range of 0.01 to 0.50 dynes/cm. **Fig. 11**shows that both gas and liquid phase relative permeabilities decrease with the increase of σ. Liquid phase relative permeability is less sensitive to σ than gas phase relative permeability. The model results are in agreement with the experimental data of Henderson et al.[13]. These authors found that the relative permeabilities of both phases to decrease with the increase of σ. The gas relative permeability reduction was, however, more pronounced.

Effect of Flow Rate. The effect of flow rate on gas and condensate relative permeabilities is graphed in **Fig. 12.** This figure shows that both k_{rg} and k_{rc} increase with the increase of Δp. Our model results are in agreement with the experimental work by Chen et al.[5] who found that gas relative permeability increased as the flow rate increased. The liquid phase relative permeabilities shown in **Fig. 12** are much less sensitive to viscous forces than the gas phase relative permeability. The model results of relative permeabilities are also consistent with the experimental observation of Henderson et al.[9] These authors found that the relative permeability of both phases increased with the increase of flow rate but that liquid relative permeability increased less than gas relative permeability.

Effect of Contact Angle Hysteresis. If the wettability of a fluid-rock system in a gas condensate reservoir near wellbore can be altered from strongly liquid-wet to intermediately gas-wet, the gas-condensate relative permeabilities behavior may also change. **Fig. 13** depicts the model results for k_{rg} and k_{rc} at different receding contact angles. This figure shows that both k_{rg} and k_{rc} increase as the wettability to liquid decreases (θ_R = 0,

40, 80° and $\theta_R < \theta_A = 90°$, $\sigma = 0.4$ dynes/cm). There is a significant increase in the gas phase relative permeability over the whole saturation range when receding contact angle increases from zero (completely liquid-wet) to 80° (intermediately gas-wet). These results suggest that if the rock wettability around wellbore can be altered from liquid-wet to intermediately or preferentially gas-wet, gas well deliverability may increase significantly. Gas phase relative permeability, k_{rg}, reduces very rapidly for the strongly liquid-wet condition ($\theta_R = 0°$) and approaches zero when S_c increases to 22%. **Fig. 13** gives a clear indication of the significance of wettability and contact angle hysteresis on gas well deliverability.

To our knowledge, the effect of wettability on relative permeabilities in gas condensate systems has not been studied before. We have embarked on an experimental research program in order to measure the relative permeabilities of gas condensate systems under varying wettability conditions. Some preliminary data on relative permeabilities are presented in Ref. 22.

Blocking Effect Due to In-situ Condensation. In some gas reservoirs, a gas well may be blocked completely and the gas production may stop[4]. The above phenomenon is a result of in-situ liquid formation near the wellbore as reservoir pressure drops below the dewpoint. The liquid formed newly in the porous medium blocks both small and large pores and reduces the effective permeability of gas phase significantly.

The distribution of the liquid condensate formed in-situ at different stages of condensation in the pore network is presented in **Fig. 14. Fig. 14a** shows the condensate distribution at $S_c = 5.0\%$. The black represents the liquid condensate and the white the gas phase. The condensate is first formed in the middle of smaller tubes in the form of liquid bridges. The capillary tubes that contain liquid bridges are blocked completely. As a result, the number of tubes for gas flow is reduced and the effective gas permeability through the whole network is decreased. The gas production will, therefore, reduce when pressure drops below the dewpoint. With further pressure decrease, more liquid drops out and condensate saturation S_c increases. **Fig. 14b** shows the liquid distribution at $S_c = 15.0$ %. The liquid occupies some large capillary tubes. The number of capillary tubes available for gas flow is further reduced. **Fig. 14c** shows the liquid distribution at the critical condensate saturation, $S_{gc} = 58.0$ %; there are almost no continuous paths available for gas flow. The effective gas permeability is almost zero; when this occurs, gas production may stop completely.

Conclusions

The major conclusions drawn from the work are:
The predictions from our simple model show that gravity generally reduces critical condensate saturation; but as interfacial tension increases the gravity effect becomes less pronounced. The effect of gravity is pronounced when viscous forces are small. These results are in agreement with experimental data.
Viscous forces may have a pronounced effect on S_{gc}, especially at a low interfacial tension. However, the most important parameter is wettability expressed in terms of the receding contact angle; wettability alteration to intermediate gas-wetness reduces critical condensate saturation dramatically irrespective of gravity and interfacial tension.

The model predicts a significant effect of interfacial tension and viscous forces on gas phase relative permeabilities. These predictions are in line with experimental data.

Model results show that there is a very significant effect of gas-wetness on gas relative permeability; gas phase relative permeability may increase orders of magnitude as the receding contact angle increases from 0 to 80°. The results imply that the most effective method for increasing gas well deliverability may be the alteration of wettability around the wellbore.

Nomenclature

G_{abs} = gas conductance of the network at single-phase state
G_{eg} = effective gas conductance of the network at two-phase state
G_{ew} = effective liquid conductance of the network at two-phase state
h_c = height of liquid column
h_{cr} = critical height of liquid column
I = total electrical current through the network in the vertical direction
I_i = electric current through the conductance G_i (i = 3, 4, 6, 7, 8)
k_{rg} = gas-phase relative permeability
k_{rw} = liquid-phase relative permeability
L = capillary tube length
p_A = pressure at the bottom
p_R = pressure at the top
P_c = capillary pressure between gas and condensate
Δp = total pressure differential
Δp_c = pressure differential across condensate phase
Δp_g = pressure differential across gas phase
Δp_i = pressure differential between two ends of the capillary tube i
Q_g = flow rate of gas
Q_i = flow rate of fluid through the capillary tube i
Q_c = flow rate of condensate
r = radius of a capillary tube
r_i = radius of the capillary tube i
r_p = threshold radius
S_c = condensate saturation
S_{cr} = critical condensate saturation
V_o = the voltage at the top of the effective network
V_1 = voltage at point A
V_2 = voltage at point B
V_t = voltage at the bottom of the effective network
θ_A = advancing contact angle
θ_R = receding contact angle
ρ_c = condensate density
ρ_g = gas density
$\Delta\rho$ = density difference between condensate and gas
σ = interfacial tension
μ = fluid viscosity
μ_g = gas viscosity
μ_c = condensate viscosity

References

1. Allen, F. H. and Roe, R.P.: "Performance Characteristics of a Volumetric Condensate Reservoir," Petroleum Transactions, AIME, Vol. 189, 1950, 83-90.
2. Engineer, R.: "Cal Canal Field California: Case History of a Tight and Abnormally Pressure Gas Condensate Reservoir," paper SPE 13650, presented at the 1985 California Regional Meeting, Bakersfield, California, March 27-29.
3. Barnum, R.S., Brinkman, F.P., Richardson, T.W., and Spillete, A.G.: "Gas Condensate Reservoir Behavior: Productivity and Recovery Reduction Due to Condensation," paper SPE 30767, presented at the 1995 Annual Technical Conference and Exhibition, Dallas, TX, Oct. 22-25.
4. Gravier, J. F., Lemouzy, P., Barroux, C., and Abed, A. F.: "Determination of Gas condensate Relative Permeability on Whole Cores Under Reservoir Conditions," SPE *Formation Evaluation J.* (Feb.1986) 9-15.
5. Chen, H. L., Wilson, S. D., and Monger-McClure, T. G.: "Determination of Relative Permeability and Recovery for North Sea Gas Condensate Reservoirs," paper SPE 30769, presented at the 1995 SPE Annual Technical Conference & Exhibition, Dallas, TX, Oct. 22-25.
6. Munkerud, P. K.: "Measurement of Relative Permeability and Flow Properties of a Gas Condensate System During Pressure Depletion and Pressure Maintenance," paper SPE 19071, presented at the 1989 SPE Gas Technology Symposium, Dallas, Texas, June 7-9.
7. Saeidi, A., and Handy, L. L.: "Flow and Phase Behavior of Gas Condensate Volatile Oils in Porous Media," paper SPE 4891, presented at the 1974 Annual California Regional Meeting, San Francisco, California, April 4-5.
8. Munkerud, P. K., and Toaster, O.: "The Effects of Interfacial Tension and Spreading on Relative Permeability in Gas Condensate Systems," presented at the 1995 Eighth European Symposium on Improved Oil Recovery, Vienna, Austria, May 15-17.
9. Morel, D. C., Lomer, J-F. , Morineau, Y.M., and Putz, A. G.: "Mobility of Hydrocarbon Liquids in Gas Condensate Reservoirs: Interpretation of Depletion Laboratory Experiments," paper SPE 24939, presented at the 1992 Annual Technical Conference and Exhibition, Washington, DC, Oct. 4-7.
10. Danesh, A., Henderson, G. D., and Peden, J. M.: "Experimental Investigation of Critical Condensate Saturation and its Dependence on Interstitial Water Saturation in Water-Wet Rocks," SPE *Reservoir Engineering* (Aug., 1991) 336-342.
11. Ali, J. K., Butler, S., Allen, L., and Wardle, P.: "The Influence of Interfacial Tension on Liquid Mobility in Gas Condensate Systems," paper SPE 26783, presented at the 1993 Offshore European Conference, Aberdeen, Sept. 7-10.
12. Henderson, G. D., Danesh, A., Tehrani, D. H., and Peden, J. M.: "An Investigation into the Process Governing Flow and Recovery in Different Flow Regimes Present in Gas Condensate Reservoirs," paper SPE 26661, presented at the 1993 Annual Technical Conference and Exhibition, Houston, Texas, Oct. 3-6.
13. Henderson, G.D., Danesh, A., Tehrani, D.H., Al-Shaidi, S., and Peden, J.M.: "Measurement and Correlation of Gas Condensate Relative Permeability by the Steady-State Method," paper SPE 30770, presented at the 1995 Annual Technical Conference and Exhibition, Dallas, Texas, Oct. 22-25.
14. Haniff, M.S. and Ali, J.K.: "Relative Permeability and Low Tension Fluid Flow in Gas Condensate Systems," paper SPE 20917, presented at the Europec 1990, The Hague, Netherlands, Oct. 22-24.
15. Mohammadi, S., Sorbie, K.S., Danesh, A., and Peden, J.M.: "Pore-Level Modelling of Gas-Condensate Flow Through Horizontal Porous Media," paper SPE 20479, presented at the 1990 Annual Technical Conference and Exhibition, New Orleans, LA, Sept. 23-26.
16. Fang, F., and Firoozabadi, A., Abbaszadeh, M, and Radke, C.: "A Phenomenological Network Model of Critical Condensate Saturation," paper SPE 36716, presented at the 1996 Annual Technical Conference and Exhibition, Denver, Colorado, Oct. 6-9.

17. Firoozabadi, A.: "Thermodynamics of Hydrocarbon Reservoirs," Chapter II, McGraw-Hill, 1998.
18. Stinchcombe, B. and Watson, B.P.: "Renormalization Group Approach for Percolation Conductivity," *Phys. Rev.* C (1976), 9, 3221.
19. King, P.R.: "The Use of Renormalization for Calculating Effective Permeability," *Tansport in Porous Media* (1989) 4, 237.
20. King, P.R.: "Renormalization Calculations of Immiscible Flow," *Tansport in Porous Media* (1993) 12, 237.
21. Filippi, G., and Toledo, P.G.: "Prediction of Effective Permeability from Local Distributions of Conductances," *Reservoirs* (1993), PDVSA, Caracas.
22. Li, K. and Firoozabadi, A.: "Experimental Study of Wettability Alteration to Preferential Gas-Wetness in Porous Media," Chapter III, Part II.

Appendix A: Gas Conductance in a Single Circular Tube

When both gas and liquid phases flow in a circular tube (see **Fig. 2b**), the gas flow rate can be calculated by the Poiseuille equation:

$$Q_g = \frac{\pi r^4 \Delta p_g}{8\mu_g (L - h_c)}, \qquad \text{(A-1)}$$

where Δp_g is the differential pressure across gas phase, and h_c is the liquid height. The effect of gravity and compressibility are both neglected. The expression for the liquid condensate flow rate is:

$$Q_c = \frac{\pi r^4}{8\mu_c}\left(\frac{\Delta p_c}{h_c} + \rho_c g\right), \qquad \text{(A-2)}$$

where μ_c is the condensate viscosity and Δp_c the differential pressure across the condensate phase. The differential pressure Δp between the two ends of a tube is given by:

$$\Delta p = \Delta p_g + \Delta p_c + P_c, \qquad \text{(A-3)}$$

where P_c is the capillary pressure between gas and condensate phase. The gas flow rate is equal to the liquid flow rate when the fluid compressibility is neglected. That is:

$$Q_g = Q_c \qquad \text{(A-4)}$$

Combining the above equations (Eqs.A-1 to A-4), the gas phase differential pressure can be obtained:

$$\Delta p_g = \frac{1}{1 + \frac{\mu_c}{\mu_g}\frac{h_c}{L - h_c}}\left(\Delta p - P_c + \rho_c g h_c\right), \qquad \text{(A-5)}$$

Substituting Eq. (A-5) into Eq. (A-1):

$$Q_g = \frac{\pi r^4}{8\mu_g (L-h_c)} \frac{1}{1+\frac{\mu_c}{\mu_g}\frac{h_c}{L-h_c}} (\Delta p - P_c + \rho_c g h_c), \qquad \text{(A-6)}$$

The gas conductance is then determined as:

$$G_{gas} = \frac{\pi r^4}{8\mu_g (L-h_c)} \frac{1}{1+\frac{\mu_c}{\mu_g}\frac{h_c}{L-h_c}}, \qquad \text{(A-7)}$$

For tube i in the network, the condensate saturation is given by:

$$S_{ic} = h_c / L, \qquad \text{(A-8)}$$

Equation (7) in the text can be provided by Substituting Eq. (A-8) into Eq. (A-7).

Appendix B: Effective Conductance in Vertical Direction for n_b=2

The effective network in vertical direction for n_b=2 is shown in **Fig. 6c**. One can write the following equations based on the theory of electric circuits:

$$I_3 = G_3(V_2 - V_t), \qquad \text{(B-1)}$$
$$I_4 = G_4(V_2 - V_1), \qquad \text{(B-2)}$$
$$I_6 = G_6(V_0 - V_2), \qquad \text{(B-3)}$$
$$I_7 = G_7(V_0 - V_1), \qquad \text{(B-4)}$$
$$I_8 = G_8(V_1 - V_t), \qquad \text{(B-5)}$$

At points A and B

$$\sum_i I_i = 0, \text{ (at point A: } i\text{=4,7,8)} \qquad \text{(B-6)}$$
$$\sum_i I_i = 0, \text{ (at point B: } i\text{=3,4,6)} \qquad \text{(B-7)}$$

The total electric current through the system, $I = I_6 + I_7$, is given by

$$I = G_z(V_0 - V_t), \qquad \text{(B-8)}$$

In the above equations, I_i (i = 3, 4, 6, 7, 8) is the electric current through the conductance G_i (i = 3, 4, 6, 7, 8); V_o and V_t are the voltages at the top and the bottom of the effective network, respectively; V_1 and V_2 are the voltages at points A and B, respectively. G_z is effective conductance of the network in the vertical direction.

Combining Eqs.(B-1) – (B-7):

$$V_1 = \frac{G_4(G_6V_0 + G_3V_t) + (G_3 + G_4 + G_6)(G_7V_0 + G_8V_t)}{(G_4 + G_7 + G_8)(G_3 + G_4 + G_6) - G_4^2}, \qquad \text{(B-9)}$$

$$V_2 = \frac{G_4(G_7V_0 + G_8V_t) + (G_4 + G_7 + G_8)(G_6V_0 + G_3V_t)}{(G_4 + G_7 + G_8)(G_3 + G_4 + G_6) - G_4^2}, \qquad \text{(B-10)}$$

Substitute Eqs.(B-3) and (B-4) into Eq.(B-9):

$$G_z = \frac{(G_6 + G_7)V_0 - (G_6V_2 + G_7V_1)}{V_0 - V_t}, \qquad \text{(B-11)}$$

Equation (9) in the text can be obtained by Substituting Eqs.(B-9) and (B-10) into Eq.(B-11).

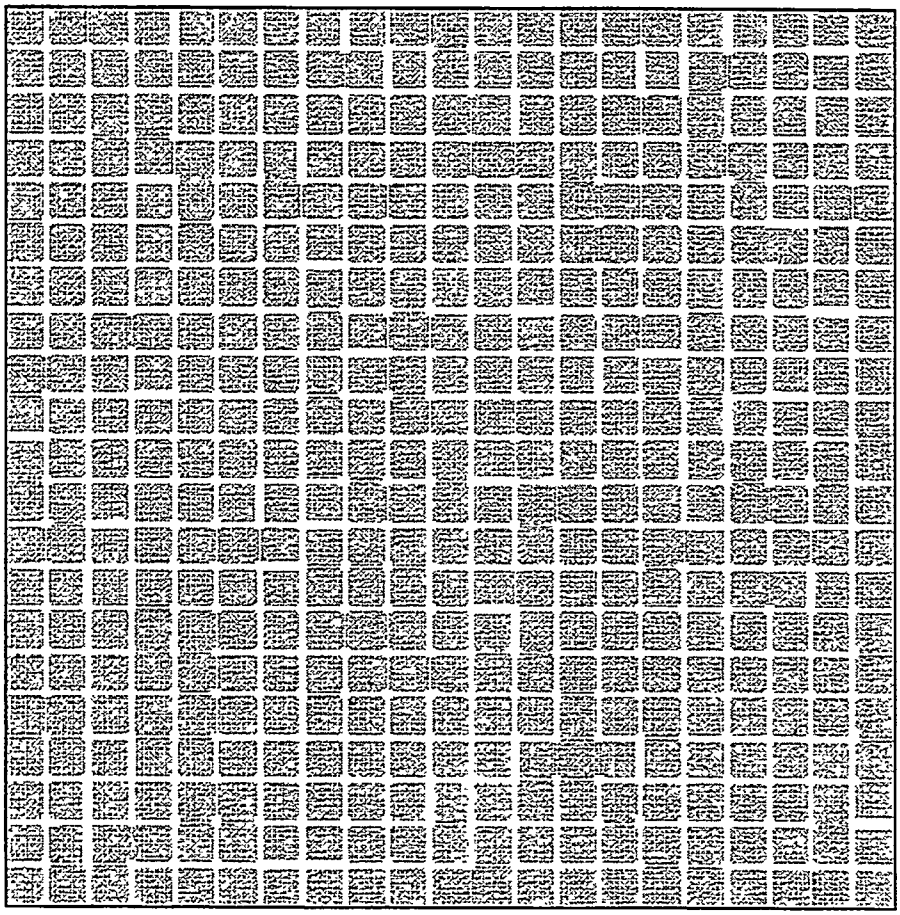

Fig.1 Size distribution of the 20×20 network

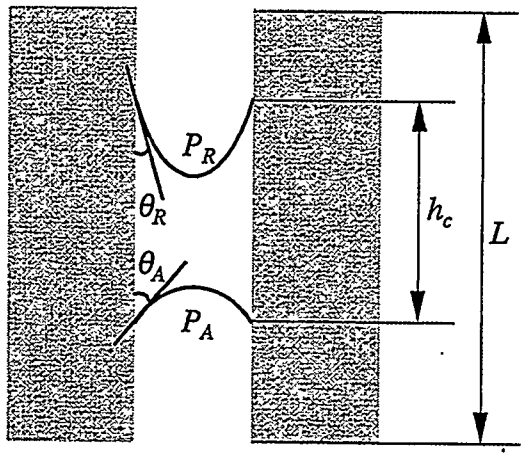

(*a*) Liquid bridge in a circular tube after formation

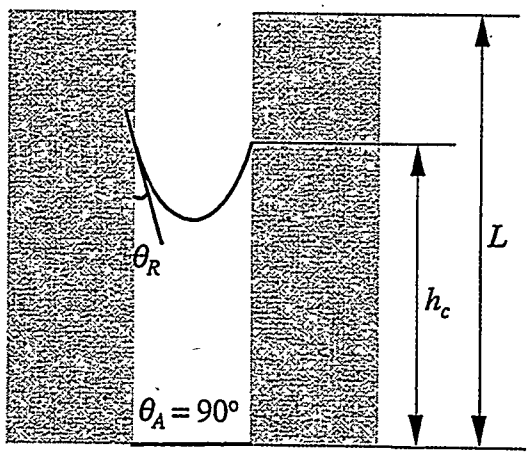

(*b*) Liquid bridge at the bottom of a circular tube

Fig.2 Liquid configuration in a single circular tube

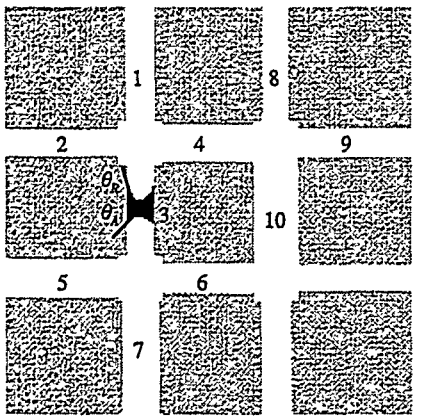

Step 1

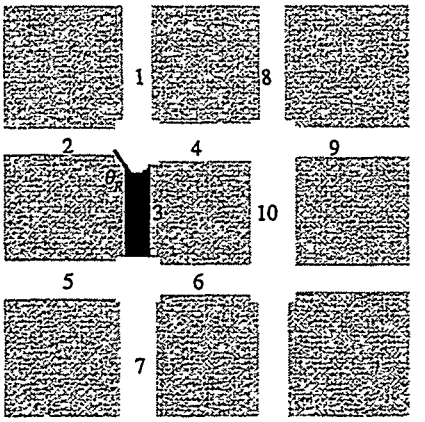

Step 2

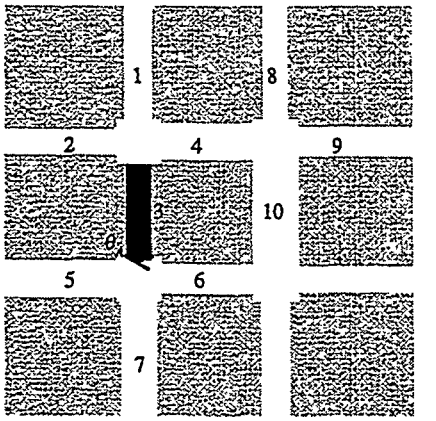

Step 3

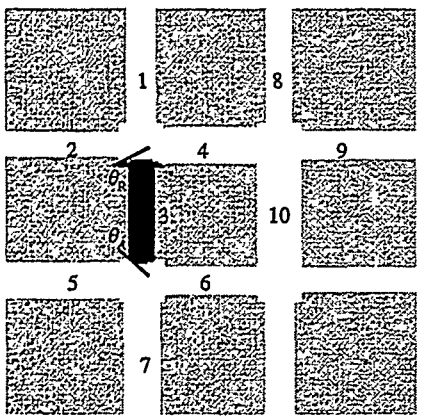

Step 4

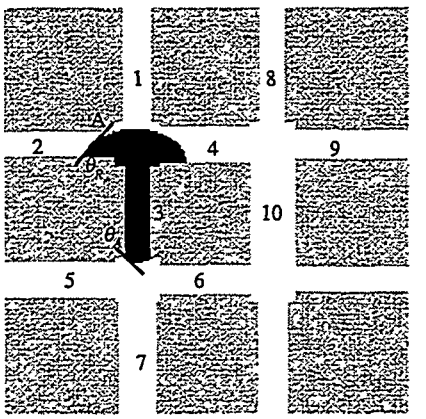

Step 5

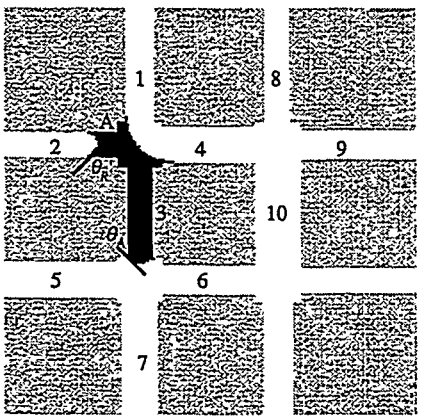

Step 6

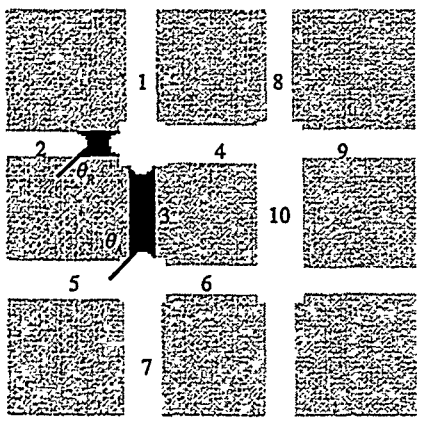

Step 7

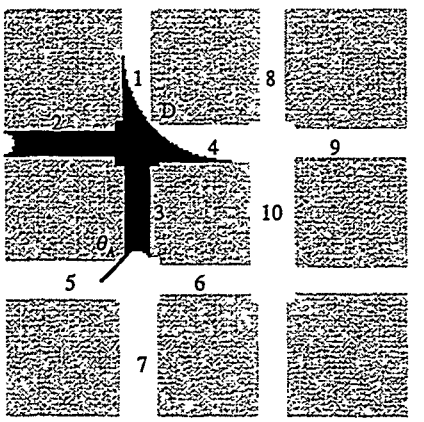

Step 8

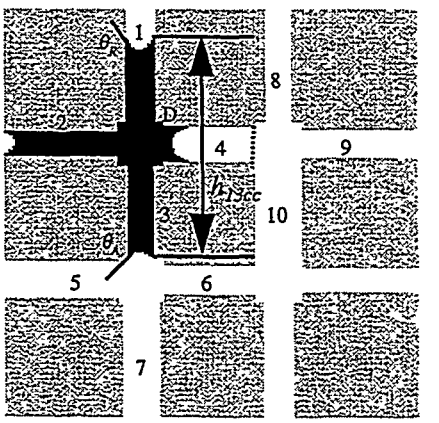

Step 9

Fig.3 Condensation in a network, $h_{cc} > L$

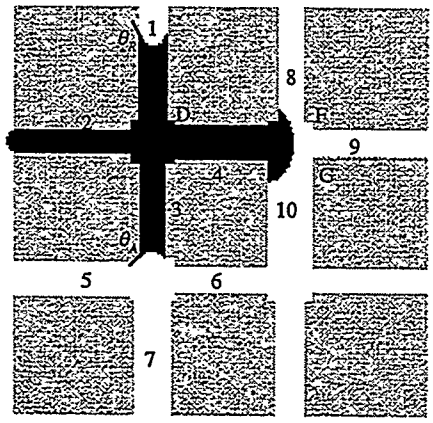

Step 10

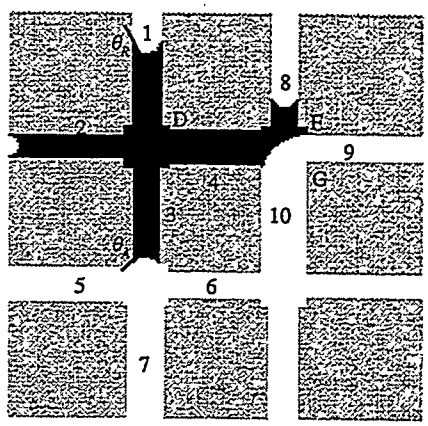

Step 11

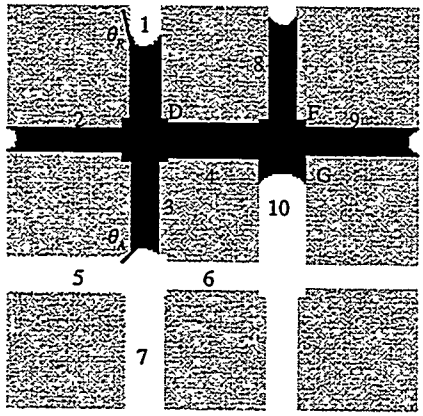

Step 12

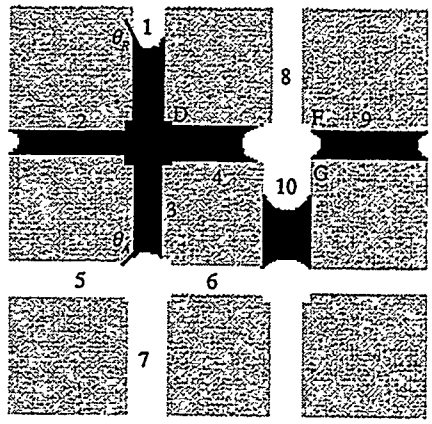

Step 13

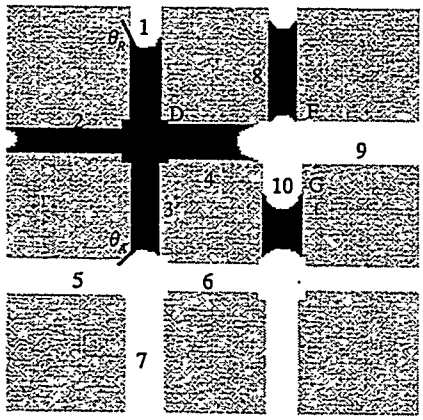

Step 14

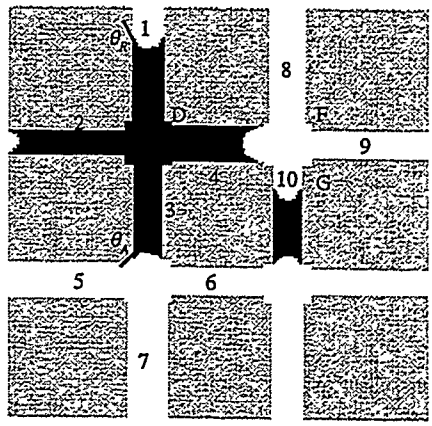

Step 15

Fig.3 Condensation in a network, $h_{cc} > L$ (Continued)

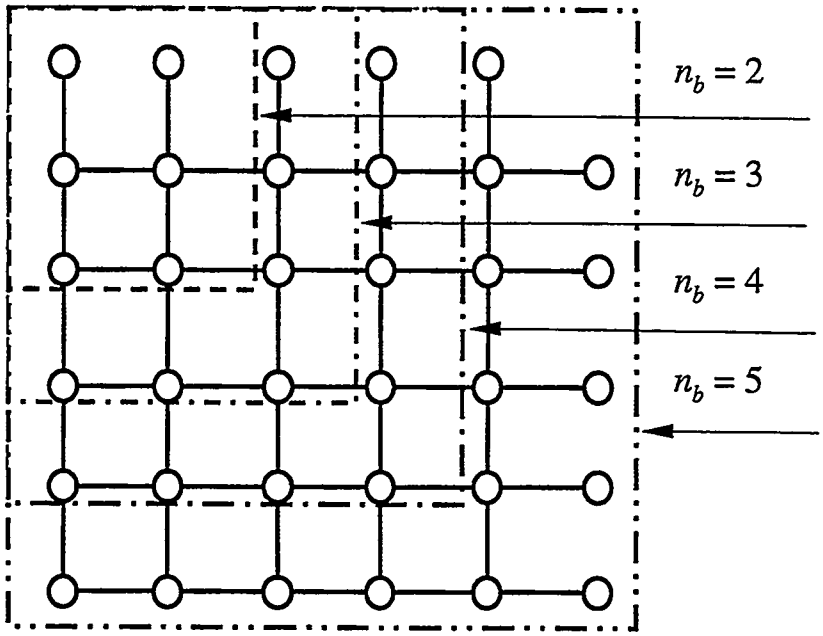

Fig.4 Schematic of renormalization for different cell numbers

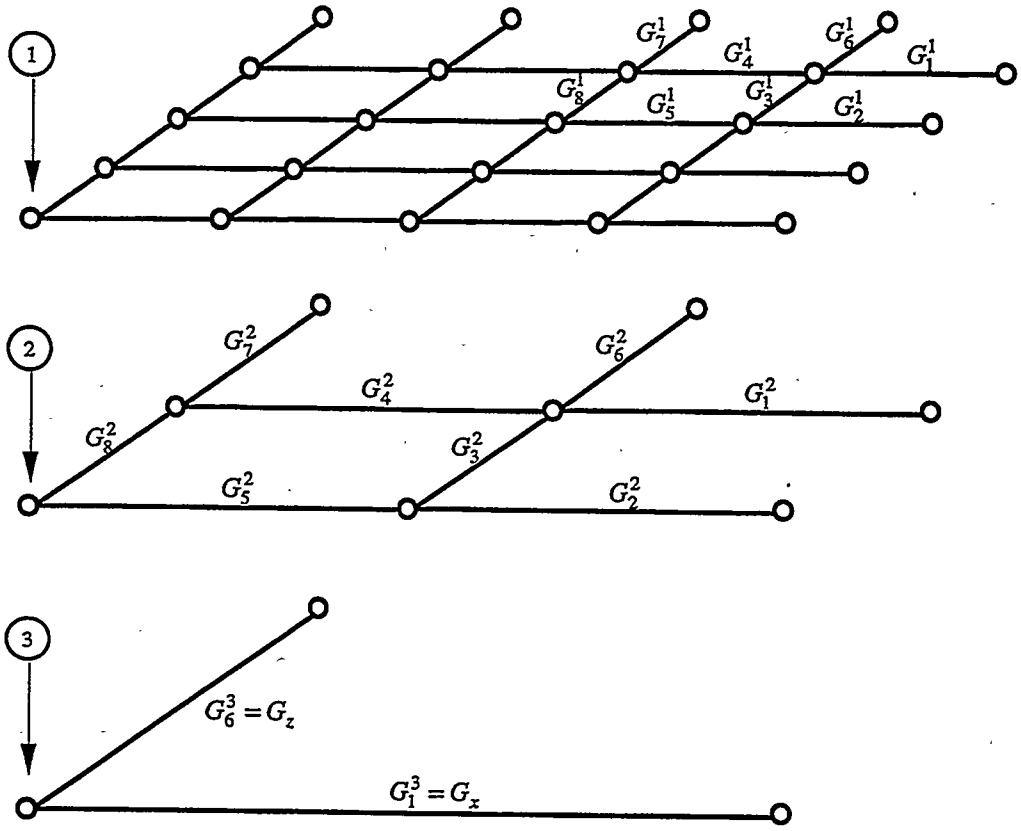

① Primary conductance network

② Conductance network after one renormalization step

③ Conductance network at the last step

Fig.5 Schematic of the renormalization procedures (n_b=2)

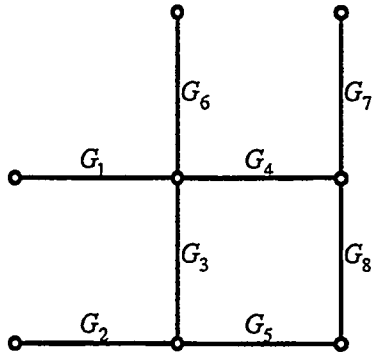

(*a*) Conductance network

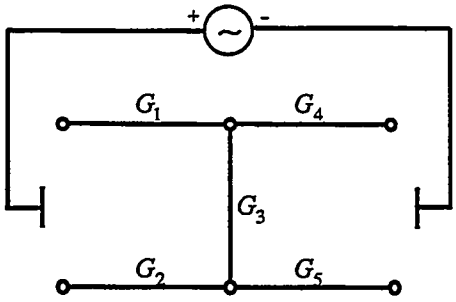

(*b*) Effective conductance in the horizontal direction

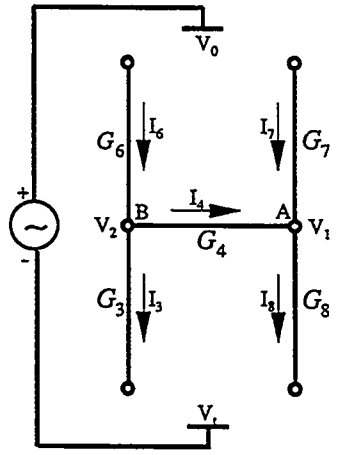

(*c*) Effective conductance in the vertical direction

Fig.6 Effective conductance in the horizontal and vertical directions ($n_b = 2$)

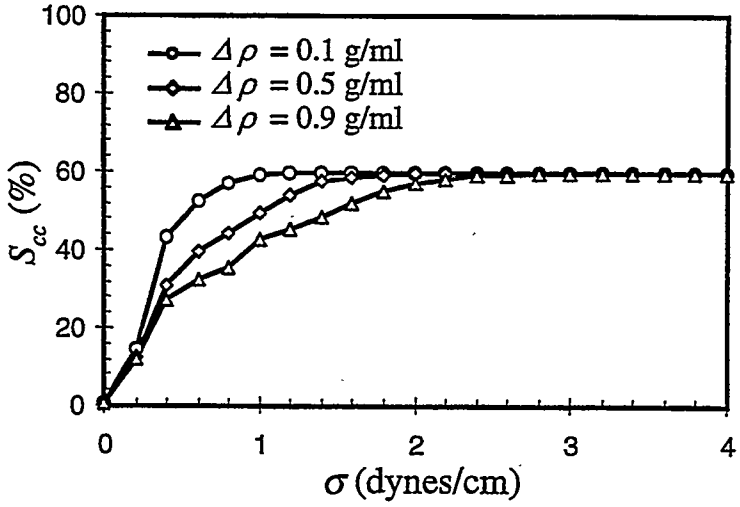

(*a*) $\Delta p = 0.05$ psi

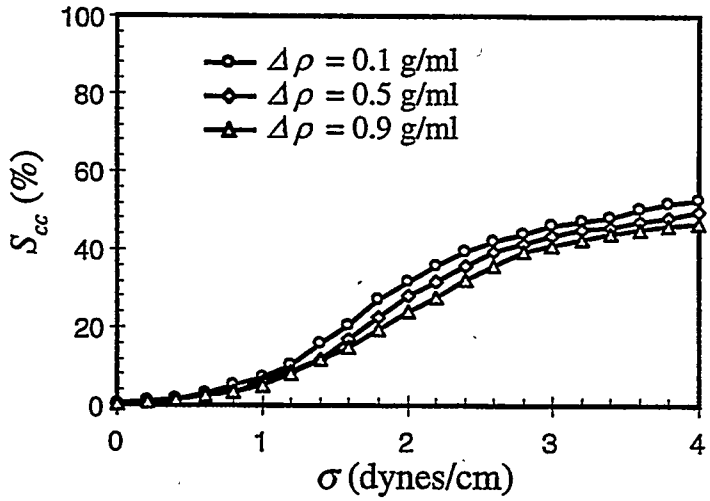

(*b*) $\Delta p = 0.40$ psi

Fig.7 Effect of σ and gravity on S_{cc} (θ_R =0°, 0° < θ_A < 90°)

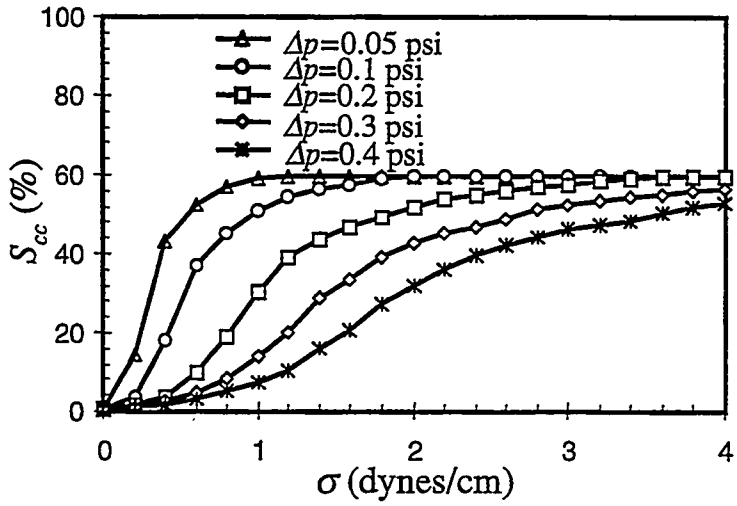

(*a*) $\Delta\rho = 0.1$ g/ml

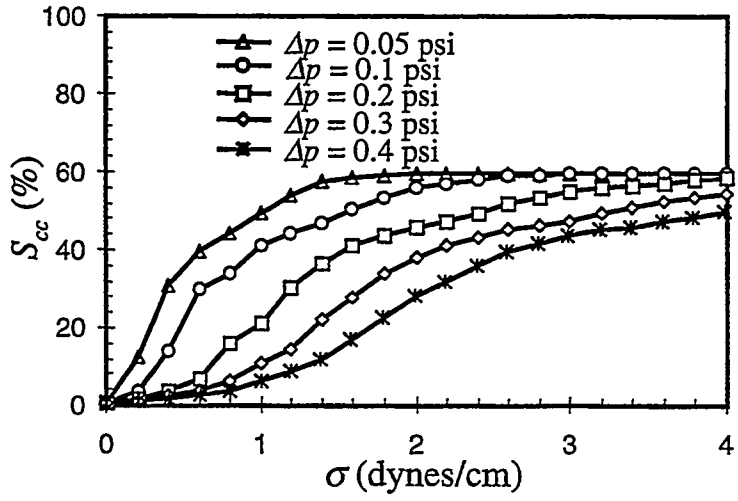

(*b*) $\Delta\rho = 0.5$ g/ml

Fig.8 Effect of σ and viscous force on S_{cc} (θ_R =0°, 0° < θ_A < 90°)

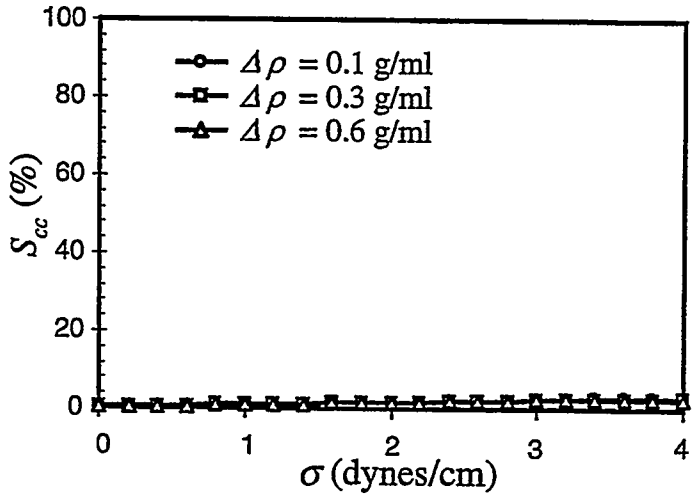

(*a*) Effect of σ and gravity on S_{cc}
(Δp =0.2 psi, θ_R =85°, 85° < θ_A < 90°)

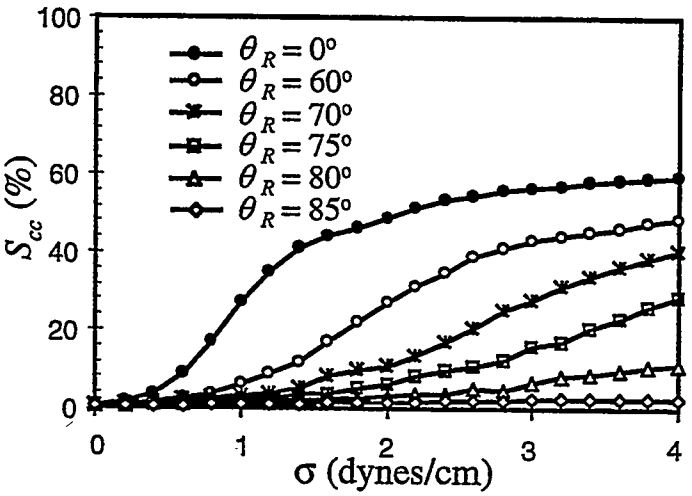

(*b*) Effect of σ and wettability on S_{cc}
($\Delta\rho$ = 0.3 g/ml, θ_R =0 - 85°, θ_R < θ_A < 90°)

Fig.9 Effect of σ, gravity, and wettability on S_{cc}

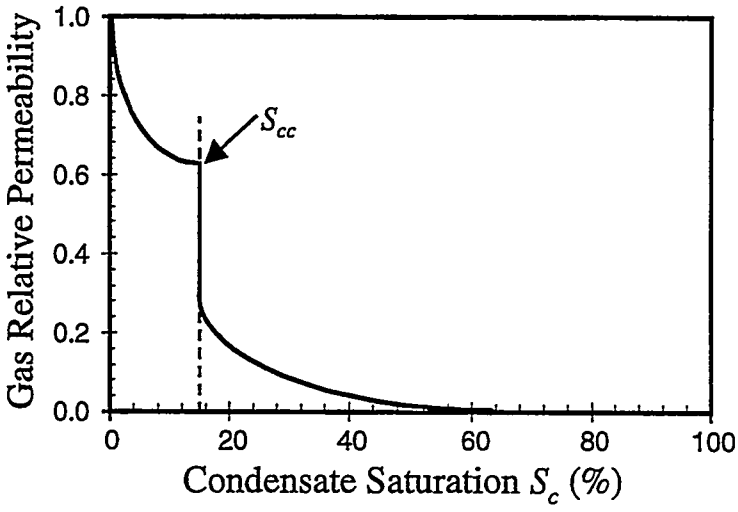

(a) Sketch of experimental data (Gravier, et al.[4])

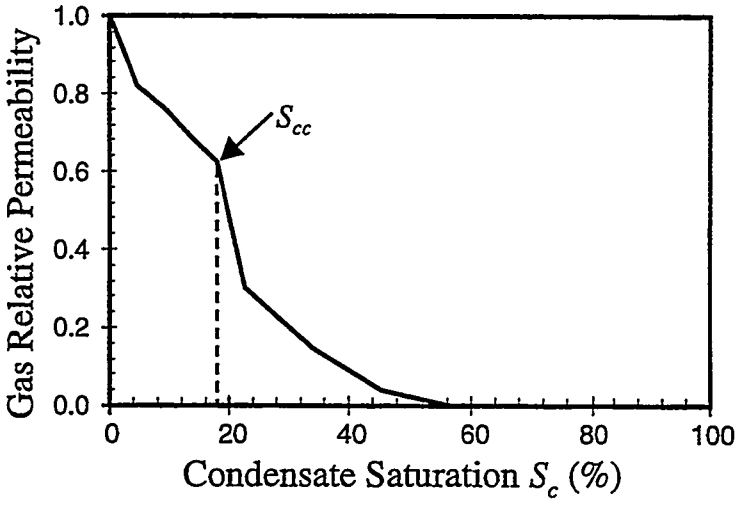

(b) Model result

(σ = 0.5 dynes/cm, Δp =0.2 psi, $\Delta\rho$ = 0.5 g/ml, θ_R =0°, 0° < θ_A < 90°)

Fig.10 Gas-phase relative permeability in gas-condensate systems

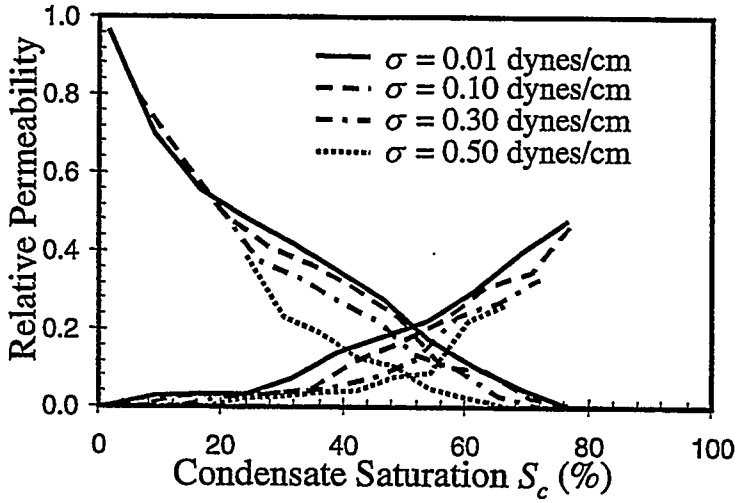

Fig.11 Effect of σ on relative permeability
(Δp =0.3 psi, $\Delta\rho$ = 0.5 g/ml, θ_R =0°, 0° < θ_A < 90°)

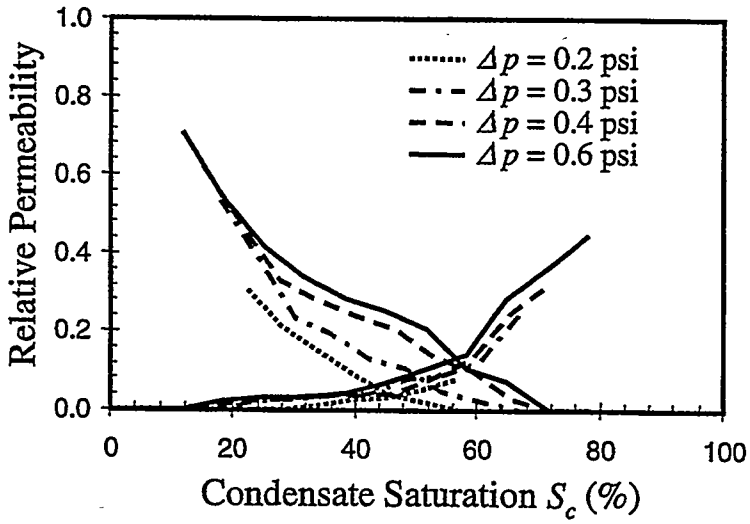

Fig.12 Effect of viscous force on relative permeability
(σ =0.5 dynes/cm, $\Delta\rho$ = 0.5 g/ml, θ_R =0°, 0° < θ_A < 90°)

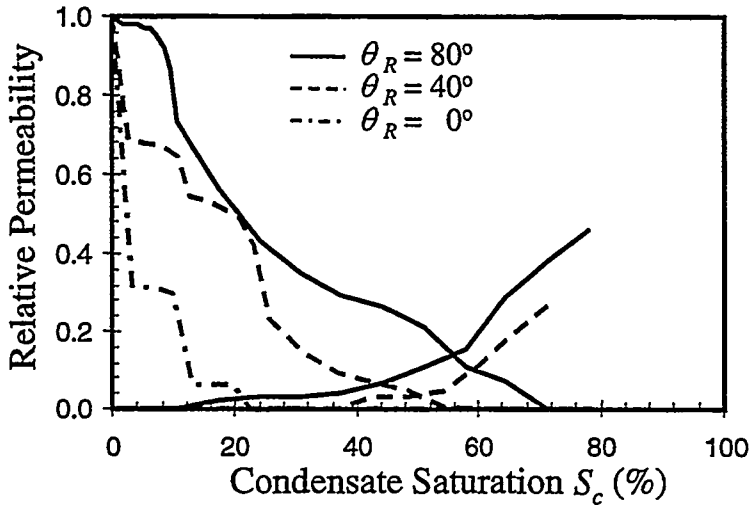

Fig.13 Effect of θ_R on relative permeability
(σ =0.4 dynes/cm, Δp =0.2 psi, $\Delta\rho$ = 0.5 g/ml, $\theta_R < \theta_A < 90°$)

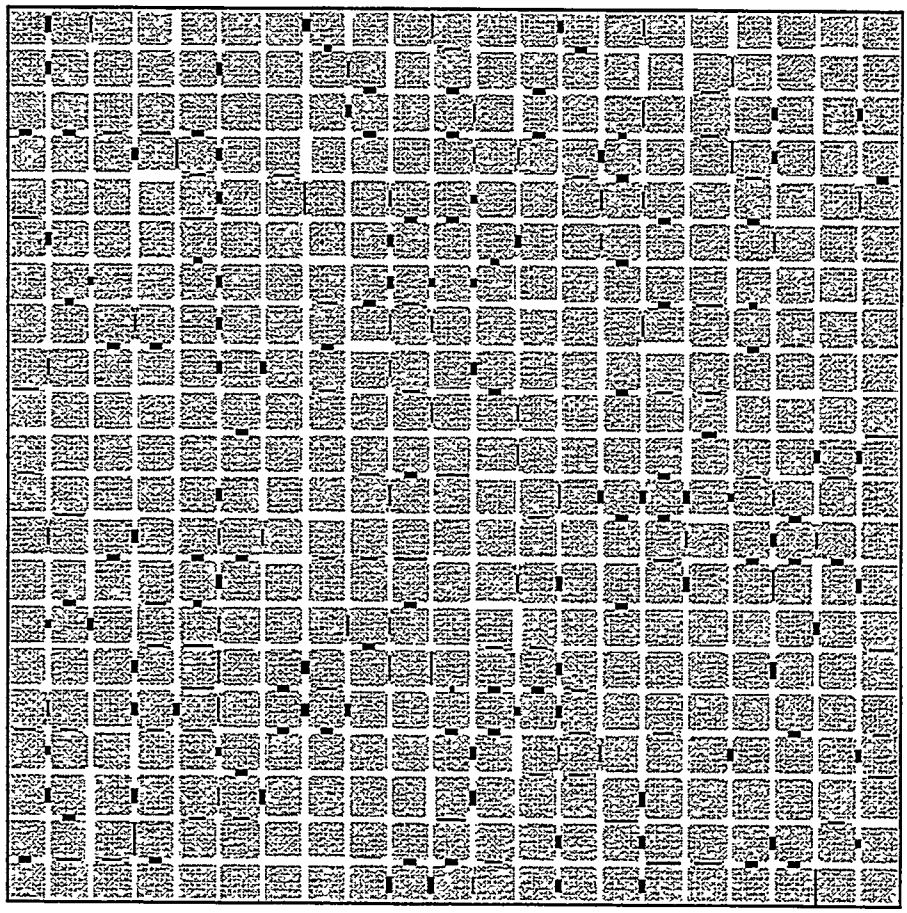

Fig.14a Saturation distribution at $S_c = 5$ %
(σ=0.5 dynes/cm, Δp =0.02 psi, $\Delta\rho = 0.1$ g/ml, θ_R =0°, 0° < θ_A < 90°)

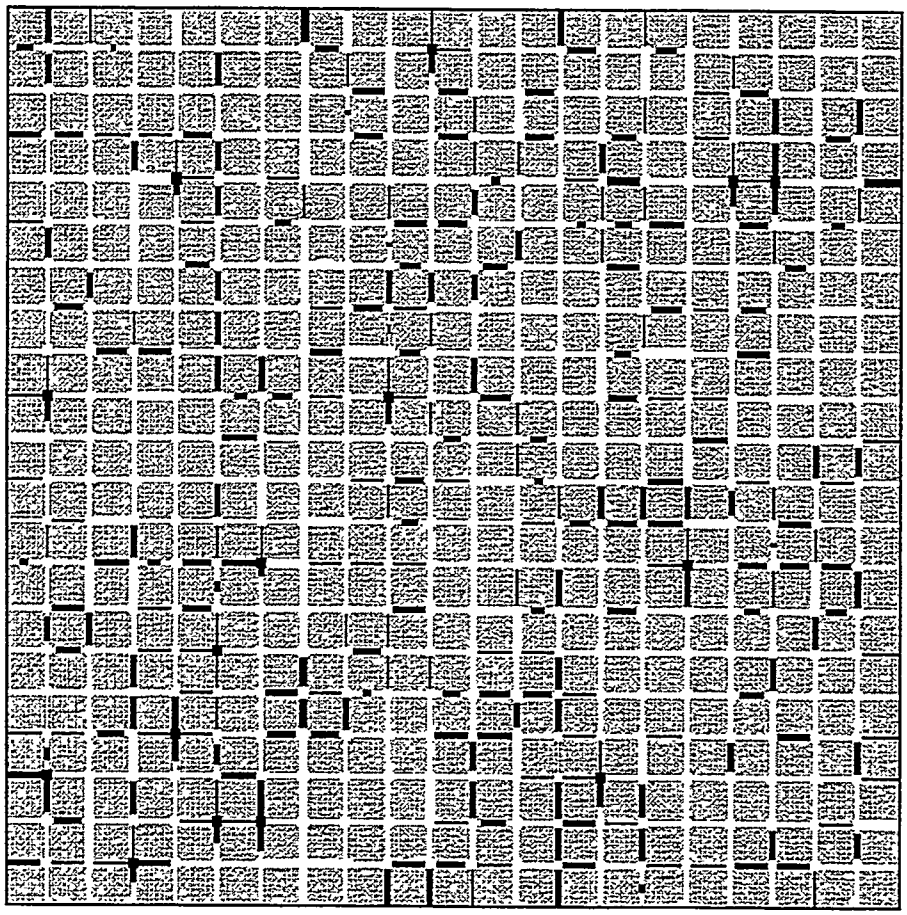

Fig.14b Saturation distribution at $S_c = 15$ %
(σ=0.5 dynes/cm, Δp=0.02 psi, $\Delta\rho$ = 0.1 g/ml, θ_R=0°, 0° < θ_A < 90°)

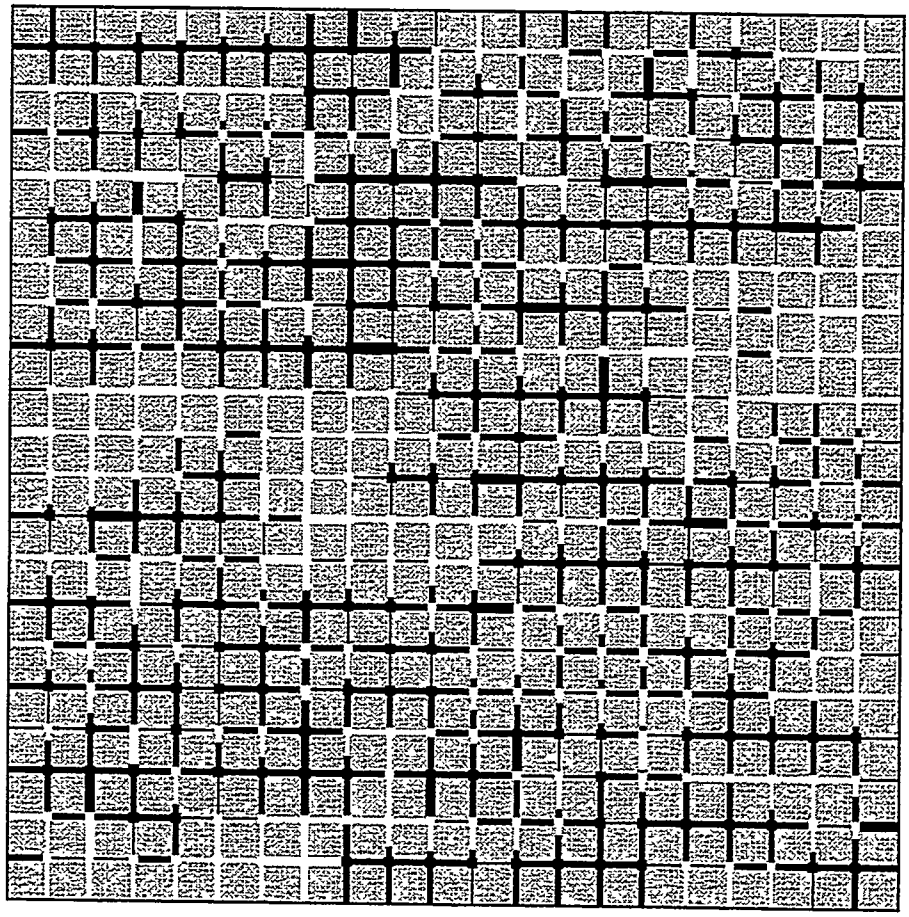

Fig.14c Saturation distribution at $S_c = 58$ %
(σ=0.5 dynes/cm, Δp =0.02 psi, $\Delta\rho = 0.1$ g/ml, θ_R =0°, 0° < θ_A < 90°)

Part II – Experimental Study of Wettability Alteration to Preferential Gas-Wetting in Porous Media and its Effects

KEWEN LI AND ABBAS FIROOZABADI

Abstract

In a recent theoretical study, Li and Firoozabadi showed that if the wettability of porous media can be altered from preferentially liquid-wet to preferentially gas-wet, then gas well deliverability in gas condensate reservoirs can be increased. In this paper, we present the results that the wettability of porous media can indeed be altered from preferentially liquid-wet to preferentially gas-wet. In the petroleum literature, it is often assumed that the contact angle through liquid phase θ is equal to 0° for gas-liquid systems in porous media. As this paper will show, while θ is always small, it may not always be zero as is often assumed. In laboratory experiments, we altered the wettability of porous media to preferentially gas-wet by using two chemicals, FC754 and FC722. Results show that in the capillary tube θ changes from about 50° to 90° and from 0° to 60° after wettability alteration by FC754 for water-air and normal decane-air systems, respectively. While untreated Berea saturated with air has a 60% imbibition of water, its imbibition of water after chemical treatment is almost zero and its imbibition of normal decane is substantially reduced. FC722 has a more pronounced effect on the wettability alteration to preferential gas-wetting. In a glass capillary tube θ changes from 50° to 120° and from 0° to 60° for water-air and normal decane-air systems, respectively. Similarly, because of wettability alteration with FC722, there is no imbibition of either oil or water in both Berea and chalk samples with or without initial brine saturation. Entry capillary pressure measurements in Berea and chalk give a clear demonstration that the wettability of porous media can be permanently altered to preferential gas-wetting.

Introduction

In a theoretical work[1], we have modeled gas and liquid relative permeabilities for gas condensate systems in a simple network. The results imply that when one alters the wettability of porous media from strongly non-gas-wet to preferentially gas-wet or intermediately gas-wet, there may be a substantial increase in gas well deliverability. The increase in gas well deliverability of gas condensate reservoirs is our main motivation for altering the wettability of porous media to preferentially gas-wet.

Certain gas condensate reservoirs experience a sharp drop in gas well deliverability when the reservoir pressure drops below the dewpoint[2-4]. Examples include many rich gas condensate reservoirs that have a permeability of less than 100md. In these reservoirs, it seems that the viscous forces alone cannot enhance gas well deliverability. One may suggest removing liquid around the wellbore via phase behavior effects through CO_2 and propane injection. Both have been tried in the field with limited success; the effect of fluid injection around the wellbore for the removal of the condensate liquid is temporary. Wettability can be a very important parameter for the enhancement of gas well deliverability. If one can alter the

wettability of the wellbore region to intermediate gas-wetness, gas may flow efficiently in porous media.

As early as 1941, Buckley and Leverett[5] recognized the importance of wettability on water flooding performance. Later, many authors studied the effect of wettability on capillary pressure, relative permeability, initial water saturation, residual oil saturation, oil recovery, electrical properties of reservoir rocks, and reserves[6-11, 13-16]. In 1959, Wagner and Leach[7] reported that it might be possible to improve oil displacement efficiency by wettability adjustment during water flooding. In 1967, Froning and Leach[8] reported a field test in Clearfork and Gallup reservoirs for improving oil recovery by wettability alteration. Kamath[9] then reviewed wettability detergent flooding. He noted that it was difficult to draw a definite conclusion regarding the success of detergent floods from the data available in the literature. Penny et al.[12] presented a technique to improve well stimulation by changing the wettability for gas-water-rock systems. They added a surfactant in the fracturing fluid. This yielded impressive results; the production following cleanup after fracturing in gas wells generally was 2 to 3 times greater than field averages or offset wells treated with conventional techniques. Penny et al.[12] believed that increased production was due to wettability alteration. However, they did not demonstrate that wettability had been altered.

Recently, Wardlaw and McKellar[17] reported that only 11% pore volume (PV) water imbibed into the Devonian dolomite samples with bitumen. The water imbibition test was conducted vertically in a dry core (saturated with air). Based on the imbibition experiments, they hypothesized that some gas reservoirs in the western Alberta foothills of the Rocky Mountains were partially dehydrated and their wettability altered to a somewhat hydrophobic condition due to bitumen deposits (that is, weakly water-wet or strongly oil-wet).

All the studies described above, except those in Refs 12 and 17, were conducted on oil-water-rock systems instead of gas-liquid-rock systems (gas-oil- or gas-water-rock systems). Refs 12 and 17 do not provide a direct measurement of wettability. In the petroleum literature, gas is often assumed to be the non-wetting phase and liquid the strongly wetting phase. For gas-liquid systems in porous media, it is commonly assumed that the contact angle, θ equals 0° and $\cos\theta$ equals 1 (contact angle is measured through the liquid phase). While the contact angle for gas-liquid systems may be small, it may not be zero as is often assumed in the literature. When a small amount of liquid is put inside a capillary tube and it is held in the vertical position, the liquid does not flow. Analysis of this simple experiment using the following equation

$$h_l = \frac{2\sigma}{\Delta\rho g r}(\cos\theta_R - \cos\theta_A), \qquad (1)$$

reveals that the contact angle is not zero. Eq.1 is derived from the balance between the gravity and capillary forces. The symbols are: h_l the liquid height in a circular capillary tube of radius r, θ_R the receding contact angle and θ_A the advancing contact angle, $\Delta\rho$ the density difference between the gas and liquid phase, and σ the surface tension. There are also indications that in porous media the contact angle may not be zero in gas-liquid systems; it is of the order of several degrees or more but not intermediately gas-wet. Al-Siyabi et al.[18]

measured the gas-oil contact angles of four binary mixtures (C_1/nC_4, C_1/nC_8, C_1/nC_{10}, and C_1/nC_{14},) at reservoir conditions. Their results showed that the gas-oil contact angles were about 20° for surface tension values greater than about 0.2 dynes/cm. It is also often understood that the contact angle for a gas-liquid system may not be altered substantially in rocks. In this paper, we present the results for the wettability alteration to preferential gas-wetness with or without initial water saturation and study its effect on the characteristics of liquid (oil and water) imbibition, oil drainage, permeability, and relative permeability. We also study the thermal stability and longevity of the rock in which wettability was altered.

Theory

To the best of our knowledge, wettability alteration to preferential gas-wetness in rocks has not been suggested in the petroleum literature. Consider the sketches in **Fig. 1**. When the contact angle $\theta < 90°$ the liquid will rise in the circular capillary tube inserted vertically in the liquid, as shown in **Fig. 1a**. If $\theta = 90°$, there will not be liquid rise, and the gas-oil interface will be flat (that is, P_c=0, see **Fig. 1b**). When $\theta > 90°$, the liquid level will go down in the circular capillary tube as sketched in **Fig. 1c**. The rise and fall of the liquid level are given by

$$h_l = \frac{2\sigma\cos\theta}{\Delta\rho g r}, \qquad (2)$$

Eq. 2 can be used to estimate θ in a capillary tube, once h_l, σ, $\Delta\rho$, and r are known.

According to Eq. 2, for a gas-liquid system, one may define preferential liquid-wetting when $\theta < 90°$, and preferential gas-wetting when $\theta > 90°$. However, this definition is related to the geometry of the substrate. Let us consider a capillary tube with an equilateral triangle cross section. The gas-liquid interface will be flat when $\theta = 60°$ for this geometry (Fang et al.[19]). Therefore, one may define preferential liquid-wetting when $\theta < 60°$ and preferential gas-wetting when $\theta > 60°$. For a capillary tube of square cross section, the gas-liquid interface will be flat when $\theta = 45°$, which implies preferential liquid-wetting for $\theta < 45°$ and preferential gas-wetting for $\theta > 45°$. When the capillary tube assumes triangular curved interfaces and rough wall surfaces, other complications arise so that the contact angle looses some of its significance. The contact angle for the gas-liquid-rock system due to complex geometry and surface roughness may have a qualitative definition. A simple definition is adopted here from the expression for capillary pressure

$$P_C = \frac{\sigma\cos\theta}{\sqrt{\frac{k}{\phi}}}, \qquad (3)$$

where k and ϕ are permeability and fractional porosity, respectively.

One can measure entry capillary pressure (that is, threshold capillary pressure), and then infer θ from Eq. 3, when σ, k and ϕ are available. The contact angle calculated from Eq. 3

may not have the same physical meaning as the contact angle in Eq. 2. In order to emphasize the difference, we will represent the contact angle in Eq. 3 by θ_p, and call it the pseudo contact angle.

Experimental

In the experimental work, brine, distilled water, and normal-decane were used as the liquid phase, air as the gas phase, and glass capillary tube, Berea, and chalk (from Kansas outcrop and from a North Sea reservoir) as the substrate. Two types of chemicals were employed to alter the wettability of the substrates. The experiments were conducted at a room temperature of around 20°C.

Fluids: Normal-decane was used as the oil phase; its specific gravity and viscosity are 0.73, 0.95cp at 20°C, respectively. The surface tension of air-normal decane is 23.4 dynes/cm at 20°C. Brine of 1.0 percent (wt) NaCl was used as the water phase in the Berea and chalk experiments; its specific gravity and viscosity are 1.01 and 1.0cp at 20°C. Distilled water was used as the water phase for the experiments in the capillary tube; the surface tension of air-distilled water is 72.1 dynes/cm at 20°C.

Core and Capillary Tube: In order to study the alteration of wettability to preferential gas-wetting, we used two different substrates: 1) capillary tube, and 2) rock (Berea and chalk). The glass capillary tube used in our work has an internal diameter of 0.23 mm. The relevant data for Berea and chalk samples are summarized in Table 1.

Chemicals: In our work, two chemicals with brand names, FC754 and FC722, were used to alter the wettability: 1) FC754 (inexpensive) and 2) FC722 (more expensive). FC754 is a cationic surfactant and is water-soluble. Its specific gravity (at 25°C) and flash point are 1.15 and 23°C, respectively. FC722 is a polymer with molecular weight of about 100,000; it is neither water nor oil soluble. FC722 can be dissolved in a fluorocarbon-type solvent in a wide temperature range; the specific gravity of the solvent is around 1.7 at 25°C.

Procedure: The chemicals FC754 and FC722 were dissolved in water, and the solvent in various concentrations, respectively, and the glass capillary tube, Berea, and chalk were aged in them. The aging period depends on temperature and can vary from several minutes to several hours. After saturation with the chemical, the capillary tube, the Berea, or the chalk was evacuated for a certain period and then dried in order to remove the extra liquid chemicals. A very small amount lingers in the substrate as an adsorbed layer; as a result of adsorption the surface energy decreases and the solid surface is rendered to preferentially gas-wet.

Prior to wettability alteration, we measured the capillary rise of liquid (both oil and water) in the tube and the imbibition of water and oil into the air-saturated Berea and chalk samples. We repeated the same measurements after wettability alteration, and performed oil gravity drainage tests on the Berea cores with and without wettability alteration. After wettability alteration, we also measured the entry capillary pressure of oil and water in the air-saturated Berea and chalk samples in order to demonstrate the preferential gas-wetting.

The following describes the procedure for establishing initial water saturation. First, Berea was saturated with water (1.0%wt NaCl brine) and initial water saturation was established by wet air displacement. We used wet air instead of dry air because it was found that the distribution of initial water saturation established by dry air may not be uniform. Wet air was prepared by forcing air to pass through a 1.0%wt brine before entering the core sample. The initial water saturation was determined by direct weighing. Since it is difficult to establish low initial water saturation (say 10%) in Berea by only wet air displacement, we used dry air displacement following wet air displacement in order to establish a low initial water saturation. Then, wet air displacement was implemented again and the water saturation in the core increased slowly. The displacement direction was changed from time to time in order to make the distribution of initial water saturation more uniform. We stopped air displacement only after the desired initial water saturation had been established. Following that, the core was saturated with FC722 in the presence of initial water saturation. After a certain aging period, the chemical was removed by wet air displacement at a velocity less than that for establishing the initial water saturation. Care was taken to avoid water production. The imbibition tests were then performed using the apparatus shown in **Fig. 3.**

For measuring gas phase relative permeability before and after wettability alteration, the core was first saturated with oil (normal decane). The absolute permeability of the core was measured. The air displacement in the core without the chemical treatment was then carried out in the vertical direction at room temperature with a confining pressure of 500psi. The air was passed through the oil before entering the core sample and its pressure at the inlet was kept at 3.0psi while the outlet was open to the atmosphere. Oil recovery, residual oil saturation, and end-point value of gas phase relative permeability were measured. The oil relative permeability was also calculated at low oil saturations. After the air displacement without chemical treatment, the core was cleaned, dried, and treated by 2.0%wt FC722. Following that, the core was saturated with oil. Air displacement was performed again. Oil recovery, residual oil saturation, and gas phase relative permeability were then measured.

Imbibition and Drainage: Traditionally, spontaneous imbibition tests are conducted by immersing the core samples saturated with one liquid in another one. This type of imbibition is countercurrent imbibition. For water imbibition in oil-water systems, the traditional method for performing imbibition has an unavoidable disadvantage; one may have to remove the produced fluid on the rock surface from time to time. Berea and chalk without chemical treatment are strongly liquid-wet in gas-liquid systems. The early spontaneous imbibition may also be too rapid to record the data accurately. This classic method is difficult to implement in gas-liquid systems due to the limitation described above. The schematic of the apparatus used in our study for the measurement of liquid spontaneous imbibition into an air-saturated rock (Berea or chalk) is shown in **Fig. 2.** The core sample was kept in a vertical direction. When the bottom of the rock touched the liquid (oil or water), the liquid was spontaneously imbibed into the rock. The scale then recorded the change in weight of liquid with imbibition time. The average liquid saturation in the rock was calculated using the data from the scale. After the imbibition test, the core sample is weighed and the final average liquid saturation in the core can be obtained from the weight of the core. The experimental imbibition data recorded by the scale was in agreement with the final liquid saturation determined by weighing. The readability of the

scale was 0.01g. When the wettability of the rock is altered to neutral-wet or preferentially gas-wet, there should be no imbibition of liquid into the rock.

In order to avoid errors due to evaporation, especially for water imbibition measurements, in the setup shown in **Fig. 2**, we developed a different approach to perform liquid imbibition into the air-saturated core samples; the schematic is depicted in **Fig. 3**. The core samples pressed strongly by the heat shrink tubing were kept vertically. The liquid level in the container is about 2 mm higher than the bottom of the core. The tubing from the valve to the container is filled with liquid while the section from the valve to the bottom of the core is empty. The liquid (oil or water) will rise and touch the bottom of the rock and imbibe into the rock spontaneously after the valve is opened. The time when liquid touches the rock bottom can be identified from the plot of the weight change of the container vs. time; an abrupt change in the reduction rate of liquid weight occurs when liquid touches the rock bottom due to liquid imbibition into the rock. The average liquid saturation and the amount of liquid imbibed into the core is readily calculated through the data recorded by the scale.

The equipment used to measure air permeability, liquid permeability, end-point gas phase relative permeability, and gravity drainage performance is shown in **Fig. 4**. A confining pressure of up to 3000psi may be applied in the Hassler type core holder. For air permeability measurement in Berea, the differential pressure between top and bottom ends is measured using a U-shape tube. A Validyne differential pressure transducer was used for the chalk with an accuracy of ±0.25% FS. Both drainage and imbibition tests may be performed in the same setup. A pump is used to apply a confining pressure to the core holder.

Entry Capillary Pressure: The schematic of the setup for measuring entry capillary pressure is shown in **Fig. 5**. When entry capillary pressure is small, it is measured by adjusting the height of the liquid level referenced to the bottom of the core sample; in this case compressed air is not required to pressurize the liquid. Otherwise, the entry capillary pressure is measured by applying air pressure to the liquid (see **Fig. 5**); the pressure is determined using a Validyne differential pressure transducer with an accuracy of ±0.25% FS. Other components in **Fig. 5** are similar to those in **Fig. 4**.

Results

We have conducted different tests in a capillary tube as well as in Berea and chalk samples. Following text discusses our experimental results.

Capillary Tube Tests: Fig. 6a shows liquid rise vs. the concentration of FC754 (from the treatment process) for both the gas-oil and gas-water systems; the liquid rise in the capillary tube decreases with an increase of the concentration and then stays constant when the concentration reaches around 0.2%wt. The reduction in the water rise due to wettability alteration is much more pronounced than that of the oil. The contact angle can be calculated using Eq. 2. **Fig. 6b** plots the computed contact angle vs. the concentration of FC754 for the gas-oil and gas-water systems. Note that the contact angle prior to treatment

is about 50° for the gas-water system and about 0° for the normal decane-air system. This figure shows that the contact angle increases with the increase of the concentration; the contact angle of the gas-water systems increases to about 90° at a concentration of about 0.1 percent. This implies that wettability of the gas-water-glass system has been altered to intermediate gas-wetting by FC754. The contact angle of gas-oil increases to about 60° at a concentration of 0.1 percent. The wettability alteration in the gas-water system by FC754 is more pronounced than that in the gas-oil system.

The effect of the concentration of FC722 on the liquid level is shown in **Fig. 7a** for both the gas-oil and gas-water systems; liquid level in the capillary tube decreases with an increase of the concentration. The effect of the chemical concentration on the liquid level is reduced when the concentration is higher than about 0.1 percent. The interesting observation in this figure is the fall of the water level to negative values in the capillary tube, which confirms the wettability alteration instead of the decrease of the surface tension. It is definitely determined from Eq. 2 that the liquid height in a circular capillary tube shown in **Fig. 1** cannot be negative by reducing the surface tension. The only means to have a fall of the liquid level is to alter wettability from preferential liquid-wetness ($\theta < 90°$) to preferential gas-wetness ($\theta > 90°$). **Fig. 7b** depicts the computed contact angle vs. the concentration of FC722 for both gas-oil and gas-water systems; the contact angle is calculated using Eq. 2. This figure shows that the contact angles of both gas-oil and gas-water in the capillary tube increases with the increase of the concentration. The contact angles of gas-water and gas-oil increase to about 118° and 60° at 1.0 percent concentration, respectively. The wettability alteration in the gas-water system by FC722 is much more pronounced than that in the gas-oil system.

Berea Imbibition Tests: We measured both imbibition of oil and imbibition of water into a Berea core saturated with air. The measurements included Berea before and after chemical treatment with FC754 and FC722, and with or without initial water saturation. We conducted the tests in the setup shown in **Fig. 2.**

Fig. 8 plots the gas recovery by both oil and water spontaneous imbibition in an air-saturated Berea before and after treatment with FC754 and FC722 chemicals, respectively. The gas recovery is represented by the fraction of GOIP (gas originally in-place). Note that the residual gas saturation to oil is not the same as the residual gas saturation to water for the untreated Berea; the residual gas saturation to oil is about 38%, and to water is about 44% (see **Fig. 8**). The residual oil saturation of Berea from water imbibition is about 45 percent[20]. The properties of the rock samples (Berea) used here are about the same. Therefore, the main factor that influences gas recovery by spontaneous liquid imbibition is wettability. There is no related literature on the effect of wettability on recovery in gas-liquid systems. Oil recovery in oil-water-rock systems may increase when the wettability varies from oil-wetting to water-wetting in uniformly-wet porous media as summarized by Anderson[21]. Other experimental results for rocks with heterogeneous wettability show that oil recovery in weakly water-wet reservoir rocks is sometimes greater than that in strongly water-wet rocks[22]. Compared with oil-water systems, it seems reasonable to assume that the gas recovery by liquid spontaneous imbibition is greater when rocks are more liquid-wet. Based on the above analysis, one possible explanation for the lower residual gas saturation to oil is that the oil wettability in gas-oil-Berea (GOB) systems is stronger than the water

wettability in gas-water-Berea (GWB) systems. This hypothesis seems to be consistent with the previous contact angle measurements in gas-oil and gas-water systems with capillary tubes. Our results showed that the contact angle through liquid phase in gas-oil systems is less than that in gas-water systems.

Gas recovery by water imbibition in Berea treated (sample No.1) by FC754 is much less than that in Berea without the chemical treatment (see **Fig. 8**). The spontaneous imbibition is related to wettability; gas recovery by spontaneous water imbibition decreases from liquid-wetting to preferential gas-wetness. Therefore, **Fig. 8** demonstrates that the wettability of a GWB system has been altered from strong liquid-wetting to somewhat intermediate gas-wetness by FC754. The gas recovery by spontaneous oil imbibition in Berea (sample No.1) when treated with FC754 is also less than that without the treatment for a GOB system, demonstrating that the wettability of the gas-oil-rock (Berea) system has been altered to less liquid-wet after treatment by FC754. Similar to the glass tube, the wettability alteration by FC754 in a GWB system is more pronounced than that in a GOB system.

Neither oil nor water imbibes into Berea (sample No.2) when treated by FC722 due to wettability alteration. It can be seen from **Fig. 8** that the wettability in both GOB and GWB systems has been altered from strong liquid-wetting to intermediate wetting or preferential gas-wetting by FC722. We will soon confirm that the wettability was altered to preferential gas-wetting by measuring the entry capillary pressure. It can be seen from the results shown in **Fig. 8** that FC722 is more effective than FC754 for altering the wettability in gas-liquid-Berea systems.

The rate of spontaneous imbibition for both oil and water in gas-oil and gas-water systems is shown in Fig. 9 in units of GOIP per minute. It can be seen from this figure that the rate of spontaneous oil imbibition is somewhat higher than that of water imbibition in Berea. The process shown in Fig. 9 may be because of the stronger liquid- wetting in GOB systems than in GWB systems. We will discuss liquid imbibition rates in more detail later.

As described above, the Berea cores were treated without initial water saturation. In order to examine the influence of initial water saturation on wettability alteration, we treated the core after establishing different initial water saturations. The experimental results depicted in **Fig. 10a** show that there is no water imbibition in Berea (sample No.3) after wettability alteration by FC722 with initial water saturation ranging from 0 to 40.1 percent. The imbibition process was completed after approximately 20 minutes. The same imbibition results were obtained when we extended the test time to about 1000 minutes. **Fig. 10a** shows that FC722 could alter rock wettability in the presence of initial water saturation in gas-water systems.

Gas recovery by water imbibition decreases with the increase of initial water saturation as shown in **Fig. 10a.** The effect of initial water saturation on imbibition rates was also studied. **Fig. 10b** shows that imbibition rate increases with the increase of initial water saturation at an early stage of imbibition. We did not find literature data on the effect of initial water saturation on imbibition recovery and rate in gas-liquid systems. Viksund, et al.[23] reported that the rate of spontaneous water imbibition in strongly water-wet rocks saturated with oil might increase or decrease with an increase in initial water saturation for sandstones and chalks; the trend depends on the range of initial water saturation. Our experimental results,

as discussed above, show a consistent increase of initial rate with increasing initial water saturation (see **Figs. 10 and 11**). Oil and water imbibition tests at the initial water saturation of 50% were also performed without chemical treatment. The same phenomenon as described above was found (results are not shown in **Figs. 10 and 11**).

Fig. 11a shows that there is no oil imbibition in Berea (sample No.4) after wettability alteration by FC722 when initial water saturation ranges from 0 to 40.5 percent. This implies that FC722 would also alter rock wettability in the presence of initial water saturation in gas-oil systems.

Gas recovery by oil imbibition also decreases with the increase of initial water saturation as shown in **Fig. 11a.** The effect of initial water saturation on oil imbibition rate is shown in **Fig. 11b.** The relationship between oil imbibition rate and initial water saturation at the early and late stage of oil imbibition in gas-oil systems is the same as in gas-water systems. From a comparison of **Figs. 10b and 11b,** it seems that in Berea the water imbibition rate is more sensitive to the initial water saturation than the oil imbibition rate.

Chalk Imbibition Tests: In order to verify that FC722 can alter the wettability of different rock types, Kansas chalk was used to perform liquid (oil and water) imbibition tests with and without chemical treatment using the setup shown in **Fig. 2.** The gas recovery by spontaneous oil and water imbibition in Kansas chalk (sample No.5) with and without chemical treatment by FC722 is shown in **Fig. 12.** Neither oil nor water imbibes into Kansas chalk due to the wettability alteration after the treatment with FC722. It can be seen from this figure that the wettability in a gas-water-chalk (GWC) or a gas-oil-chalk (GOC) system has been altered from strong water-wetness to intermediate wetness or preferential gas-wetness by FC722. The state of wettability alteration will be determined more precisely later.

The imbibition characteristics of oil and water in Kansas chalk is different from that in Berea as shown in **Fig. 13** (see also **Fig. 9**). Gas production rate by spontaneous water imbibition in a GWC system is higher than that by spontaneous oil imbibition in a GOC system at the early stage of imbibition. The process observed in **Fig. 13** may be due to the pore structure of the chalk. The feature of oil and water imbibition is opposite at the late stage. It can also be seen from **Fig. 12** that the ultimate gas recovery by spontaneous oil imbibition in a GOC system is greater than that by the spontaneous water imbibition in a GWC system. This may be due to the difference in wettability of liquid phase in GOC and GWC systems.

The comparison of gas recovery by spontaneous water imbibition in Berea with that in Kansas chalk is shown in **Fig. 14a.** This figure demonstrates that the residual gas saturation by the spontaneous water imbibition in Kansas chalk is about four times less than that in Berea. **Fig. 14b** shows that the water imbibition rate in Berea is greater than that in chalk during the early imbibition process.

The residual gas saturation by spontaneous oil imbibition in Kansas chalk is about three times less than that in Berea as shown in **Fig. 15a,** which has a similar characteristics to those of water imbibition in Berea and chalk (see **Fig. 14**). **Fig. 15b** illustrates similar results for oil imbibition rate as in **Fig. 14b.** It is noted, however, that the difference in oil and

water imbibition rates is greater in Kansas chalk than in Berea. Our residual gas saturation data in chalk reveal a unique feature which has not been reported in the literature.

Berea Drainage Tests: The effect of wettability alteration on oil production by gravity drainage was studied using the apparatus shown in **Fig. 4.** The core sample was first saturated with oil (normal decane). The absolute permeability was then measured. A gravity drainage test was performed without the chemical treatment at a confining pressure of 500psi. The production outlet was located 23cm below the bottom of the core because the threshold height is about 35cm. After gravity drainage without chemical treatment, the core was cleaned, dried, and then treated with FC722. The gravity drainage test was repeated after the core was saturated with oil following the chemical treatment. Two sandstone cores were used in the drainage tests. One (sample No.6) was treated with a low concentration (0.18%wt) of FC722. The oil production by gravity drainage in this core with and without treatment with FC722 is presented in **Fig. 16a.** The incremental oil recovery (OOIP) was around 15 percent in the core treated with 0.18 % wt FC722 due to wettability alteration.

Another core (sample No.7) was treated by a high concentration (2.0%wt) of FC722. The oil production by gravity drainage in this core with and without treatment with FC722 is shown in **Fig. 16b.** The incremental oil recovery due to the wettability alteration in the core with the treatment of 2.0 %wt FC722 was around 35 percent.

Oil production can be enhanced by treatment with FC722 (see **Fig. 16**). Incremental oil recovery by gravity drainage increases with the increase in concentration of FC722. Not much analysis can be made on the state of gas-wetting from the drainage tests due to breakthrough of the gas at the core outlet. The results, however, show that drainage and imbibition processes have different features from chemical treatment.

Preferential Gas-Wetting: The zero imbibition of oil or water in an air-saturated core after wettability alteration shown in **Fig. 8** for Berea, and in **Fig. 12** for chalk does not establish the extent of wettability alteration. A more precise test is the entry capillary pressure measurement. Any positive pressure on a liquid entering an air-saturated core would establish the degree of preferential gas-wetting of a treated core. Entry capillary pressures for both GOB and GWB systems were measured after the treatment of Berea sample (sample No.9) with 2.0%wt FC722. The porosity and permeability of this core are 19.5% and 616.7md, respectively. The entry capillary pressure after the chemical treatment in the GWB system was measured by using the equipment shown in **Fig. 5**; it is about 35cm of water column. The pseudo contact angle calculated using Eq. 3 is around 95°. The measured entry capillary pressure in the GOB system is about 12cm oil column; the pseudo contact angle calculated using Eq. 3 is around 93°.

The entry capillary pressure in a North Sea chalk (sample No.10) after treatment with 2.0%wt FC722 in both GOC and GWC systems was also measured; the porosity and permeability of this North Sea chalk were 29.0% and 1.47md, respectively. The measured entry capillary pressure was about 10.28 psi in the GWC system. The pseudo contact angle calculated using Eq. 3 was around 94°. The water phase used in the measurement was the 1%wt NaCl brine. The measured entry capillary pressure in the GOC system was about 1.49psi; the pseudo contact angle calculated using Eq. 3 was around 92°. Note that these two pseudo contact angles in both gas-oil- and gas-water-rock systems, unlike the more

direct measurements established before and the new one that will be discussed next, are physically less realistic.

We can also study wettability alteration by placing a droplet of water or oil on an air-saturated core. **Fig. 17** shows the fate of a droplet of water on the surface of an air-saturated Berea core before and after treatment. **Fig. 17a** shows that a droplet of water imbibes into the rock instantaneously as soon as it is placed on a Berea core (sample No.1) before chemical treatment. An oil droplet also imbibes. On the other hand, when a droplet of water is placed on an air-saturated Berea (sample No.2) which has undergone wettability alteration with 2.0%wt FC722, the droplet forms a shape that is compatible with its wettability. **Fig. 17b** shows that a water droplet forms a contact angle of about 125° indicating strong preferential gas-wetting. When a water droplet is placed on a Berea treated with 0.18%wt FC722, the contact angle is around 120° (see **Fig. 17c**). As expected the treated Berea does not imbibe any water. **Fig. 17d** shows a droplet of oil on an air-saturated Berea (sample No.2) treated by 2.0%wt FC722; oil does not imbibe into the rock. This figure shows that the contact angle through the oil phase is less than that in gas-water-rock system; the measured contact angle through the oil phase is around 60°.

Fig. 18a shows a droplet of water (or oil) on the top of an air-saturated chalk (sample No.8) without chemical treatment; water (or oil) imbibes into the rock instantaneously when it contacts the rock. After the treatment with 2.0%wt FC722, water does not imbibe into the rock (sample No.8) as shown in **Fig. 18b**; the contact angle is around 120° through the water phase. **Fig. 18c** shows a droplet of oil on the chalk (sample No.8) treated by 2.0%wt FC722; oil does not imbibe into the rock. It can be seen in **Fig. 18c** that the contact angle in GOC systems is less than that in GWC systems; the measured contact angle through the oil phase is also around 60°.

The results of the simple tests shown in **Figs. 17 and 18** also provide a strong evidence of wettability alteration to preferential gas-wetting.

Thermal Stability of Chemical: To demonstrate the thermal stability of FC722, a Berea was saturated with FC722 at room temperature. After removing the liquid chemical, the core was dried and then heated to a temperature of 210°F and maintained for around two hours. Neither water nor oil imbibes into this core when saturated with air; the imbibition tests were then performed at room temperature. Therefore, FC722 appears to possess good thermal stability under these conditions.

Longevity of Chemical: The longevity of FC722 was studied by oil displacement and gas displacement in the treated core. One Berea sample was treated by FC722 and saturated with oil after it was dried. The core was dried again following 100PV of oil displacement in a single phase state. Then both water and oil imbibition tests were performed. It was found that there was neither water imbibition nor oil imbibition in the core after 100PV of oil displacement. The same procedures were repeated after about 10,000PV of gas displacement. Neither water nor oil imbibed into the air-saturated core. The core was then left in the air for approximately 4 months; there was still no liquid imbibition. The above results show that FC722 might be suitable for permanent wettability alteration.

Effect of Chemical on Permeability: In order to study the effect of chemical treatment on rock property, the permeabilities of both Berea and chalk samples before and after the treatment with FC722 were measured using nC_{10}. The setup used to measure the rock

permeability is shown in Fig. 4. The permeabilities of two Berea cores (samples No.7 and 9) without chemical treatment were 975 and 616md, respectively; they varied to 938 and 592md after it was treated by 0.18%wt FC722, respectively. The permeability of the North Sea chalk (sample No.10) changed from 1.47md to 1.18md after it was treated by 2.0%wt FC722. The above experimental results show that there is no significant permeability reduction in Berea or chalk samples after treatment with FC722.

All the tests described above confirm that the wettability of porous media can be altered to preferentially gas-wet, and the wettability alteration is permanent. Furthermore, there is no significant reduction in permeability after the wettability of porous media is altered. In the following, we will discuss the measurement of gas and liquid relative permeabilities of the treated and untreated Berea to confirm the results from our theoretical work presented in Ref. 1.

Effect of Wettability Alteration on Relative Permeability: Gas well deliverability in gas-condensate reservoirs is related to the relative permeabilities. If the relative permeabilities can be increased by wettability alteration, the gas well production may be enhanced. Berea (sample No.11) with length of 17.85cm and diameter of 2.48cm was used to study the effect of wettability alteration on oil and gas phase relative permeability; the permeability and porosity of this core sample are 632.3md and 20.5%, respectively.

The measured final oil recovery (OOIP) by gravity drainage increased from 83.8 to 91.9%; residual oil saturation decreased from 16.2to 8.1%; and end-point gas phase relative permeability increased from 0.54 to 0.95 after the core was treated with 2.0%wt FC722.

Gas relative permeability at an oil saturation of about 16.2% increased from 0.54 to 0.89 and oil relative permeability at an oil saturation of about 27.1% increased from 0.025 to 0.030 after it was treated with 2.0%wt FC722. It seems that the effect of wettability alteration on oil and gas relative permeabilities supports the network modeling predictions by Li and Firoozabadi[1]. An extensive effort to measure gas and liquid relative permeabilities in the entire saturation range is currently planned.

Conclusions

In addition to new data on residual gas saturation to oil and water imbibition in strongly liquid-wet chalk, the following conclusion related to wettability alteration can be drawn from the work:

1. The wettability of gas-water-rock systems can be altered from strong water-wetting to intermediate gas-wetting by FC754 and can be altered from strong water-wetting to preferential gas-wetting by FC722.
2. The wettability of gas-oil-rock systems can be altered from strong oil-wetting to less oil-wetting by FC754 and can be altered from strong oil-wetting to preferential gas- wetting by FC722.
3. The oil recovery and gas phase relative permeability in gas-oil systems could be increased by the treatment of FC722 due to the wettability alteration.
4. FC722 is thermally stable and seems to alter gas wettability permanently.

5. The gas recovery by spontaneous oil imbibition is greater than that by spontaneous water imbibition in both Berea and Kansas chalk.
6. The gas recovery by both spontaneous oil and water imbibition in a Kansas chalk is larger than that in Berea.

Nomenclature

D = diameter of core
h_l = height of liquid column
k = permeability
L = length of core
P_c = capillary pressure
PV = pore volume of core
r = radius of a capillary tube
ϕ = porosity
θ = contact angle
θ_A = advancing contact angle
θ_P = pseudo contact angle
θ_R = receding contact angle
σ = surface tension
μ = fluid viscosity

Acknowledgements

We thank Djamel . E. Ouzzane of Imperial College of Science,Technology and Medicine for his help to study the effect of initial water saturation on imbibition.

References

1. Li, K., and Firoozabadi, A.: "Phenomenological Modeling of Critical Condensate Saturation and Relative Permeabilities in Gas Condensate Systems, Chapter III, Part I.
2. Allen, F. H. and Roe, R.P.: "Performance Characteristics of a Volumetric Condensate Reservoir," Petroleum Transactions, *AIME* (1950), 189, 83-90.
3. Engineer, R.: "Cal Canal Field California: Case History of a Tight and Abnormally Pressure Gas Condensate Reservoir," paper SPE 13650, presented at the 1985 California Regional Meeting, Bakersfield, California, March 27-29.
4. Bamum, R.S., Brinkman, F.P., Richardson, T.W., and Spillete, A.G.: "Gas Condensate Reservoir Behavior: Productivity and Recovery Reduction Due to Condensation," paper SPE 30767, presented at the 1995 Annual Technical Conference and Exhibition, Dallas, TX, Oct. 22-25.
5. Buckley, S. E. and Leverett, M. C.: "Mechanism of Fluid Displacement in Sands," Petroleum Transactions, *AIME* (1942), 146, 187-196.

6. Morris, E. E. and Wieland, D. R.: "A Microscopic Study of the Effect of Variable Wettability Conditions on Immiscible Fluid Displacement," paper SPE 704, presented at the 1963 Annual Technical Conference and Exhibition, New Orleans, Oct. 6-9.
7. Wagner, O. R. and Leach, R. O.: "Improving Oil Displacement Efficiency by Wettability Adjustment," paper SPE 1101-G, presented at the 1958 Annual Meeting, Houston, Texas, Oct. 5-8.
8. Froning, H. R. and Leach, R. O.: "Determination of Chemical Requirements and Applicability of Wettability Alteration Flooding," paper SPE 1563, presented at the 1966 Annual Meeting of the Society of Petroleum Engineers of AIME, Texas, Oct. 2-5.
9. Kamath, I. S.: "A Fresh Look at Wettability Detergent Flooding and Secondary Recovery Mechanisms," paper SPE 2862, presented at the 1970 Biennial Production Techniques Symposium, Wichita Falls, Texas, May 14-15.
10. Donaldson, E. C. and Thomas, R. D.: "Microscopic Observations of Oil Displacement Water-Wet and Oil-Wet Systems," paper SPE 3555, presented at the 1971 Annual Meeting of the Society of Petroleum Engineers of AIME, Texas, Oct. 3-6.
11. Morrow, N. R., Cram, P. J., and McCaffery, F. G.: "Displacement Studies in Dolomite With Wettability Control by Octanoic Acid," paper SPE 3993, presented at the 1971 Annual Meeting of the Society of Petroleum Engineers of AIME, San Antonio, Texas, Oct. 8-11.
12. Penny, G. S., Soliman, M. W., and Briscoe, J. E.: "Enhanced Load Water-Recovery Technique Improves Stimulation Results," paper SPE 12149, presented at the 1983 Annual Meeting of the Society of Petroleum Engineers of AIME, San Francisco, CA, Oct. 5-8.
13. Menezes, J. L., Yan, J., and Sharma, M. M.: "The Mechanism of Wettability Alteration Due to Surfactants in Oil-Based Muds," paper SPE 18460, presented at the 1989 International Symposium of Oilfield Chemistry, Houston, TX, February 8-10.
14. Cockcroft, P. J., Guise, D. R., and Waworuntu, I. D.: "The Effect of Wettability on Estimation of Reserves," paper SPE 19484, presented at the 1989 Asia-Pacific Conference, Sydney, Australia, Sept. 13-15.
15. Jia, D., Buckley, J. S., and Morrow, N. R.: "Control of Core Wettability with Crude Oil," paper SPE 21041, presented at the 1991 International Symposium of Oilfield Chemistry, Anaheim, CA, Feb. 20-22.
16. Buckley, J.S., Bousseau, C., and Liu, Y.: "Wetting Alteration By Brine and Crude Oil: From Contact Angles to Cores," paper SPE 30765, presented at the 1995Annual Technical & Exhibition, Dallas, Oct. 22-25.
17. Wardlaw, N.C. and McKellar, M.: "Wettability and Connate Water Saturation in Hydrocarbon Reservoirs with Bitumen Deposits," *J. of Petroleum Science and Engineering* (1998), 20, 141-146.
18. Al-Siyabi, Z.K., Daniesh, A., Tohidi, B., and Todd, A.C.: "Measurement of Gas-Oil Contact Angle at Reservoir Conditions," Proceedings of 1997 European Symposium on Improved Oil Recovery, The Hague, The Netherlands, Oct.20-22.
19. Fang, F., and Firoozabadi, A., Abbaszadeh, M, and Radke, C.: "A Phenomenological Network Model of Critical Condensate Saturation," paper SPE 36716, presented at the 1996 Annual Technical Conference and Exhibition, Denver, Colorado, Oct. 6-9.
20. Ivan, E.Terez and Firoozabadi, A: "Water Injection in Water-Wet Fractured Porous Media: Experiments and a New Model Using Modified Buckley-Leverett Theory," paper SPE 39605, presented at the 1998 Improved Oil Recovery Symposium, Tulsa, Oklahoma, April 19-22.

21. Anderson, W.G.: "Wettability Literature Survey – Part 6: The Effect of Wettability on Waterflooding," *JPT* (Dec. 1987), 1605-1622.
22. Morrow, N.R., Lim, H.T., and Ward, J.S.: "Effect of Crude-Oil-Induced Wettability Changes on Oil Recovery," *SPEFE* (Feb. 1986), 89-103.
23. Viksund, B.G., Morrow, N.R., Ma, S., Wang, W. and Graue, A.: "Initial Water Saturation and Oil Recovery from Chalk and Sandstone by Spontaneous Imbibition," Proceedings of 1998 International Symposium of the Society of Core Analysts, The Hague, Netherlands, Sept. 14-16.

Table 1: Data on Core Samples

Sample No.	Permeability, md	Porosity, %	Length, cm	Diameter, cm	PV, ml	Rock type
1	*	20.6	5.05	5.02	20.55	Berea
2	*	21.8	5.06	5.02	21.82	Berea
3	*	22.8	4.93	5.00	22.07	Berea
4	*	22.2	5.00	4.98	21.65	Berea
5	★	25.0	5.30	3.71	14.32	Kansas chalk
6	1089	21.9	18.9	2.64	22.65	Berea
7	975	21.3	18.9	2.64	22.03	Berea
8	★	24.8	5.11	5.02	25.06	Kansas chalk
9	616	19.5	18.15	2.53	17.81	Berea
10	1.47	29.0	12.55	5.03	72.47	North Sea chalk
11	632	20.5	17.85	2.48	17.67	Berea

*: k = 500md; ★: k = 5md

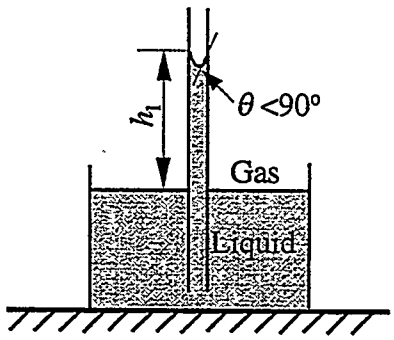

(a) Strong liquid-wet (θ<90°)

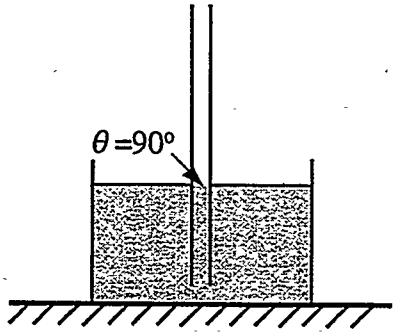

(b) Intermediate gas-wet (θ=90°)

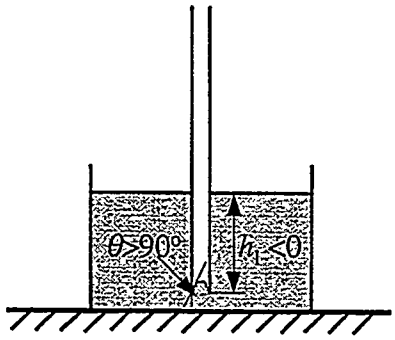

(c) Gas-wet (θ>90°)

Fig.1: Liquid level rise or fall in a capillary tube at various wettability conditions

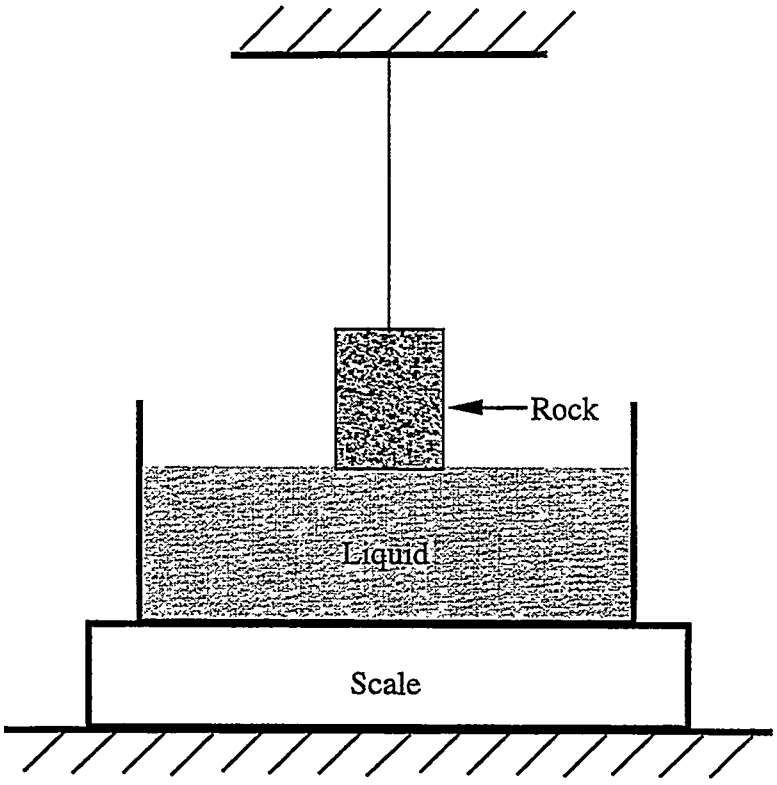

Fig. 2: Instant surface contact method for measuring liquid imbibition into an air-saturated rock

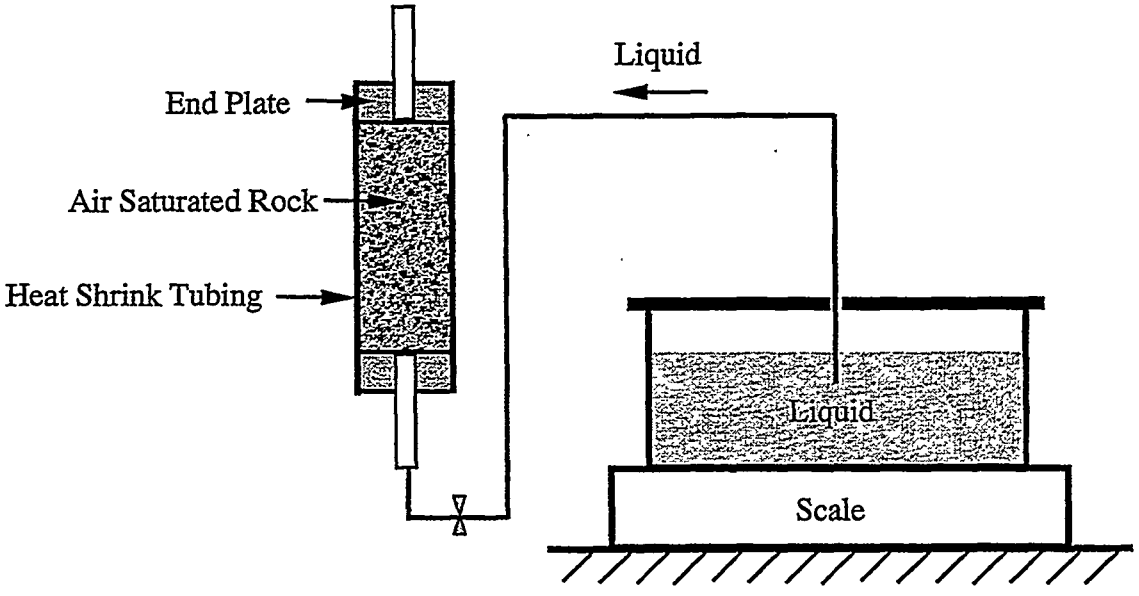

Fig. 3: Liquid rise method for measuring liquid imbibition into an air-saturated rock

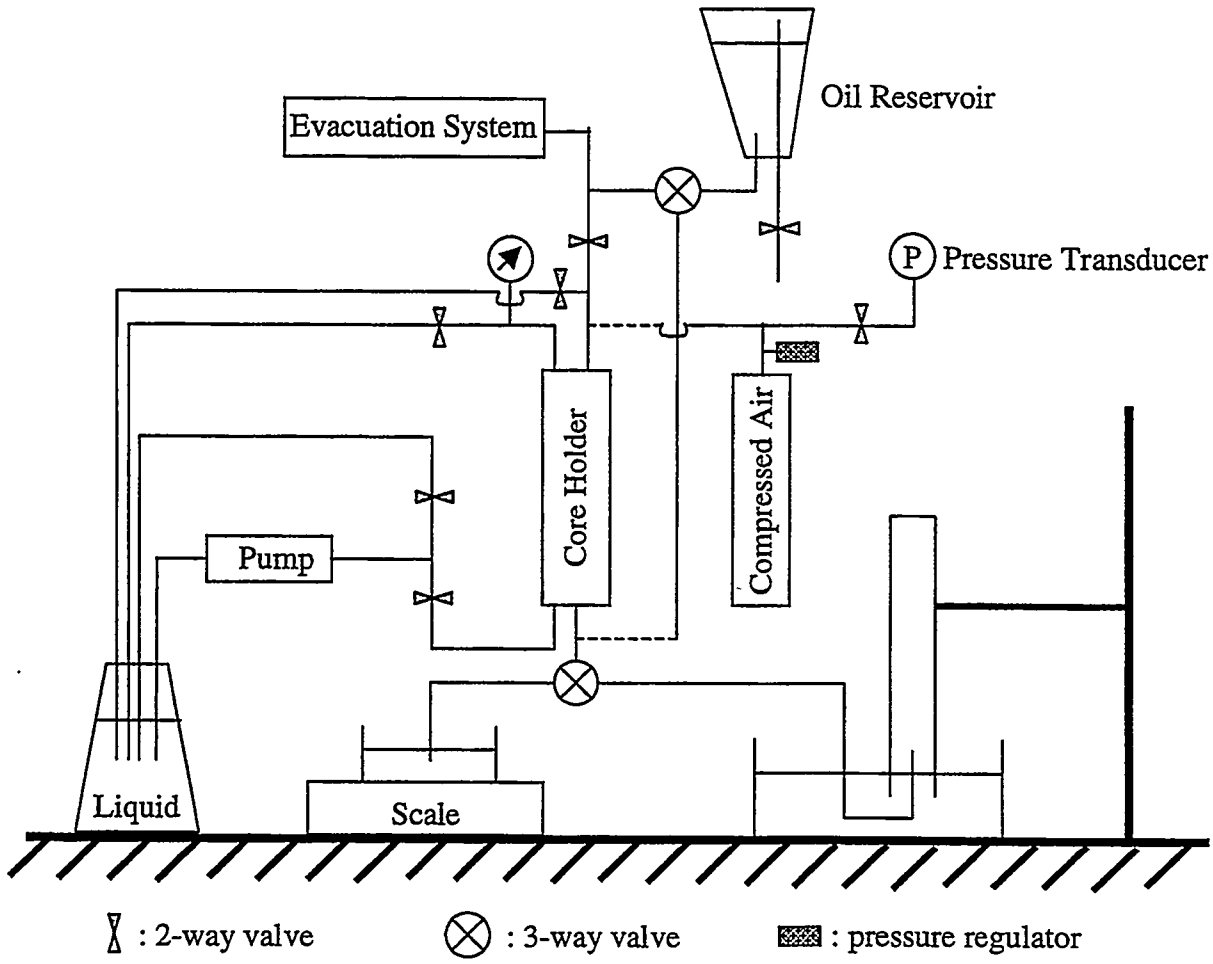

Fig. 4: Schematic of the apparatus used for measuring drainage and imbibition

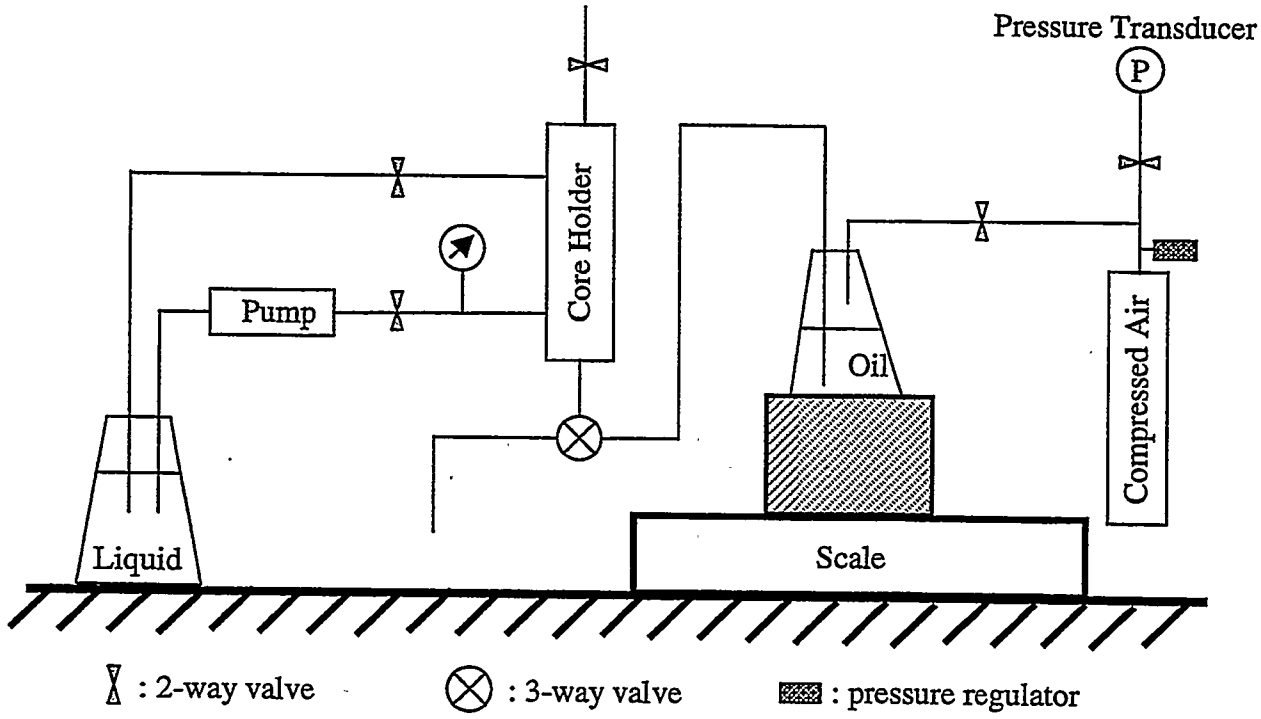

Fig. 5: Schematic of the apparatus used for measuring the entry capillary pressure

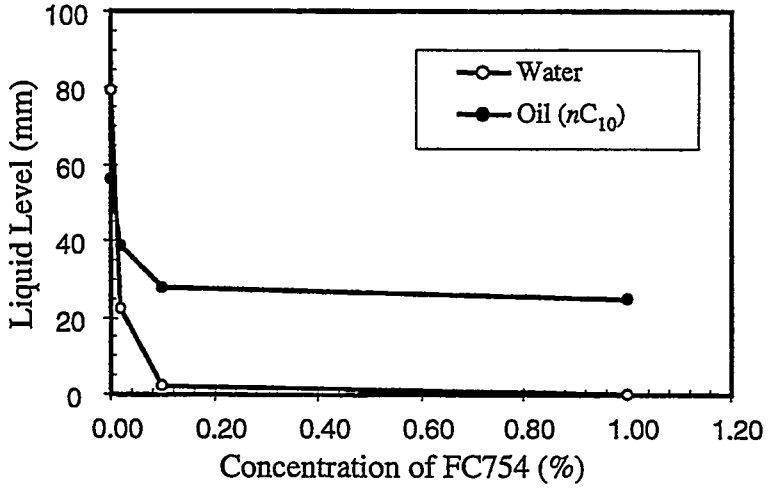

(*a*) Liquid level

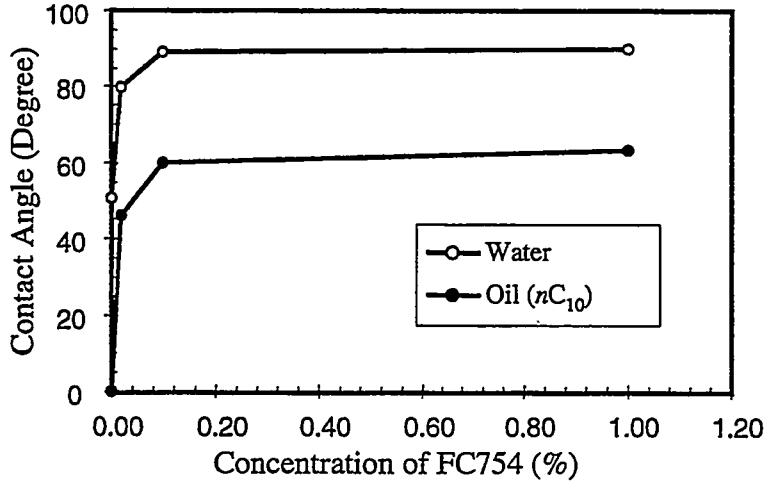

(*b*) Contact angle

Fig. 6: Liquid level and contact angle vs. the concentration of FC754 — glass tube

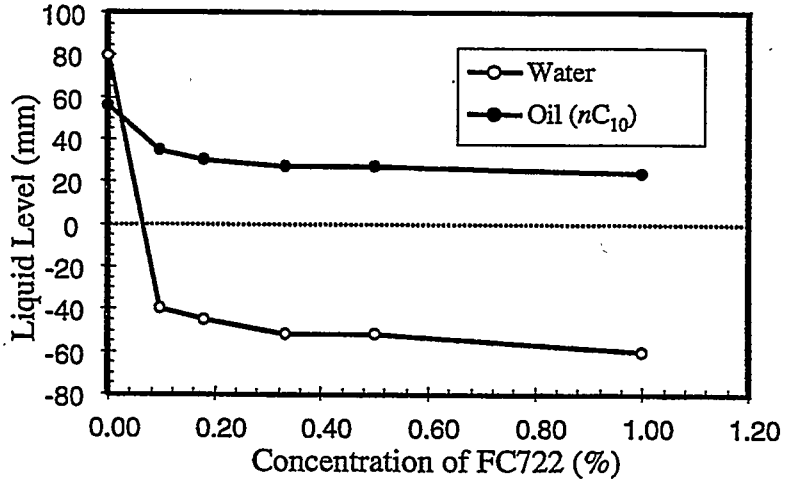

(*a*) Liquid level

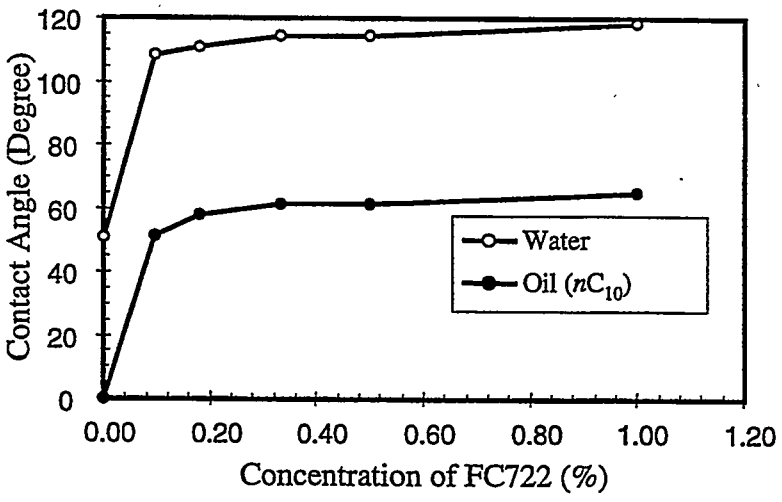

(*b*) Contact angle

Fig. 7: Liquid level and contact angle vs. the concentration of FC722 — glass tube

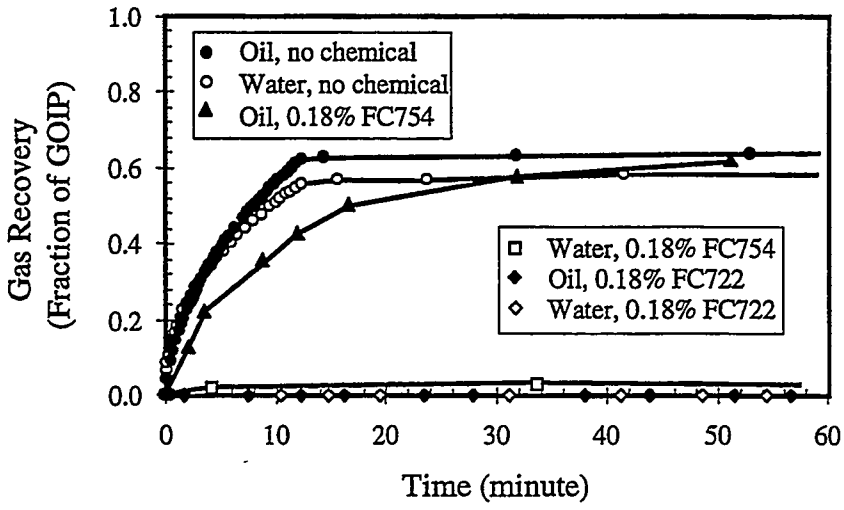

Fig. 8: Gas recovery by oil and water imbibition into the air-saturated Berea with and without chemical treatment

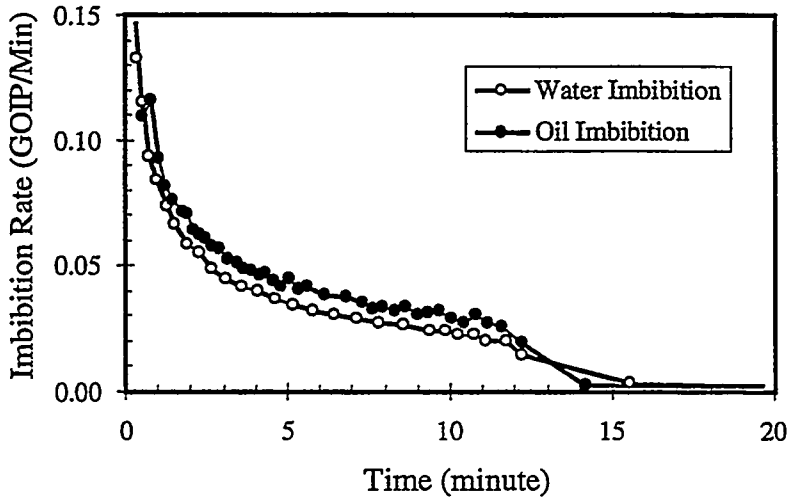

Fig. 9: Oil and water imbibition rates for the air-saturated Berea without chemical treatment

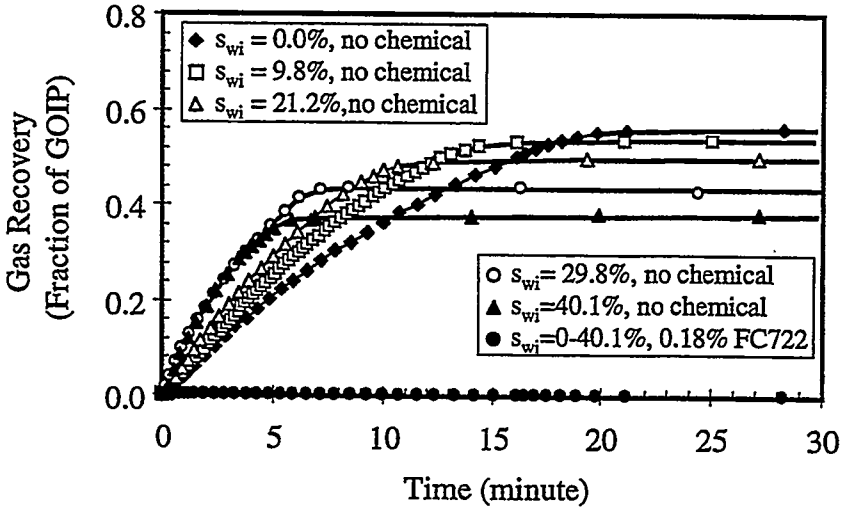

(*a*) Gas recovery

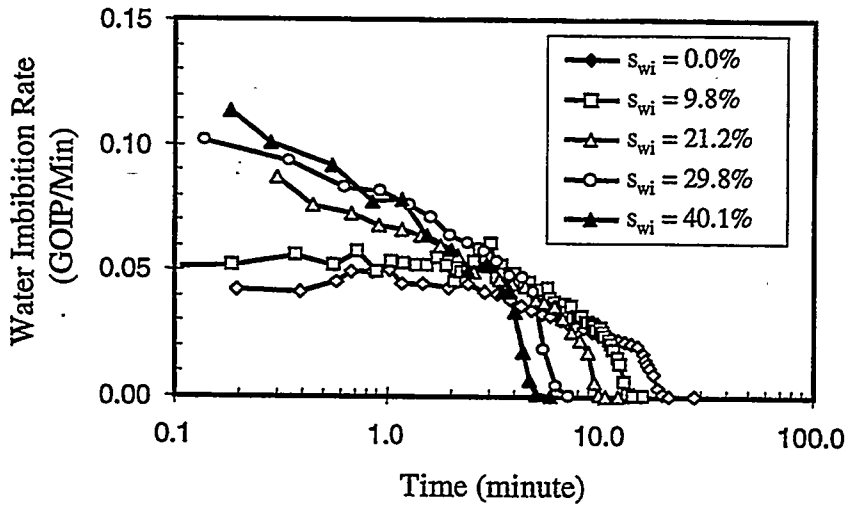

(*b*) Imbibition rate

Fig.10: Effect of initial water saturation on water imbibition into the air-saturated Berea with and without treatment with FC722

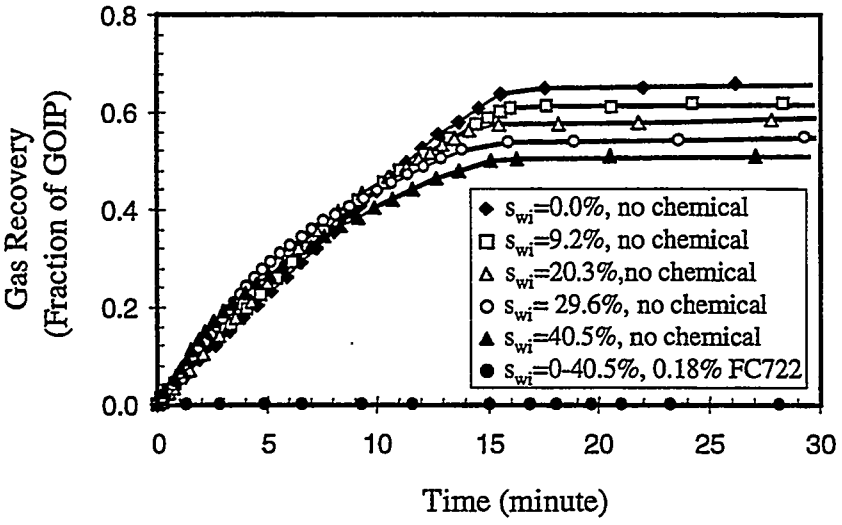

(*a*) Gas recovery

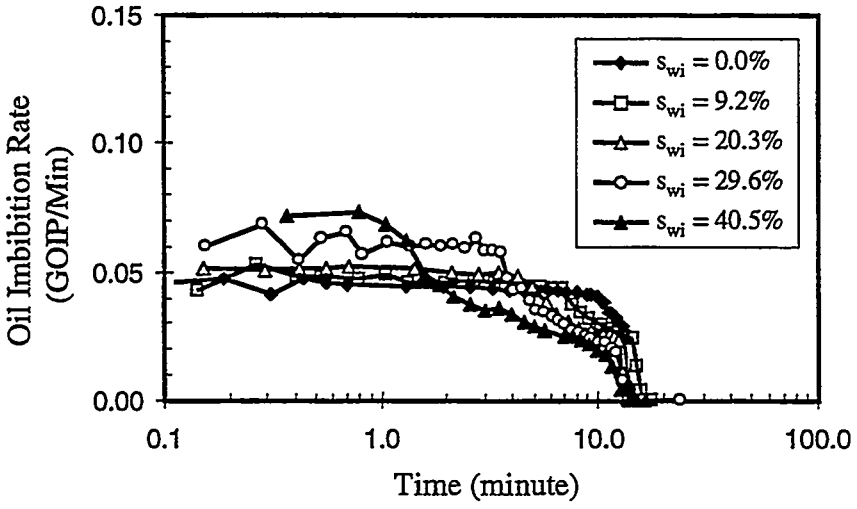

(*b*) Imbibition rate

Fig.11: Effect of initial water saturation on oil imbibition into the air-saturated Berea with and without treatment with FC722

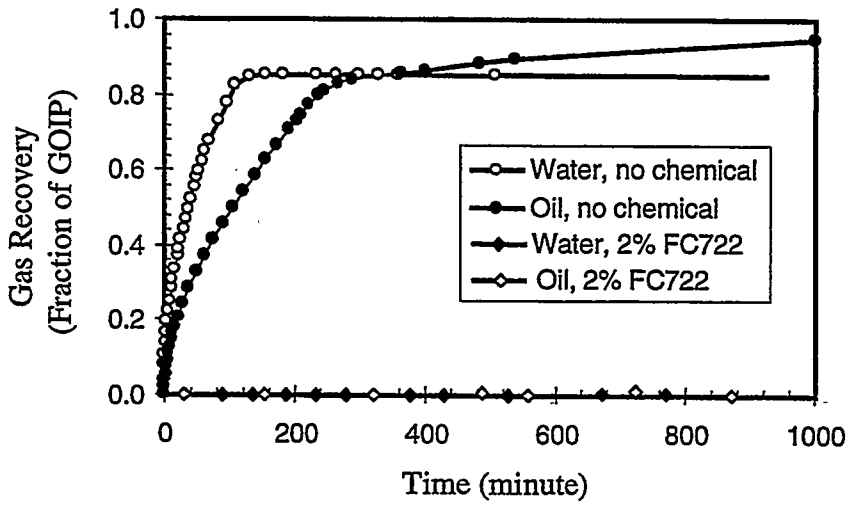

Fig. 12: Gas recovery by liquid imbibition into
the air-saturated chalk with and without treatment with FC722

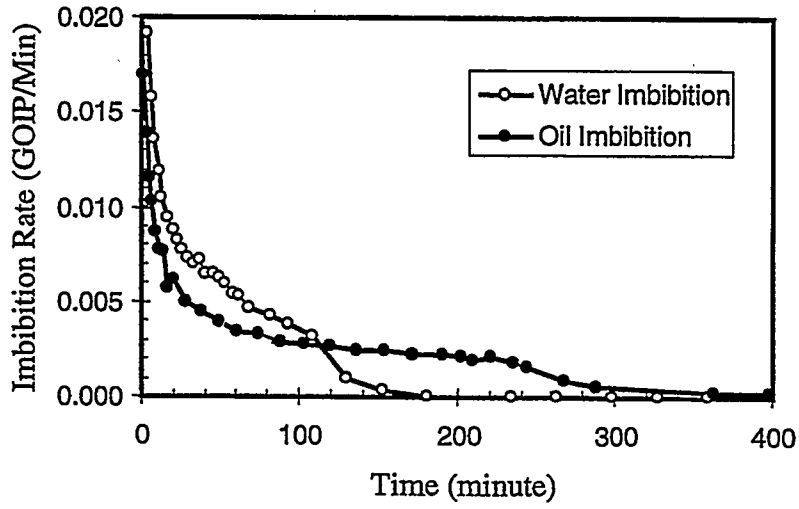

Fig. 13: Oil and water imbibition rates for
the air-saturated chalk without chemical treatment

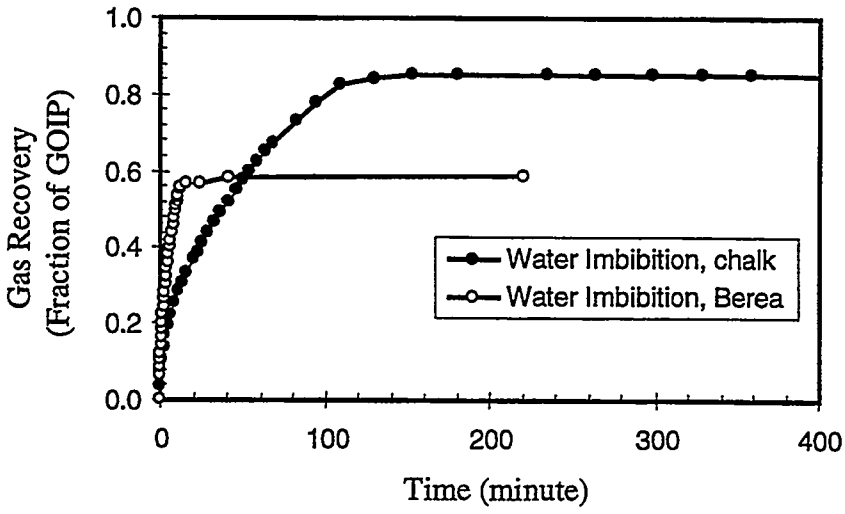

(*a*) Gas recovery

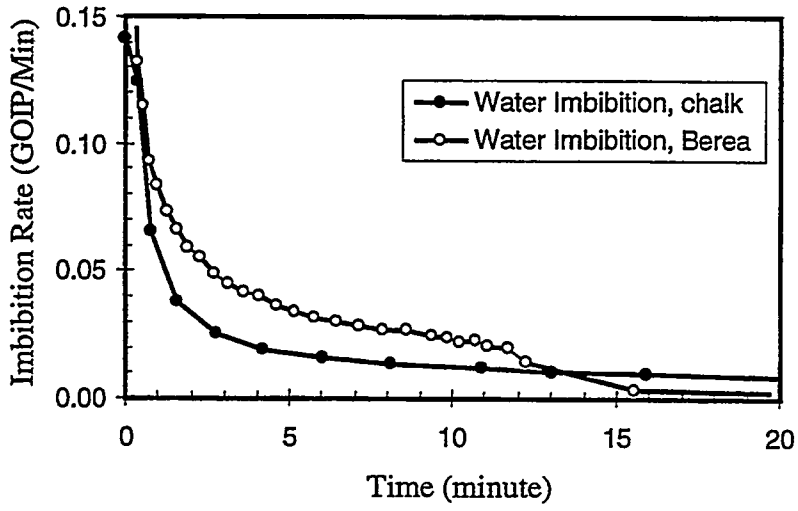

(*b*) Imbibition rate

Fig.14 Water imbibition and rate of the air-saturated Berea and chalk samples without chemical treatment

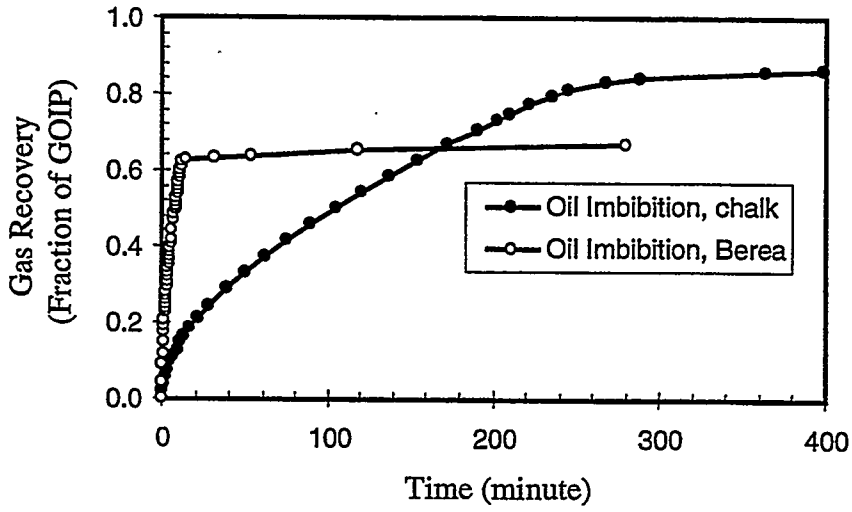

(*a*) Gas recovery

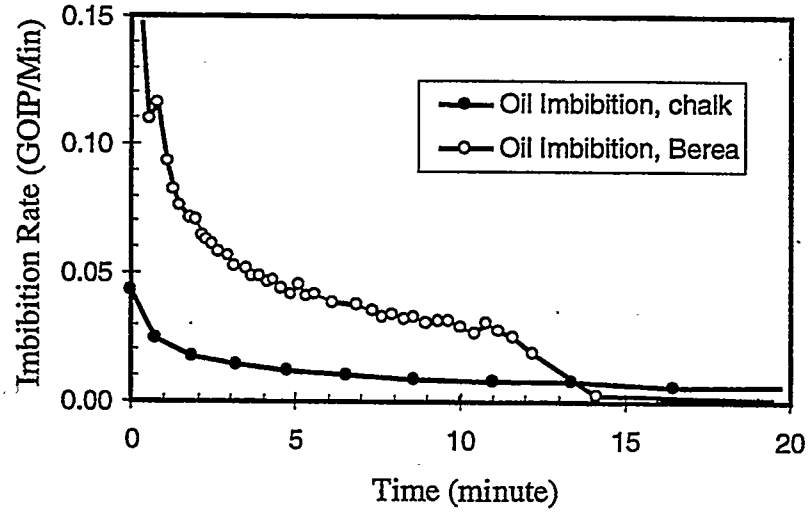

(*b*) Imbibition rate

Fig.15 Oil imbibition and rate of the air-saturated Berea and chalk samples without chemical treatment

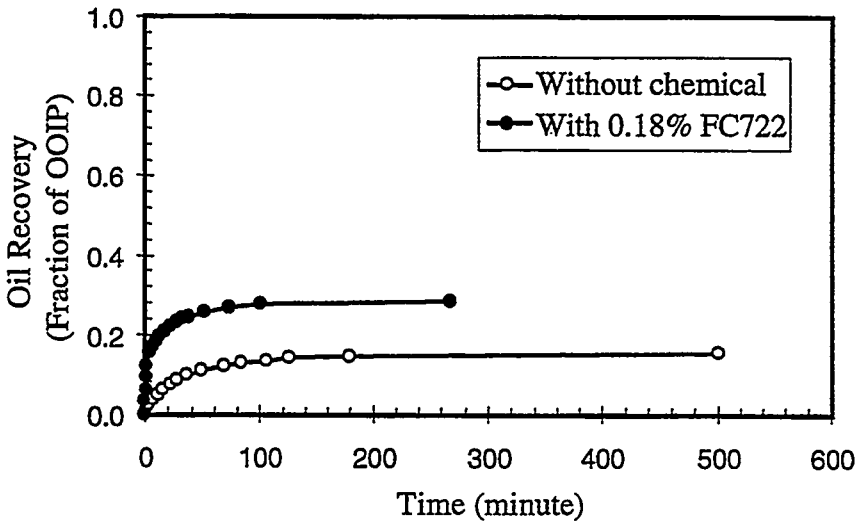

(*a*) 0.18% FC722 (k=1089md)

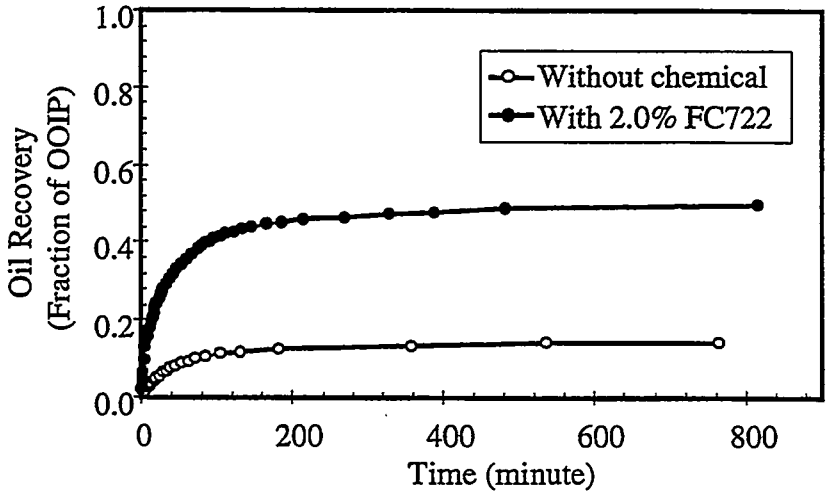

(*b*) 2.0% FC722 (k=975md)

Fig.16: Oil recovery by gravity drainage with and without treatment of Berea with FC722

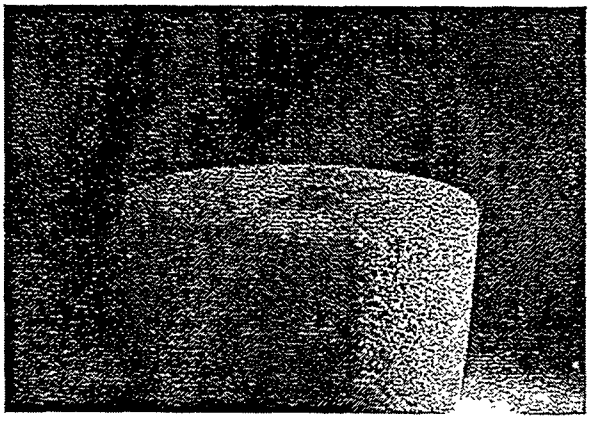

(*a*) Water (without chemical treatment)

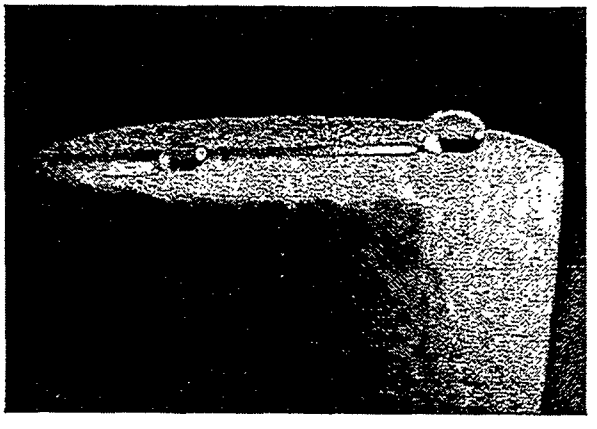

(*b*) Water (treatment with 2.0% FC722 , θ=125°)

Fig. 17: Liquid droplets on the surface of the air-saturated Berea before and after treatment with FC722

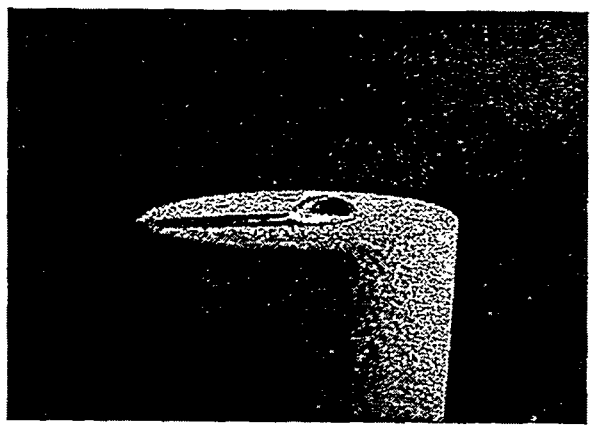

(*c*) Water (treatment with 0.18% FC722 , θ=120°)

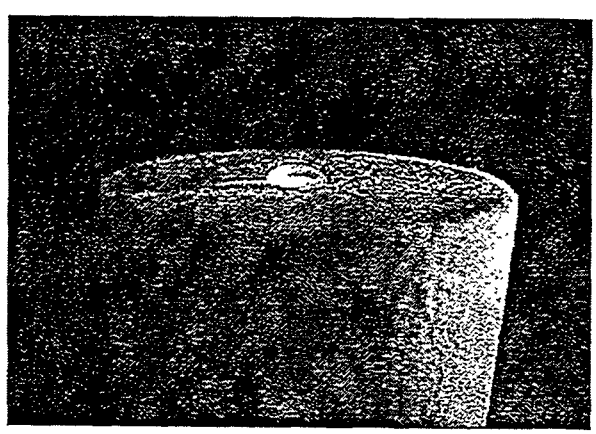

(*d*) Oil (treatment with 2.0% FC722 , θ=60°)

Fig. 17: Liquid droplets on the surface of the air-saturated Berea before and after treatment with FC722(continued)

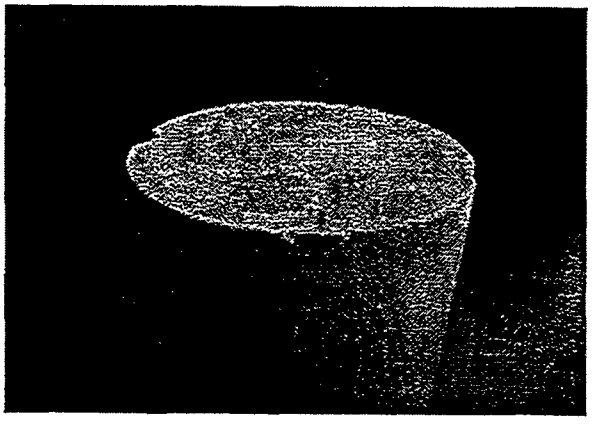

(*a*) Water (without chemical treatment)

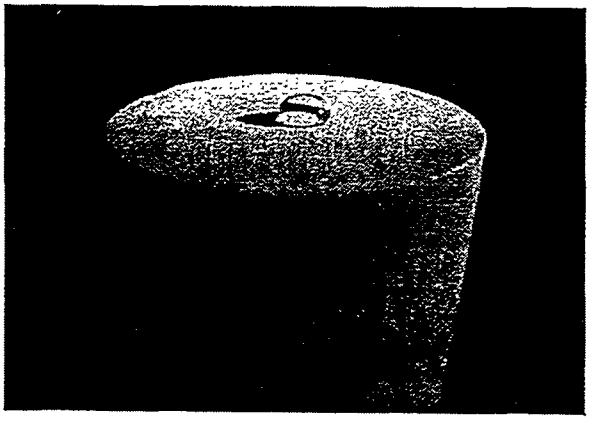

(*b*) Water (treatment with 2.0% FC722 , θ=120°)

Fig. 18: Liquid droplets on the surface of the air-saturated chalk before and after treatment with FC722

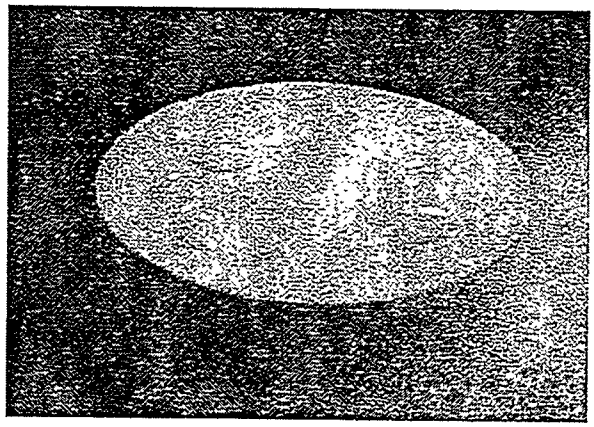

(*c*) Oil (treatment with 2.0% FC722, θ=60°)

Fig. 18: Liquid droplets on the surface of the air-saturated chalk before and after treatment with FC722 (continued)

Part I - Molecular, Pressure, and Thermal Diffusion Flux in Non-Ideal Multicomponent Mixtures

KASSEM GHORAYEB AND ABBAS FIROOZABADI

1 Summary

A formalism based on powerful concepts of thermodynamics of irreversible processes is derived for calculating multicomponent diffusions flux both at the critical point and away from the critical point. The derivations are based on the entropy balance expression combined with the phenomenological equations and the Onsager reciprocal relations. The formalism results in a clear expression for the thermal contribution in the diffusion flux for non-ideal multicomponent mixtures. An analysis of the diffusion flux at the critical point is also performed. This analysis reveals that unlike isothermal and isobaric conditions where molecular diffusion flux is zero, molecular diffusion flux is finite and nonzero at the critical point. The thermal contribution in the diffusion flux is also finite at the critical point in multicomponent mixtures. This analysis shows that at non-isothermal conditions, also at non-isothermal and non-isobaric conditions, the composition gradient reaches infinity at the critical point; therefore, the mole fraction plot vs. spatial coordinates has an inflection point.

2 Introduction

Multicomponent diffusions (molecular, pressure, and thermal) are important in a variety of disciplines including oceanography, geology, metallurgy, material science, geophysics, chemical engineering, and hydrocarbon reservoir engineering [1, 2, 3, 4, 5, 6]. The share of molecular, pressure, and thermal diffusion to the total diffusion flux depends on the non-ideality of the fluid mixture and the imposed boundary conditions. Our motivation for the study of the subject is the understanding of irreversible phenomena in hydrocarbon reservoirs (cavities). An understanding of thermal, pressure, and molecular diffusion is required to determine the distribution of various species of a hydrocarbon fluid mixture in cavities with dimensions of the order of hundreds of meters and more. The fluid mixture contains a number of components each having a significant amount; it can be at the critical region in certain parts of a large cavity.

There is a vast literature on the subject of multicomponent molecular diffusion, pressure diffusion (sometimes referred to as gravitational effect) and thermal diffusion (often referred to as the Soret effect). The literature on thermal diffusion is, however, mainly

limited to two-component mixtures. To the best of our knowledge, there are no reported measured thermal diffusion factors (which are a measure of thermal diffusion) for a single ternary mixture or higher mixtures. This may be due to the lack of proper formulation of thermal diffusion flux in multicomponent mixtures.

Multicomponent molecular diffusion flux has been established to be zero at the critical point for both binary and multicomponent mixtures at isobaric and isothermal conditions [7, 8, 9, 10, 11] (throughout the study our focus is gas-liquid critical point). One purpose of this work is to establish the formulation that allows the determination of molecular diffusion flux at the critical point for 1) isothermal and non-isobaric, 2) non-isothermal and isobaric, and 3) non-isothermal and non-isobaric conditions. We are also interested in determining thermal diffusion flux at the critical point for multicomponent non-ideal mixtures.

The behavior of the thermal diffusion coefficient for binary mixtures in the critical region has been subject of several studies in the three last decades [12, 13, 14, 15, 16, 17, 18, 19, 20, 21, 22, 23, 24, 25, 26, 27, 28]. It has been shown using the mode-mode coupling analysis [24, 25] that thermal diffusion coefficients of a binary mixture have a finite value at the critical point. It is of interest to examine the finiteness of thermal diffusion at the critical point for multicomponent mixtures. In this work we show, by simple analysis of the diffusion flux for non-ideal binary mixtures, that the compositional gradient becomes infinity at the critical point. We extend our analysis to multicomponent non-ideal mixtures and show, for the first time, that the composition gradient of all the components undergo an inflexion point.

The cross effects characterize molecular diffusion and to a larger extent thermal diffusion in multicomponent mixtures. When those effects are significant, concentration gradients may change radically. To be specific, consider binary mixtures of methane(C_1)/ethane(C_2), methane(C_1)/propane(C_3) and methane(C_1)/n-butane(nC_4), where experimental thermal diffusion data are available [21, 27, 28]. In all those methane binaries of C_1/C_2, C_1/C_3, and C_1/nC_4, methane segregates to the hot side at isobaric conditions. On the other hand, in a ternary mixture of $C_1/C_2/nC_4$, methane may segregate to the cold side [29]. The segregation of methane in binary mixtures to the hot side and in a ternary mixture to the cold side implies that one may not use effective thermal diffusion factors to study thermal diffusion in ternary and higher mixtures in a non-isothermal process.

Cross-molecular diffusion coefficients have also been shown to be important in some ternary and higher mixtures. Larre *et al.* [30] investigated the stability of a horizontal layer heated from below filled with a water-isopropanol-ethanol mixture. The authors neglected the cross-molecular diffusion coefficients and assumed that the thermal diffusion factor of a given component could be expressed as the sum of the thermal diffusion factors of the binaries consisting of this component and the two others, respectively. The model results do not, however, agree with the experimental data. A similar conclusion has been reported by Krupiczka and Rotkegel [31] who investigated mass transfer in ternary mixtures of isopropanol-water-air and isopropanol-water-helium. Considerable discrepancies between experimental data and theoretical predictions were observed when cross-diffusion terms were neglected.

The main goal of this paper is to present a consistent and clear formulation of diffusion flux expression for multicomponent mixtures. We include diffusion processes due to 1)

molecular, 2) pressure, and 3) thermal effects for complex near-critical mixtures. The derivations are based on the powerful concepts of irreversible thermodynamics. Part of our derivations are somewhat similar to those of de Groot and Mazur [32] and Haase [7]. However, these authors have not attempted to present a complete formulation of multicomponent diffusions. We will repeat some aspects of the work of these authors for completeness in advancing concepts.

3 Phenomenological Equations

In a mixture consisting of N components ($N \geq 2$), where there is no heat generation, viscous dissipation, or chemical reaction and where the only external force $\vec{F}$ is the gravity, the entropy production strength σ (entropy production per unit time and volume) can be written as (see de Groot and Mazur [32])

$$\sigma = -\frac{1}{T^2}\vec{J}_q.\vec{\nabla}T - \frac{1}{T}\sum_{k=1}^{N}\vec{J}_k.\left(\frac{T}{M_k}\vec{\nabla}\frac{\mu_k}{T} - \vec{F}\right), \tag{1}$$

where $\vec{J}_q$ is the heat flux, T is the temperature, and M_k, μ_k, $\vec{J}_k$ are the molecular weight, the chemical potential, and the diffusion mass flux relative to the mass average velocity of component k, respectively. A different form of the entropy production can be obtained by using

$$T\vec{\nabla}\frac{\mu_k}{T} = \vec{\nabla}\mu_k - \frac{\mu_k}{T}\vec{\nabla}T \tag{2}$$

$$= \vec{\nabla}_T\mu_k - \left(\mu_k - T\left.\frac{\partial\mu_k}{\partial T}\right|_{\mathbf{n},P}\right)\frac{\vec{\nabla}T}{T}, \tag{3}$$

where $\mathbf{n} \equiv (n_1, n_2, ..., n_k, ..., n_N)$, n_k is the number of moles of component k, and P is the pressure. The subscript T implies that the gradient is calculated at constant temperature. The Gibbs free energy G is given by

$$G = \sum_{k=1}^{N} n_k\mu_k, \tag{4}$$

and, the Gibbs-Duhem relation reads

$$\sum_{k=1}^{N} n_k d\mu_k = -SdT + VdP, \tag{5}$$

where S and V are the entropy and the total volume of the mixture, respectively. From Eq. (5)

$$\bar{S}_k = -\left.\frac{\partial\mu_k}{\partial T}\right|_{\mathbf{n},P}, \qquad k = 1, \ ..., \ N, \tag{6}$$

where $\bar{S}_k$ is the partial molar entropy of component k. The partial molar enthalpy of component k can be expressed by

$$\bar{H}_k = \mu_k + T\bar{S}_k, \qquad k = 1, \ ..., \ N. \tag{7}$$

From Eqs. (6) and (7)

$$\bar{H}_k = \mu_k - T \left. \frac{\partial \mu_k}{\partial T} \right|_{\mathrm{n},P}, \qquad k = 1, \ ..., \ N. \tag{8}$$

Eqs. (1), (3) and 8 imply that

$$\sigma = -\frac{1}{T^2}\left(\vec{J}_q - \sum_{k=1}^{N} \frac{\bar{H}_k}{M_k}\vec{J}_k\right).\vec{\nabla}T - \frac{1}{T}\sum_{k=1}^{N} \vec{J}_k.\left(\vec{\nabla}_T \frac{\mu_k}{M_k} - \vec{F}\right); \tag{9}$$

$\sum_{k=1}^{N}(\bar{H}_k/M_k)\vec{J}_k$ is the transfer of heat due to diffusion. By introducing a new heat flux expression defined as

$$\vec{J}'_q = \vec{J}_q - \sum_{k=1}^{N} \frac{\bar{H}_k}{M_k}\vec{J}_k, \tag{10}$$

Eq. (9) becomes

$$\sigma = -\frac{1}{T^2}\vec{J}'_q.\vec{\nabla}T - \frac{1}{T}\sum_{k=1}^{N} \vec{J}_k\left(\vec{\nabla}_T \frac{\mu_k}{M_k} - \vec{F}\right). \tag{11}$$

From $\sum_{k=1}^{N} \vec{J}_k = 0$, one can write the entropy production strength as a function of the diffusion mass flux of only $N-1$ components. Eqs. (11) then reads

$$\sigma = -\frac{1}{T^2}\vec{J}'_q.\vec{\nabla}T - \frac{1}{T}\sum_{k=1}^{N-1} \vec{J}_k.\vec{\nabla}_T\left(\frac{\mu_k}{M_k} - \frac{\mu_N}{M_N}\right). \tag{12}$$

The phenomenological equations for heat flux and diffusion flux are, therefore, (see de Groot and Mazur [32])

$$\vec{J}'_q = -L'_{qq}\frac{\vec{\nabla}T}{T^2} - \frac{1}{T}\sum_{k=1}^{N-1} L'_{qk}\vec{\nabla}_T\left(\frac{\mu_k}{M_k} - \frac{\mu_N}{M_N}\right), \tag{13}$$

$$\vec{J}_i = -L'_{iq}\frac{\vec{\nabla}T}{T^2} - \frac{1}{T}\sum_{k=1}^{N-1} L_{ik}\vec{\nabla}_T\left(\frac{\mu_k}{M_k} - \frac{\mu_N}{M_N}\right), \ i = 1, \ ..., \ N-1, \tag{14}$$

respectively. In Eqs. (13) and (14), L'_{qq}, L_{qk}, L'_{iq}, and L_{ik} are the phenomenological coefficients (see Onsager [33, 34]). The fact that the entropy production strength σ is ≥ 0, puts conditions on the sign of some, and on the relationships between some other phenomenological coefficients. The main theme of this study is the diffusion flux and, therefore, we will focus on $\vec{J}_i$.

4 Diffusion mass flux expression

Let M, n and x_j denote the total molecular weight ($M = m/n$, where m is the total mass), the total number of moles ($n = \sum_{k=1}^{N} n_k$), and the mole fraction of component j ($x_j = n_j/n$), respectively. The Gibbs-Duhem expression given by Eq. (5) can then be written as

$$\vec{\nabla}_T \mu_N = \frac{1}{x_N}\left(\frac{M}{\rho}\vec{\nabla}P - \sum_{j=1}^{N-1} x_j \vec{\nabla}_T \mu_j\right). \tag{15}$$

Let $\mathbf{x_j}$ and $\mathbf{x}$ denote

$$\mathbf{x_j} \equiv (x_1, ..., x_{j-1}, x_{j+1}, ..., x_{N-1})$$

and

$$\mathbf{x} \equiv (x_1, ..., x_{N-1}),$$

respectively. Then $\vec{\nabla}_T \mu_k$ can be written as

$$\vec{\nabla}_T \mu_k = \sum_{j=1}^{N-1} \left.\frac{\partial \mu_k}{\partial x_j}\right|_{\mathbf{x_j},T,P} \vec{\nabla} x_j + \left.\frac{\partial \mu_k}{\partial P}\right|_{\mathbf{x},T} \vec{\nabla} P \qquad k = 1, \ ..., \ N. \tag{16}$$

$\vec{\nabla}_T (\mu_k/M_k - \mu_N/M_N)$ which appears in Eq. (14) can be expressed as (using Eqs. (15) and (16))

$$\vec{\nabla}_T \left(\frac{\mu_k}{M_k} - \frac{\mu_N}{M_N}\right) = \sum_{j=1}^{N-1}\left(\frac{x_j}{M_N x_N} + \frac{\delta_{jk}}{M_j}\right)\sum_{l=1}^{N-1}\left.\frac{\partial \mu_j}{\partial x_l}\right|_{\mathbf{x_l},T,P}\vec{\nabla} x_l$$
$$+\left[\sum_{j=1}^{N-1}\frac{x_j}{M_N x_N}\left.\frac{\partial \mu_j}{\partial P}\right|_{\mathbf{x},T} + \frac{1}{M_k}\left.\frac{\partial \mu_k}{\partial P}\right|_{\mathbf{x},T} - \frac{M}{M_N x_N \rho}\right]\vec{\nabla} P$$
$$k = 1, \ ..., \ N-1. \tag{17}$$

By combining Eqs. (14) and (17), the diffusion mass flux becomes

$$\vec{J}_i = -L'_{iq}\frac{\vec{\nabla} T}{T^2}$$
$$-\frac{1}{T}\sum_{k=1}^{N-1} L_{ik}\sum_{j=1}^{N-1}\left(\frac{x_j}{M_N x_N} + \frac{\delta_{jk}}{M_j}\right)\sum_{l=1}^{N-1}\left.\frac{\partial \mu_j}{\partial x_l}\right|_{\mathbf{x_l},T,P}\vec{\nabla} x_l$$
$$-\frac{1}{T}\sum_{k=1}^{N-1} L_{ik}\left[\frac{1}{M_k}\left.\frac{\partial \mu_k}{\partial P}\right|_{\mathbf{x},T} + \sum_{j=1}^{N-1}\frac{x_j}{M_N x_N}\left.\frac{\partial \mu_j}{\partial P}\right|_{\mathbf{x},T} - \frac{M}{M_N x_N \rho}\right]\vec{\nabla} P$$
$$i = 1, \ ..., \ N-1. \tag{18}$$

Terms $(\partial \mu_i/\partial x_j)_{\mathbf{x_j},T,P}$ and $(\partial \mu_i/\partial P)_{\mathbf{x_j},T}$ can be written as (see Firoozabadi [6])

$$\left.\frac{\partial \mu_i}{\partial x_j}\right|_{\mathbf{x_j},T,P} = RT\left.\frac{\partial \ln f_i}{\partial x_j}\right|_{\mathbf{x_j},T,P} \qquad i = 1, \ ..., \ N, \ j = 1, \ ..., \ N-1, \tag{19}$$

$$\left.\frac{\partial \mu_i}{\partial P}\right|_{\mathbf{x},T} = \bar{V}_i \qquad i = 1, \ ..., \ N, \tag{20}$$

where f_i, and $\bar{V}_i$ are the fugacity and the partial molar volume of component i, respectively; they can be obtained using an equation of state. The new form of Eq. (18) after using Eqs. (19) and (20) is

$$\begin{aligned}\vec{J}_i &= -\frac{MRL_{ii}}{M_i x_i M_N x_N}\left\{\frac{M_i x_i M_N x_N L'_{iq}}{MRL_{ii}}\frac{\vec{\nabla}T}{T^2}\right. \\ &+\frac{M_i x_i}{ML_{ii}}\sum_{k=1}^{N-1}L_{ik}\sum_{j=1}^{N-1}\frac{M_j x_j + M_N x_N \delta_{jk}}{M_j}\sum_{l=1}^{N-1}\left.\frac{\partial \ln f_j}{\partial x_l}\right|_{x_1,T,P}\vec{\nabla}x_l \\ &\left.+\frac{M_i x_i}{MRTL_{ii}}\sum_{k=1}^{N-1}L_{ik}\left[\sum_{j=1}^{N-1}x_j\bar{V}_j+\frac{M_N x_N}{M_k}\bar{V}_k-\frac{M}{\rho}\right]\vec{\nabla}P\right\} \\ &\qquad i=1,\ ...,\ N-1. \end{aligned} \tag{21}$$

Let

$$a_{iN} = \frac{M_i M_N}{M^2}, \qquad i=1,\ ...,\ N-1, \tag{22}$$

$$D_{iN} = \frac{M^3 RL_{ii}}{\rho M_i^2 M_N^2 x_i x_N}, \qquad i=1,\ ...,\ N-1, \tag{23}$$

$$k_{Ti} = \frac{M_i x_i M_N x_N L'_{iq}}{MRTL_{ii}} = \alpha_{Ti} x_i x_N, \qquad i=1,\ ...,\ N-1, \tag{24}$$

where k_{Ti} and α_{Ti} denote the thermal diffusion ratio and the thermal diffusion factor of component i, respectively. An important results of this work is the simple expression for the thermal diffusion factor of multicomponent mixtures given by Eq. 24 (that is, $k_{Ti} = \alpha_{Ti} x_i x_N$). For a binary mixture, the coefficient a_{12} is equal to $M_1 M_2/M^2$ and $k_{T1} = \alpha_{T1} x_1 (1-x_1)$. The expression $k_{Ti} = \alpha_{Ti} x_i (1-x_i)$ has been used erroneously in the literature [35, 36] to represent the thermal diffusion ratio in multicomponent mixtures. For an ideal binary mixture, the molecular diffusion coefficient reduces to $a_{12}D_{12}$; the nonideality could, however, be incorporated into $a_{12}D_{12}$ by multiplication with $\partial \ln f_1/\partial \ln x_1$; that is, the molecular diffusion coefficient is equal to $a_{12}D_{12}\,(\partial \ln f_1/\partial \ln x_1)$.

From Eqs. (21) to (24),

$$\begin{aligned}\vec{J}_i &= -\rho a_{iN} D_{iN}\left\{k_{Ti}\frac{\vec{\nabla}T}{T}+\right. \\ &\frac{M_i x_i}{ML_{ii}}\sum_{l=1}^{N-1}\sum_{k=1}^{N-1}L_{ik}\sum_{j=1}^{N-1}\frac{M_j x_j + M_N x_N \delta_{jk}}{M_j}\left.\frac{\partial \ln f_j}{\partial x_l}\right|_{x_1,T,P}\vec{\nabla}x_l + \\ &\left.\frac{M_i x_i}{MRTL_{ii}}\sum_{k=1}^{N-1}L_{ik}\left[\sum_{j=1}^{N-1}x_j\bar{V}_j+\frac{M_N x_N}{M_k}\bar{V}_k-\frac{M}{\rho}\right]\vec{\nabla}P\right\} \\ &\qquad i=1,\ ...,\ N-1. \end{aligned} \tag{25}$$

We define the following column vectors and matrices

$$\mathbf{J} \equiv [\mathbf{J}_i] \equiv \vec{J}_i \qquad i=1,\ ...,\ N-1,$$

$$
\begin{aligned}
\mathbf{L} &\equiv [\mathbf{L}_{ij}] \equiv L_{ij} \qquad i,j = 1,\ ...,\ N-1, \\
\mathbf{D} &\equiv [\mathbf{D}_{ij}] \equiv a_{iN} D_{iN} \delta_{ij} \qquad i,j = 1,\ ...,\ N-1, \\
\mathbf{M} &\equiv [\mathbf{M}_{ij}] \equiv \frac{M_i x_i}{M L_{ii}} \delta_{ij} \qquad i,j = 1,\ ...,\ N-1, \\
\mathbf{W} &\equiv [\mathbf{W}_{ij}] \equiv \frac{M_j x_j + M_N x_N \delta_{ij}}{M_j} \qquad i,j = 1,\ ...,\ N-1, \\
\mathbf{F} &\equiv [\mathbf{F}_{ij}] \equiv \left. \frac{\partial \ln f_i}{\partial x_j} \right|_{\mathbf{x_j},T,P} \qquad i,j = 1,\ ...,\ N-1, \\
\nabla \mathbf{x} &\equiv [\nabla \mathbf{x}_i] \equiv \vec{\nabla} x_i \qquad i = 1,\ ...,\ N-1, \\
\mathbf{K_T} &\equiv [\mathbf{K_{T}}_i] \equiv \frac{k_{Ti}}{T} \qquad i = 1,\ ...,\ N-1, \\
\mathbf{V} &\equiv [\mathbf{V}_i] \equiv \frac{1}{RT} \left[\sum_{j=1}^{N-1} x_j \bar{V}_j + \frac{M_N x_N}{M_i} \bar{V}_i - \frac{M}{\rho} \right] \qquad i = 1,\ ...,\ N-1,
\end{aligned}
$$

to write the expression for diffusion flux in the vector form

$$
\mathbf{J} = -\rho \left(\mathbf{D.M.L.W.F.} \nabla \mathbf{x} + \mathbf{D.K_T}\ \vec{\nabla} T + \mathbf{D.M.L.V}\ \vec{\nabla} P \right). \tag{26}
$$

Let

$$
\mathbf{D^M} = \mathbf{D.M.L.W.F}, \tag{27}
$$

$$
\mathbf{D^T} = \mathbf{D.K_T}, \tag{28}
$$

and

$$
\mathbf{D^P} = \mathbf{D.M.L.V}; \tag{29}
$$

then the expression for diffusion flux in a compact vector form is

$$
\mathbf{J} = -\rho \left(\mathbf{D^M}.\nabla \mathbf{x} + \mathbf{D^T}\ \vec{\nabla} T + \mathbf{D^P}\ \vec{\nabla} P \right). \tag{30}
$$

On the right side, the first term represents molecular diffusion, the second term represents thermal diffusion, and the third term represents pressure diffusion. The elements D_{il}^M, D_i^T and D_i^P are given by,

$$
D_{il}^M = a_{iN} D_{iN} \frac{M_i x_i}{M L_{ii}} \sum_{k=1}^{N-1} L_{ik} \sum_{j=1}^{N-1} \frac{M_j x_j + M_N x_N \delta_{jk}}{M_j} \left. \frac{\partial \ln f_j}{\partial x_l} \right|_{\mathbf{x_l},T,P}, \qquad i,l = 1,\ ...,\ N-1, \tag{31}
$$

$$
D_i^T = a_{iN} D_{iN} \frac{k_{Ti}}{T}, \qquad i = 1,\ ...,\ N-1, \tag{32}
$$

$$
D_i^P = a_{iN} D_{iN} \frac{M_i x_i}{MRT L_{ii}} \sum_{k=1}^{N-1} L_{ik} \left[\sum_{j=1}^{N-1} x_j \bar{V}_j + \frac{M_N x_N}{M_k} \bar{V}_k - \frac{M}{\rho} \right] \qquad i = 1,\ ...,\ N-1. \tag{33}
$$

The diffusion flux of component i, $i = 1, \ldots, N-1$, in a mixture of N components is a function of the composition gradients of $N-1$ components and of temperature and pressure gradients as well. The molecular diffusion coefficients D_{il}^M, $i,l = 1, \ldots, N-1$ (including D_{ii}^M) are functions of the phenomenological coefficients L_{ik}, $k = 1, \ldots, N-1$ and of the quantities $(\partial \ln f_j/\partial x_l)_{x_1,T,P}$, $l = 1, \ldots, N-1$, as well as the mole fractions. The molecular diffusion coefficient D_{ii}^M cannot be generally assumed to be the binary molecular diffusion coefficient measured in binary mixtures of components i and N. Likewise, the thermal diffusion ratio k_{Ti}, for component i is not the same in binary and ternary mixtures, even at the same pressure, temperature, and mole fraction of component i.

From Eq. (27) one can deduce the relation between the phenomenological coefficients and the molecular diffusion coefficients, which reads

$$\mathbf{L} = (\mathbf{D.M})^{-1}.\mathbf{D^M}.(\mathbf{W.F})^{-1}. \tag{34}$$

Using the relation $[\mathbf{A.B}]^T = \mathbf{B}^T.\mathbf{A}^T$ ($\mathbf{A}^T$ is the transpose of $\mathbf{A}$) and the fact that $\mathbf{L}$ is symmetric (the Onsager reciprocal relations [33, 34]) and that $\mathbf{D.M}$ is a diagonal matrix ($[\mathbf{D.M}]^T = \mathbf{D.M}$; $\mathbf{D}$ and $\mathbf{M}$ are both a diagonal matrix), one obtains the following relationship between $\mathbf{D^M}$ and $\mathbf{D^{M^T}}$

$$\mathbf{D^{M^T}} = (\mathbf{W.F})^T.\mathbf{D^M}.(\mathbf{W.F})^{-1}. \tag{35}$$

Eqs. (34) and (35) are valid provided $\det(\mathbf{W.F}) \neq 0$ which implies that $\det(\mathbf{W}) \neq 0$ and $\det(\mathbf{F}) \neq 0$ ($\det(\mathbf{W.F}) = \det(\mathbf{W}).\det(\mathbf{F})$). From Eqs. (34) and (35),

$$\mathbf{L.W.F} = \mathbf{D}^{-1}.\mathbf{M}^{-1}.\mathbf{D^M} \tag{36}$$

and

$$\mathbf{D^{M^T}.W.F} = (\mathbf{W.F})^T.\mathbf{D^M}, \tag{37}$$

respectively. One thus obtains the equations relating the phenomenological coefficients to the molecular diffusion coefficients (from Eq. (36))

$$\sum_{l=1}^{N-1}\sum_{k=1}^{N-1}\frac{M_k x_k + M_N x_N \delta_{lk}}{M_k}\left.\frac{\partial \ln f_k}{\partial x_j}\right|_{x_j,T,P} L_{li} = \frac{\rho M_N x_N}{R} D_{ij}^M, \quad i,j = 1, \ldots, N-1, \tag{38}$$

and those relating the diffusion coefficients to each other (from Eq. (37))

$$\sum_{l=1}^{N-1}\sum_{k=1}^{N-1}\frac{M_k x_k + M_N x_N \delta_{lk}}{M_k}\left.\frac{\partial \ln f_k}{\partial x_j}\right|_{x_j,T,P} D_{li}^M = \sum_{l=1}^{N-1}\sum_{k=1}^{N-1}\frac{M_k x_k + M_N x_N \delta_{lk}}{M_k}\left.\frac{\partial \ln f_k}{\partial x_i}\right|_{x_i,T,P} D_{lj}^M, \quad i,j = 1, \ldots, N-1. \tag{39}$$

The $(N-1)^2$ relations appearing in Eq. (39) are not all independent. For $i = j$ the two members of the equality are identical. This means that the number of independent

relations reduces to $(N-1)^2-(N-1)$. Furthermore, by replacing i with j and j with i in Eq. (39), one obtains the same equations. Thus, the number of independent equations relating the molecular diffusion coefficients reduces to $\left[(N-1)^2-(N-1)\right]/2$, and then the number of independent molecular diffusion coefficients reduces to $(N-1)^2-\left[(N-1)^2-(N-1)\right]/2 = N(N-1)/2$.

4.1 Example I : binary mixtures

For binary mixtures, Eq. (30) reduces to (after substitution $a_{12} = M_1M_2/M^2$)

$$\vec{J}_1 = -\rho D_{12}\frac{M_1M_2}{M^2}\left[\left.\frac{\partial \ln f_1}{\partial \ln x_1}\right|_{P,\,T}\vec{\nabla}x_1 + \frac{x_1}{RT}\left(\bar{V}_1 - \frac{M_1}{\rho}\right)\vec{\nabla}P + \frac{k_{1T}}{T}\vec{\nabla}T\right]. \tag{40}$$

The above equation appears in Bird *et al.* [37].

4.2 Example II : ternary mixtures

We focus now on a ternary mixture since it is the simplest mixture for which the Onsager reciprocal relation (that is, Eq. (39)) can be applied. Multicomponent mixtures with more than three components are logical extensions of a ternary mixture, differing primarily in algebraic complexity. Let

$$c_1 = \frac{M_1x_1 + M_3x_3}{M_1}f_{12} + x_2f_{22}, \tag{41}$$

$$c_2 = x_1f_{12} + \frac{M_2x_2 + M_3x_3}{M_2}f_{22}, \tag{42}$$

$$c_3 = \frac{M_1x_1 + M_3x_3}{M_1}f_{11} + x_2f_{21}, \tag{43}$$

$$c_4 = x_1f_{11} + \frac{M_2x_2 + M_3x_3}{M_2}f_{21}, \tag{44}$$

where $f_{ij} \equiv (\partial \ln f_i/\partial x_j)_{x_j,T,P}$. For ternary mixtures, Eqs. (31-33) then read ($L_{ii} > 0$; this results from the fact that the entropy production $\sigma \geq 0$, see De Groot and Mazur [32]).

$$D_{11}^M = a_{13}D_{13}\frac{M_1x_1}{M}\left(c_3 + c_4\frac{L_{12}}{L_{11}}\right), \tag{45}$$

$$D_{12}^M = a_{13}D_{13}\frac{M_1x_1}{M}\left(c_1 + c_2\frac{L_{12}}{L_{11}}\right), \tag{46}$$

$$D_{21}^M = a_{23}D_{23}\frac{M_2x_2}{M}\left(c_4 + c_3\frac{L_{21}}{L_{22}}\right), \tag{47}$$

$$D_{22}^M = a_{23}D_{23}\frac{M_2x_2}{M}\left(c_2 + c_1\frac{L_{21}}{L_{22}}\right), \tag{48}$$

$$D_1^T = a_{13}D_{13}\frac{k_{T1}}{T}, \tag{49}$$

$$D_2^T = a_{23}D_{23}\frac{k_{T2}}{T}, \tag{50}$$

$$D_1^P = a_{13}D_{13}\frac{M_1x_1}{MRT}\left[\frac{M_1x_1+M_3x_3}{M_1}\bar{V}_1+x_2\bar{V}_2-\frac{M}{\rho}+\left(\frac{M_2x_2+M_3x_3}{M_2}\bar{V}_2+x_1\bar{V}_1-\frac{M}{\rho}\right)\frac{L_{12}}{L_{11}}\right], \quad (51)$$

$$D_2^P = a_{23}D_{23}\frac{M_2x_2}{MRT}\left[\frac{M_2x_2+M_3x_3}{M_2}\bar{V}_2+x_1\bar{V}_1-\frac{M}{\rho}+\left(\frac{M_1x_1+M_3x_3}{M_1}\bar{V}_1+x_2\bar{V}_2-\frac{M}{\rho}\right)\frac{L_{21}}{L_{22}}\right]. \quad (52)$$

Eqs. (38) and (39) imply

$$\left(\frac{M_1x_1+M_3x_3}{M_1}f_{1j}+x_2f_{2j}\right)L_{1i}+\left(x_1f_{1j}+\frac{M_2x_2+M_3x_3}{M_2}f_{2j}\right)L_{2i} = \frac{\rho M_N x_N}{R}D_{ij}, \quad i,j=1,2, \quad (53)$$

and

$$\left(\frac{M_1x_1+M_3x_3}{M_1}f_{1j}+x_2f_{2j}\right)D_{1i}^M+\left(x_1f_{1j}+\frac{M_2x_2+M_3x_3}{M_2}f_{2j}\right)D_{2i}^M = \left(\frac{M_1x_1+M_3x_3}{M_1}f_{1i}+x_2f_{2i}\right)D_{1j}^M+\left(x_1f_{1i}+\frac{M_2x_2+M_3x_3}{M_2}f_{2i}\right)D_{2j}^M, \quad i,j=1,2, \quad (54)$$

respectively. From Eq. (53),

$$c_3L_{11}+c_4L_{21} = \frac{\rho M_3x_3}{R}D_{11}^M, \quad (55)$$

$$c_1L_{11}+c_2L_{21} = \frac{\rho M_3x_3}{R}D_{12}^M, \quad (56)$$

$$c_3L_{12}+c_4L_{22} = \frac{\rho M_3x_3}{R}D_{21}^M, \quad (57)$$

$$c_1L_{12}+c_2L_{22} = \frac{\rho M_3x_3}{R}D_{22}^M, \quad (58)$$

Provided that $\det(\mathbf{W}) \neq 0$ and $\det(\mathbf{F}) \neq 0$, one obtains

$$L_{11} = \frac{\rho M_3x_3}{R\,(c_2c_3-c_1c_4)}\left(c_2D_{11}^M-c_4D_{12}^M\right), \quad (59)$$

$$L_{21} = \frac{-\rho M_3x_3}{R\,(c_2c_3-c_1c_4)}\left(c_1D_{11}^M-c_3D_{12}^M\right), \quad (60)$$

$$L_{12} = \frac{\rho M_3x_3}{R\,(c_2c_3-c_1c_4)}\left(c_2D_{21}^M-c_4D_{22}^M\right), \quad (61)$$

$$L_{22} = \frac{-\rho M_3x_3}{R\,(c_2c_3-c_1c_4)}\left(c_1D_{21}^M-c_3D_{22}^M\right), \quad (62)$$

($c_2c_3-c_1c_4 = \det(\mathbf{W})\det(\mathbf{F})$). For $i=j$ the two members of Eq. (54) are identical. Furthermore, by repalcing i by j and j by i in Eq. (54), one obtains two identical equations. Eq. (54) thus reads

$$c_1D_{11}^M+c_2D_{21}^M = c_3D_{12}^M+c_4D_{22}^M. \quad (63)$$

Similar relations between the molecular diffusion coefficients have been reported by de Groot and Mazur [32] and Haase [7]. Eqs. (60), (61) and (63) are not independent. By combining Eqs. (60) and (63) one obtains Eqs. (61) (that is, $L_{12} = L_{21}$).

5 Critical point

Let us present features of multicomponent diffusion at the critical point. We start by presenting the problem in the general case of N components. Then, we discuss in more detail the case of binary mixtures. One of two criticality conditions reads [6, 8] $\det(\mathbf{F}) = 0$; which implies

$$\det\left(\mathbf{D}^{\mathrm{M}}\right) = 0 \tag{64}$$

at the critical point. Eq. (64) provides the well known result that in a binary mixture the molecular diffusion coefficient D_{11}^{M} vanishes and that for a mixture of $N \geq 3$, and that the diffusion coefficient determinant vanishes at the critical point. From Eq. (64),

$$\mathrm{rank}\left(\mathbf{D}^{\mathrm{M}}\right) \leq N-2. \tag{65}$$

Let us discuss the case of equality in Eq. (65) (the same reasoning applies in the general case); at isothermal and isobaric conditions, one has only $N-2$ independent diffusion mass fluxes: $\vec{J}_i$, $i = 1, \ldots, N-2$; $\vec{J}_{N-1}$ and $\vec{J}_N$ are linear combinations of the $N-2$ remaining independent diffusion mass fluxes. This implies that there exist constants $\alpha_1, \ldots, \alpha_{N-2}$ such that

$$D_{(N-1)i}^{M} = \sum_{j=1}^{N-2} \alpha_j D_{ji}^{M}, \qquad i = 1, \ldots, N-1. \tag{66}$$

Therefore, at isothermal and isobaric conditions

$$\begin{aligned} \vec{J}_{N-1} &= \sum_{i=1}^{N-1} D_{(N-1)i}^{M} \nabla x_i \\ &= \sum_{i=1}^{N-1} \sum_{j=1}^{N-2} \alpha_j D_{ji}^{M} \nabla x_i \\ &= \sum_{j=1}^{N-2} \alpha_j \vec{J}_j. \end{aligned} \tag{67}$$

Let $\mathbf{D_i} = \left(D_{i1}^{M}, \ldots, D_{i(N-2)}^{M}\right)$, $i = 1, \ldots, N-2$; and $\mathbf{A} = (\alpha_1, \ldots, \alpha_{N-2})$. Eq. (66) reads

$$D_{(N-1)i}^{M} = \mathbf{A} \,.\, \mathbf{D_i^M}, \qquad i = 1, \ldots, N-1. \tag{68}$$

Let $\mathbf{D_{N-1}} = \left(D_{(N-1)1}^{M}, \ldots, D_{(N-1)(N-2)}^{M}\right)$, and, $\mathbf{D_1^M} = \left[D_{ij}^{M}\right]$, $i, j = 1, \ldots, N-2$. $\det\left(\mathbf{D_1^M}\right) \neq 0$ since $\mathrm{rank}\left(\mathbf{D_1^M}\right) = N-2$. One thus obtains

$$\mathbf{A} = \left(\mathbf{D_1^M}\right)^{-1} .\mathbf{D_{N-1}} \tag{69}$$

which allows the determination of A knowing the molecular diffusion coefficients. For $i = N-1$, Eq. (68) reads

$$D^M_{(N-1)(N-1)} \;=\; \mathbf{A}\,.\,\mathbf{D_{N-1}}. \tag{70}$$

Eqs. (69) and (70) imply

$$D^M_{(N-1)(N-1)} \;=\; \left[\left(\mathbf{D_1^M}\right)^{-1}.\mathbf{D_{N-1}}\right]\,.\,\mathbf{D_{N-1}}; \tag{71}$$

at the critical point, in addition to the results from the reciprocal relations in Eq. (39), there exists one more relationship between the diffusion coefficients. This means that, for a ternary mixture for example, two molecular diffusion coefficients, say the mutual diffusion coefficients, describe molecular diffusion flux. For ternary mixtures, $(D^M_{21}D^M_{22} - D^M_{12}D^M_{21})$ vanishes at the critical point. Experimental support can be drawn from the work of Vitagliano *et al.* [38] for a water-chloroform-acetic acid ternary mixture. Analysis of diffusion in ternary mixtures at the critical point has also been made by Taylor and Krishnan [8]. The authors show that the criticality condition establishes a relation between the molecular diffusion coefficients. The combination of the criticality and the Onsager reciprocal relation implies that, for a ternary mixture at the critical point, only two diffusion coefficients are independent.

If we consider a multicomponent mixture at isothermal conditions and neglect the pressure gradient, at the steady state one obtains $\mathbf{D^M}.\nabla\mathbf{x} = \mathbf{0}$, which implies $\nabla\mathbf{x} = \mathbf{0}$ unless $\det\left(\mathbf{D^M}\right) = 0$. This means that at isothermal and isobaric conditions at the critical point, the steady state may be reached with compositional gradients in the system. However, away from the critical point the mixture is, in principle, homogeneous. At isothermal and non-isobaric conditions at steady state, Eq. (30) reduces to

$$\mathbf{D^M}.\nabla\mathbf{x} + \mathbf{D^P}\vec{\nabla}P \;=\; 0. \tag{72}$$

The solution of this equation can be written as

$$\vec{\nabla}x_i \;=\; -\vec{\nabla}P\frac{\det\left(\mathbf{B}_i\right)}{\det\left(\mathbf{D^M}\right)}. \tag{73}$$

where $\mathbf{B}_i$, $i = 1, \ldots, N-1$ is the matrix $\mathbf{D^M}$ with column i replaced by column vector $\mathbf{D^P}$. $\mathbf{D^P}\vec{\nabla}P$ is, in principle, different from zero at the critical point; so is $\det\left(\mathbf{B}_i\right)$. From Eqs. (64) and (73), one may deduce that $\nabla\mathbf{x}$ reaches infinity at the critical point. The mole fraction plot vs. the vertical coordinate for each component has an inflection point at critical conditions. The same reasoning applies when $\vec{\nabla}P$ and $\vec{\nabla}T$ are both different from zero. This is discussed in more detail, for binary mixtures, in the following subsection.

5.1 Binary mixtures

One of the two criteria of criticality reduces to $(\partial \ln f_1/\partial \ln x_1)_{T,P} = 0$ for binary mixtures. The coefficient $D_{12} \;=\; (M^3RL_{11})\,/\,(\rho M_1^2M_2^2x_1x_2)$ has, generally, a finite value at the

critical point [11]. The molecular diffusion coefficient $D_{11}^M = a_{12} D_{12} \left(\partial \ln f_1 / \partial \ln x_1\right)_{T,P}$ thus vanishes at the critical point which has been established by various authors; it decreases asymptotically when one approaches the critical state (see, for example, Haase [7], Taylor and Krishna [8], Ackerson and Hanely [10], Kiselev and Huber [15], Luettmer-Strathmann and Sengers [18], Cheng *et al.* [20] and Sakonidou *et al.* [21]). With regard to the thermal diffusion coefficient, it is well established, using the mode-mode coupling theory that this coefficient has a finite value at the critical point [24, 25, 17]. In the following, we discuss the behavior of diffusion in a binary mixture at the critical point for 1) isothermal and non-isobaric, and 2) non-isothermal and isobaric conditions.

For a binary mixture at isothermal and isobaric conditions, Eq. (40) at the steady state reduces to

$$\left.\frac{\partial \ln f_1}{\partial \ln x_1}\right|_{P,\,T} \vec{\nabla} x_1 \;=\; 0 \tag{74}$$

which is valid for any value of the composition gradient $\vec{\nabla} x_1$.

Let us now consider a binary mixture at isothermal and non-isobaric conditions. It should be mentioned that the contribution of the pressure gradient in the diffusion mass flux has often been neglected in the studies treating diffusion in multicomponent systems. At steady state, Eq. (40) reduces to

$$\left.\frac{\partial \ln f_1}{\partial \ln x_1}\right|_{P,\,T} \vec{\nabla} x_1 + \frac{x_1}{RT}\left(\bar{V}_1 - \frac{M_1}{\rho}\right)\vec{\nabla} P \;=\; 0. \tag{75}$$

Since $\vec{\nabla} P \neq 0$ (say from gravity), and since $\left(\bar{V}_1 - M_1/\rho\right)$ has generally a finite value different from zero, $\left(\partial \ln f_1 / \partial \ln x_1\right)_{T,P} \vec{\nabla} x_1$ must have a finite value. The fact that $\left(\partial \ln f_1 / \partial \ln x_1\right)_{T,P}$ vanishes at the critical point, implies that $\vec{\nabla} x_1$ should be infinity at this point. Fig. 1 sketches the compositional variation in the critical region in a one dimensional vertical medium with a critical point at height z^0. Although $\left(\partial \ln f_1 / \partial \ln x_1\right)_{T,P} \to 0$ and $\vec{\nabla} x_1 \to \infty$ when one approaches the critical point, their product is a finite value.

The same reasoning can be applied at non-isothermal and isobaric conditions. In that case, at the steady state, Eq. (40) reduces to

$$\left.\frac{\partial \ln f_1}{\partial \ln x_1}\right|_{P,\,T} \vec{\nabla} x_1 + \frac{k_{1T}}{T}\vec{\nabla} T \;=\; 0. \tag{76}$$

The product $\left(\partial \ln f_1 / \partial \ln x_1\right)_{T,P} \vec{\nabla} x_1$ can be finite and non-zero at the critical point where $\left(\partial \ln f_1 / \partial \ln x_1\right)_{T,P} = 0$; this may occur when $\vec{\nabla} x_1 \to \infty$. Therefore, at the critical point for a finite temperature gradient, k_{1T} may also have a finite value. Note that this analysis is provided on very simple terms. Next, we discuss in more detail the finiteness of the thermal diffusion ratio k_{1T} in view of some results presented in the literature [12, 13, 14, 15, 16, 17, 18, 19, 20, 21, 22, 23, 24, 25, 26, 27, 28].

Away from the critical point, the transport properties of a mixtures vary generally slowly with temperature and composition. However, when the critical point is approached,

the transport properties exhibit singular behavior. The diffusion flux for a binary mixture can be written as

$$\vec{J}_1 = \alpha \vec{\nabla} \mu - \beta \vec{\nabla} T, \tag{77}$$

where $\mu = \mu_1/M_1 - \mu_2/M_2$. Eq. (77) can be readily obtained from Eq. (14) (for $N = 2$) by replacing L_{11} and L'_{1q} by $-T\alpha$ and $T^2\left(\beta - \alpha\left(\partial\mu/\partial T\right)_{x_1,P}\right)$, respectively. In the critical region, coefficients α and β can be separated into background values and critical enhancements [24, 25]

$$\alpha = \alpha_b - \delta\alpha = \alpha + \frac{k_B T \rho}{6\pi\tilde{\eta}\xi}\left(\frac{\partial x_1}{\partial \mu}\right)_{P,T}, \tag{78}$$

$$\beta = \beta_b + \delta\beta = \beta + \frac{k_B T \rho}{6\pi\tilde{\eta}\xi}\left(\frac{\partial x_1}{\partial T}\right)_{P,\mu}, \tag{79}$$

where k_B, ξ, and $\tilde{\eta}$ are the Boltzmann constant, the correlation length divergent at the critical point [17], and the shear viscosity, respectively; The subscript b denotes the part of the transport coefficient which is not affected by criticality (the so-called background value); $\delta\alpha$ and $\delta\beta$ are the critical enhancements of α and β, respectively. Away from the critical point, the transport coefficients are described by their background values. The behavior of the transport properties in the region close to the critical point, has been investigated by extending the concept of the critical point universality [17] to binary mixtures (generalized isomorphism approach) [12, 14, 15, 17, 19, 20]. In the intermediate region where the transport properties can not be described either by their background values or by the the generalized isomorphism approach, the transport properties are investigated using a crossover approach [13, 15, 16, 18, 21]. Mode-mode coupling calculations have been performed by Gorodetski [23] and Mistura [24, 25] to investigate the transport properties in the critical region (see the summary in Anisimov *et al.* [17]). From Eqs. (77), (78) and (79) one obtains

$$\delta\alpha = -\left(\frac{\partial \mu}{\partial T}\right)_{P,\mu} \delta\beta. \tag{80}$$

It is shown [17, 23, 24, 25] that α and β diverge at the critical point. Furthermore, those coefficients have the same power law when approaching the critical point [17]. The coefficients α and β are not directly measurable. To relate those coefficients to some experimentally accessible properties (the diffusion coefficients), the diffusion flux $\vec{J}_1$ has been expressed in terms of the diffusion coefficients as [17, 25]

$$\vec{J}_1 = -\rho D_{11}^M \left(\vec{\nabla} x_1 + k_{1T}^* \frac{\vec{\nabla} T}{T}\right). \tag{81}$$

where D_{11}^M is the molecular diffusion coefficient and k_{1T}^* is the thermal diffusion ratio (as defined by some authors [18, 21]); $D_1^T = D_{11}^M k_{1T}^*$ is the thermal diffusion coefficient. α, β,

D_{11}^M, and k_{1T}^* are related by

$$D_{11}^M = \frac{\alpha}{\rho}\left(\frac{\partial \mu}{\partial x_1}\right)_{P,T}, \tag{82}$$

$$k_{1T}^* D_{11}^M = \frac{T}{\rho}\left[\alpha\left(\frac{\partial \mu}{\partial T}\right)_{P,x_1} + \beta\right]. \tag{83}$$

It should be mentioned that Eq. (81) for the diffusion flux can not be extended to multicomponent non-ideal mixtures.

Eqs. (78) and (82) imply that the diffusion coefficient D_{11}^M vanishes at the critical point as ξ^{-1}. The thermal diffusion coefficient ,D_1^T, however, has a finite value at the critical point since the critical enhancments compensate each other according to Eq. (83); the coefficient $k_{1T}^* = D_1^T/D_{11}^M$, therefore, diverges as ξ towards the critical point. This has been supported by experimental data by Haase *et al.* [26].

Haase *et al.* [26], from experimental data, claim that the thermal diffusion factor α_T and the related quantities approach infinity in the critical state for binary mixtures. However, the expression these authors use for the diffusion mass flux is not appropriate for non-ideal systems. At steady state, by representing the gradients of temperature and mole fraction by ΔT and Δx_1, respectively, Haase *et al.* provide the following relation, from which they calculate the thermal diffusion factor using the experimental data

$$\Delta x_1 = \alpha_T x_1 (1 - x_1)\frac{\Delta T}{T}. \tag{84}$$

This expression ignores the thermodynamic factor $(\partial \ln f_1/\partial \ln x_1)_{T,P}$ which approaches zero when one approaches the critical state. Thus, the coefficient α_T used by Haase *et al.* [26] is in reality the thermal diffusion factor divided by the thermodynamic factor.

In their investigation of the crossover behavior of the transport properties in the critical region, Luettmer-Strathmann and Sengers [18] and Sakonidou *et al.* [21] used Eq. (81) to express the diffusion flux. Eq. (81) can be also written in the following form

$$\vec{J}_1 = -\rho a_{12} D_{12}\left(\left.\frac{\partial \ln f_1}{\partial \ln x_1}\right|_{P,\,T}\vec{\nabla} x_1 + \left.\frac{\partial \ln f_1}{\partial \ln x_1}\right|_{P,\,T} k_{1T}^* \frac{\vec{\nabla} T}{T}\right). \tag{85}$$

From the comparison of Eq. (85) and Eq. (40) (for isobaric condition), one deduces that the appropriate expression for the thermal diffusion ratio is $k_{1T} = (\partial \ln f_1/\partial \ln x_1)_{T,P}\, k_{1T}^*$. Luettmer-Strathmann and Sengers [18] and Sakonidou *et al.* [21] used the mode-mode coupling analysis to calculate the molecular diffusion and the thermal diffusion coefficient by fitting the crossover equation of the thermal conductivity to thermal conductivity data in the vicinity of the critical point. These authors concluded that $D_{11}^M k_{1T}^*$ reaches a finite value at the critical point [18, 21]. Since D_{12} has generally finite value at the critical point, the thermal diffusion ratio, k_{1T} should also have a finite value. Luettmer-Strathmann and Sengers [18] conclude that D_{11}^M vanishes at the critical point and that k_{1T}^*, on the other hand, diverges at the critical point. This conclusion is in agreement with our simple analysis of Eq. (76)

One could summarize then that at the critical point, 1) the molecular diffusion coefficient vanishes, 2) the thermal diffusion ratio reaches a finite value, and 3) the mole fraction gradient reaches infinity with either temperature or pressure gradient or both; that is, the mole fraction has an inflexion point when plotted vs. depth.

6 Concluding Remark

A general formalism is provided to describe multicomponent molecular, pressure, and thermal diffusion flux for non-ideal mixtures. The treatment is within the framework of thermodynamics of irreversible processes. The formalism allows us to evaluate thermal diffusion factors for ternary and higher mixtures which has not been attempted in the past (Firoozabadi *et al.* [39]). The general expression also allows the determination of various diffusion processes at the critical point. One main conclusion of this study is that molecular diffusion is finite at the critical point for non-isothermal, and for isothermal, non-isobaric conditions.

References

[1] J. S. Turner, Ann. Rev. Fluid. Mech. **17**, 11 (1985).

[2] J. S. Turner, *Buoyancy Effects in Fluids*, (Cambridge Univ. Press, 1973).

[3] J. S. Turner, Ann. Rev. Fluid. Mech. **6**, 37 (1974).

[4] H. E. Huppert and J. S. Turner, J. Fluid Mech. **106**, 299 (1981).

[5] W. R. Wilcox, Prog. Crystal Growth and Charact., **26**, 153 (1993).

[6] A. Firoozabadi, *Thermodynamics of Hydrocarbon Reservoirs*, (McGraw-Hill, New York, 1998).

[7] R. Haase, *Thermodynamics of Irreversible Processes*, (Dover Edition, New York, 1990).

[8] R. Taylor and R. Krishna, *Multicomponent Mass Transfer*, (John Wiley and Sons, 1993).

[9] E. L. Cussler, *Multicomponent Diffusion*, (Elsevier Sci. Pub. Co., 1976).

[10] B. J. Ackerson and H. J. M. Hanely, J. Chem. Phys. **73**, 3568 (1980).

[11] A. S. Myerson and D. Senol, AIChE J. **30**, 1004 (1984).

[12] P.C. Hohenberg and B.I. Halperin, Rev. Mod. Phys. **49**, 435 (1977).

[13] J.V. Sengers and J.M.H. Levelt Sengers, Ann. Rev. Phys. Chem. **37**, 189 (1986).

[14] M.A Anisimov and S.B. Kiselev, Int. J. Therm. **13**, 873 (1992).

[15] S.B. Kiselev and V.D. Kulikov, Int. J. Therm. **15**, 283 (1994).

[16] J. Luettmer-Strathmann and J. V. Sengers, Int. J. Therm. **15**, 1241 (1994).

[17] M.A Anisimov, E.E. Gorodetskii, V.D. Kulikov, A.A. Povodyrev and J.V. Sengers, Physica A. **220**, 277 (1995).

[18] J. Luettmer-Strathmann and J. V. Sengers, J. Chem. Phys. **104 (8)**, 3026 (1996).

[19] S.B. Kiselev, Fluid Phase Equilibria **128**, 1 (1997).

[20] H. Cheng, M. Anisimov and J. V. Sengers, Fluid Phase Equilibria **128**, 67 (1997).

[21] E. P. Sakonidou, H. R. van der Berg, C. A. Ten Seldam and J. V. Sengers, J. Chem. Phys. **109**, 717 (1998).

[22] S.B. Kiselev and M.L. Huber, Fluid Phase Equilibria **142**, 253 (1998).

[23] E.F. Gorodetski and M.S. Giterman, Sov. Phys., JETP **30**, 348 (1970).

[24] L. Mistura, Nuevo Smento B **12**, 35 (1972).

[25] L. Mistura, J. Chem. Phy. **62**, 4571 (1975).

[26] R. Haase, K. H. Ducker, H. Buchner and J. Schwinum, Zeitschrift fur physikalishe chemie **186**, 113 (1994).

[27] R. Haase, H. W. Borgmann, K. H. Duker and W. L. Lee, Z. Naturforsch, Teil A. **26**, 1224 (1971).

[28] W. M. Rutherford and J. G. Roof, J. Phys. Chem. **63**, 1506 (1959).

[29] K. Ghorayeb and A. Firoozabadi, SPE paper 51932, also submitted to Society of Petroleum Engineers Journal, January 1999.

[30] J. P. Larre, K. K. Platten and G. Chavepeyer, Int. J. Heat Mass Trans. **40**, 545 (1997).

[31] R. Krupiczka and A. Rotkegel, Chem. Eng. Sci. **52**, 1007 (1997).

[32] S. R. de Groot and P. Mazur, *Non-Equilibrium Thermodynamics*, (Dover Edition, New York, 1984).

[33] L. Onsager, Phys. Rev. **37**, 405 (1931).

[34] L. Onsager, Phys. Rev. **38**, 2265 (1931).

[35] L. J. T. M. Kempers, J. Chem. Phys. **90**, 6541 (1989).

[36] S. Van Vaerenbergh and J. C. Legros, Entropie **198/199**, 77 (1996).

[37] R. B. Bird, W. E. Stewart and E. N. Lightfoot, *Transport Phenomena*, (John Wiley and Sons, New York, 1960).

[38] V. Vitagliona, R. Sartoria, S. Scala and D. Spaduzzi, J. Sol. Chem. **7**, 605 (1978).

[39] A. Firoozabadi, K. Ghorayeb and K. Shukla, submitted to J. Chem. Phys., April 1999.

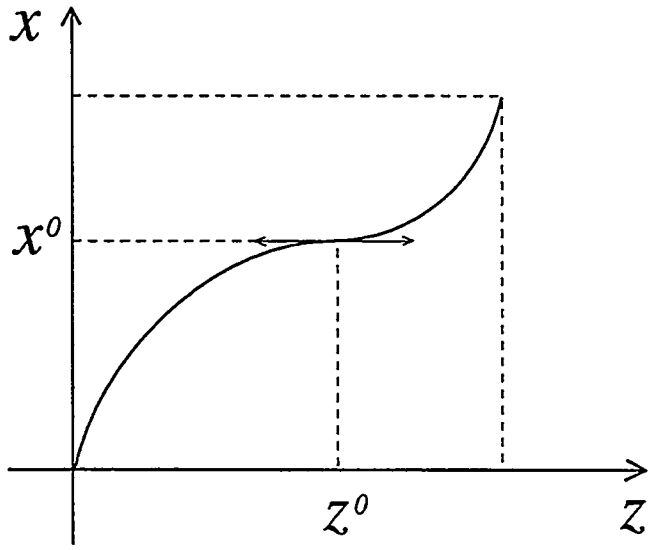

Figure 1: Sketch of the composition vs. height for a binary mixture in an isothermal non isobaric process in the critical region.

Part II - Theoretical Model of Thermal Diffusion Factors in Multicomponent Mixtures

ABBAS FIROOZABADI, KASSEM GHORAYEB
and KESHAWA SHUKLA

1 Summary

Unlike molecular diffusion, where expressions are available for molecular diffusion coefficients in multicomponent mixtures, there are surprisingly neither measured thermal diffusion coefficients, nor theoretical framework for the estimation of thermal diffusion coefficients in non-ideal multicomponent mixtures. In this work, we derive a theoretical model for thermal diffusion coefficients in ideal and non-ideal multicomponent mixtures (number of components ≥ 3). Our model is based on the thermodynamics of irreversible processes and the molecular kinetic approach incorporating the explicit effects of non-equilibrium properties, such as the net heat of transport and molecular diffusion coefficients, and of the equilibrium properties of the mixture. The equilibrium properties of the mixture are determined from the Peng-Robinson equation of state. The net heat of transport is expressed in terms of equilibrium properties and viscosity. An interesting feature of the proposed model for the estimation of thermal diffusion coefficients in non-ideal multicomponent mixtures is the dependency on molecular diffusion coefficients. For binary mixtures, such a dependency does not occur. The model successfully describes thermal diffusion factors of binary mixtures for which experimental data are available, even those in extreme non-ideal conditions and close to the critical point. Since experimental data for thermal diffusion factors in multicomponent hydrocarbon mixtures (number of components ≥ 3) are not available, we are unable to test the accuracy of our model in multicomponent mixtures at this moment. However, the model has been found to be successful in predicting the experimental data of spatial variation of composition in a ternary mixture of $nC_{24}/nC_{16}/nC_{12}$, providing an indirect verification. The model is used for predicting the thermal diffusion factors in a six-component mixture of $C_1/C_3/nC_5/nC_{10}/nC_{16}/C_2$. The results show significant dependency of the thermal diffusion factors on the distance to the critical point. Another interesting feature of the model is that it demonstrates for the first time that there is no need to adopt a sign convention for thermal diffusion coefficients in binary and higher mixtures. From thermodynamic stability analysis, it is shown that when the thermal diffusion coefficient is positive, the component should go to the cold region in a binary mixture.

2 Introduction

Thermal diffusion or the Soret effect is important for the study of compositional variation in hydrocarbon reservoirs [1] and for separating isotopic mixtures [2], among others. In this process, in a convection-free mixture a temperature gradient develops the corresponding composition gradient of the mixture constituents. Previous studies indicate that thermal diffusion factors are sensitive to the details of intermolecular interactions, size and shape of the molecules, and their magnitude are governed by thermodynamic conditions [3, 4]. In many mixtures, accurate measurement of thermal diffusion factors is difficult to perform because of the obscuring effect of natural convection. Experiments in microgravity (10^{-5} of normal gravity g) have been proposed to alleviate the difficulties with convection [5]. Thermal diffusion factor data are sparse; they are available for some binary mixtures only [6, 7, 8, 9, 10, 11, 12, 13, 14, 15, 16, 17]. Recently, Zhang *et al.* [18] have presented a detailed analysis of the different methods for measuring thermal diffusion factors. Again, only binary mixtures have been considered.

Several theoretical approaches have been suggested in the literature to describe thermal diffusion factors in binary mixtures with varying degrees of success. Important among them are the models based on the kinetic theory of irreversible thermodynamics [19], the phenomenological theory of irreversible thermodynamics [20], and the maximization of the partition function of two idealized bulbs [21]. These models were found to describe thermal diffusion factors in some binary hydrocarbon mixtures only qualitatively because of the several approximations involved in their formulations and calculations. In fact, thermal diffusion factors from the above models incorporate only equilibrium properties and ignore the dependence on the non-equilibrium properties. It is known that the thermal diffusion factor is a non-equilibrium property, and its proper formulation requires the knowledge of both the equilibrium and non-equilibrium properties.

Recently, Shukla and Firoozabadi [22] developed a new theoretical model for the prediction of thermal diffusion factors in binary hydrocarbon mixtures using irreversible thermodynamics. Unlike the previous models, their work incorporates both equilibrium and non-equilibrium properties of mixtures. In that model, equilibrium properties are obtained from the volume translated Peng-Robinson equation of state, while non-equilibrium properties are determined using the energy of viscous flow estimated from viscosity data. The Shukla and Firoozabadi [22] model has been applied for the prediction of binary thermal diffusion factors of several mixtures consisting of hydrocarbon species (C_1/C_3, C_1/C_4, C_7/C_{12}, C_7/C_{16}), non-hydrocarbon species (Ar/CO_2, N_2/CO_2, H_2/N_2, H_2/CO_2), and hydrocarbon and non-hydrocarbon species (C_1/CO_2), for which experimental data were available. Comparisons of theoretical results with experimental data showed a good performance of the model, except in the near-critical region (in the critical region due to factoring the term $(\partial \ln f_1/\partial \ln x_1)_{P,T}$ out in accord with the practice of the experimentalists, the model should not be applied in the form presented in Ref. [23]). The model was also found to offer a significant improvement over the earlier models [19, 20] and was able to predict the sign of thermal diffusion factors of the above mixtures to be consistent with experiment.

The variation of thermal diffusion factors in three- and multicomponent non-ideal mixtures may significantly differ from those in binary mixtures. For example, experimental

data of thermal diffusion factors in binary mixtures C_1/C_2, C_1/C_3 and C_1/C_4 show that methane segregates toward the hot region [23, 24, 25], leading to a negative value of the thermal diffusion factor of the first component, C_1 (we will later show that there is no need to adopt a sign convention for thermal diffusion factors). In contrast, in hydrocarbon reservoirs more methane has often been seen in the cold region (top of the reservoir) [26, 27] (experimental data for thermal diffusion factors in multicomponent mixtures are not available). These results show that the segregation of methane in a non-ideal mixture with more than two components for a non-isothermal process cannot be determined using the binary results, and the sign of thermal diffusion factors is immaterial in defining the direction of component segregation in the hot and cold regions. Consequently, a detailed quantitative study of thermal diffusion factors in multicomponent mixtures is needed for a proper understanding of the thermal diffusion process not only of industrial interest but also of academic interest to investigate the size and shape of the molecules and intermolecular interactions taking part in the mixture.

Our literature survey shows that the study of thermal diffusion factors in multicomponent mixtures has not been performed previously in a systematic way, probably, because 1) equations of mass flux in multicomponent mixtures become too complicated to be evaluated analytically and require a special effort, and 2) no experimental data are available for thermal diffusion factors in multicomponent mixtures (more than two components) for testing the models.

The goal of this work is to derive a model for thermal diffusion factors in multicomponent non-ideal mixtures. The model is derived from the thermodynamics of irreversible processes where the effects of both equilibrium and non-equilibrium properties are incorporated.

3 Thermal diffusion factors

We consider a mixture consisting of n components at a given temperature, T, and pressure, P, where the only external force, $\vec{F}$, is the gravity. If we assume that there is no heat generation, viscous dissipation, or chemical reaction, the entropy production strength can be written as [28]

$$\sigma = -\frac{1}{T^2}\left(\vec{J}_q - \sum_{k=1}^{n}\frac{\bar{H}_k}{M_k}\vec{J}_k\right).\vec{\nabla}T - \frac{1}{T}\sum_{k=1}^{n}\vec{J}_k.\left(\vec{\nabla}_T\frac{\mu_k}{M_k} - \vec{F}\right), \tag{1}$$

where $\vec{J}_q$ is the heat flux, M_k, $\bar{H}_k$, μ_k, and $\vec{J}_k$ are the molecular weight, the partial molar enthalpy, the chemical potential, and the molar diffusion flux relative to the molar average velocity of component k, respectively. $\sum_{k=1}^{n}(\bar{H}_k/M_k)\vec{J}_k$ is the transfer of heat due to diffusion. By introducing a new heat flux expression, $\vec{J}'_q$, defined as

$$\vec{J}'_q = \vec{J}_q - \sum_{k=1}^{n}\frac{\bar{H}_k}{M_k}\vec{J}_k, \tag{2}$$

and using $\sum_{k=1}^{n-1}\vec{J}_k = 0$, Eq. (1) becomes

$$\sigma = -\frac{1}{T^2}\vec{J}'_q.\vec{\nabla}T - \frac{1}{T}\sum_{k=1}^{n-1}\vec{J}_k.\vec{\nabla}_T\left(\frac{\mu_k}{M_k} - \frac{\mu_n}{M_n}\right). \tag{3}$$

Another method of expressing the heat flux, $\vec{J}_q$, is based on combining the concept of irreversible thermodynamics and molecular kinetic theory involving the heat of transport [29, 30]

$$\vec{J}_q = \sum_{k=1}^{n} \frac{Q_k}{M_k} \vec{J}_k, \tag{4}$$

where Q_k is the heat of transport of component k. The expression for $\vec{J}'_q$ then becomes

$$\vec{J}'_q = \sum_{k=1}^{n} \frac{Q_k - \bar{H}_k}{M_k} \vec{J}_k = \sum_{k=1}^{n} \frac{Q_k^*}{M_k} \vec{J}_k; \tag{5}$$

where $Q_k^* = Q_k - \bar{H}_k$ is the net heat of transport of component k. Consequently, Eq. (3) can be expressed in terms of the net heat of transport as

$$\sigma = -\frac{1}{T} \sum_{k=1}^{n-1} \left[\left(\frac{Q_k^*}{M_k} - \frac{Q_n^*}{M_n} \right) \frac{\vec{\nabla} T}{T} + \vec{\nabla}_T \left(\frac{\mu_k}{M_k} - \frac{\mu_n}{M_n} \right) \right] . \vec{J}_k. \tag{6}$$

Using Eqs. (3) and (6) of the entropy production strength, one can write the phenomenological equations for the diffusion flux in the two following forms

$$\vec{J}_i = -L'_{iq} \frac{\vec{\nabla} T}{T^2} - \frac{1}{T} \sum_{k=1}^{n-1} L_{ik} \vec{\nabla}_T \left(\frac{\mu_k}{M_k} - \frac{\mu_n}{M_n} \right), \; i = 1, \; ..., \; n-1, \tag{7}$$

and

$$\vec{J}_i = -\frac{1}{T} \sum_{k=1}^{n-1} L_{ik} \left[\left(\frac{Q_k^*}{M_k} - \frac{Q_n^*}{M_n} \right) \frac{\vec{\nabla} T}{T} + \vec{\nabla}_T \left(\frac{\mu_k}{M_k} - \frac{\mu_n}{M_n} \right) \right], \quad i = 1, \; ..., \; n-1, \tag{8}$$

respectively; L'_{iq} and L_{ik} are the phenomenological coefficients [31, 32]. Eqs. (7) and (8) imply

$$L'_{iq} = \sum_{k=1}^{n-1} L_{ik} \left(\frac{Q_k^*}{M_k} - \frac{Q_n^*}{M_n} \right), \qquad i = 1, \; ..., \; n-1. \tag{9}$$

At steady state, the diffusion flux vanishes and Eq. (8) implies (L_{ik}'s, $i, \; k = 1, \; ..., \; n-1$ are independent)

$$Q_k^* \frac{\vec{\nabla} T}{T} + \vec{\nabla}_T \mu_k = 0, \qquad i = 1, \; ..., \; n-1, \tag{10}$$

$$Q_n^* \frac{\vec{\nabla} T}{T} + \vec{\nabla}_T \mu_n = 0. \tag{11}$$

From the Gibbs-Duhem relation under isothermal and isobaric conditions

$$\vec{\nabla}_{T,P} \mu_n = -\frac{1}{x_N} \sum_{j=1}^{n-1} x_j . \vec{\nabla}_{T,P} \mu_j \tag{12}$$

Substituting the above Gibbs-Duhem relation in Eq. (11) for the isobaric condition one obtains

$$x_n Q_n^* \frac{\vec{\nabla} T}{T} - \sum_{k=1}^{n-1} x_k \vec{\nabla}_{T,P} \mu_k \;=\; 0; \tag{13}$$

and from Eq. (10) one obtains for the isobaric condition

$$-\sum_{k=1}^{n-1} \left[Q_k^* \frac{\vec{\nabla} T}{T} + \vec{\nabla}_{T,P} \mu_k \right] x_k \;=\; 0. \tag{14}$$

Eqs. (13) and (14) imply that

$$\sum_{k=1}^{n} x_k Q_k^* = 0, \tag{15}$$

which is valid only under isobaric conditions. From the following matrix and column vectors

$$\begin{aligned} \mathbf{L} &\equiv [L_{ij}] \equiv L_{ij} \qquad i,j = 1,\ ...,\ n-1, \\ \mathbf{L_q} &\equiv \left[L'_{iq}\right] \qquad i = 1,\ ...,\ n-1, \\ \mathbf{Q} &\equiv \left[\frac{Q_k^*}{M_k} - \frac{Q_n^*}{M_n}\right] \qquad i = 1,\ ...,\ n-1; \end{aligned}$$

Eq. (9) can be written in a compact form as

$$\mathbf{L_q} \;=\; \mathbf{L}.\mathbf{Q}. \tag{16}$$

Using Eq. (7), the diffusion flux vector $\mathbf{J} = \left(\vec{J}_1,\ ...,\ \vec{J}_{n-1}\right)$ reads [33]

$$\mathbf{J} \;=\; -c\left(\mathbf{D^M}.\nabla \mathbf{x} + \mathbf{D^T}\vec{\nabla} T + \mathbf{D^P}\vec{\nabla} P\right), \tag{17}$$

where $\mathbf{D^M} \equiv [D_{ij}]$, $\mathbf{D^T} = \left(D_1^T,\ ...,\ D_{n-1}^T\right)$, $\mathbf{D^P} = \left(D_1^P,\ ...,\ D_{n-1}^P\right)$, and $\nabla \mathbf{x} = \left(\vec{\nabla} x_1,\ ...,\ \vec{\nabla} x_{n-1}\right)$. The molecular diffusion coefficients D_{ij} ($\mathrm{m^2\ s^{-1}}$), the thermal diffusion coefficients D_i^T ($\mathrm{m^2\ s^{-1}\ K^{-1}}$), and the pressure diffusion coefficients D_i^P ($\mathrm{m^2\ s^{-1}\ Pa^{-1}}$) are expressed by

$$D_{ij} \;=\; a_{in} D_{in} \frac{M_i x_i}{L_{ii}} \sum_{k=1}^{n-1} L_{ik} \sum_{l=1}^{n-1} \frac{M_l x_l + M_n x_n \delta_{lk}}{M_l} \left.\frac{\partial \ln f_l}{\partial x_j}\right|_{\mathbf{x_j},T,P}, \qquad i,j = 1,\ ...,\ n-1, \tag{18}$$

$$D_i^T \;=\; a_{in} D_{in} M \frac{k_{Ti}}{T}, \quad i = 1,\ ...,\ n-1, \tag{19}$$

$$D_i^P \;=\; a_{in} D_{in} \frac{M_i x_i}{RT L_{ii}} \sum_{k=1}^{n-1} L_{ik} \left[\sum_{j=1}^{n-1} x_j \bar{V}_j + \frac{M_n x_n}{M_k} \bar{V}_k - \frac{M}{\rho} \right] \qquad i = 1,\ ...,\ n-1, \tag{20}$$

respectively. $\bar{V}_i$, f_i, and M are the partial molar volume of component i, the fugacity of component i, and the total molecular weight, respectively; $\bar{V}_i$ and f_i can be obtained using an equation of state [34]. The subscription $\mathbf{x_j}$ is defined by $(x_1, ..., x_{j-1}, x_{j+1}, ..., x_{n-1})$. The coefficients a_{in}, D_{in} and k_{Ti} are given by

$$a_{in} = \frac{M_i M_n}{M^2}, \qquad i = 1, \ ..., \ n-1, \tag{21}$$

$$D_{in} = \frac{M^3 R L_{ii}}{\rho M_i^2 M_n^2 x_i x_n} \qquad i = 1, \ ..., \ n-1, \tag{22}$$

$$\begin{aligned} k_{Ti} &= \frac{M_i x_i M_n x_n L'_{iq}}{MRTL_{ii}} \\ &= \alpha_{Ti} x_i x_n, \qquad i = 1, \ ..., \ n-1; \end{aligned} \tag{23}$$

k_{Ti} and α_{Ti} are the thermal diffusion ratio, and the thermal diffusion factor of component i, respectively. For binary mixtures, the diffusion flux of component 1 can be obtained from Eq. (17);

$$\begin{aligned} \vec{J}_1 = -cD_{12}\frac{M_1 M_2}{M}\Bigg[& \left.\frac{\partial \ln f_1}{\partial \ln x_1}\right|_{P,\,T} \vec{\nabla} x_1 + \frac{k_{T1}}{T}\vec{\nabla} T + \\ & \frac{x_1}{RT}\left(\bar{V}_1 - \frac{M_1}{\rho}\right)\vec{\nabla} P\Bigg]; \end{aligned} \tag{24}$$

k_{T1} is equal to $x_1(1-x_1)\alpha_{T1}$. From Eq. (24) at steady state, under isobaric conditions, when $k_{T1} > 0$, thermal diffusion causes component 1 to segregate towards the cold region (from stability analysis [34] $(\partial \ln f_1 / \partial \ln x_1)_{P,T} \geq 0$). Note that there is no need for adopting a sign convention for k_T in a binary mixture despite the practice in the literature. In a non-ideal multicomponent mixture, the sign of k_{Ti} in general may have no relation with the segregation of a particular component to the hot or cold regions. At steady state under isobaric conditions, $\nabla x_i = -\nabla T \det(\mathbf{B}_i) / \det\left(\mathbf{D^M}\right)$, where $\mathbf{B}_i$ is the matrix $\mathbf{D^M}$ with column i replaced by column vector $\mathbf{D^T}$; therefore, the sign of D_i^T (and thus k_{Ti}) alone may not determine the sign of ∇x_i. From Eq. (23) one obtains

$$L'_{iq} = \frac{MRTL_{ii}}{M_i x_i M_n x_n} k_{Ti}. \tag{25}$$

When one adopts the following definitions

$$\begin{aligned} \mathbf{D} &\equiv [\mathbf{D}_{ij}] \equiv a_{in} D_{in} \delta_{ij} \qquad i,j = 1, \ ..., \ n-1, \\ \mathbf{M} &\equiv [\mathbf{M}_{ij}] \equiv \frac{M_i x_i}{L_{ii}} \delta_{ij} \qquad i,j = 1, \ ..., \ n-1, \\ \mathbf{W} &\equiv [\mathbf{W}_{ij}] \equiv \frac{M_j x_j + M_n x_n \delta_{ij}}{M_j} \qquad i,j = 1, \ ..., \ n-1, \\ \mathbf{K_T} &\equiv [\mathbf{K}_{Ti}] \equiv k_{Ti} = x_i x_n \alpha_{Ti} \qquad i = 1, \ ..., \ n-1; \end{aligned}$$

then $\mathbf{D^M}$ and $\mathbf{L_q}$ read

$$\mathbf{D^M} = \mathbf{D.M.L.W.F}, \tag{26}$$

and

$$\mathbf{L_q} = \frac{MRT}{M_n x_n}\mathbf{M^{-1}}.\mathbf{K_T}, \tag{27}$$

respectively. Eqs (16) and (27) give

$$\mathbf{K_T} = \frac{M_n x_n}{MRT}\mathbf{M}.\mathbf{L}.\mathbf{Q}, \tag{28}$$

which can be written as

$$k_{Ti} = \frac{M_i x_i M_n x_n}{MRTL_{ii}} \sum_{j=1}^{n-1} L_{ij}\left(\frac{Q_j^*}{M_j} - \frac{Q_n^*}{M_n}\right), \; i = 1, \; ..., \; n-1. \tag{29}$$

Under isobaric conditions, using Eq. (15), Eq. (29) becomes

$$k_{Ti} = \frac{M_i x_i}{MRTL_{ii}} \sum_{j=1}^{n-1} \left(\sum_{k=1}^{n-1} L_{ik}\frac{M_j x_j + M_N x_N \delta_{kj}}{M_j}\right) Q_j^*, \; i = 1, \; ..., \; n-1. \tag{30}$$

We propose to use Eq. 29 (Eq. 30 for isobaric systems) for the estimation of thermal diffusion ratios in multicomponent mixtures. For binary mixtures, Eq. (29) reduces to

$$k_{T1} = x_1(1-x_1)\alpha_{T1} = \frac{M_1 x_1 M_2 x_2}{MRT}\left(\frac{Q_1^*}{M_1} - \frac{Q_2^*}{M_2}\right), \tag{31}$$

which, from Eq. (15), can be written as

$$k_{T1} = \frac{x_1}{RT} Q_1^*. \tag{32}$$

Eq. (32) was used by Shukla and Firoozabadi [22] for thermal diffusion ratio in binary mixtures (with the sign convention and the definition of the thermal diffusion factor from Ref. [22]).

Eq. (29) (30 for isobaric systems) allows the determination of the thermal diffusion factors for a given composition having, 1) the net heat of transport of all the components in the mixture, and 2) the phenomenological coefficients (which can be readily obtained from the molecular diffusion coefficients). It should, however, be mentioned that, if cross-molecular diffusion coefficients are neglected, that is, the phenomenological coefficients $L_{ij} = 0$ for $i \neq j$, then the expression for thermal diffusion ratios in multicomponent mixtures simplifies to

$$k_{Ti} = \frac{M_i x_i M_n x_n}{MRT}\left(\frac{Q_i^*}{M_i} - \frac{Q_n^*}{M_n}\right) \qquad i = 1, \; ..., \; n-1 \tag{33}$$

Thus, like in binaries, for a multicomponent mixture where the cross-molecular diffusion coefficients are negligible, the thermal diffusion ratios do not depend on molecular diffusion coefficients; they are functions of temperature, composition, molecular weight and the net heat of transport. However, even in this case, thermal diffusion factors for multicomponent mixtures are different from those for binary mixtures, since the net heat of

transport of each component differs from binary to multicomponent mixtures. Furthermore, for non-ideal mixtures where the cross-molecular diffusion coefficients are important in comparison with the mutual diffusion coefficients, they significantly affect the thermal diffusion factors. In the remaining part of this section we explain how the net heat of transport Q_i^* and the phenomenological coefficients L_{ij} can be obtained.

The net heat of transport for the *ith* component in an n component mixture can be determined by generalizing, for n components, the expression used by Shukla and Firoozabadi [22]

$$Q_i^* = -\frac{\Delta\bar{U}_i}{\tau_i} + \left[\sum_{j=1}^{n} \frac{x_j \Delta\bar{U}_j}{\tau_j}\right] \frac{\bar{V}_i}{\sum_{j=1}^{n} x_j \bar{V}_j} \qquad i = 1, \ ..., \ n, \tag{34}$$

where $\Delta\bar{U}_i$ is the partial molar internal energy departure of component i and $\tau_i = \Delta U_i^{vap}/\Delta U_i^{vis}$; ΔU_i^{vap} and ΔU_i^{vis} are the energy of vaporization and the energy of viscous flow of pure component i, respectively [35].

From Eq. (26), one obtains the expression relating the phenomenological coefficient matrix $\mathbf{L}$ to the molecular diffusion coefficient matrix $\mathbf{D^M}$

$$\mathbf{L} = (\mathbf{D.M})^{-1}.\mathbf{D^M}.(\mathbf{W.F})^{-1}; \tag{35}$$

which can be written as [33]

$$\sum_{l=1}^{n-1}\sum_{k=1}^{n-1} \frac{M_k x_k + M_n x_n \delta_{lk}}{M_k} \left.\frac{\partial \ln f_k}{\partial x_j}\right|_{x_j,T,P} L_{li} = \frac{\rho M_n x_n}{MR} D_{ij}^M, \qquad i,j = 1, \ ..., \ n-1. \tag{36}$$

Thus, having the molecular diffusion coefficients, one can readily obtain the phenomenological coefficients. It should be mentioned that the measurement of the molecular diffusion coefficients is less complicated than that of the thermal diffusion coefficients since the existence of the temperature gradient in the latter normally generates convection within the system which can cause erroneous results for the thermal diffusion factors. This may not be the case for the measurement of the molecular diffusion coefficients where the experiment can be performed in isothermal cavities. The molecular diffusion coefficients used in the next section have been calculated using the model proposed by Kooijman and Taylor [36]. Reference [37] provides a complete procedure for the estimation of the molecular diffusion coefficients.

4 Results and discussion

We start by studying our model for some binary mixtures near and far from the critical point; then we present results for ternary and higher mixtures. El Maâtaoui [38] reports compositional data for the ternary mixture of $nC_{24}/nC_{16}/nC_{12}$ in a thermogravitational column [39, 40, 41]; our model is used to indirectly compare the results. Recently, we incorporated [37] the molecular diffusion coefficients using Kooijman and Taylor's correlation [36] and those of the thermal diffusion factors from this work into a numerical

model for a thermogravitational column filled with a porous medium [37]. This was our only comparison for mixtures with more than two components.

In order to obtain the thermal diffusion ratios using Eq. (28), equilibrium properties such as partial molar volumes, partial internal energies and fugacities were determined using the Peng-Robinson equation of state (PR EOS) [42] with or without volume correction [43] along with the van der Waals mixing rules. For most of the cases we studied, we found that the effect of the volume translation on the thermal diffusion factors was insignificant. However, for heavy components, the volume correction was found to be important to match the experimental volumetric data and had significant effect on the thermal diffusion factors. In the following, all the results we present for thermal diffusion factors are obtained without volume correction unless mentioned otherwise. The binary interaction parameters used in the PR EOS are taken from Katz and Firoozabadi [44]. Table I presents the critical temperature, critical pressure, accentric factor, and the molecular weight of the components considered in this study. The value of the parameter τ_i is assumed to be the same for all the components; $\tau_i = 4$. This value is based on the observation that at the normal boiling point, $\ln \eta$, where η is the liquid viscosity, varies linearly with $1/T$ over a wide range of temperature; τ_i variations are in the range [35] of 3 to 5. Moreover, the universal value of $\tau_i = 4$ gave satisfactory results for thermal diffusion factors for binary mixtures as was shown by Shukla and Firoozabadi [22] and is shown in this study.

4.1 Binary mixtures

Here we further test our thermal diffusion factor model with binary mixture data of CO_2/C_2 [45], C_7H_8/nC_7 (toluene/n-hexane) [17, 8, 46], and nC_{24}/nC_{12} [38]. In order to make the comparison as clear as possible, we keep, as long as it does not create confusion, the same parameters that were obtained in the experimental work. The Soret coefficient, S_T, for binary mixtures used by some authors is defined by $S_T = D_1^T / \left(D_{11}^M \, x_{10}(1 - x_{10})\right)$, where x_{10} is the initial mole fraction of component 1.

Fig. 1 presents the thermal diffusion ratio k_{T1} vs. the molar density for the binary mixture CO_2/C_2 ($x_{CO_2} = 0.60$, $x_{C_2} = 0.40$) in the critical region. The predictions are in agreement with data of Walther [45]. The figure also shows that as the critical point approaches, the predicted thermal diffusion factor increases, as expected. Note that, depending on the molar density, CO_2 can segregate to the hot side ($k_{T1} < 0$) or the cold side ($k_{T1} > 0$)

Fig. 2 shows the Soret coefficient in the binary mixture toluene/n-hexane. An excellent agreement between experimental data of Li *et al.* [46] and Köhler and Müller [17] and our theoretical results is obtained. The Soret coefficients reported by Ecenarro *et al.* [8] using the thermogravitational column are almost half of those obtained by Li *et al.* [46] using the small angle Rayleigh scattering method, and those of Köhler and Müller [17] using the forced Rayleigh scattering method.

El Maâtaoui [38] reports the measured Soret coefficient in a binary mixture of nC_{24}/nC_{12} at the initial composition 8.15% nC_{24}; 91.85% nC_{12}. The average temperature for the measurements is $T_0 = 321.5$. The value of S_T reported by El Maâtaoui under these conditions is $S_T = 0.90$ K^{-1}. The results from our model are in excellent agreement with the

experimental data of El Maâtaoui; we obtain $S_T = 0.85\ K^{-1}$. This value is obtained by taking into account volume correction in the PR-EOS.

Various authors have used the mode-mode coupling analysis showing that thermal diffusion coefficients in binary mixtures exhibit a finite enhancement in the critical region [48, 49, 50]. Fig. 3 depicts a plot of $-TD_1^T$ vs. $(T - T_c)/T$ near the critical point for an equimolar mixture of C_1/C_2 (at the critical pressure). This figure shows that our theory gives reasonable results in the critical region for this binary, in view of the deficiency in the PR-EOS predictions in the critical region [34]. The results obtained by Sakonidou *et al.* [24] (by fitting the crossover equation of the thermal conductivity to the thermal conductivity data which allows to calculate the molecular and thermal diffusion coefficients in the vicinity of the critical point) and those from our model show the same trend when we approach the critical point; TD_1^T reaches a finite value at the critical point.

Luettmer-Strathmann and Sengers [47] investigated, using the mode-mode coupling calculations, the transport properties in a CO_2/C_2 binary mixture (25%/75%) in the critical region. They reported that D_{11}^M decreases asymptotically towards zero when one approaches the critical point. They also reported that k_{T1}/D_{11}^M diverges at the critical point. However, these authors reported that D_{11}^M vanishes as ξ^{-2} (ξ is the correlation length divergent at the critical point), and k_{T1}/D_{11}^M diverges as ξ^2 when one approaches the critical point. Consequently, their product, k_{T1}, is finite at the critical point. The results from our model for the thermal diffusion ratio, k_{T1}, near the critical point (at the critical pressure) is depicted for this mixture in Fig. 4.

4.2 Ternary mixture

The main goal of this work is to present a model for thermal diffusion factors of multicomponent mixtures. However, there are no experimental data for multicomponent thermal diffusion factors in the literature to the best of our knowledge. There are, however, spatial concentration data in ternary systems that can be used to verify the validity of our proposed model.

For the ternary mixture $nC_{24}/nC_{16}/nC_{12}$, the experimental data by El Maâtaoui [38] show nC_{24} segregates towards the bottom of the column. The data also show no significant compositional variation across the column for nC_{16}. There is excellent agreement between the measured compositional data and the results obtained using our model where volume correction is taken into account (see Table II). The maximal relative error between predictions and measurements is less that 10%. For this mixture, the predicted Soret coefficients of components 1 (nC_{24}) and 2 (nC_{16}) from our model are $S_{T1} = 0.1552 \times 10^{-2}$ and $S_{T2} = 0.8695 \times 10^{-4}$, respectively.

4.3 Six-component mixture

We used our model to predict thermal diffusion factors of a mixture of $C_1/C_3/nC_5/nC_{10}/nC_{16}/C_2$ for the composition 40/12/5/2/1/40 mole % at different temperatures and pressures. The magnitude and the sign of the thermal diffusion factors depend obviously on the choice of the *nth* component (component 6 in this example). In the following, C_1, C_3, nC_5, nC_{10}, and nC_{16} represent components 1, 2, 3, 4, and 5, respectively; C_2 represents component

6. Fig. 5 depicts the predicted saturation pressure of this mixture. We performed two sets of thermal diffusion factors calculations; first, we fixed the temperature equal to the critical temperature and varied the pressure. Then, we fixed the pressure equal to the critical pressure and varied the temperature. The dashed lines on the figure represent the above two sets of calculations. The volume correction was taken into account. The predicted results are presented in Tables III and IV. Note that for heavier components, the thermal diffusion factor is larger than for lighter components.The thermal diffusion factor α_{T1} of the lightest component, C_1, in the mixture is negative; the others are positive. In an isobaric system where cross-molecular diffusion can be neglected, this may imply that methane may segregate toward the cold region which may not be always true. Similarly, component 2, C_3, may not segregate to the hot side. Tables III and IV also show that, the closer the system is to the critical point the larger is the absolute value of the thermal diffusion factors. Far from the critical point, the change of temperature (pressure) at fixed pressure (temperature) does not affect the thermal diffusion factors as it does near the critical point. The distance to the critical point is the main parameter which affects the thermal diffusion factors in multicomponent mixtures.

5 Concluding remark

We have formulated a model for thermal diffusion factors for non-ideal multicomponent mixtures. The model shows explicit dependency of the thermal diffusion factors in non-ideal mixtures of more than two components on molecular diffusion coefficients. The single validation of the model for a ternary mixture shows success. The results for a six-component mixture show that the thermal diffusion factors in multicomponent mixtures are mostly affected by the distance to the critical point. The model presented in this paper, combined with the formalism of diffusion flux in multicomponent mixtures presented in our earlier paper [33], provide a comprehensive theoretical framework for future experimental investigation of thermal diffusion factors in multicomponent mixtures. We believe the model also enjoys simplicity for practical applications.

References

[1] C.H. Whitson and P. Belery, SPE 28000, paper presented at the University of Tulsa Centennial Petroleum Symposium, Tulsa, OK, USA, 29-31 August 1994.

[2] G.D. Rabinovich, V.I. Shinkevich and K.K. Azroyan, J. Eng. Phys. **37**, 808 (1979).

[3] J.M. Kincaid, E.G.D. Cohen and M. López de Haro, J. Chem. Phys. **15**, 963 (1986).

[4] J.C. Legros, P. Greomare and J.K. Platten, Phys. Rev. A **32**, 1903 (1985).

[5] Ph. Georis, M. Montel, S. Van Vaerenbergh, Y. Decroly and J.C. Legros, SPE 50573, paper presented at the 1998 SPE European Petroleum Conference, The Hague, The Netherlands, 20-22 October 1998.

[6] N.B. Vergaftik, *Tables on the Thermophysical Properties of Liquids and Gases* (Hemisphere, Washington, D.C., 1975).

[7] O. Ecenarro, J.A. Madariaga, J. Navarro, C.M. Santamaria, J.A. Carrion and J.M. Saviron, Separation Sci. Technol. **24**, 555 (1989).

[8] O. Ecenarro, J.A. Madariaga, J. Navarro, C.M. Santamaria, J.A. Carrion and J.M. Saviron, J. Phys. Condens. Matter **2**, 2289 (1990).

[9] H.J.V. Tyrrel, *Diffusion and Heat Flow in Liquids* (Butterworths, London, 1961).

[10] J.L. Lin, W.L. Taylor, W.M. Rutherford and J. Millat, *in Measurement of the Transport Properties of Fluids*, edited by W.A. Wakeman, A. Nagashima and J.V. Sengers, (Blackwell Scientific, Oxford, 1991).

[11] N.Y.R. Ma and A.L. Beyerlein, J. Phys. Chem. **87**, 245 (1983).

[12] D.W. Pohl, S.E. Schwarz and V. Irniger, Phys. Rev. Lett. **31**, 32 (1973).

[13] H.J. Eichler, P. Gunter and D.W. Pohl, *Laser Induced Dynamic Gratings* (Springer-Verlag, Berlin, 1986).

[14] K. Thyagarajan and P. Lallemand, Opt. Commun. **26**, 54 (1978).

[15] W. Köhler, J. Chem. Phys. **98**, 660 (1993).

[16] W. Köhler, C. Rosenauer and P. Rossmanith, Int. J. Thermophys. **16**, 11 (1995).

[17] W. Köhler and B. Müller, J. Chem. Phys. **103**, 4367 (1995).

[18] 18 K.J. Zhang, M.E. Briggs, R.W. Gammon and J.V. Sengers, J. Chem. Phys. **104**, 6881 (1996).

[19] W.M. Rutherford, AIChE J. **9**, 841 (1963).

[20] R. Haase, Z. Phys. Chem. **196**, 219 (1950).

[21] L. J. T. M. Kempers, J. Chem. Phys. **90**, 6541 (1989).

[22] K. Shukla, and A. Firoozabadi, Ind. Eng. Chem. Res. **37**, 3331 (1998).

[23] R. Haase, K. H. Ducker, H. Buchner and J. Schwinum, Zeitschrift fur physikalishe chemie **186**, 113 (1994).

[24] E. P. Sakonidou, H. R. van der Berg, C. A. Ten Seldam and J. V. Sengers, J. Chem. Phys. **109**, 717 (1998).

[25] R. Haase, H. W. Borgmann, K. H. Duker and W. L. Lee, Z. Naturforsch, Teil A. **26**, 1224 (1971).

[26] P. Belery and F. V. da Silva, Gravity and thermal diffusion in hydrocarbon reservoirs, Third North Sea chalk research symposium, Copenhagen, June 11-12 (1990).

[27] K. O. Temeng, M. J. Al-Sadeg and W. A. Al-Mulhim, SPE 49270 paper prepared for presentation at the 1998 SPE Annual Conference and Exhibition, New Orleans, Louisiana, 685 (1998).

[28] S. R. de Groot and P. Mazur, *Non-Equilibrium Thermodynamics*, (Dover Edition, New York, 1962).

[29] L.J. Tichacek, W.S. Kmak and H.G. Drickamer, J. Phys. Chem. **60**, 660 (1956).

[30] K.G. Denbigh, The Thermodynamics of the Steady State (John Wiley and Sons, Inc., New York, 1951).

[31] L. Onsager, Phys. Rev. **37**, 405 (1931).

[32] L. Onsager, Phys. Rev. **38**, 2265 (1931).

[33] K. Ghorayeb and A. Firoozabadi, submitted to J. Chem. Phys., January (1999).

[34] A. Firoozabadi, *Thermodynamics of Hydrocarbon Reservoirs*, (McGraw-Hill, New York, 1998).

[35] S. Glasstone, K. J. Laidler and H. Eyring, *The Theory of Rate Processes*, (McGraw-Hill, 1941).

[36] H. A. Kooijman and R. Taylor, Ind. Eng. Chem. Res. **30**, 1217 (1991).

[37] K. Ghorayeb and A. Firoozabadi, SPE 51932 paper presented at the 15th Reservoir Simulation Symposium, 14-17 February 1999, Houston, TX, also submitted to SPE J., February (1999).

[38] M. El Maâtaoui, Conséquences de la thermodiffusion en milieu poreux sur l'hydrolyse des solutions de chlorures ferriques et sur les migrations d'hydrocarbures dans les mélanges de n-alcanes et dans un pétrole brut: implications géochimiques, PhD thesis, Université Paul Sabatier, Toulouse, France, (1986).

[39] W. H. Furry, R. C. Jones and L. Onsager, Phys. Rev. **55**, 1083 (1939).

[40] M. Lorenz and A. H. J. Emery, Chem. Eng. Sci. **11**, 16 (1959).

[41] Ph. Jamet, D. Fargue, P. Costesèque, G. De. Marsily and A. Cernes, Transp. in Porous Media **9**, 223 (1992).

[42] D. Y. Peng and D. B. Robinson, Ind. Eng. Chem. Fund. **15**, 59 (1976).

[43] B. S. Jhaveri and G. K. Youngren, SPE Res. Eng., p. 1033, August (1988).

[44] D. L. Katz and A. Firoozabadi, J. Pet. Tech., p. 1694, Nov. (1978).

[45] J. E. Walther, Thermal diffusion in non-ideal gases, PhD Thesis, Univ. of Illinois (1957).

[46] W. B. Li, P. N. Segrè, R. W. Gammon and J. V. Sengers, Phys. A **204**, 399 (1994).

[47] J. Luettmer-Strathmann and J. V. Sengers, J. Chem. Phys. **104**, 3026 (1996).

[48] L. Mistura, Nuevo Smento B **12**, 35 (1972).

[49] L. Mistura, J. Chem. Phy. **62**, 4571 (1975).

[50] M.A Anisimov, E.E. Gorodetskii, V.D. Kulikov, A.A. Povodyrev and J.V. Sengers, Physica A. **220**, 277 (1995).

Table 1: Properties of pure components used in this study

Component	T_c (K)	P_c ($\times 10^5$ Pa)	ω	M
C_1	190.60	46.00	0.008	16.04
C_2	305.40	48.83	0.098	30.07
C_3	369.80	41.90	0.152	44.09
nC_5	469.60	33.30	0.251	72.15
nC_6	507.40	29.30	0.296	86.18
nC_{10}	617.60	20.80	0.490	142.28
nC_{12}	658.30	18.00	0.562	170.34
nC_{16}	717.00	14.00	0.742	226.45
nC_{24}	845.00	10.50	0.995	338.63
CO_2	304.20	72.80	0.225	44.01
C_7H_8	591.70	41.14	0.257	92.14

Table 2: Composition at the top and bottom of the thermogravitational column of the ternary mixture $nC_{24}/nC_{16}/nC_{12}$; initial composition 12.67 (nC_{24}), 37.41 (nC_{16}), and 49.92% (nC_{12}); T_0 = 321.5 K, ΔT = 25, Column height = 120 cm, permeability = 6.1×10^{-11} m^2.

	$(nC_{24})_{bottom}$	$(nC_{24})_{top}$	$(nC_{16})_{bottom}$	$(nC_{16})_{top}$
experiment	0.240	0.140	0.415	0.380
model	0.265	0.135	0.408	0.389

Table 3: Thermal diffusion factors for the mixture $C_1/C_3/nC_5/nC_{10}/nC_{16}/C_2$ (40/12/5/2/1/40%, mole); $P = 1.24 \times 10^7$ Pa. C_1, C_3, nC_5, nC_{10}, and nC_{16} represent components 1, 2, 3, 4, and 5, respectively; C_2 represents component 6.

T K	α_1	α_2	α_3	α_4	α_5
225	−0.8380	0.5912	1.2417	2.4412	3.2569
235	−0.8655	0.6107	1.3181	2.6466	3.6192
245	−0.8990	0.6341	1.4049	2.8774	4.0236
255	−0.9393	0.6619	1.5032	3.1377	4.4777
265	−0.9869	0.6942	1.6147	3.4323	4.9901
275	−1.0424	0.7315	1.7407	3.7656	5.5699
285	−1.1060	0.7738	1.8823	4.1415	6.2248
295	−1.1773	0.8206	2.0386	4.5602	6.9581
305	−1.2538	0.8702	2.2059	5.0147	7.7607
315	−1.3301	0.9184	2.3740	5.4825	8.5987

Table 4: Thermal diffusion factors for the mixture $C_1/C_3/nC_5/nC_{10}/nC_{16}/C_2$ (40/12/5/2/1/40%, mole); $T = 318$ K. C_1, C_3, nC_5, nC_{10}, and nC_{16} represent components 1, 2, 3, 4, and 5, respectively; C_2 represents component 6.

$P \times 10^{-5}$ Pa	α_1	α_2	α_3	α_4	α_5
125	−1.3511	0.9312	2.4221	5.6221	8.8548
135	−1.2524	0.8647	2.2319	5.1504	8.0713
145	−1.1720	0.8105	2.0771	4.7669	7.4349
155	−1.1049	0.7653	1.9478	4.4472	6.9049
165	−1.0480	0.7267	1.8379	4.1756	6.4549
175	−0.9988	0.6935	1.7430	3.9412	6.0666
185	−0.9558	0.6644	1.6599	3.7361	5.7271
195	−0.9177	0.6387	1.5864	3.7361	5.7271
205	−0.8838	0.6157	1.5208	3.3929	5.1588

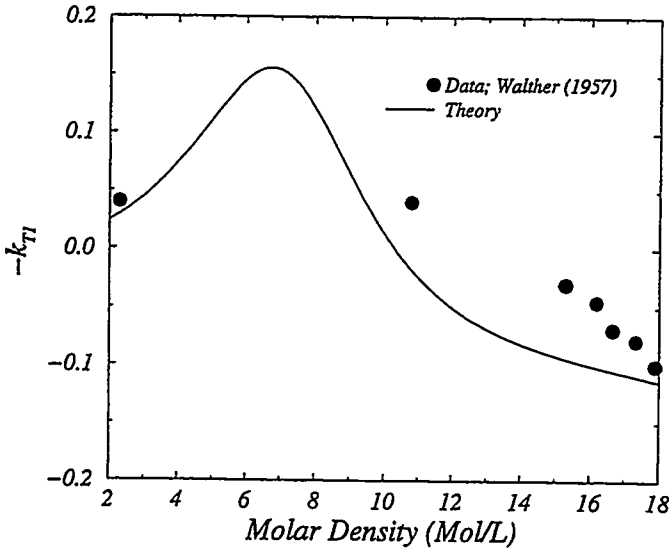

Figure 1: Thermal diffusion ratio vs. molar density at $T = 305.15$ K for the binary mixture CO_2/C_2 at composition 60/40 mole %.

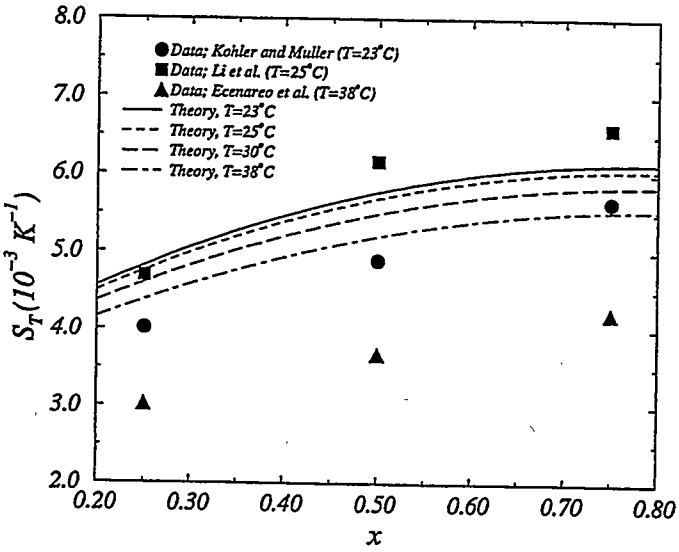

Figure 2: Soret coefficient in a toluene/n-hexane binary mixture vs. composition (of toluene) at different temperatures and at atmospheric pressure.

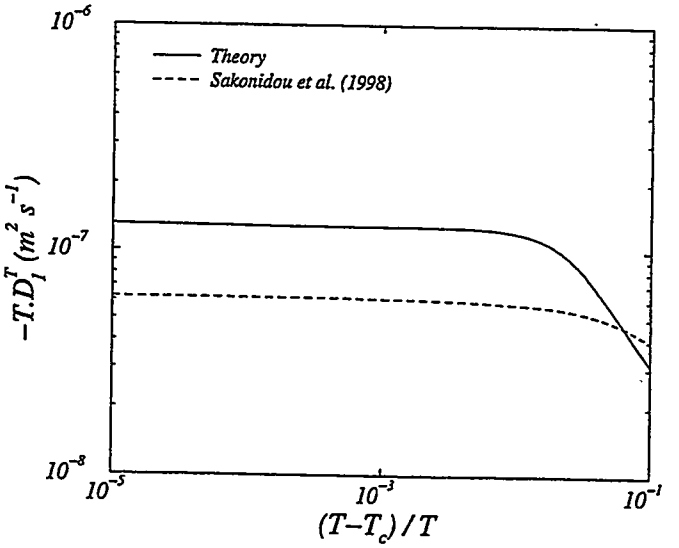

Figure 3: $-TD_1^T$ vs. $(T-T_c)/T$ for the equimolar mixture of C_1/C_2; $P = P_c = 6.84 \times 10^6$ Pa.

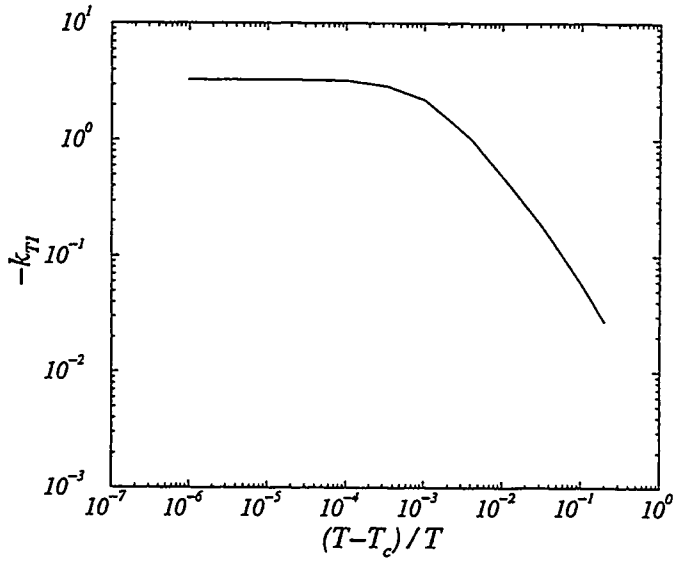

Figure 4: Thermal diffusion ratio vs. $(T - T_c)/T$ at the critical pressure for the binary mixture CO_2/C_2 at composition 25/75 mole %.

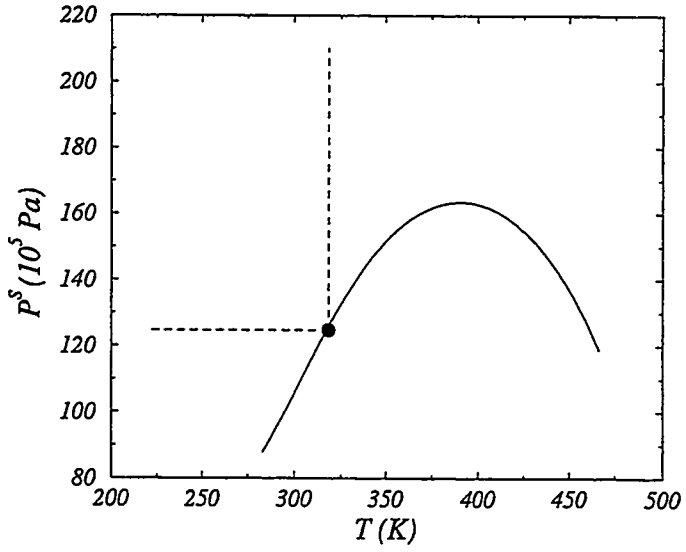

Figure 5: $P - T$ diagram for the mixture $C_1/C_2/C_3/nC_5/nC_{10}/nC_{16}$ at the composition 50/40/5/3/1/1 mole %. • denotes the critical point.

Part III - Features of Convection and Diffusion in Porous Media for Binary Systems.

KASSEM GHORAYEB AND ABBAS FIROOZABADI

1 Summary

Compositional variation in a vertical rectangular porous medium containing a two-component single phase fluid in the presence of a prescribed linear temperature field is considered. We investigate by using a finite volume method, the effects of convection, thermal diffusion and pressure diffusion on the compositional variation. Calculations show that, for high permeabilities, convective mass transfer overrides both thermal and pressure diffusion; it is the main phenomenon affecting compositional variation within the porous medium. In this case, the permeability increase makes the composition variation less pronounced. For low permeabilities, compositional variation is mainly affected by the ratio $(-C^T T_z)/(C^P P_z)$ where C^P, C^T, P_z and T_z are the pressure and thermal diffusion coefficients and the vertical pressure and thermal gradients, respectively. When this ratio is > 1, thermal diffusion is the main phenomenon affecting compositional variation and the horizontal composition gradient reaches a maximum at some permeability. For $(-C^T T_z)/(C^P P_z) < 1$, compositional variation is mostly affected by pressure diffusion and the horizontal compositional gradient decreases monotonically with permeability increase.

2 Introduction

Composition variation in hydrocarbon reservoirs has been a mystery until very recently. Measured data indicate several trend of compositional variation. There is mainly vertical compositional variation of the hydrocarbon components in some reservoirs [1]. Some other reservoirs show pronounced horizontal compositional variation [2]. In some other reservoirs there is very little compositional variation with depth [3].

There are four distinct mechanisms that affect the variation of composition in a single-phase hydrocarbon reservoir. These mechanisms are: 1) molecular diffusion, 2) pressure diffusion, 3) thermal diffusion, and 4) natural convection. Molecular diffusion is the tendency to mix due to concentration gradient. Pressure diffusion (gravitational segregation) is the separation by pressure gradient; it is negligible in the horizontal direction even when there exists natural convection, but may be pronounced in the vertical direction due to high vertical pressure gradient. Because of the pressure diffusion, the bottom fluid is richer in heavy components than the top. Thermal diffusion is the tendency of a convection-free

mixture to separate under a thermal gradient. Natural convection is the convective circulation due to density gradient. Density gradient is established due to temperature and concentration gradients. Steady state convection in hydrocarbon reservoirs is caused by horizontal temperature gradient.

A considerable amount of investigations of compositional variation in hydrocarbon reservoirs exist in the literature [4 – 10]. Those studies consider mainly the gravitational effect in a 1D convection-free system [4 – 7] where it has been shown that gravitational effect causes the heavier components to segregate towards the bottom of the reservoir. From Refs. [8 – 10] one concludes that thermal diffusion may have the same order of magnitude and may have an opposite effect than pressure diffusion. However, the above studies [4 – 10] neglect the effect of convection on compositional variation and do not consider horizontal compositional variation.

There are very few studies that combine the effect of convection and diffusion on the compositional variation in binary and multicomponent mixtures in porous media that take into account pressure diffusion. These studies include the works of Jacqmin [11], and Riley and Firoozabadi [12]. Both studies address compositional variation in homogeneous porous media. Jacqmin neglects thermal diffusion and uses a perturbation analysis where approximations are made to the governing equations. Based on his study, Jacqmin concludes that, under certain conditions the fluid composition reorients itself in such a way as to inhibit convection. Riley and Firoozabadi [12] studied the effect of thermal, pressure and molecular diffusion and natural convection on compositional variation in a cross-sectional reservoir with a prescribed linear temperature field. The behavior is investigated using a method of successive approximations which iterates on Poisson's equation. At high permeabilities certain difficulties were encountered in the calculations [12]. They incorporated the features of the solution from the Poisson's equation in a simplified perturbation solution which provides accurate results for horizontal composition variation. Riley and Firoozabadi [12] show that a small amount of convection can cause the horizontal composition gradient to increase until a maximum is reached and then decays as $1/k$. One purpose of this work is to find out if this conclusion has general validity.

This work investigates the steady state spatial compositional variation in a vertical rectangular reservoir using a numerical model. The main goals of the work are to investigate features of compositional variation in a porous medium for a binary mixture of methane/normal-butane by including all basic four mechanisms and reasonable variations of the coefficients of diffusion. Compositional variation of methane in a multicomponent mixture (the case of hydrocarbon reservoirs) may drastically differ from that in binary mixtures [13]. The study of compositional variation of methane in binary mixtures, however, provides a basis for a better understanding of more realistic situations in which the mixture consists of more than two components.

3 Mathematical Formulation

We consider a two-dimensional porous medium with width W and height H (Fig. 1) saturated by a binary mixture of C_1/nC_4. We assume that the Oberbeck-Boussinesq approximation is valid in the range of temperature, pressure and composition expected so

that the density ρ is constant except in the buoyancy term ($\rho g z$) where it varies linearly with the temperature T and the weight fraction w:

$$\rho(T,w) = \rho_0 \left[1 - \beta_T (T - T_0) - \beta_w (w - w_0)\right], \tag{1}$$

where ρ_0, $\beta_T = (-1/\rho_0)(\partial\rho/\partial T)_w$ and $\beta_w = (-1/\rho_0)(\partial\rho/\partial w)_T$ are the density at temperature T_0 and weight fraction w_0, the thermal expansion coefficient, and the compositional expansion coefficient, respectively. The coefficients β_T and β_w are calculated for the system C_1/nC_4, using the Peng-Robinson equation of state (PR EOS) [14]. The validity of Eq. 1 has been demonstrated by Ghorayeb and Firoozabadi [15] for the same range of temperature and pressure considered in this study.

The unsteady state conservation equations of mass and species are:

$$\nabla.\mathbf{v} = 0, \tag{2}$$

$$\rho_0 \frac{\partial w}{\partial t} + \rho_0 \nabla.(w\mathbf{v}) + \nabla.\mathbf{J} = 0, \tag{3}$$

where $\mathbf{v}$ and $\mathbf{J}$ are the velocity and the diffusive mass flux for component 1, respectively.

The bulk velocity, $\mathbf{v}$, is given by Darcy's law:

$$\mathbf{v} = -\frac{k}{\phi\mu}\left[\nabla P + \rho_0 \left(1 - \beta_T (T - T_0) - \beta_w (w - w_0)\right) g\mathbf{z}\right], \tag{4}$$

where P, g, k, μ and ϕ are the pressure, the acceleration due to gravity, the permeability, the viscosity and the porosity, respectively. The unit vector $\mathbf{z}$ points upwards. The substitution of Eq. 4 into Eq. 2 and the assumption that $(k/\phi\mu)$ is constant lead to the pressure equation:

$$\nabla^2 P = \rho_0 g \left(\beta_T \frac{\partial T}{\partial z} + \beta_w \frac{\partial w}{\partial z}\right). \tag{5}$$

The above equation will be used later in the numerical solution to the problem. The reservoir is assumed to be bounded by an impervious rock that has constant temperature gradients T_x and T_z in horizontal and vertical directions, respectively. We also assume that the conductive flow of heat is much greater than the convective flow and that thermal diffusivity is very large compared with compositional diffusivity. With these assumptions, the solution of the energy equation will have roughly the same temperature gradients as the bounding rock. In the following, the temperature field is assumed to be a linear function of x and z: $T = T_x x + T_z z + a$, where a is a constant. If we set the temperature at $x = W/2$ and $z = H/2$ equal to T_0, then,

$$T = T_x (x - W/2) + T_z (z - H/2) + T_0. \tag{6}$$

The diffusive mass flux is given by the expression (see Bird *et al.* [16]):

$$\mathbf{J} = C^w \nabla w + C^P \nabla P + C^T \nabla T, \tag{7}$$

where C^w, C^P and C^T are the coefficients of molecular diffusion, pressure diffusion and thermal diffusion, respectively. These coefficients are described in Refs. [12, 16]. The

diffusive flux, $\mathbf{J}$, results from the deviation in the velocity of component one from the velocity of the bulk fluid. Since, in the case of a two-component system, the diffusive flux of component two is equal to $-\mathbf{J}$ and the weight fraction of component two is equal to $1-w$, the equation expressing conservation of mass of component two will be a linear combination of Eqs. 2 and 3. The coefficients C^w, C^P and C^T are the result of the phenomenological laws, the Gibbs-Duhem relation, and an equation of state (see Bird *et al.* [16], de Groot and Mazur [17], and Firoozabadi [18]); they generally depend on the concentration, temperature and thermo-physical properties of the mixture. In this work, those coefficients are assumed, for convenience, to be constant in the whole reservoir. In the range of parameters we consider in this study, this assumption has only a small effect on the results as we will discuss later.

3.1 Boundary Conditions

The boundary conditions for Eqs. 2, 3 and 4 are that the fluid does not cross the outer boundaries (Fig. 1):

$$\mathbf{J}.\mathbf{n} = 0 \qquad x=0,\ W \text{ and } \quad z=0,\ H, \tag{8}$$

$$\mathbf{v}.\mathbf{n} = 0 \qquad x=0,\ W \text{ and } \quad z=0,\ H, \tag{9}$$

where $\mathbf{n}$ is the unit normal vector. Eqs. 8 and 9 imply that:

$$C^w\frac{\partial w}{\partial x}+C^P\frac{\partial P}{\partial x}+C^T\frac{\partial T}{\partial x}=0, \quad \text{and} \quad v_x=0 \qquad x=0,W, \tag{10}$$

$$C^w\frac{\partial w}{\partial z}+C^P\frac{\partial P}{\partial z}+C^T\frac{\partial T}{\partial z}=0, \quad \text{and} \quad v_z=0 \qquad z=0,H. \tag{11}$$

From Eq. 4, we obtain the boundary conditions required for the integration of Eq. 5:

$$\frac{\partial P}{\partial x} = 0 \qquad x=0,W, \tag{12}$$

$$\frac{\partial P}{\partial z} = -\rho_0\left(1-\beta_T\left(T-T_0\right)-\beta_w\left(w-w_0\right)\right) \qquad z=0,H. \tag{13}$$

With the above Neumann boundary conditions, weight fraction and pressure must be assigned at one point of the medium. In this work we set $w\left(W/2,H/2\right)=w_0$ and $P\left(W/2,H/2\right)=P_0$.

4 Numerical Scheme

Eqs. 3, 4 and 5 together with the boundary conditions given by Eqs. 10 to 13 are integrated numerically using finite volume method (see Patankar [19]) with a nonuniform rectangular grid system. The spatial discretization is performed using a second-order centered scheme. A semi-implicit first-order scheme is used for the temporal integration. We seek the steady state solution and iterate on the unsteady system until the steady state is reached. In this work convergence to the steady state is assumed when the absolute relative error of concentration is found to be less than 10^{-7} between the two

successive iterations at each grid point. In all simulations, we used 301 mesh points in the horizontal direction and 41 mesh points in the vertical direction. To study the effect of grid size, numerical runs were performed with different mesh grids; we found that using finer grids than those above do not significantly improve the accuracy of the results. We also verified the numerical results from our model with the analytical work presented in Ref. [12]. Fig. 2 depicts the horizontal gradient of mole fraction in the center of the reservoir vs. permeability; the agreement, as shown in this figure, is good.

5 Results and Discussion

First, calculations were performed using the PR EOS, instead of the Boussinesq approximation, to predict the fluid density. This was done for two reasons: 1) to justify the use of the Boussinesq approximation in the range of temperature, concentration and pressure expected in this study; and 2) to estimate the variation of the coefficients C^w, C^P and C^T in the x-z plane. We calculated C^w, C^P, and C^T using the expressions presented in Ref. [12] where the density, fugacity and partial molar volume are calculated using the PR EOS and where the molecular diffusion coefficient and the thermal diffusion ratio are given by Sigmund [20] and Rutherford and Roof [21], respectively. Fig. 3 presents C^w, C^P, and C^T contour lines for $k = 1$ md. This figure shows that, the variation of C^w, C^P, and C^T in the whole medium is less than 21% for C^w and C^P, and less than 7% for C^T. The same results (not depicted) are valid for other permeabilities. We compared the numerical results obtained using C^w, C^P, and C^T in Fig. 3 to those obtained using the average values of C^w, C^P, and C^T ($C^w = -2.91 \times 10^{-7}$ kg/m.s °K, $C^P = -1.15 \times 10^{-15}$ kg/m.Pa.s, $C^T = 2.68 \times 10^{-10}$ kg/m.s) and the Boussinesq approximation. The results show that by taking C^w, C^P, and C^T as constants equal to their average and using the Boussinesq approximation, has only a small effect on the compositional variation in the reservoir. In this work we are rather concerned with the understanding of the fluid behavior trend when the physical parameters of the problem vary, and we present all the results using the Boussinesq approximation with constant values of C^w, C^P, and C^T. The data used in our simulations are presented in Table 1. The choice of data used in this work is motivated by the earlier study (Riley and Firoozabadi [12]). We start with the investigation of the thermal diffusion effect on composition variation. Toward this end, calculations are performed using $C^T = 0$, 1.5×10^{-10}, 2.0×10^{-10}, 2.5×10^{-10}, 3.0×10^{-10}, 3.5×10^{-10} kg/m.s °K, and $C^P = -1.15 \times 10^{-15}$ kg/m.Pa.s. Then, pressure diffusion effect on compositional variation is investigated using $C^P = -2.0 \times 10^{-15}$, -1.15×10^{-15}, and 0 kg/m.Pa.s, and $C^T = 2.5 \times 10^{-10}$ kg/m.s °K. The permeabilities considered in this work vary between 0 (convection-free) and 100 md. Note that when $k = 0$, the convective velocity is also zero; therefore by assigning zero to permeability, we model convection-free case. We did not perform calculations for $k > 100$ md because the reservoir composition becomes homogeneous in this range of permeability. Although C^T and C^P are not independent, their effect on compositional variation is studied by assuming one constant and varying the other. C^w is set equal to -2.88×10^{-7} kg/m.s.

5.1 Thermal diffusion

Fig. 4 shows a typical behavior of methane mole fraction contour lines for different permeabilities. For $k = 0$ (convection free), mole fraction varies linearly in both horizontal and vertical directions. Note that the vertical compositional gradient is much more pronounced than the horizontal gradient for convection free systems. Also note that since methane segregates to the hot region, its concentration is higher in the bottom than in the top of the reservoir. When k increases, the linear horizontal variation of the mole fraction still occurs except for a very thin region near the vertical boundaries. Fig. 5 depicts the mole fraction at $z = W/2$ vs. x for $k = 0$, 1, 10 and 100 md (similar behavior occurs at other values of z). This figure clearly shows the linear horizontal variation of mole fraction mentioned above. Furthermore, Figs. 4 and 5 show that more compositional variation occurs for $k = 1$ md than $k = 0$ and $k = 10$ md. This behavior has been observed by Riley and Firoozabadi [12]. They report that compositional variation reaches a maximum when the permeability increases and then decays as $1/k$. This maximum occurs in the neighborhood of $k = 0.5$ md.

Fig. 6 depicts the horizontal gradient of mole fraction (at $x = H/2$ and $z = W/2$) vs. k for three values of thermal diffusion coefficient C^T. Since the horizontal variation of the mole fraction is linear, this gradient does not depend on x. Results show that, in the range of permeabilities studied, the behavior reported by Riley and Firoozabadi [12] (maximum segregation for a permeability of about 0.5 md) occurs only for high values of C^T (for the specific value of the pressure diffusion coefficient $C^P = -1.15 \times 10^{-15}$ kg/m.Pa.s). For $C^T = 1.5 \times 10^{-10}$ kg/m.s °K, for instance, such behavior is not observed; the horizontal gradient of mole fraction decreases monotonically with k (Fig. 6). The change of trend of the behavior of the horizontal compositional gradient occurs for a critical value, C^T_c, of the thermal diffusion coefficient: $1.5 \times 10^{-10} < C^T_c < 2.0 \times 10^{-10}$ kg/m.s °K. Thermal diffusion effect on compositional variation becomes less significant for high permeabilities where mass transport due to natural convection overrides that due to diffusion phenomena. As permeability increases, the reservoir composition becomes almost homogeneous. This is clearly shown in Fig. 4 for $k = 100$ md. Similar behavior is observed for different values of C^T. Figs. 7 to 10 show mole fraction contour lines for different values of C^T for permeabilities from 0 to $k = 100$ md. Those figures show that, the increase of C^T results in more compositional variation. From Fig. 7, one observes that, at $k = 0$ (convection-free), the mole fraction contour lines are straight lines; the slope of those lines changes with C^T. For $C^T = 0$, for instance, the mole fraction contour lines are horizontal. The slope of the mole fraction contour lines is negative for $C^T = 1.5 \times 10^{-10}$ kg/m.s °K but becomes positive at $C^T = 2.0 \times 10^{-10}$ kg/m.s °K. For $C^T > C^T_c$, the slope remains positive.

5.2 Pressure diffusion

For the two-component hydrocarbon mixture of C_1/nC_4, thermal diffusion and pressure diffusion affect compositional variation in opposite directions. Pressure diffusion causes the bottom richer in heavier component while thermal diffusion results the segregation of the heavier component to the cold boundary at the top. The resulting effect of those two diffusion phenomena depends mainly on the ratio $(-C^T T_z)/(C^P P_z)$, where P_z is

the vertical pressure gradient (which is nearly constant). Numerical results show that, for $C^T \approx C_c^T$, this ratio reaches 1; that is $C_c^T \approx -C^P P_z/T_z$. Given that the reservoir height considered in our simulation is $H = 150$m and that the pressure at the center is assigned the value 1.103×10^7 Pa, P_z is roughly equal to -4.829×10^3 Pa/m and then $P_z/T_z \approx 1.325 \times 10^5$ Pa/°K; thus $C_c^T \approx -(1.325 \times 10^5$ Pa/°K)$\times C^P$. For $C^P = -1.15 \times 10^{-15}$ kg/m.Pa.s, one obtains: $C_c^T \approx 1.523 \times 10^{-10}$ kg/m.s. °K, which is in good agreement with the results reported above. Compositional variation closely depends on $(-C^T T_z)/(C^P P_z)$; thermal diffusion overrides pressure diffusion when this ratio is larger than 1 whereas pressure diffusion is the main phenomenon which affects compositional variation when $(-C^T T_z)/(C^P P_z) < 1$. The horizontal variation of mole fraction behaves differently when $(-C^T T_z)/(C^P P_z) > 1$ and $(-C^T T_z)/(C^P P_z) < 1$. For $(-C^T T_z)/(C^P P_z) > 1$, the horizontal gradient of mole fraction reaches a maximum around $k = 1$ md. For $(-C^T T_z)/(C^P P_z) < 1$, the horizontal gradient of mole fraction decreases monotonically when the permeability increases.

Figs. 11, 12 and 13 show the mole fraction contour lines for $C^P = 0$, -1.15×10^{-15}, and -2.0×10^{-15} kg/m.Pa.s, respectively. Since pressure and thermal diffusion have opposite effects on vertical compositional variation, we observe that, for impermeable media, as well as low permeability media, more vertical composition variation occurs for $C^P = 0$ than $C^P = -1.15 \times 10^{-15}$ and $C^P = -2.0 \times 10^{-15}$ kg/m.Pa.s, that is the mole fraction contour lines are near vertical for $C^P = -1.15 \times 10^{-15}$ and $C^P = -2.0 \times 10^{-15}$ kg/m.Pa.s than $C^P = 0$. When the permeability increases, the two approach each other (in terms of reservoir composition) both in horizontal and vertical directions. This maybe due to the fact that, at high permeabilities, natural convection overrides both diffusion phenomena and composition becomes homogeneous. Nevertheless, for all permeabilities (up to 100 md), more compositional variation occurs when pressure diffusion is neglected.

Fig. 14 depicts horizontal gradient of mole fraction vs. permeability at three different values of C^P. For $k = 0$, the same horizontal gradient of mole fraction realizes for different values of C^P and the horizontal pressure gradient is identically zero. For $C^P = 0$ and $C^P = -1.15 \times 10^{-15}$ kg/m.Pa.s the horizontal composition gradient reaches a maximum for some permeability of say $k = 1$ md and then decays. Furthermore, when C^P varies at constant permeability, the horizontal gradient of mole fraction reaches a maximum for $C^P = 0$. For $C^P = -2.0 \times 10^{-15}$ kg/m.Pa.s, the horizontal gradient of mole fraction decreases monotonically when the permeability increases; for this value of C^P, $C_c^T \approx -(1.325 \times 10^5$ Pa/°K)$\times C^P = 2.65 \times 10^{-15}$, whereas $C^T = 2.0 \times 10^{-10}$ kg/m.s °K. As mentioned above, when $C^T < C_c^T$, pressure diffusion overrides thermal diffusion and the above trend of horizontal compositional gradient occurs.

6 Conclusions and Remark

This work investigates the compositional variation of a single phase two-component system due to combined effects of natural convection and diffusion. We studied the effect of permeability, thermal diffusion and pressure diffusion on the compositional variation by using a numerical model. From the results presented we conclude that convection can enhance or weaken the horizontal composition variation depending on the magnitude of the

thermal diffusion and pressure diffusion coefficients. For the specific example presented in this work, the horizontal gradient of mole fraction reaches a maximum in the neighborhood of $k = 0.5$ md for $(-C^T T_z)/(C^P P_z) > 1$, whereas it decreases monotonically when k increases for $(-C^T T_z)/(C^P P_z) < 1$. However, for high permeabilities ($k > 10$ md), natural convection is the main phenomenon which affects compositional variation within the reservoir and results in nearly homogeneous system.

We finally mention that, due to the cross-diffusion effects, compositional variation in multicomponent mixtures may drastically differ from that in binary mixtures [13].

7 Nomenclature

C^w coefficient of molecular diffusion in **J**
C^P coefficient of pressure diffusion in **J**
C^T coefficient of thermal diffusion in **J**
C_c^T critical value of the coefficient of thermal diffusion
g gravity acceleration
H reservoir height
J diffusive mass flux
k permeability
n normal vector
P pressure
P_0 pressure at the reservoir center
T temperature
T_0 temperature at the reservoir center
T_x horizontal thermal gradient
T_z vertical thermal gradient
t time
v_x horizontal velocity
v_z vertical velocity
v velocity vector
W reservoir width
w weight fraction
w_0 weight fraction at the reservoir center
x, z coordinates
z upward vertical unit vector

Greek symbols

β_w compositional expansion coefficient
β_T thermal expansion coefficient
χ mole fraction
ϕ porosity
μ dynamic viscosity
ρ density
ρ_0 density at w_0 and T_0

References

[1] R.S. Metcalfe, J.L. Vogel and R.W. Morris, Compositional gradients in the Anschutz Ranch East field, *SPE Res. Eng., pp. 1025-1032, August 1988.*

[2] A.N. Hamoodi, A.F. Abed and A. Firoozabadi, Compositional modeling of two-phase hydrocarbon reservoirs, *SPE 36244 presented at the 7th Abu Dhabi International Petroleum Exhibition and Conference, Abu-Dhabi, UAE, 13-16 October 1996.*

[3] S.T. Lee and M. Chaverra, Modeling and interpretation of condensate banking for the near critical Cupiagua Field, *SPE 49265 presented at the 1998 SPE Annual Technical Conference and Exhibition, New Orleans, Louisiana, September 27-30, 1998.*

[4] A.M. Schulte, Compositional variation whiten a hydrocarbon column due to gravity, *SPE 9235 presented at the 1980 SPE Annual Technical Conference and Exhibition, Dallas, Texas, September 21-24, 1980.*

[5] F. Montel and P.L. Gouel, Prediction of compositional grading in a reservoir fluid column, *SPE 14410 presented at the 1985 SPE Annual Technical Conference and Exhibition, Las Vegas, Nevada, September 22-25, 1985.*

[6] A. Hirscberg, Role of asphaltenes in compositional grading of a reservoirs's fluid column, *J. Pet. Tech., pp. 89-94, January 1988.*

[7] R.J. Wheaton, Treatment of variations of composition in gas-condensate reservoirs, *SPE Res. Eng., pp. 239-244, May 1991.*

[8] T. Holt, E. Lindeberg, and S.K. Ratkje The effect of gravity and temperature gradients on methane distribution in oil reservoirs, *SPE 11761, 1983.*

[9] P. Belery, F.V. da Silva, Gravity and thermal diffusion in hydrocarbon reservoirs, *Third North Sea Chalk Research Symposium, Copenhagen, June 11-12, 1990.*

[10] C.H. Whitson and P. Belery, Compositional Gradients in Petroleum Reservoirs, *SPE 28000 prepared for presentation at the University of Tulsa Centennial Petroleum Engineering Symposium, Tulsa, Oklahoma, August 29-31, 1994.*

[11] D. Jacqmin, "Interaction of Natural Convection and Gravity Segregation in Oil/Gas Reservoirs", *SPE Res. Eng., (May 1990), pp. 233-238.*

[12] M. F. Riley and A. Firoozabadi, "Compositional Variation in Hydrocarbon Reservoirs with Natural Convection and Diffusion", *AIChE J., (Feb. 1998), pp. 452-464.*

[13] K. Ghorayeb and A. Firoozabadi, Modeling of multicomponent diffusions and convection in porous media, *SPE paper 51932 presented at the 15th Reservoir Simulation Symposium, 14-17 February 1999, Huston, TX, also submitted to SPE J., February 1999.*

[14] D. Y. Peng and D. B. Robinson, "A New Two-Constant Equation of State", *Ind. Eng. Chem. Fund., Vol. 15, pp. 59-64, 1976.*

[15] K. Ghorayeb and A. Firoozabadi, Natural convection and diffusion in fractured porous media, *submitted to SPE J., May 1998.*

[16] R. B. Bird, W. E. Stewart and E. N. Lightfoot, Transport Phenomena (chapter 18, page 568), *John Wiley and Sons, Inc. (1960).*

[17] S. R. de Groot and P. Mazur, Non-Equilibrium Thermodynamics, (chapters 4 and 5) *Dover Edition, New York, 1984.*

[18] A. Firoozabadi, Thermodynamics of Hydrocarbon Reservoirs (chapter 2, pages. 81 and 95), *Mc Graw-Hill, New York, 1998.*

[19] S. V. Patankar, Numerical Heat Transfer and Fluid Flow, (chapter 5), *Hemisphere, Washington, 1980.*

[20] P.M. Sigmund, Prediction of molecular diffusion at reservoir conditions. Part I – Measurement and prediction of binary dense gas diffusion coefficients. *J. Cand. Petr. Tech., pp. 48-57, April-June, 1976.*

[21] W.M. Rutherford and J.G. Roof, Thermal diffusion in methane–n-butane mixtures in the critical region, *J. Phys. Chem., Vol. 63, pp. 1506-1511, 1959.*

W	3000 m
H	150 m
χ_0	0.2
P_0	1.10×10^7 Pa
T_0	338.5 ^{o}K
ρ_0	495.3 kg/m^3
C^w	-2.88×10^{-7} kg/m.s
T_x	$+1.82^oK$/ 1000 m
T_z	-3.65^oK/ 100 m
ϕ	0.25
μ	200 kg/m.s
β_w	$0.58 \times 10^{+3}$
β_T	2.05×10^{-2} ^{o}K^{-1}

Table 1: Relevent Data.

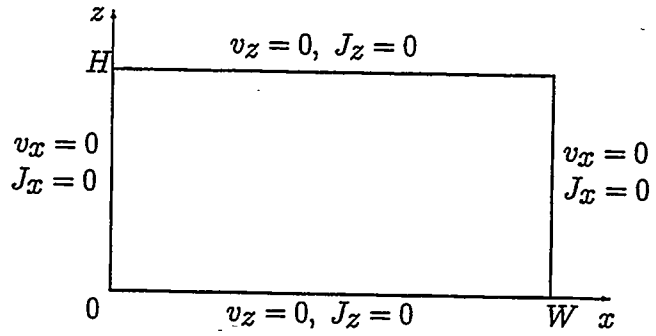

Figure 1: Geometry and boundary conditions.

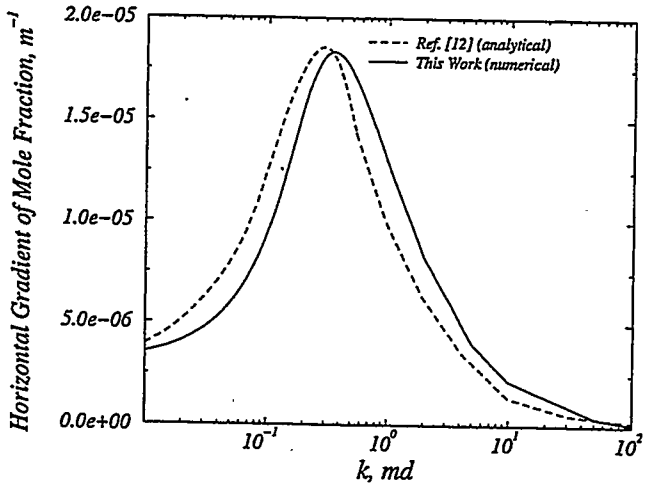

Figure 2: Horizontal gradient of mole fraction in the center of the reservoir vs. k: $C^w = -4.53 \times 10^{-7}$ kg/m.s, $C^P = -0.78 \times 10^{-15}$ kg/m.Pa.s and $C^T = 2.81 \times 10^{-10}$ kg/m.s. ^{o}K

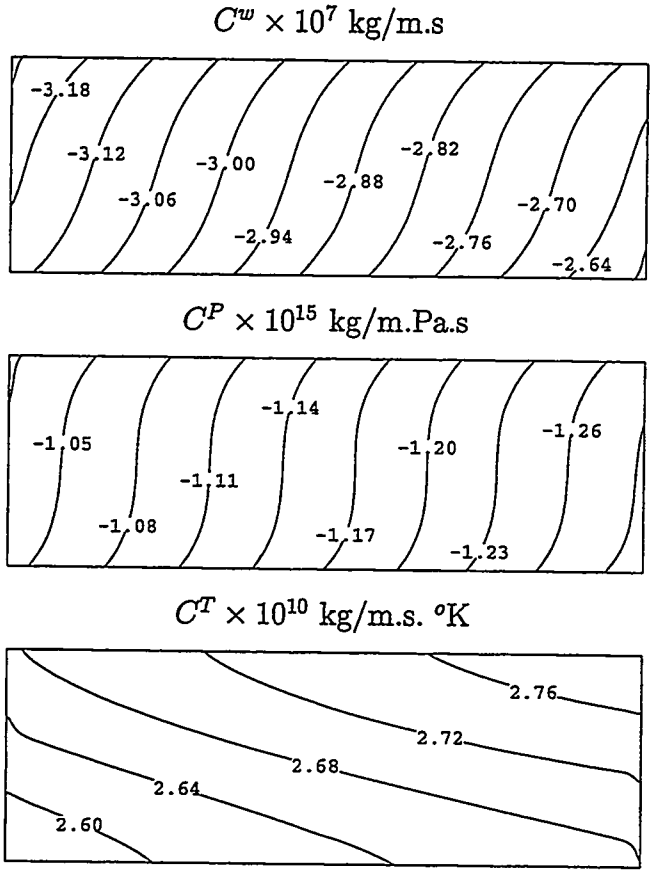

Figure 3: C^w, C^P, and C^T contour lines for $k = 1$md.

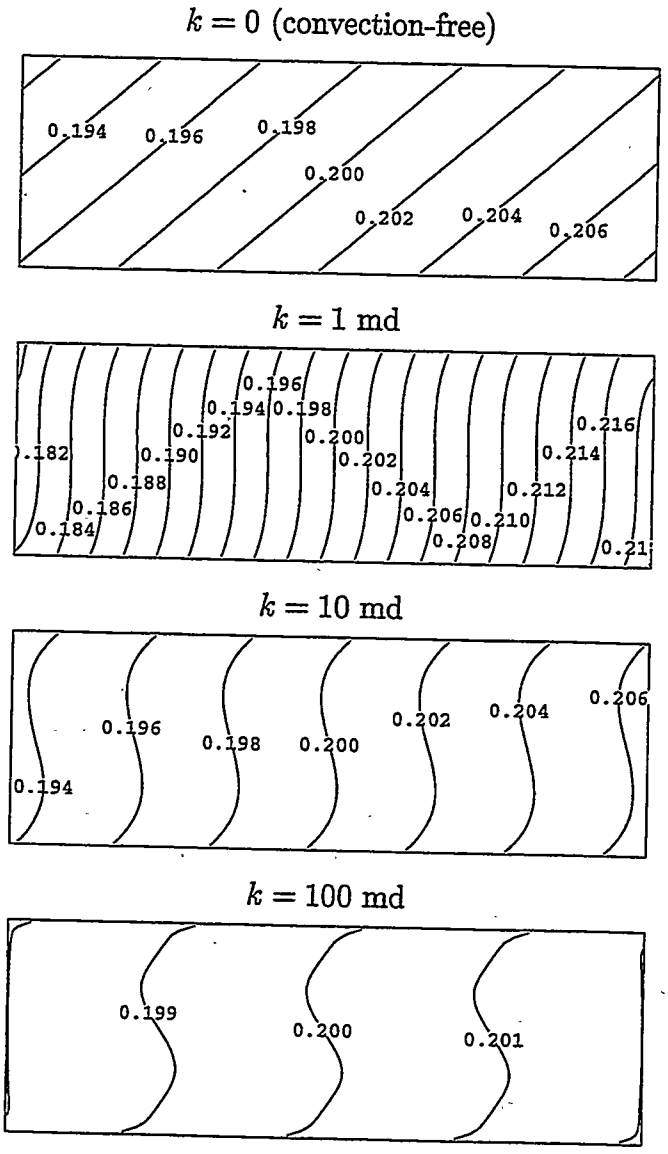

Figure 4: Mole fraction contour lines for different permeabilities: $C^T = 2.5 \times 10^{-10}$ kg/m.s. ^oK.

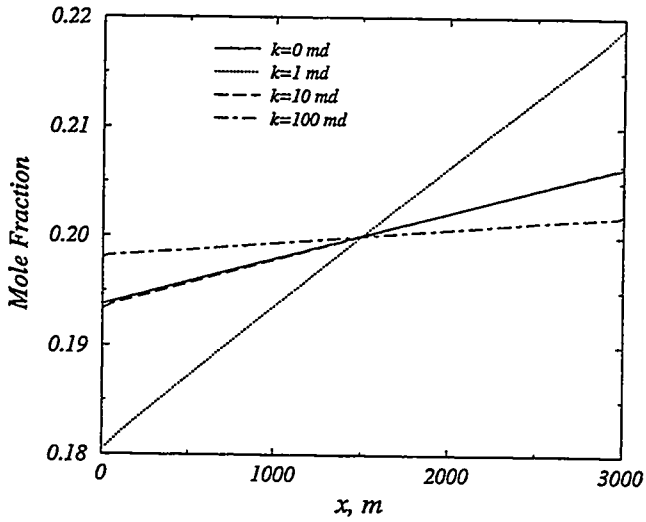

Figure 5: Mole fraction vs. x at $z = W/2$ for different permeabilities: $C^T = 2.5 \times 10^{-10}$ kg/m.s. ^{o}K, $C^P = -1.15 \times 10^{-15}$ kg/m.Pa.

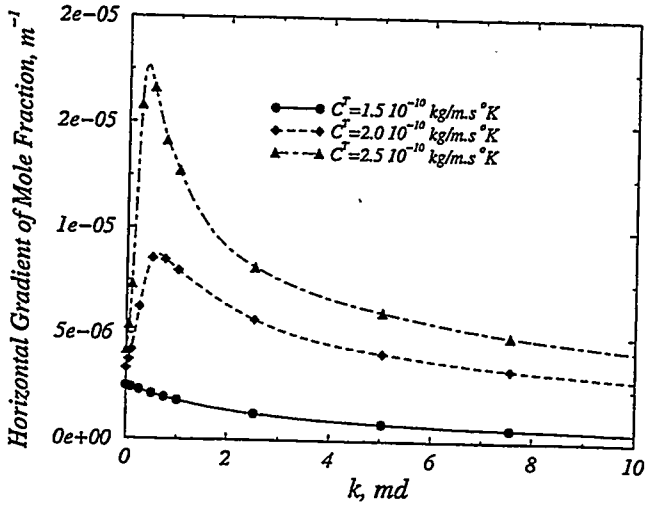

Figure 6: Horizontal gradient of mole fraction in the center of the reservoir vs. k for different values of C^T: $C^P = -1.15 \times 10^{-15}$ kg/m.Pa.

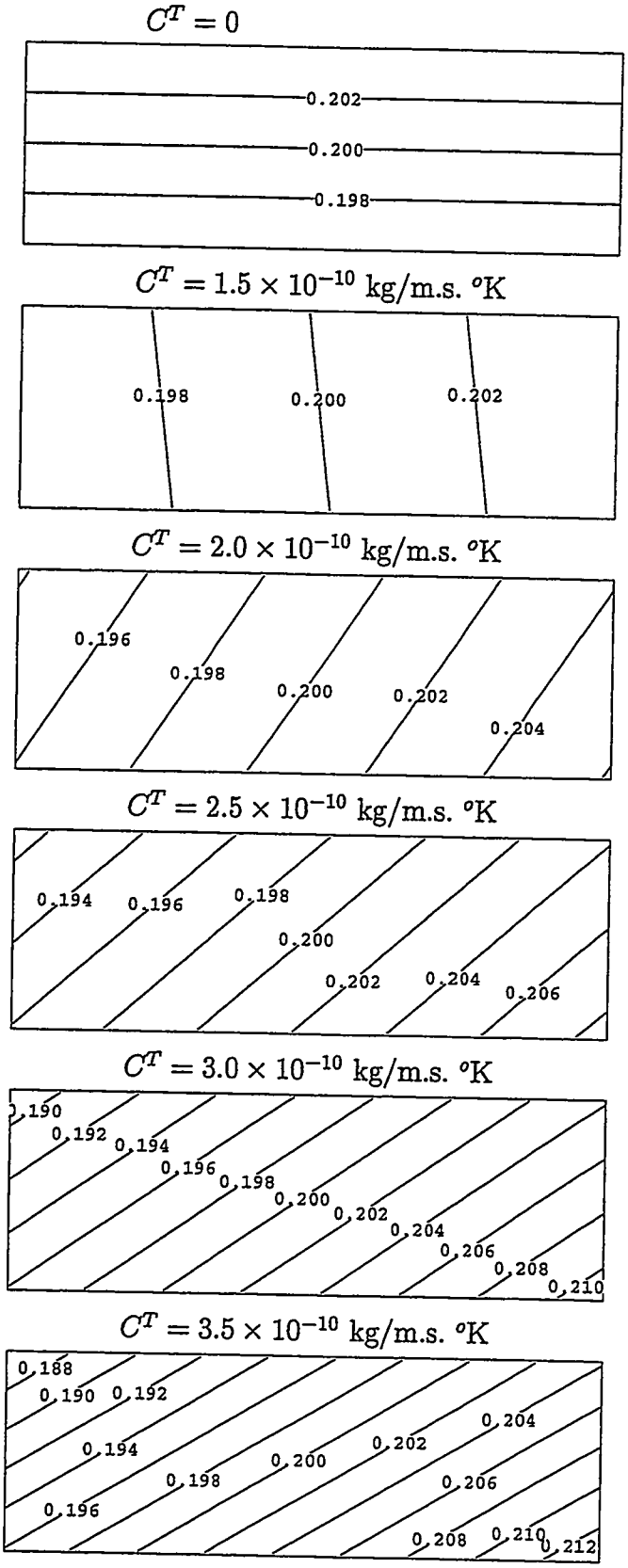

Figure 7: Mole fraction contour lines for different values of C^T: $k = 0$md (convection-free), $C^P = -1.15 \times 10^{-15}$ kg/m.Pa.

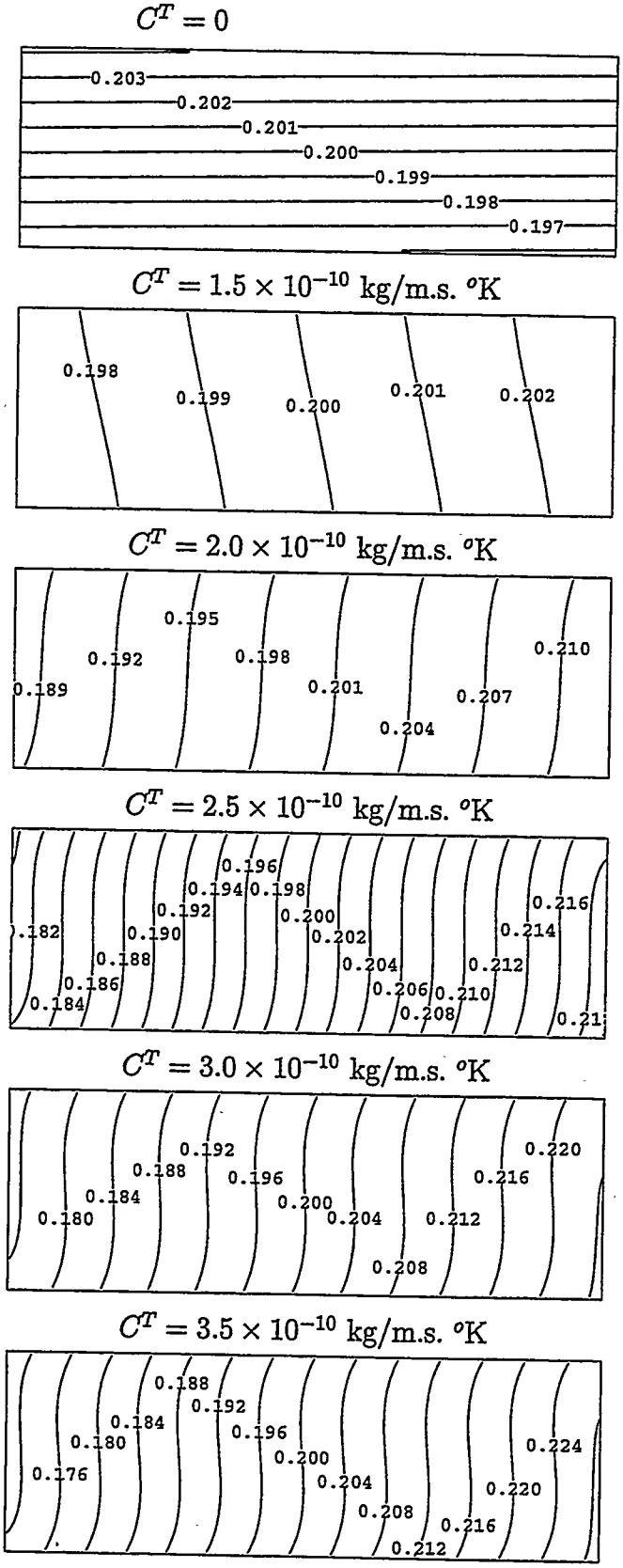

Figure 8: Mole fraction contour lines for different values of C^T: $k = 1$md, $C^P = -1.15 \times 10^{-15}$ kg/m.Pa.

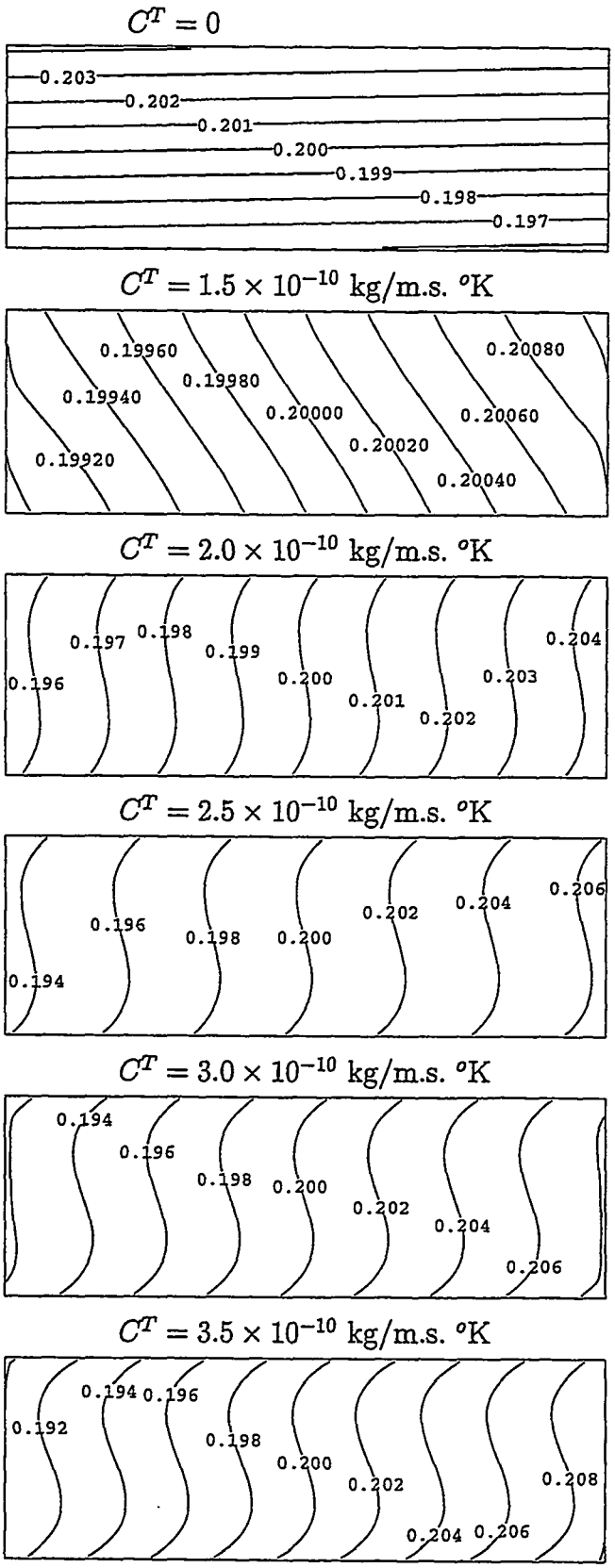

Figure 9: Mole fraction contour lines for different values of C^T: $k = 10$md, $C^P = -1.15 \times 10^{-15}$ kg/m.Pa.

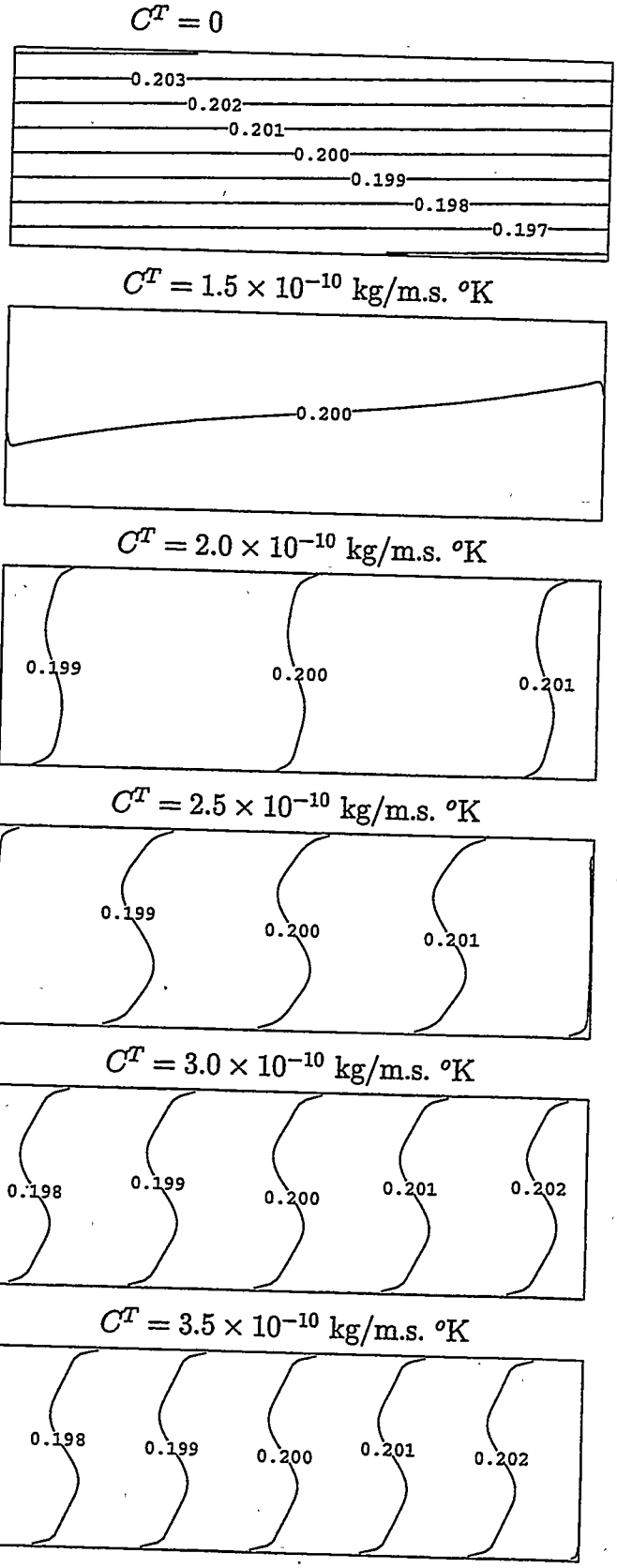

Figure 10: Mole fraction contour lines for different values of C^T: $k = 100$md, $C^P = -1.15 \times 10^{-15}$ kg/m.Pa.

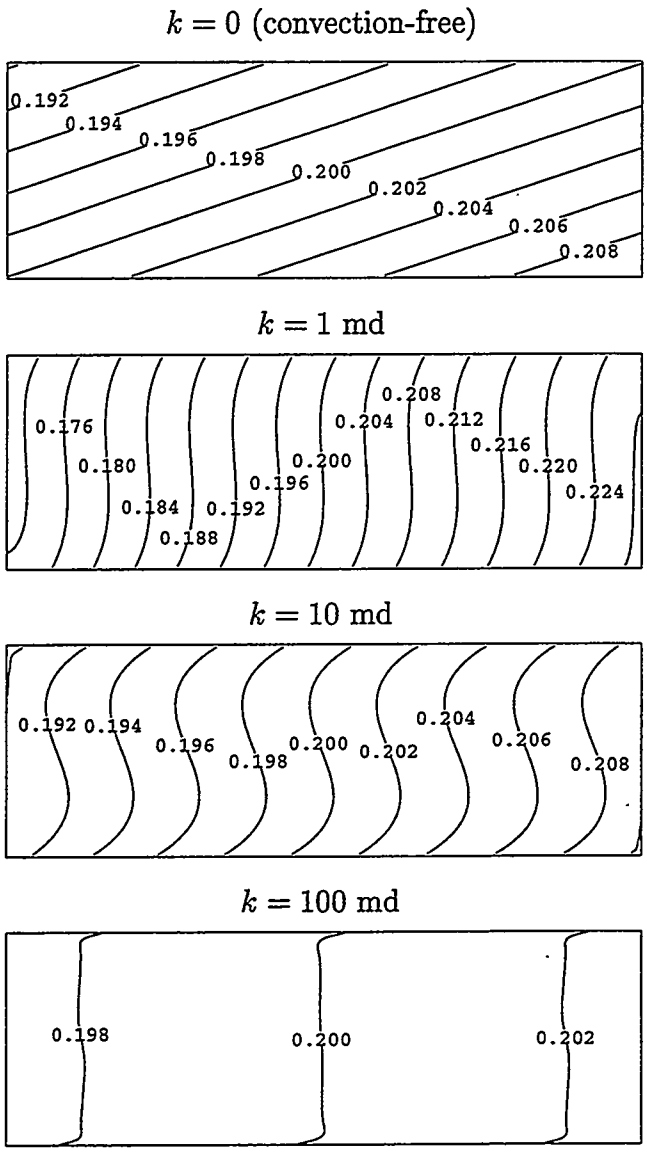

Figure 11: Mole fraction contour lines for different permeabilities: $C^P = 0$ kg/m.Pa: $C^T = 2.0 \times 10^{-10}$ kg/m.s. ^oK

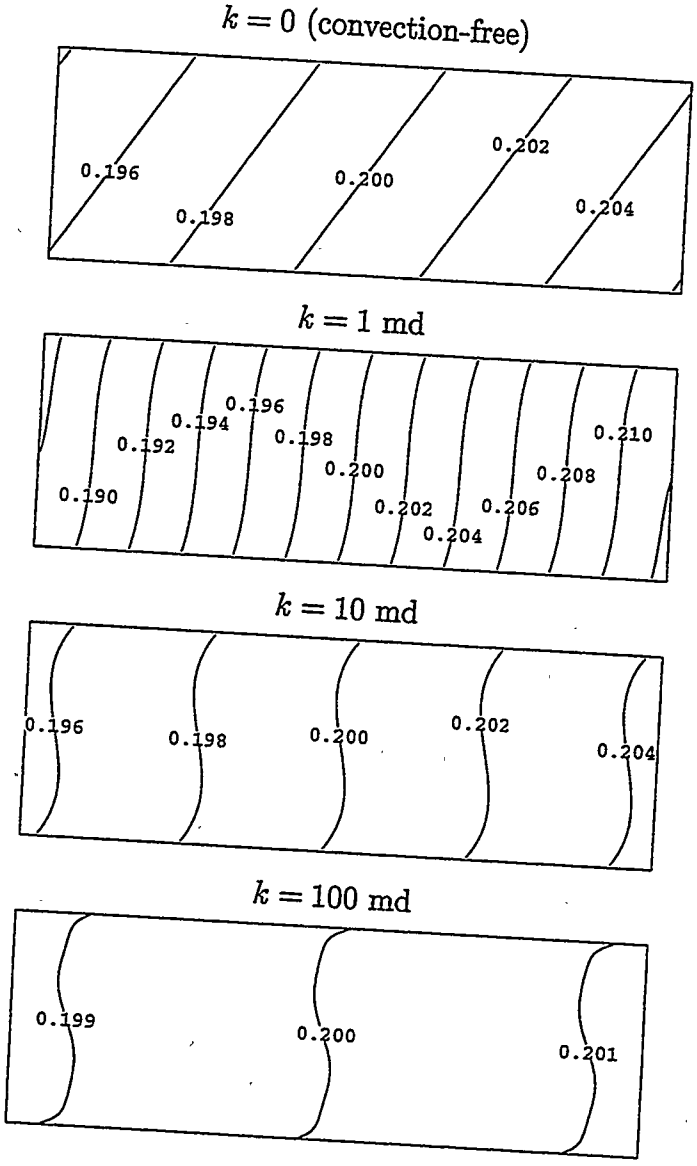

Figure 12: Mole fraction contour lines for different permeabilities: $C^P = -1.15 \times 10^{-15}$ kg/m.Pa.s: $C^T = 2.0 \times 10^{-10}$ kg/m.s. ^oK

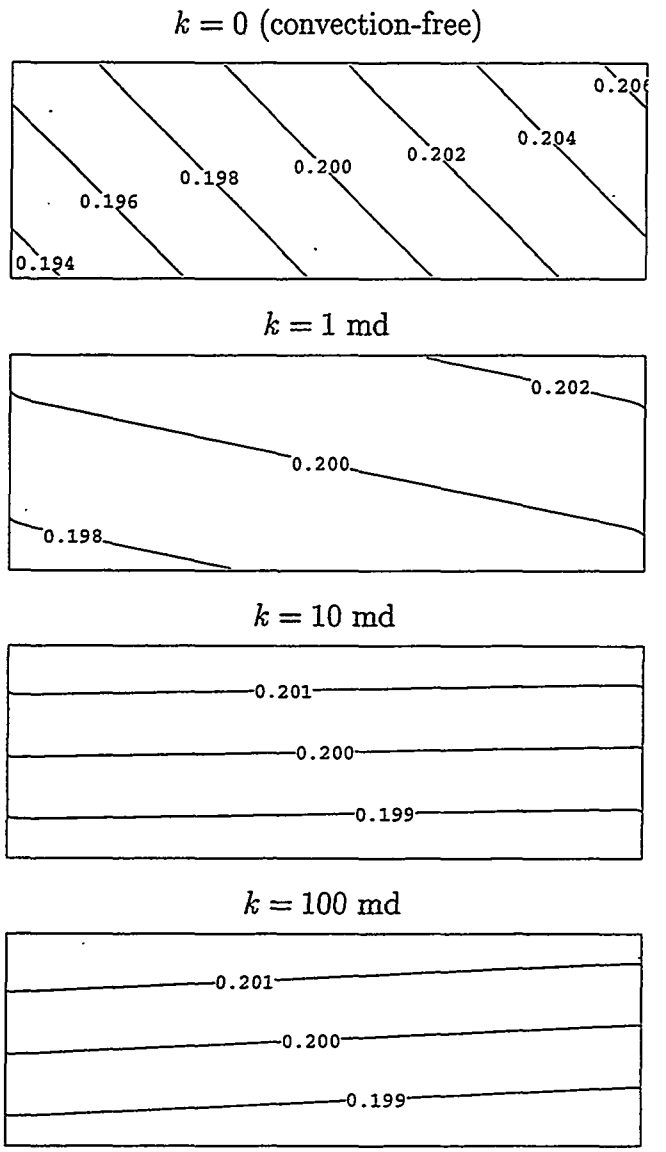

Figure 13: Mole fraction contour lines for different permeabilities: $C^P = -2.0 \times 10^{-15}$ kg/m.Pa.s: $C^T = 2.0 \times 10^{-10}$ kg/m.s. ^oK

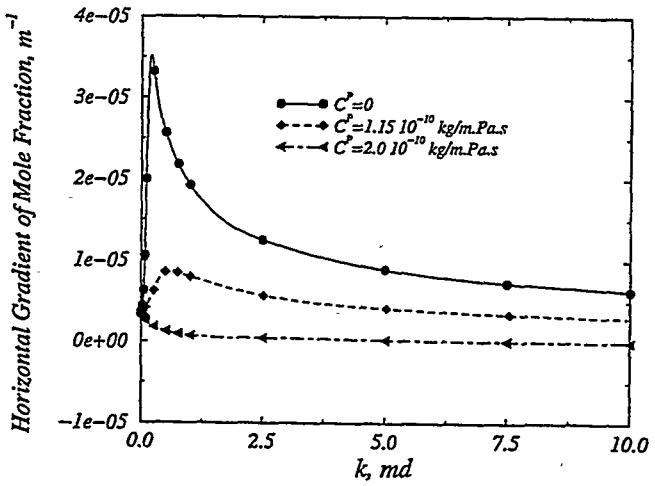

Figure 14: Horizontal gradient of mole fraction in the center of the reservoir vs. k for different values of C^P: $C^T = 2.0 \times 10^{-10}$ kg/m.s. ^{o}K

Part IV - Natural Convection and Diffusion in Fractured Porous Media

KASSEM GHORAYEB AND ABBAS FIROOZABADI

1 Summary

Compositional variation in a rectangular two-dimensional (x, z) fractured porous medium containing a two-component single phase fluid in the presence of a prescribed linear temperature field is considered. The work examines the effect of the fracture parameters: fracture permeability, fracture aperture, fracture intensity and fracture connectivity on the fluid composition variation. Numerical results reveal that, due to high fracture permeability, a pronounced convective motion within the fracture takes place, whereas the composition is only affected beyond a certain fracture permeability. Numerical results also show that the flow velocity within the fracture increases as the fracture aperture decreases; the compositional variation, however, decreases with the increased fracture aperture. The effect of connected and discrete fractures on composition variation was also studied; connected fractures influence the compositional variation much more than discrete fractures as expected. The convection cells are mainly loops which develop within the connected fractures.

2 Introduction

Examination of the compositional variation of reservoir fluids in hydrocarbon reservoirs reveals various trends. In some reservoirs there is substantial variation of composition in the horizontal direction (Hamoodi *et al.* [1]). In many other reservoirs, there is a large variation of composition in the vertical direction (Neveux and Sathikumar [2]). There are also reservoirs that have no variation of composition in the entire reservoir; such reservoirs may have an oil column thickness of 1.5 km and a horizontal extension larger than 10 km (Saidi [3]).

The purpose of this work is to understand composition variation in fractured hydrocarbon reservoirs and to relate the composition variation to reservoir characterization.

There are four distinct mechanisms that affect the variation of composition in the single phase in a hydrocarbon reservoir. These mechanisms are: 1) thermal diffusion, 2) pressure diffusion, 3) molecular diffusion, and 4) natural convection. Thermal diffusion is the tendency of a convection free mixture to separate under a thermal gradient. Molecular diffusion is the tendency to mix due to concentration gradient. Pressure diffusion is separation by pressure gradient; it is negligible in the horizontal direction even when

there exists natural convection, but may be pronounced in the vertical direction due to high vertical pressure gradient. Natural convection is the convective circulation due to density gradient. Density gradient is established due to temperature and concentration gradients. A pronounced effect of natural convection on compositional variation may occur in homogeneous media [5].

There are very few studies that combine the effect of convection and diffusion on the compositional variation in hydrocarbon reservoirs. These studies include the works of Jacqmin [4], and Riley and Firoozabadi [5]. Both studies address compositional variation in homogeneous porous media. Jacqmin's study is concerned with a wide variety of conditions, sloping reservoirs, and even two phases but does not include thermal diffusion. He uses a perturbation analysis where approximations are made to the governing equations. Based on his study, Jacqmin states that, under certain conditions the fluid composition reorients itself in such a way as to inhibit convection. Riley and Firoozabadi [5] studied the effect of thermal, pressure and Fickian diffusion and natural convection on compositional variation in a cross-sectional reservoir with a prescribed linear temperature field. The behavior is investigated using a method of successive approximations which iterates on Poisson's equation. This behavior is then incorporated in a simplified perturbation solution which provides accurate results for horizontal composition variation. Riley and Firoozabadi [5] show that a small amount of convection can cause the horizontal composition gradient to increase until a maximum is reached and then decays as $1/k$.

The work of Jacqmin, and Riley and Firoozabadi is limited to homogeneous porous media. This work is concerned with a numerical study of convection and diffusion in fractured porous media. The conservation equations of mass and species and Darcy's law, together with the boundary conditions and the matching conditions at the matrix block/fracture interface, are numerically integrated in the whole cross section (in both matrix blocks and fractures). The numerical investigations were carried out for fracture permeabilities varying by six orders of magnitude. The fracture aperture was varied from 0.1 to 1mm. However, in view of the large number of parameters, no attempt was made to present a complete parametric study.

3 Mathematical Formulation

We consider a two-dimensional fractured porous media with width W and height H (Fig. 1) saturated by a binary mixture of C_1/nC_4. The fractured porous media are comprised of matrix blocks and fractures of permeabilities k_m and k_f, respectively. The matrix and fracture porosities are assumed to be the same. We assume that the Oberbeck-Boussinesq approximation (Chandrasekhar [6]) is valid in the range of temperature, pressure and composition expected so that the density ρ is constant except in the buoyancy term ($\rho g z$) where it varies linearly with the temperature T and the weight fraction w:

$$\rho(T,w) = \rho_0 \left[1 - \beta_T (T - T_0) - \beta_w (w - w_0)\right], \tag{1}$$

where ρ_0, $\beta_T = (-1/\rho_0)(\partial\rho/\partial T)_w$ and $\beta_w = (-1/\rho_0)(\partial\rho/\partial w)_T$ are the density at temperature T_0 and weight fraction w_0, the thermal expansion coefficient, and the compositional expansion coefficient, respectively. The coefficients β_T and β_w are calculated for the system C_1/nC_4, using the Peng-Robinson equation of state [7]. Fig. 2 depicts the density ρ

vs. temperature and mole fraction χ of methane. This figure clearly shows the validity of the assumption of linear variation of ρ vs. T and χ in the range of temperature, pressure and composition expected; β_T and β_w are thus the slopes of those lines.

The unsteady state conservation equations of mass and species are:

$$\nabla.\mathbf{v} = 0, \tag{2}$$

$$\rho_0 \frac{\partial w}{\partial t} + \rho_0 \nabla.(w\mathbf{v}) + \nabla.\mathbf{J} = 0, \tag{3}$$

where $\mathbf{v}$ and $\mathbf{J}$ are the velocity and the diffusive mass flux for component 1, respectively. The diffusive mass flux is given by the expression:

$$\mathbf{J} = C^w \nabla w + C^P \nabla P + C^T \nabla T, \tag{4}$$

where C^w, C^P and C^T are the coefficients of molecular diffusion, pressure diffusion and thermal diffusion, respectively. These coefficients are described in Ref. [5]. They are assumed constant in this work. Their variation can be readily accommodated by the numerical model. The diffusive flux, $\mathbf{J}$, results from the deviation in the velocity of component one from the velocity of the bulk fluid. Since, in the case of a two-component system, the diffusive flux of component two is equal to $-\mathbf{J}$ and the weight fraction of component two is equal to $1-w$, the equation expressing conservation of mass of component two will be a linear combination of Eqs. 2 and 3.

The bulk velocity, $\mathbf{v}$, is given by Darcy's law:

$$\mathbf{v} = -\frac{k}{\phi\mu}\left[\nabla P + \rho_0 \left(1 - \beta_T (T - T_0) - \beta_w (w - w_0)\right) g\mathbf{z}\right], \tag{5}$$

where P, g, k, μ and ϕ are the pressure, the acceleration due to gravity, the permeability, the viscosity and the porosity, respectively. The unit vector $\mathbf{z}$ points upwards. The substitution of Eq. 5 into 2 and the assumption that $(k/\phi\mu)$ is constant in each medium lead to the pressure equation:

$$\nabla^2 P = \rho_0 g \left(\beta_T \frac{\partial T}{\partial z} + \beta_w \frac{\partial w}{\partial z}\right). \tag{6}$$

The above equation will be used later in the numerical solution to the problem. The cross-sectional reservoir is assumed to be bounded by an impervious rock that has constant temperature gradients T_x and T_y in horizontal and vertical directions, respectively. We also assume that the conductive flow of heat is much greater than the convective flow and that thermal diffusivity is very large compared with compositional diffusivity. With these assumptions, the solution of the energy equation will have roughly the same temperature gradients as the bounding rock. In the following, the temperature field is assumed to be a linear function of x and z: $T = T_x x + T_z z + a$, where a is a constant. If we set the temperature at $x = W/2$ and $z = H/2$ equal to T_0, then, $T = T_x (x - W/2) + T_z (z - H/2) + T_0$.

3.1 Boundary Conditions

The boundary conditions for Eqs. 2, 3 and 5 are that the fluid does not cross the outer boundaries (Fig. 1):

$$\mathbf{J}.\mathbf{n} = 0 \qquad x = 0,\ W \text{ and } \quad z = 0,\ H, \tag{7}$$

$$\mathbf{v}.\mathbf{n} = 0 \qquad x = 0,\ W \text{ and } \quad z = 0,\ H, \tag{8}$$

where $\mathbf{n}$ is the unit normal vector. Eqs. 7 and 8 imply that:

$$C^w \frac{\partial w}{\partial x} + C^P \frac{\partial P}{\partial x} + C^T \frac{\partial T}{\partial x} = 0, \quad \text{and} \quad v_x = 0 \qquad x = 0, W, \tag{9}$$

$$C^w \frac{\partial w}{\partial z} + C^P \frac{\partial P}{\partial z} + C^T \frac{\partial T}{\partial z} = 0, \quad \text{and} \quad v_z = 0 \qquad z = 0, H. \tag{10}$$

From Eq. 5, we obtain the boundary conditions required for the integration of Eq. 6:

$$\frac{\partial P}{\partial x} = 0 \qquad x = 0, W, \tag{11}$$

$$\frac{\partial P}{\partial z} = -\rho_0 \left(1 - \beta_T \left(T - T_0\right) - \beta_w \left(w - w_0\right)\right) \qquad z = 0, H. \tag{12}$$

With the above Newman boundary conditions, weight fraction and pressure must be assigned at one point of the medium. In this work we set $w\left(W/2, H/2\right) = w_0$ and $P\left(W/2, H/2\right) = P_0$.

3.2 Conditions at the matrix-fracture interface

The matching conditions at the matrix-fracture interface are given by the continuity of the normal component of the total mass flux, the normal component of the diffusive mass flux, the pressure and the mole fraction. Because of incompressibility assumption, the total mass flux across the interface reduces to the normal velocity. Let us designate by "1" and "2" the matrix and fracture media which are separated by an interface. The matching conditions can thus be expressed by:

$$\left(\mathbf{v}.\mathbf{n}\right)_1 = \left(\mathbf{v}.\mathbf{n}\right)_2 \tag{13}$$

$$\left(C^w \frac{\partial w}{\partial n} + C^P \frac{\partial P}{\partial n} + C^T \frac{\partial T}{\partial n}\right)_1 = \left(C^w \frac{\partial w}{\partial n} + C^P \frac{\partial P}{\partial n} + C^T \frac{\partial T}{\partial n}\right)_2 \tag{14}$$

$$\left(P\right)_1 = \left(P\right)_2 \tag{15}$$

$$\left(w\right)_1 = \left(w\right)_2 \tag{16}$$

Note that the matching conditions are not required for the tangential velocity at the interface. This is because we use Darcy's law to calculate the bulk velocity $\mathbf{v}$.

4 Numerical Scheme

Eqs. 3, 5 and 6 together with the boundary conditions given by Eqs. 9 to 12 and the matching conditions given by Eqs. 13 to 16 are numerically integrated using the finite

volume method (see Patankar [8]) with a nonuniform rectangular grid system. The spatial discretization is performed using a second-order centered scheme. A semi-implicit first-order scheme is used for the temporal integration. We seek the steady state solution and iterate on the unsteady system until the steady state is reached. In this work convergence to the steady state is assumed when the absolute relative error of concentration is found to be less than 10^{-7} between the two successive iterations at each grid point.

The discretization of Eqs. 3 and 6 gives rise to large sparse systems of linear equations. The matrices corresponding to those equations are pentadiagonal and are amenable to solution by iterative methods. However, the integration of those systems is a major task. The matrices are highly ill-conditioned because of 1) the spatial discontinuity in permeability of matrix and fractures, and 2) the small fracture thickness in comparison to the matrix size. Thus, iterative methods may not be suitable unless special robust preconditioners are used. For such problems, direct methods are commonly used in reservoir simulation. In this work, the direct method of D4 Gaussian Elimination is used. Details about the D4 algorithm can be found in Price and Coats [9], and Stringer *et al.* [10].

In this work, we use eight different configurations of fractured porous media to study the effect of fracture parameters on the variation of composition. These configurations are sketched in Fig. 3. Four configurations relate to connected fractures; the four other configurations relate to discrete fractures (Fig. 3). Calculations are performed using gird sizes of 309×159, 313×161, 325×125, 345×135, 345×135, 345×135, 41×135, and 345×41 to model configurations 1, 2, 3, 4, 5, 6, 7 and 8, respectively. Three mesh points are used to model the flow in the fracture. The remaining points are distributed in the matrix blocks. To study the effect of grid size, numerical runs were performed with different mesh grids either in the matrix blocks or in the fractures. We found that using finer grids than those above do not significantly improve the accuracy of the results. The nodal points are uniformly distributed in the fractures, while a nonuniform grid is used in the matrix blocks. Fig. 4 shows the grid for configurations 1 and 3 with the zooms in and around fractures (The dashed lines represent the fracture-matrix interface).

5 Results

We first verified the numerical results from our model with the analytical work presented in Ref. [5] for unfractured media. The agreement was excellent. The main goal of this study is, however, the investigation of the effect of fracture parameters on compositional variation in hydrocarbon reservoirs. We assume that the reservoir consists of matrix blocks of permeability $k_m = 1$md (constant in all the calculations) and horizontal and/or vertical fractures of permeability $k_f = 1$ to 10^6md and aperture $f_a = 1$ to 0.1mm. All the fractures of a given configuration are assumed to have the same permeability and aperture. The fractures may or may not be connected. All the numerical investigations are performed for a 30×15m cross section ($W = 30$m and $H = 15$m). The fracture parameters considered in this study are:

1) fracture permeability,

2) fracture aperture,

3) fracture intensity and

4) fracture connectivity.

Fracture permeability and fracture aperture are related through the cubic law. However, in this study we treat them as independent parameters. Configuration 1 shown in Fig. 3 consists of a large matrix surrounded by one fracture. This configuration is used to investigate the effect of fracture permeability and fracture aperture on the compositional variation. Configurations 2, 3 and 4 consist of a network of 2×2, 8×4 and 10×5 matrix blocks, respectively all surrounded by fractures (see Fig. 3). Those configurations are considered to study the effect of fracture intensity. Configurations 5, 6, 7 and 8 represent fractures that are not connected. Configuration 5 is similar to configuration 1 aside from the fact that the surrounding fracture is blocked by a rock with the matrix permeability. In configuration 6, four rocks of equal permeabilities block the surrounding fracture, one rock in the middle of each side of the fracture. Configuration 7 consists of 6 horizontal, equidistant, fractures separated by 5 matrix blocks. Configuration 8 consists of 11 vertical, equidistant, fractures separated by 10 matrix blocks. The data used in all the simulations are presented in Table 1. The coefficient of pressure diffusion term is the same as the one that was used in Ref. [5]; the coefficients of molecular diffusion and thermal diffusion are different. The effect of fracture permeability, fracture aperture, fracture intensity and fracture connectivity on the compositional variation is presented next.

5.1 Fracture permeability

The fracture aperture f_a is set to 1mm. The calculations are performed for $k_f = 1$ (that is, $k_f = k_m$), 10, 10^2, 10^3, 10^4, 10^5 and 10^6md. Mole fraction contours are presented in Fig. 5. This figure shows that with the increase in fracture permeability, the composition stays constant but beyond a certain fracture permeability the mole fraction contours become affected and tend to be vertical (in Fig. 5, the distance between the contours is set 0.002). Fig. 6 depicts the horizontal variation of mole fraction vs. x at $z = H/2$. This figure reveals the same trend as in Fig. 5. It also shows that the composition varies linearly vs. x aside from the region close to the vertical boundaries. For $k_f > 10^4$md, the variation is linear across the whole distance. The implication of this linear behavior is that, at high fracture permeabilities the composition variation is not affected by vertical boundaries. Consequently, the results obtained for a small cross section could be applicable to a total reservoir with a large width. Fig. 7 presents the horizontal mole fraction gradient (at $x = W/2$ $z = H/2$) vs. k_f. As was shown above, up to $k_f \approx 10^3$md, the horizontal mole fraction gradient decreases slightly with k_f. For $k_f > 10^3$md, the horizontal mole fraction gradient decreases sharply (Fig. 7).

The velocity field corresponding to this configuration consists mainly of a loop within the fracture. The velocity in the matrix is very small compared with that in the fracture even near the matrix-fracture interface. This is in part due to the use of Darcy's law, where no continuity conditions are required for the tangential velocity at the interface. Darcy's law allows for slip-flow at the matrix-fracture interface. The no-slip flow conditions affect only a thin boundary layer at the interface, while the flow in the remaining part of the matrix is not appreciably affected by the assumption of "slip" conditions. Fig. 8 shows the

velocity field for $k_f = 10^5$md; to facilitate the visualization of the velocity field, fracture aperture f_a, which is equal to 1mm is enlarged. Fig. 9 shows a plot of the maximum horizontal velocities in the fracture vs. k_f. Note that unlike the composition gradient, fracture velocity increases with fracture permeability over the entire range.

5.2 Fracture aperture

Configuration 1 is also used to study the effect of fracture aperture on the compositional variation for constant fracture permeability. Calculations are performed for $f_a = 1$, 0.75, 0.5, 0.25 and 0.1mm. Results for mole fraction contours and horizontal compositional variation for $f_a = 0.1$mm are presented in Figs. 10 and 11, respectively. By comparing results depicted in these two figures with the corresponding results for $f_a = 1$mm in Figs. 5 and 6, we find that compositional variation is much less affected for $f_a = 0.1$mm than for $f_a = 1$mm for the same value of fracture permeability.

Figs. 12, 13 and 14 present mole fraction contours, horizontal compositional variation and horizontal mole fraction gradient for various fracture apertures. It is seen that the increase in fracture aperture results in the homogeneity of composition (see Figs. 12 and 13). Fig. 14 (right) shows that in a log-log graph, the horizontal gradient of mole fraction varies nearly linearly with fracture aperture; this behavior implies that the function describing the variation of the horizontal gradient of mole fraction with f_a takes the form $A(f_a)^B$. By linear regression, we find the expression $0.0199(f_a)^{-0.486}$.

Figs. 15 and 16 show the fracture horizontal velocity and the maximum fracture horizontal velocity, $v_{x_{max}}$, respectively. It was intuitively expected that the fracture velocity would decrease with a decrease in f_a; for all calculations, we find that, the velocity increases when f_a decreases. The trend, however, should reverse when f_a becomes very small, of the order of microns. Similarly to the behavior of the horizontal gradient of mole fraction, the function describing the variation of $v_{x_{max}}$ with f_a takes the form $A(f_a)^B$ (see Fig. 16 right). By linear regression, we find the expression $0.00377(f_a)^{-0.541}$.

5.3 Fracture intensity

In all the previous calculations, only configuration 1 is studied. Here, three other configurations (Fig. 3) with different fracture intensities are investigated.

Figs. 17 and 18 present the mole fraction contours, and horizontal composition variation vs. x at $z = H/2$, respectively, for $k_f = 10^5$md and $f_a = 1$mm. Compositional variation is almost the same in configurations 1 and 2. In both configurations, mole fraction contours are almost vertical, and the horizontal mole fraction gradient is constant. However, some difference on compositional variation occurs between these two configurations and configurations 3 and 4. When the number of fractures increases, mole fraction contours loose their vertical shape as seen in Fig. 17. No substantial difference, however, is noticed for the horizontal mole fraction gradient. Fig. 18 clearly shows that there is no significant effect of interior fractures on the overall horizontal compositional gradient.

The above behavior could be explained by observing the velocity fields of configurations 1 to 4 (see Fig. 19) for $k_f = 10^5$md and $f_a = 1$mm. This figure shows that, the flow velocity in the interior fractures is small compared with the flow velocity in the main

surrounding fracture. The flow mainly occurs in the loop of the main fracture. Smaller loops occur in the interior core but fluid movement in these loops is relatively slow. Fig. 20 depicts, in more detail, the horizontal fracture velocity (top) and the vertical fracture velocity (bottom) of configurations 1, 2, 3 and 4. This figure shows that horizontal (vertical) velocity increases or decreases because of incoming or outgoing flow in the vertical (horizontal) fractures. The negative vertical fracture velocity in Fig. 20 indicates that the velocity is in the downward direction.

5.4 Fracture connectivity

In configurations 1 to 4 studied above, the connected fractures form a network and the fluid circulates without being stopped by a rock matrix of low permeability. Let us now consider configurations with discrete fractures to study the influence of fracture discreteness on compositional variation. Configurations 5, 6, 7 and 8 (Fig. 3) are studied toward this end. The results are presented in Fig. 21 for $k_f = 10^5$md and $f_a = 1$mm. This figure shows the effect of blocking the surrounding fracture by a 6m long porous medium of low permeability ($k = 1$md) for configuration 5. Fig. 21 also shows that discrete horizontal and vertical fractures have less influence on compositional variation than connected fractures. Furthermore, the composition is more affected by horizontal fractures than by vertical fractures. Composition in configuration 6 is more homogeneous than in configuration 7 although the number of fractures in configuration 7 is twice the number of horizontal fractures in configuration 6.

The fracture velocity fields of configurations 1, 5, 6 and 7 are depicted in more detail in Fig. 22. This figure shows that the maximum horizontal fracture velocity in configuration 1, for instance, is more than twice those in configurations 5, 6 and 7 for the same value of k_f and f_a. The same behavior occurs regarding the maximum vertical velocity; $v_{z_{max}}$ in configuration 1 is more than twice those in configurations 5, 6 and 8 for the same value of k_f and f_a.

6 Conclusions

This study centers on the features of composition variation in fractured porous media. The numerical results show that fracture permeability above a certain value influences the composition variation, whereas the fracture convective velocity increases with an increase in fracture permeability. Other conclusion from this study are:

1) The fluid flow consists mainly of a loop within the surrounding fracture. Smaller loops occur in the interior connected fractures. The flow velocity within the rock matrix is negligible in comparison to fracture velocity.

2) The fracture flow velocity increases when the fracture aperture decreases. On the other hand, with larger fractures, the compositional variation is less significant.

3) The main effect on compositional variation is due to the surrounding fractures. The interior fractures affect the shape of the mole fraction contour lines, but the horizontal compositional variation is not significantly affected by those fractures.

Nomenclature

C^w coefficient of molecular diffusion in **J**
C^P coefficient of pressure diffusion in **J**
C^T coefficient of thermal diffusion in **J**
f_a fracture aperture
g gravity acceleration
H reservoir height
J diffusive mass flux
k permeability
k_f fracture permeability
k_m matrix permeability
n normal vector
P pressure
P_0 pressure at the reservoir center
T temperature
T_0 temperature at the reservoir center
T_x horizontal thermal gradient
T_z vertical thermal gradient
t time
v_x horizontal velocity
v_z vertical velocity
v velocity vector
W reservoir width
w weight fraction
w_0 weight fraction at the reservoir center
x, z coordinates
z upward vertical unit vector

Greek symbols

β_w compositional expansion coefficient
β_T thermal expansion coefficient
χ mole fraction
ϕ porosity
μ dynamic viscosity
ρ density
ρ_0 density at w_0 and T_0

References

[1] A. N. Hamoodi, A. F. Abed and A. Firoozabadi, "Composition Modeling of Two-Phase Hydrocarbon Reservoirs," SPE 36244 paper presented at the 7th Abu Dhabi International Petroleum Exhibition and Conference, Abu Dhabi, UAE, Oct. 133-16, 1996.

[2] A. R. Neveux and S. Sathikumar, "Delineation and Evaluation of a North Sea Reservoir Containing Near-Critical Fluids", SPE Res. Eng. (Aug. 1988), pp. 842-848, 1988.

[3] A. M. Saidi, Reservoir Engineering of Fractured Reservoirs (Fundamental and Practical Aspects), Total Edition Press, 1987.

[4] D. Jacqmin, "Interaction of Natural Convection and Gravity Segregation in Oil/Gas Reservoirs," SPE Res. Eng., (May 1990), pp. 233-238.

[5] M. F. Riley and A. Firoozabadi, "Compositional Variation in Hydrocarbon Reservoirs with Natural Convection and Diffusion", AIChE J., (Feb. 1998), pp. 452-464.

[6] S. Chandrasekhar, Hydrodynamic and Hydromagnetic Stability, pp. 16-17, Oxford university Press, 1961.

[7] D. Y. Peng and D. B. Robinson, "A New Two-Constant Equation of State," Ind. Eng. Chem. Fund., Vol. 15, pp. 59-64, 1976.

[8] S. V. Patankar, Numerical Heat Transfer and Fluid Flow, Hemisphere, Washington, 1980.

[9] H. S. Price and K. H. Coats, "Direct Methods in Reservoir Simulation," SPE Journal, Vol. 14, pp. 295-308, 1974.

[10] J. C. Stringer, L. K. Thomas and R. G. Pierson "Efficiency of a D4 Gaussian Elimination on a Vector Computer," SPE 11082 presented at the 57th Annual Fall Technical Conference and Exhibition, New Orleans, 1982.

W	30 m
H	15 m
χ_0	0.2
P_0	1.10×10^7 Pa
T_0	338.5 ^{o}K
ρ_0	495.3 kg/m^3
C^w	-1.55×10^{-7} kg/m.s
C^P	-7.85×10^{-16} kg/m.Pa.s
C^T	$+1.71 \times 10^{-9}$ kg/m.s. ^{o}K
T_x	$+0.1^oK$/ 30 m
T_z	-1^oK/ 15 m
ϕ	0.25
μ	200 kg/m.s
k_m	1 md

Table 1: Data used in this work.

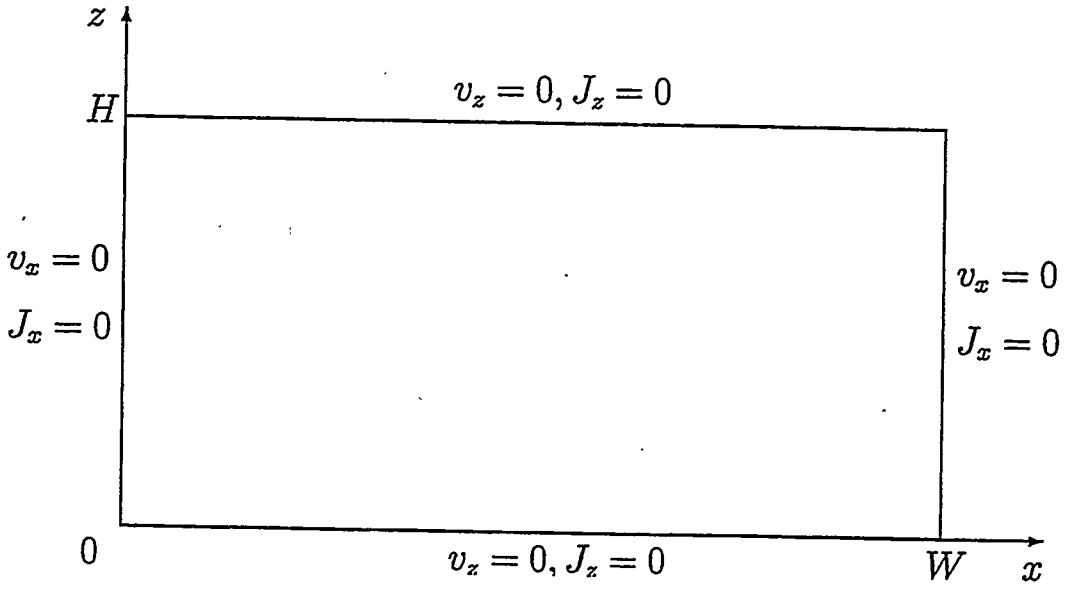

Figure 1: Geometry and boundary conditions.

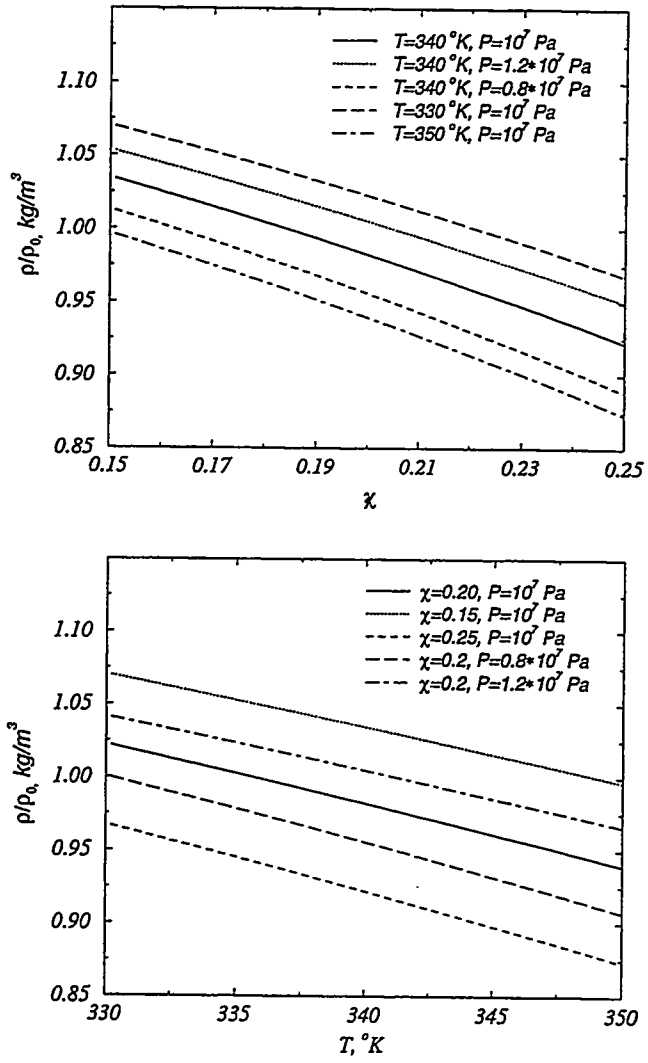

Figure 2: Density variation vs. mole fraction (top) and temperature (bottom) obtained by the Peng-Robinson equation of state for the binary mixture C_1/nC_4.

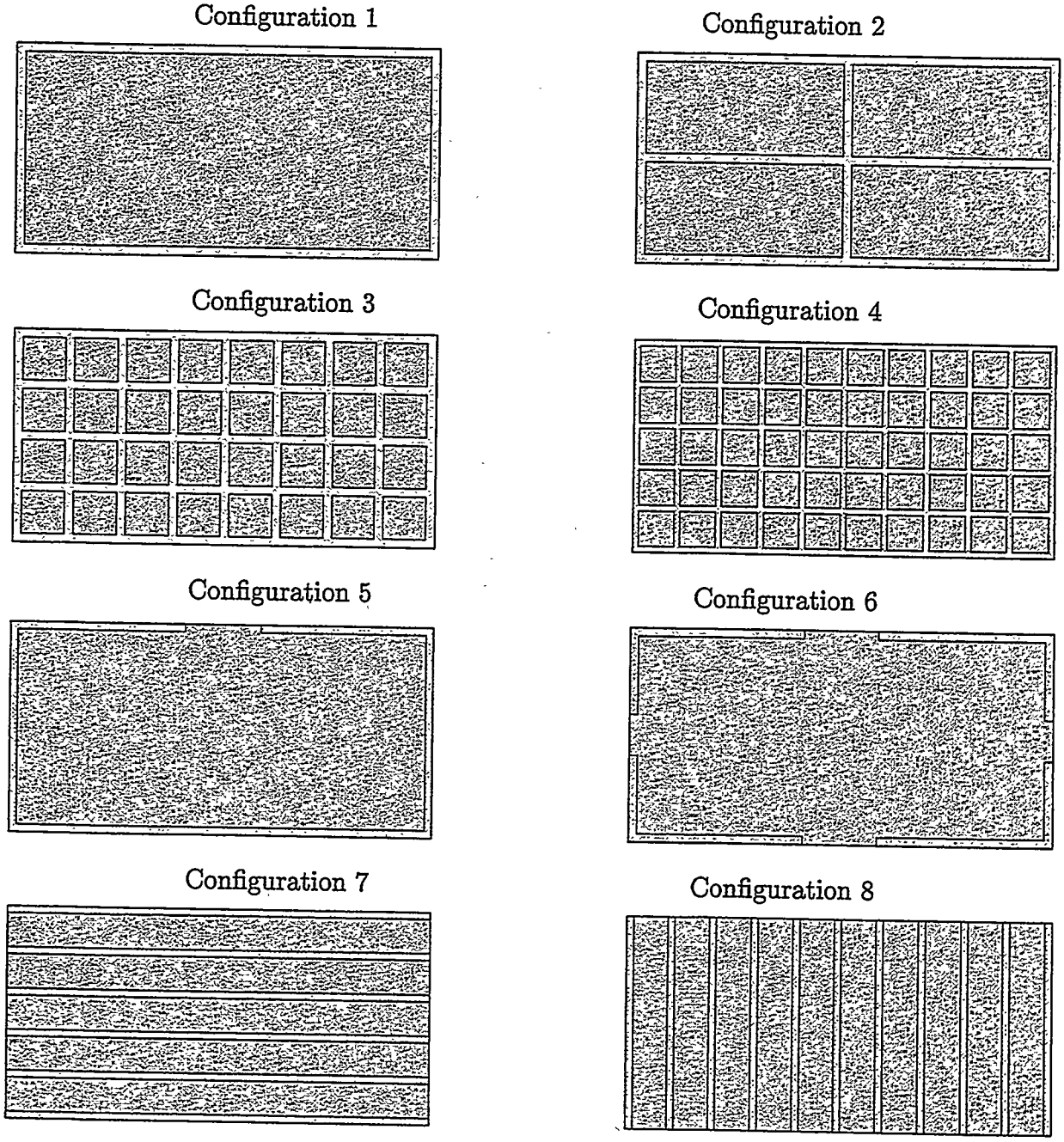

Figure 3: Sketch of the fractured porous media configurations.

Configuration 1

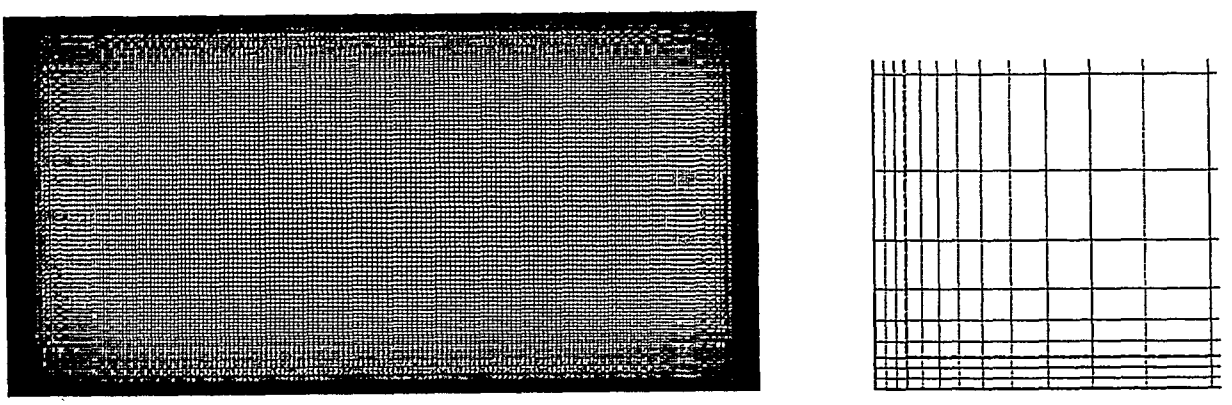

Configuration 3

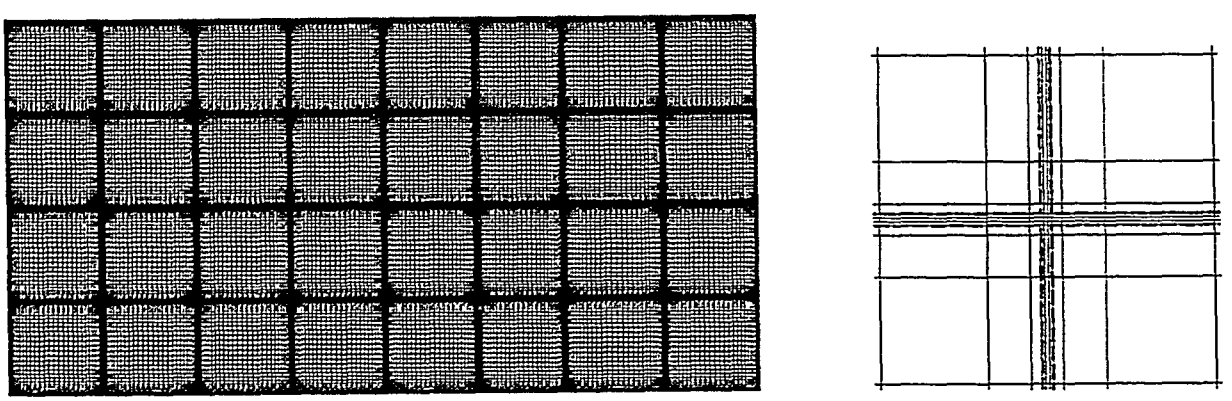

Figure 4: Meshes used in the numerical simulations: Configuration 1 (top) and Configuration 3 (bottom).

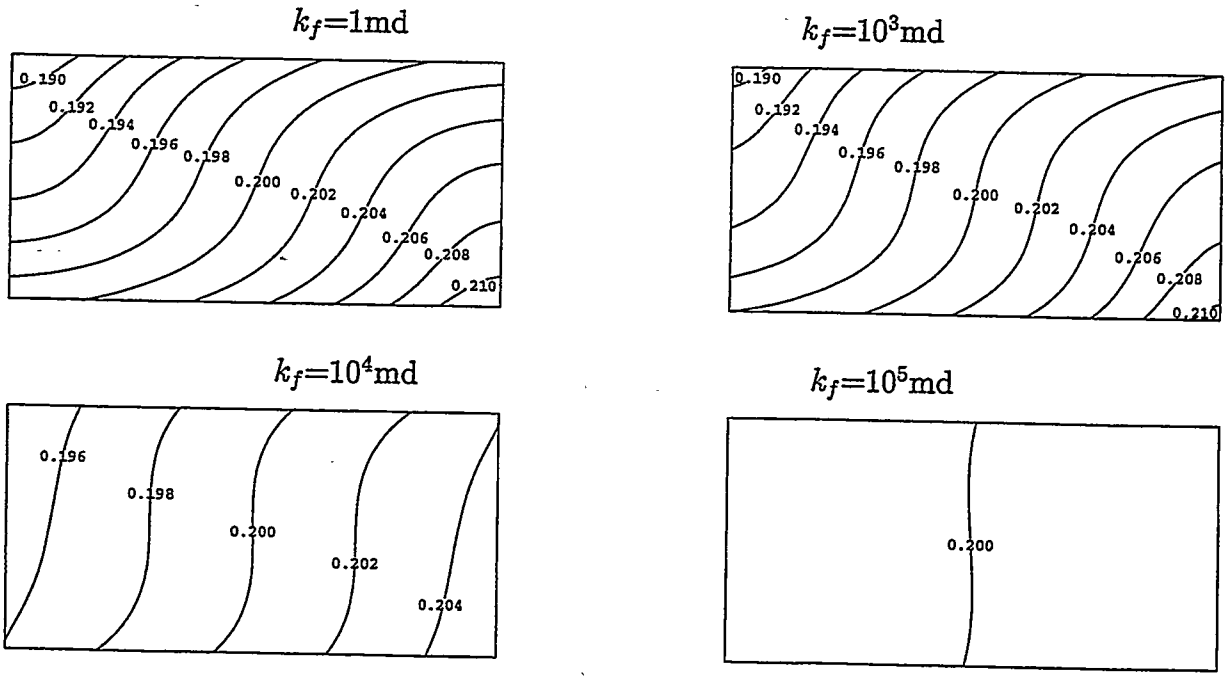

Figure 5: Mole fraction contours for different fracture permeabilities (f_a=1mm): Configuration 1.

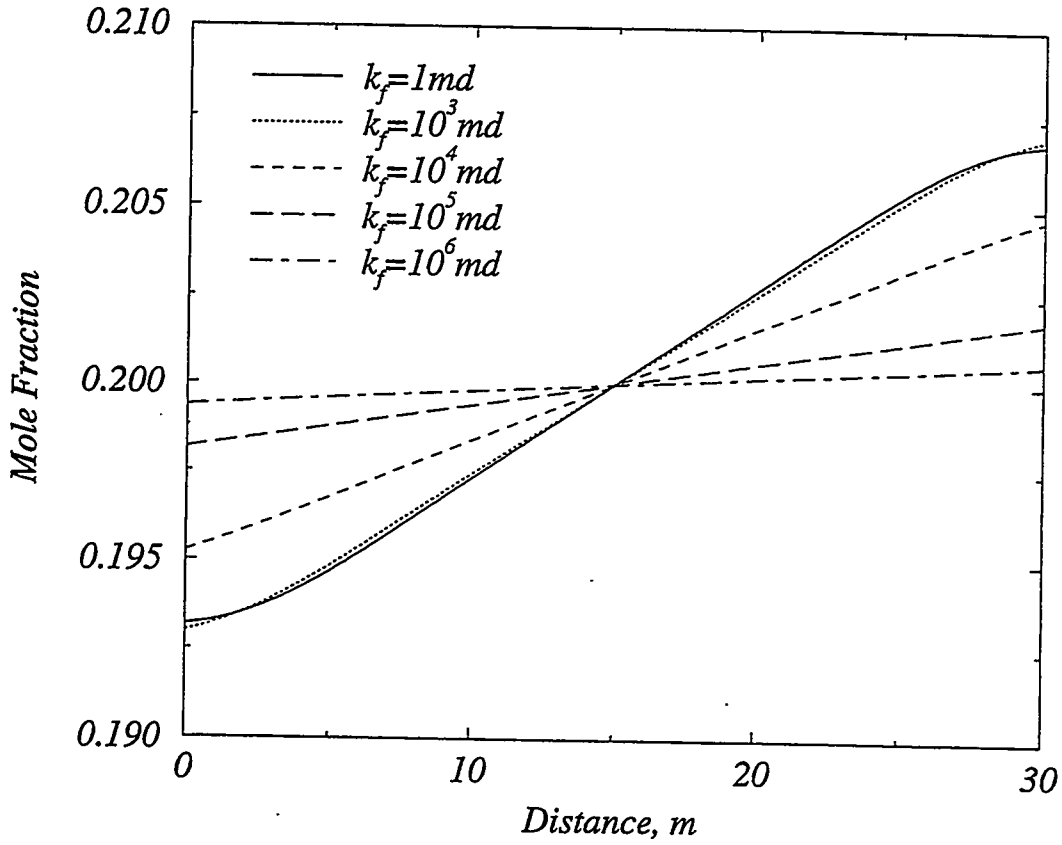

Figure 6: Mole fraction vs. distance at $z=H/2$ (f_a=1mm): Configuration 1.

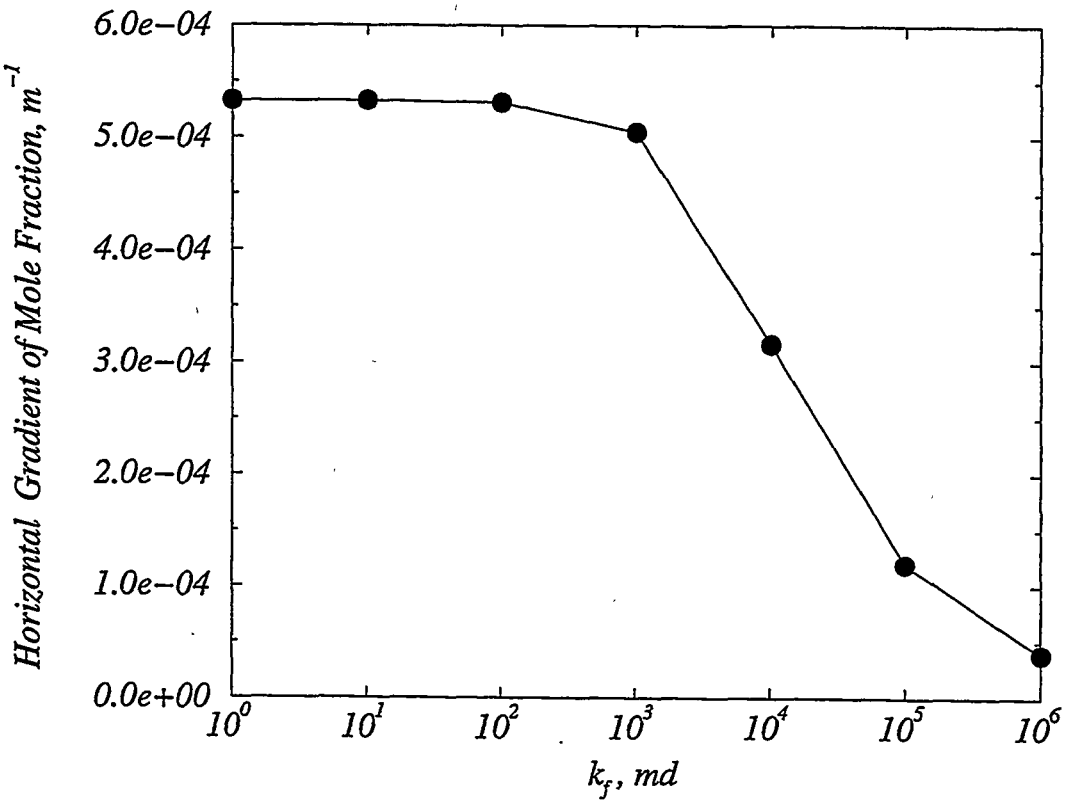

Figure 7: Horizontal gradient of mole fraction vs. fracture permeability at x=$W/2$, z=$H/2$ for f_a=1mm: Configuration 1.

Configuration 1

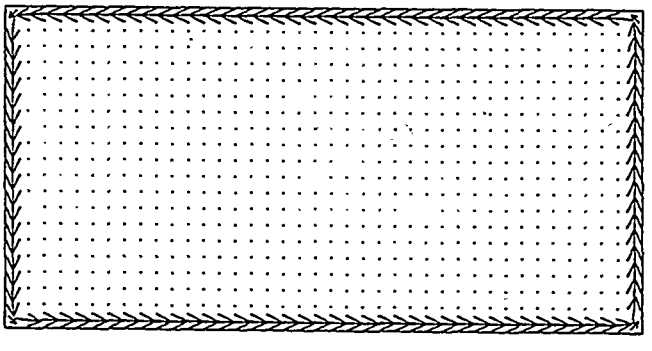

Figure 8: Velocity field for f_a=1mm, k_f=10^5md; $v_{x_{max}}$=2.648×10^{-6}m/s, $v_{z_{max}}$=2.569×10^{-6}m/s: Configuration 1.

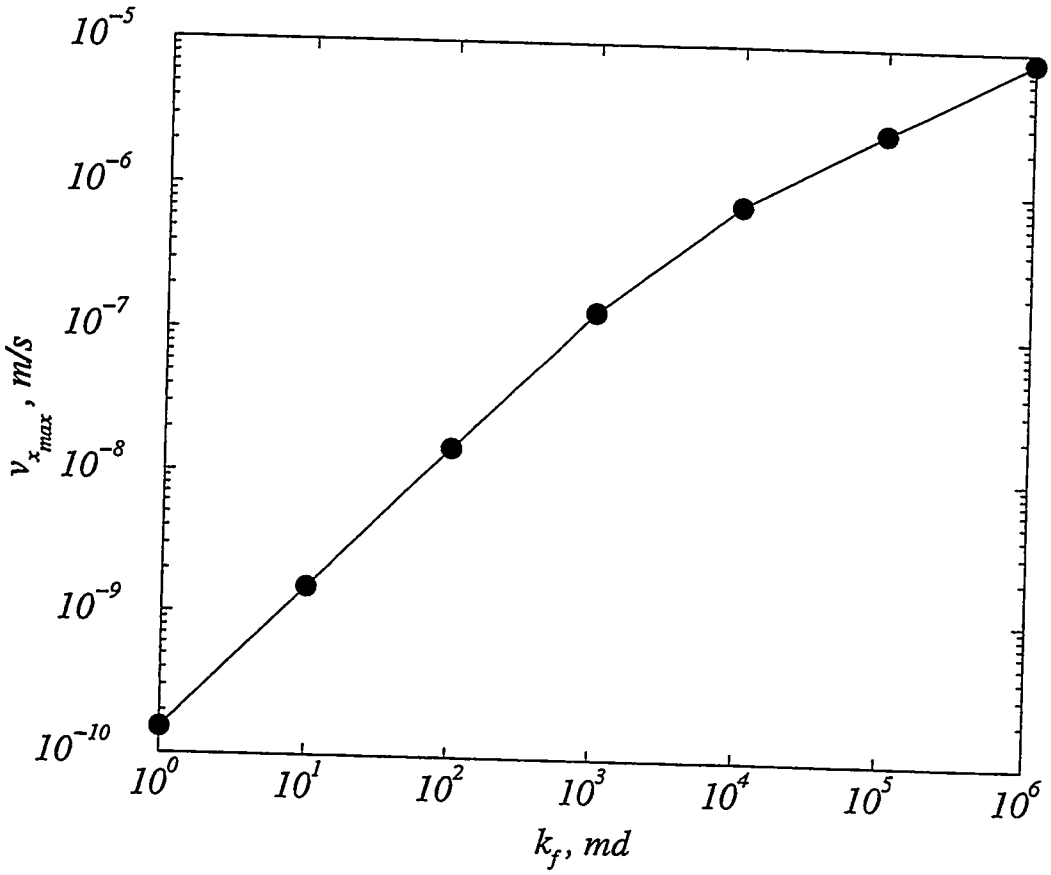

Figure 9: Maximum value of the horizontal velocity vs. fracture permeability (f_a=1mm): Configuration 1.

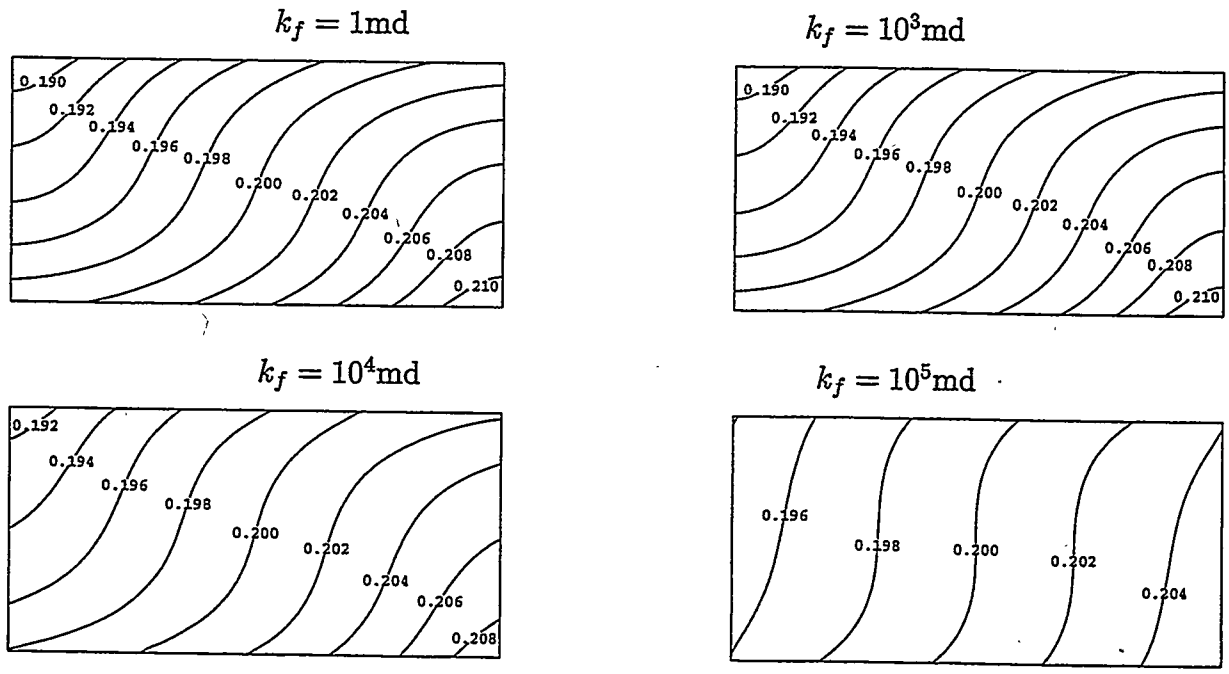

Figure 10: Mole fraction contours for different fracture permeabilities (f_a=0.1mm): Configuration 1.

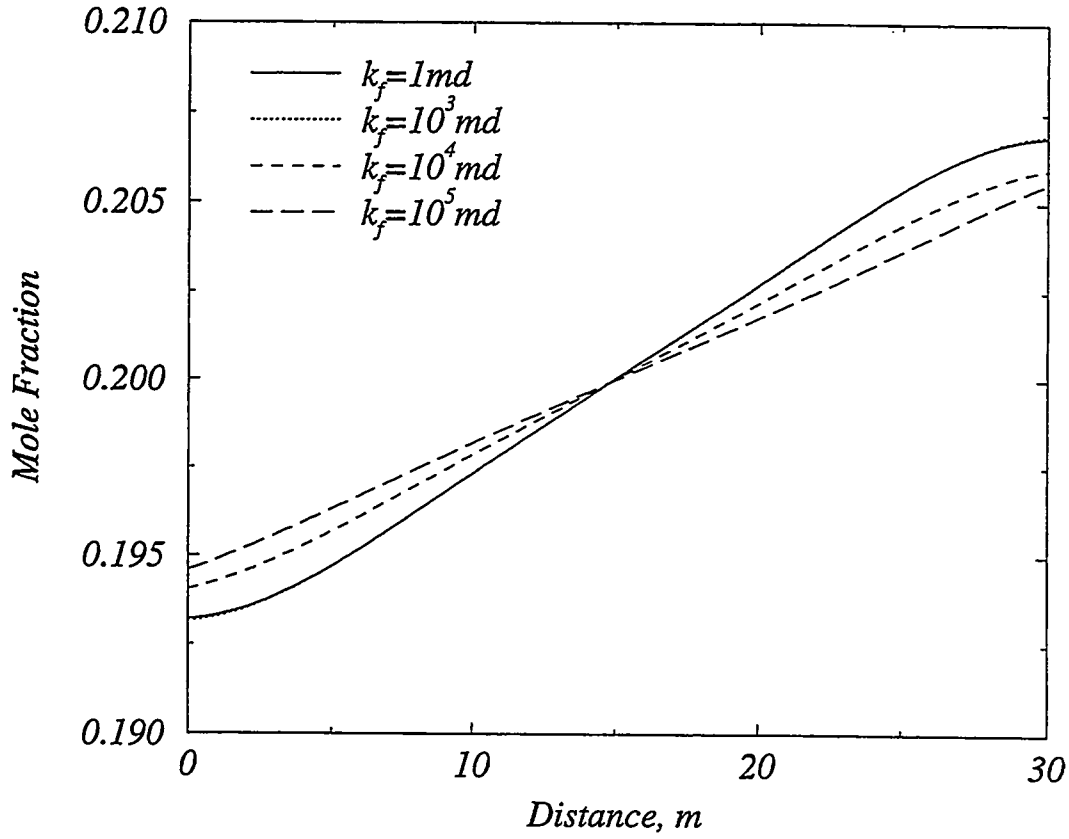

Figure 11: Mole fraction vs. distance at z=$H/2$ (f_a=0.1mm): Configuration 1.

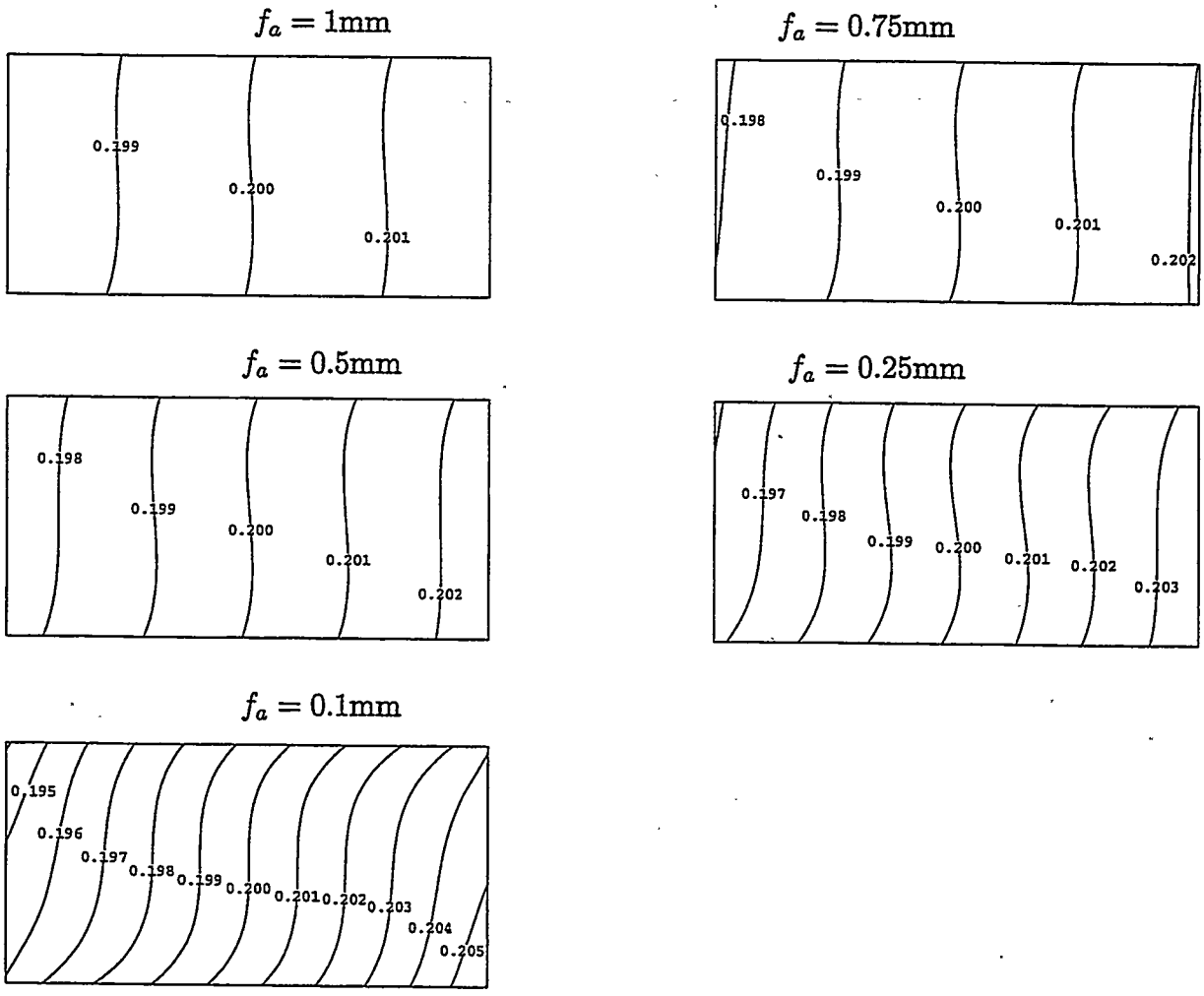

Figure 12: Mole fraction contours for various fracture apertures (k_f=10^5md): Configuration 1.

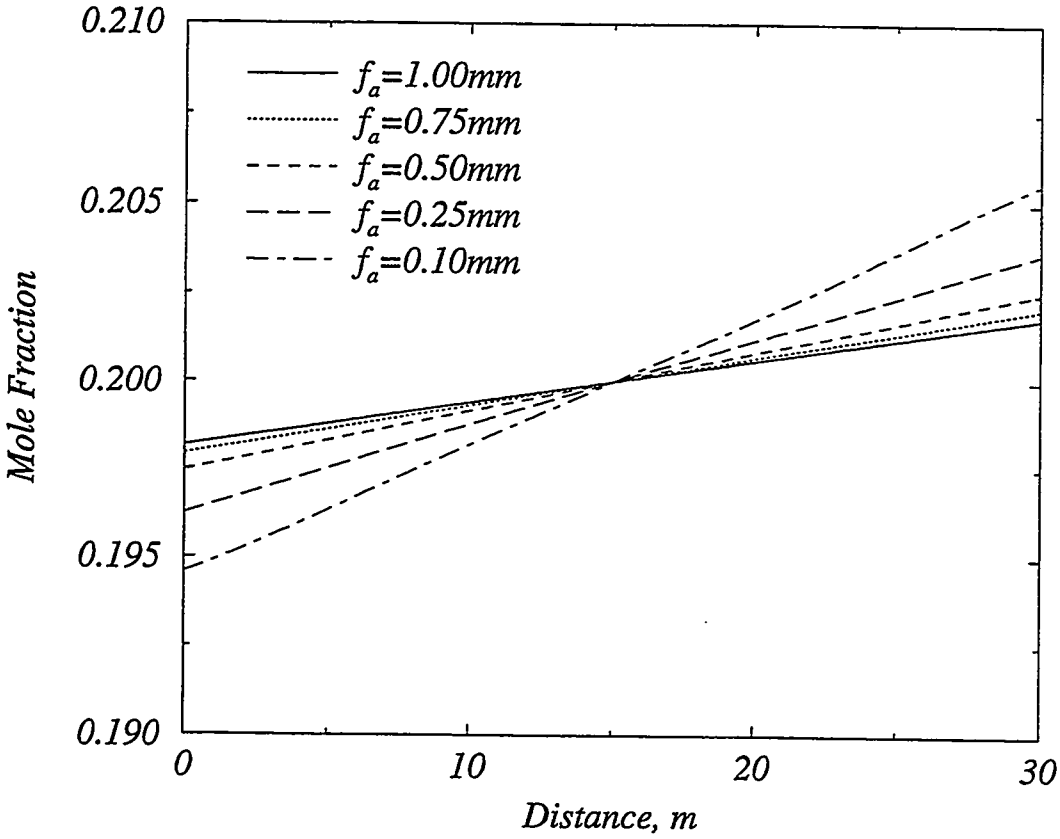

Figure 13: Configuration 1: mole fraction vs. distance at z=$H/2$ for various fracture apertures (k_f=10^5md).

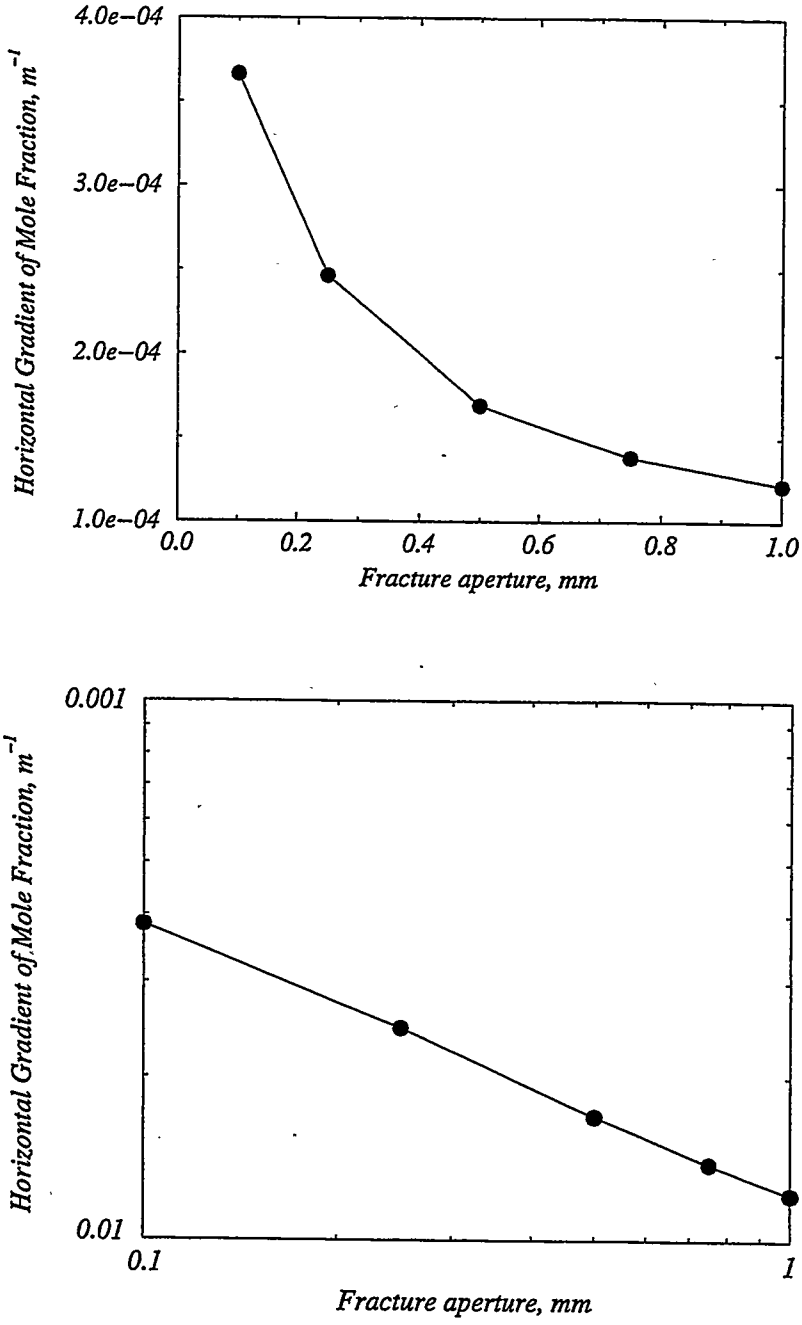

Figure 14: Horizontal gradient of mole fraction vs. fracture aperture at x=$W/2$, z=$H/2$ for k_f=10^5md. linear graph (top) and log-log graph (bottom): Configuration 1.

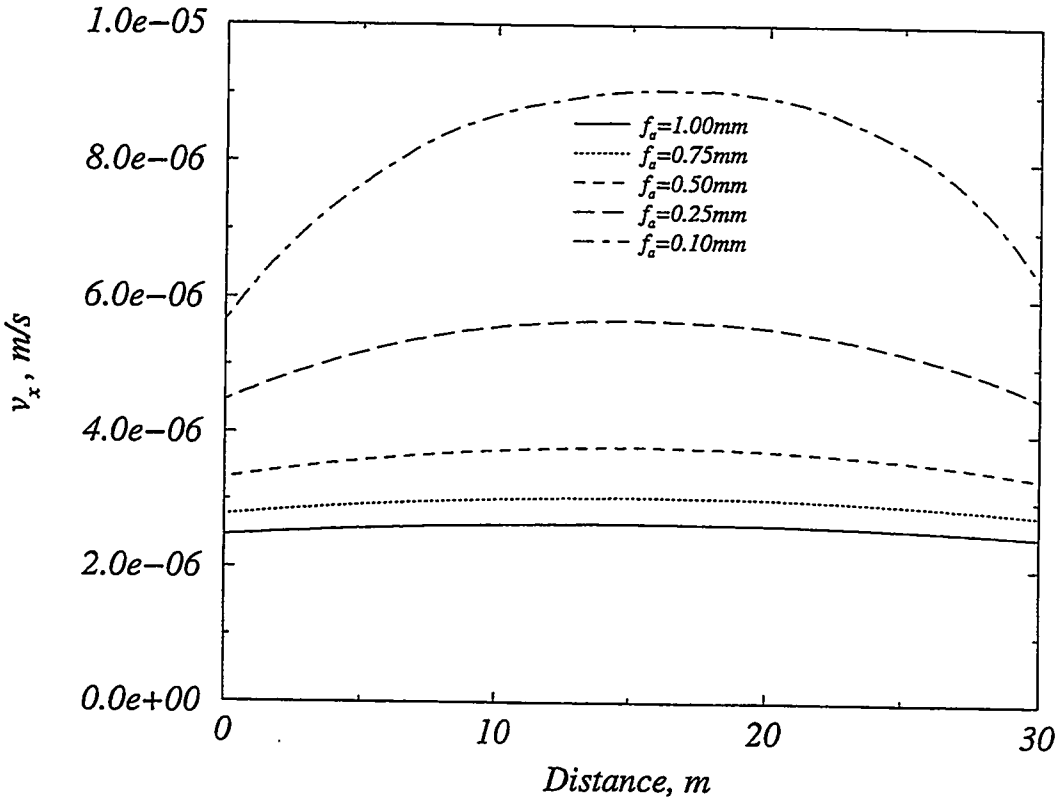

Figure 15: Horizontal fracture velocity v_x vs. fracture aperture (k_f=10^5md): Configuration 1.

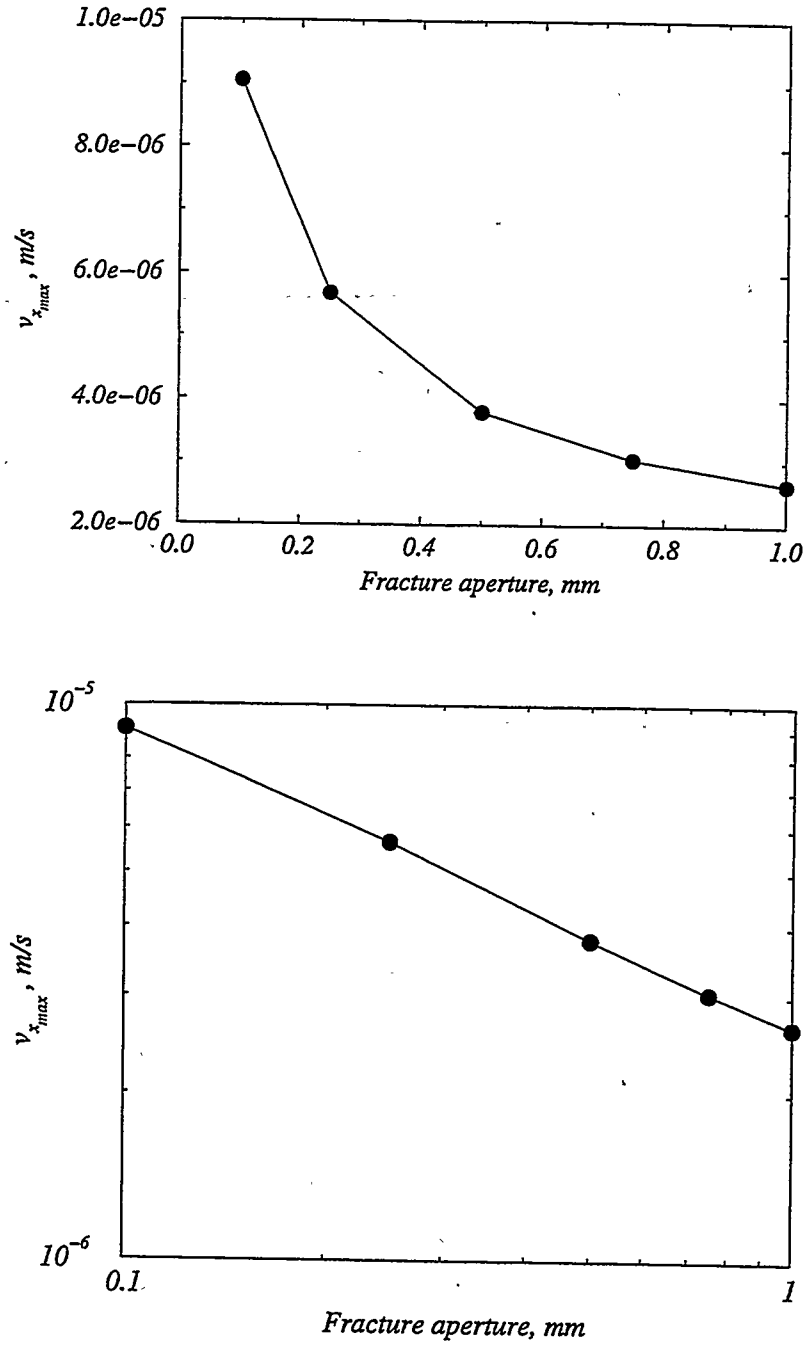

Figure 16: Maximum horizontal velocity vs. fracture aperture (k_f=10^5mm). linear plot (top) and log-log plot (bottom): Configuration 1.

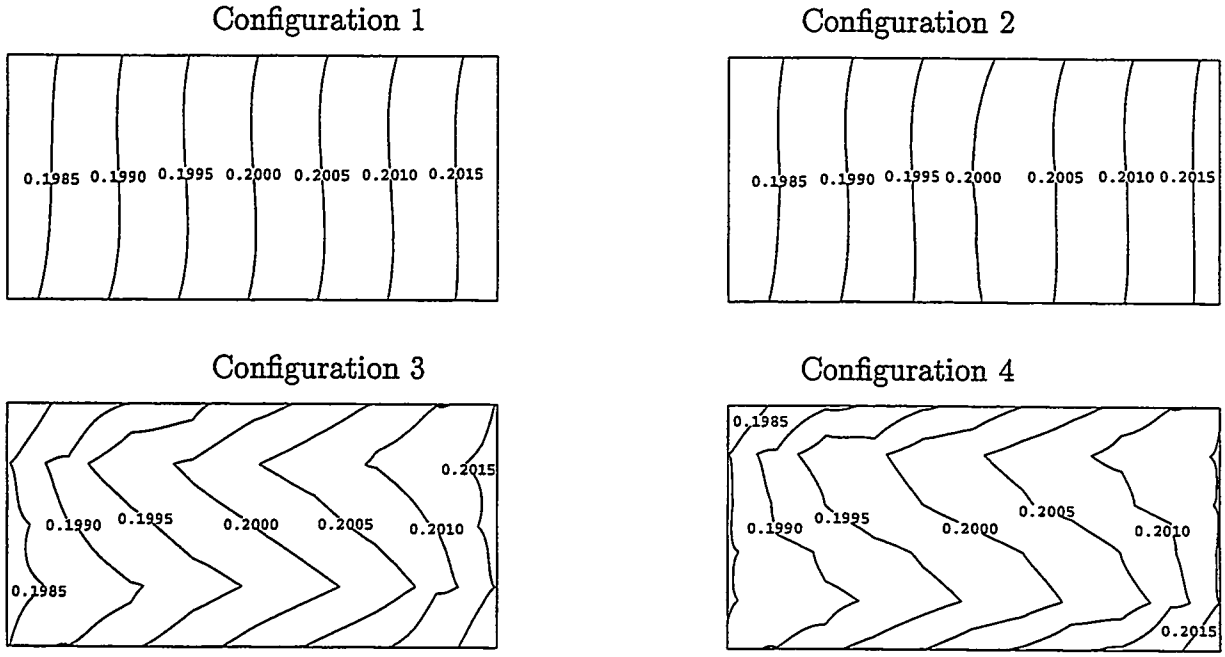

Figure 17: Mole Fraction contours for different configurations: f_a=1mm, k_f=10^5md.

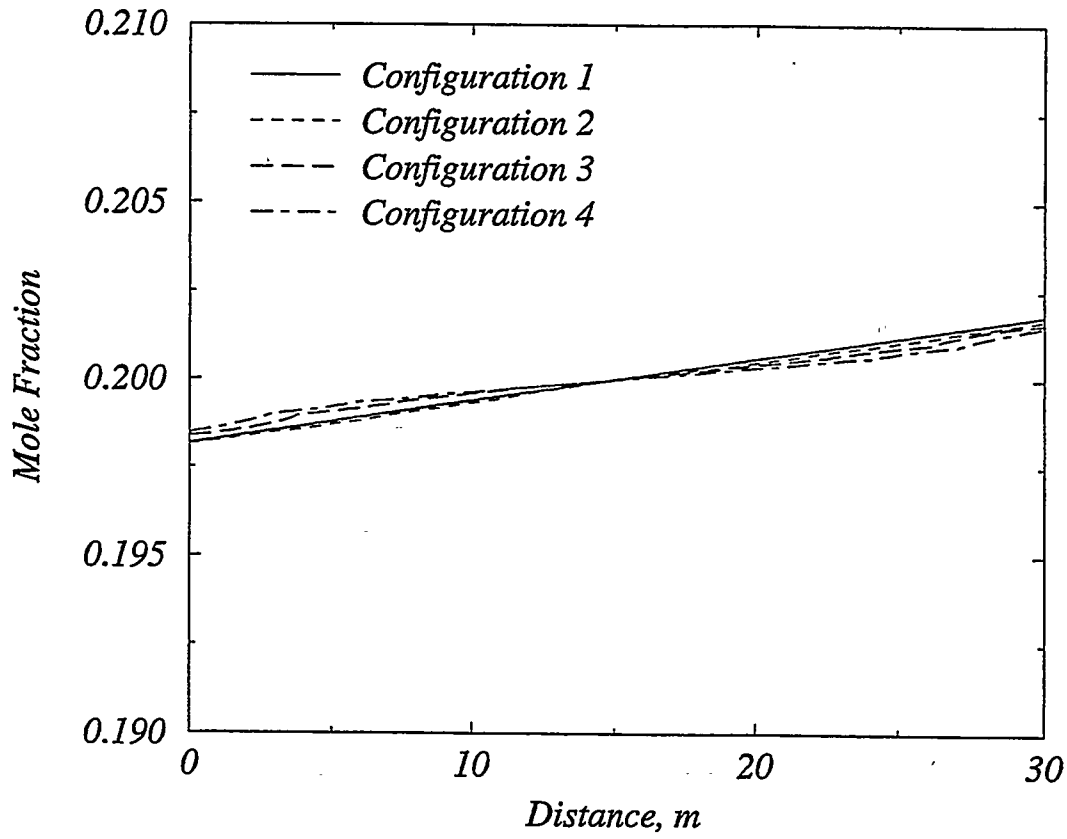

Figure 18: Mole fraction vs. distance at $z = H/2$ for different configurations: $f_a = 1\text{mm}$, $k_f = 10^5\text{md}$.

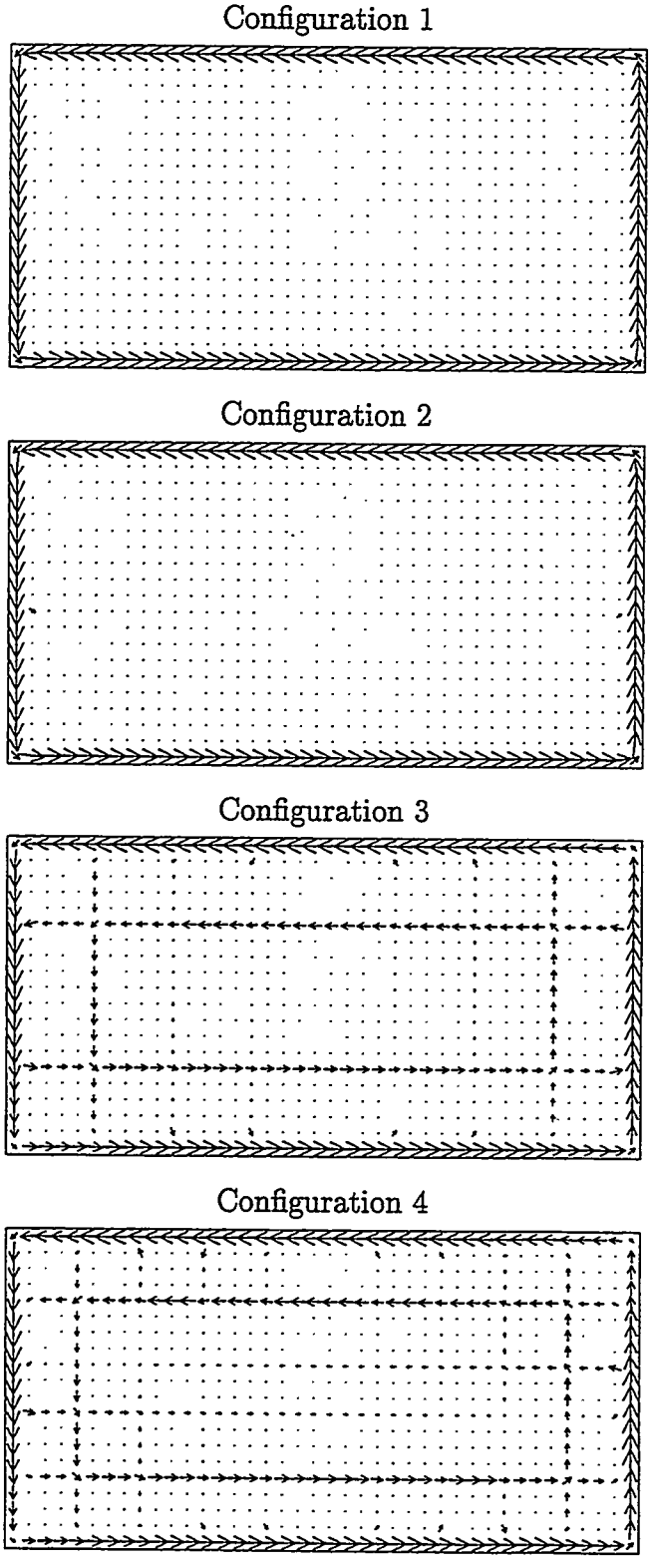

Figure 19: Velocity field for different configurations: $f_a = 1\text{mm}$, $k_f = 10^5\text{md}$.

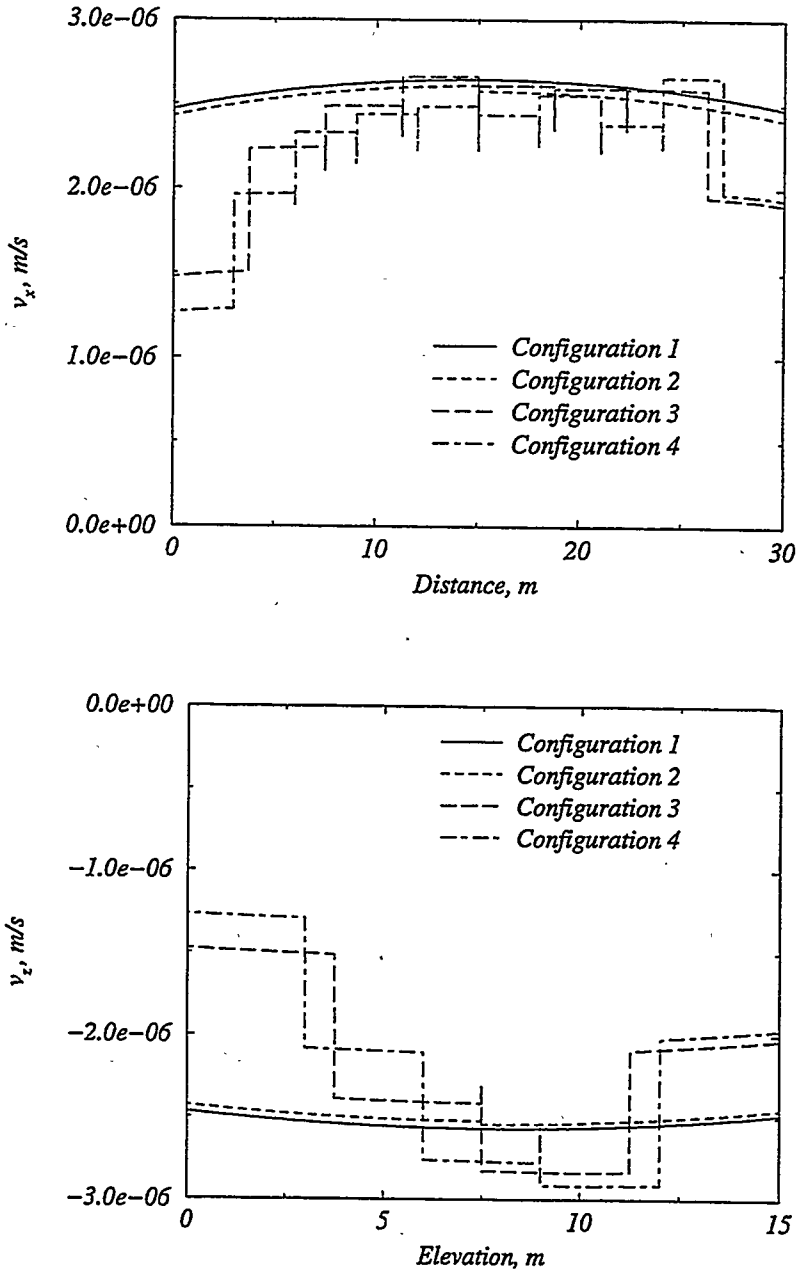

Figure 20: Fracture horizontal velocity (top) and fracture vertical velocity (bottom) for $f_a = 1\text{mm}$ and $k_f = 10^5\text{md}$.

Configuration 5

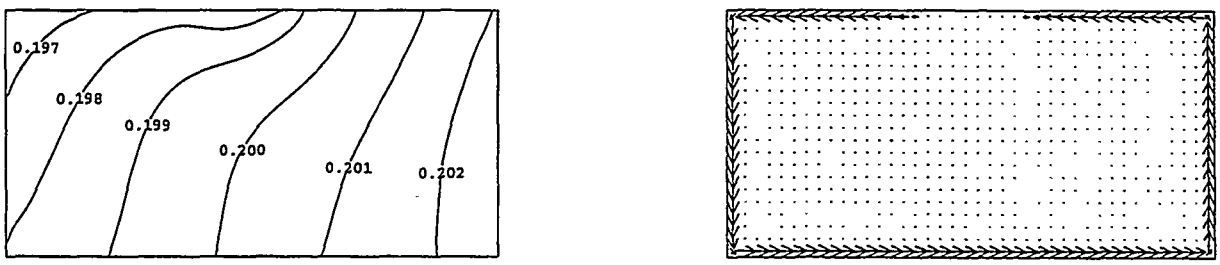

Configuration 6

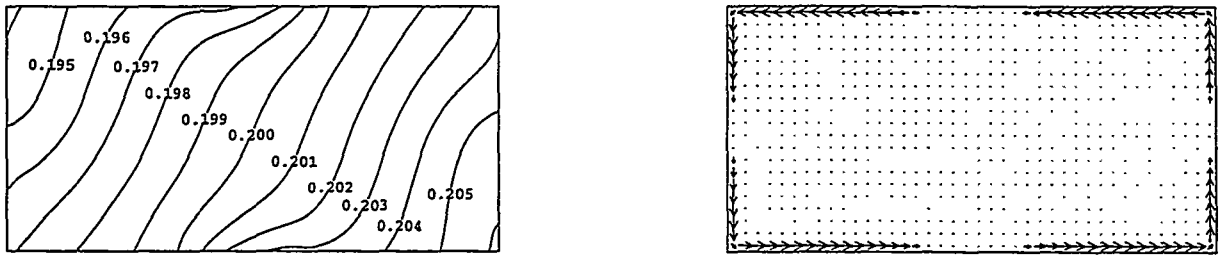

Configuration 7

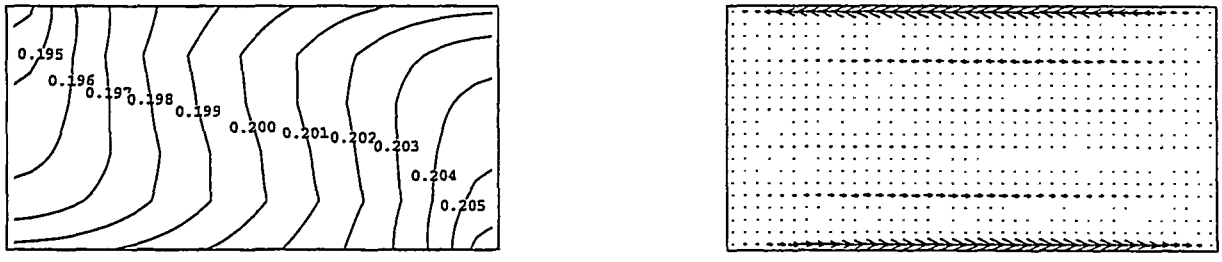

Configuration 8

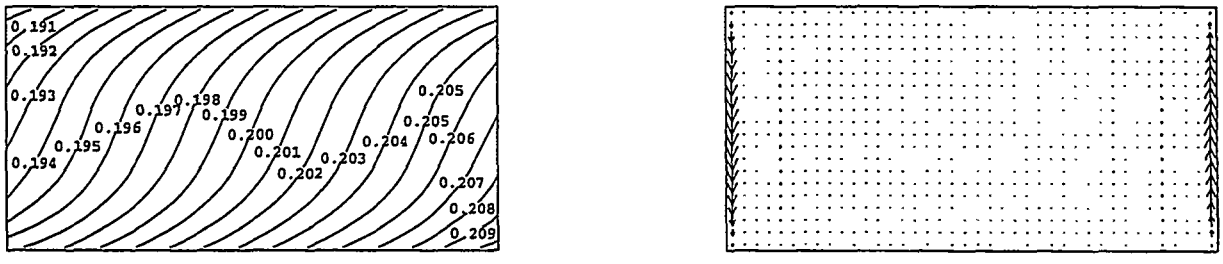

Figure 21: Mole fraction contours (left) and velocity field (right) for configurations 5, 6, 7 and 8: $f_a = 1\text{mm}$, $k_f = 10^5\text{md}$.

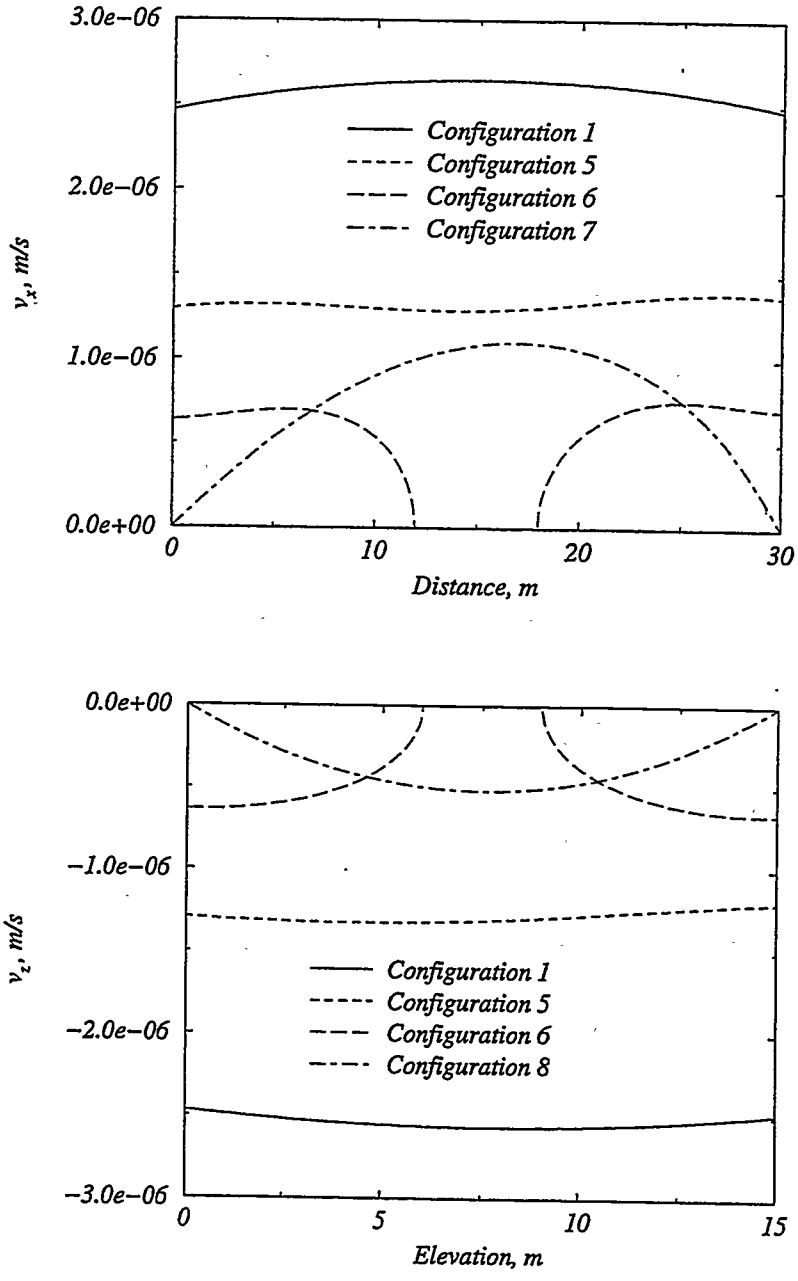

Figure 22: Fracture horizontal velocity (top) and fracture vertical velocity (bottom) for $f_a = 1\text{mm}$ and $k_f = 10^5\text{md}$.

Part V - Modeling of Multicomponent Diffusions and Convection in Porous Media

KASSEM GHORAYEB AND ABBAS FIROOZABADI

1 Summary

Numerical investigations of diffusion and convection in multicomponent hydrocarbon mixtures in 2D cross-sectional (x, z) porous media are performed using the finite volume method with nonuniform rectangular grids. Spatial discretization is performed by a second-order centered scheme. It is shown that methane, unlike in binary hydrocarbons where it segregates towards the bottom hot of the porous media, may be at higher concentration at the cold top in ternary and mixtures and multicomponent reservoir fluids. This behavior, which is in line with oil field data, is due to various cross effects which have not been properly accounted for in the past. It is also demonstrated that convection may significantly effect the compositional variation in a hydrocarbon reservoir; depending on temperature and pressure, a weak convection may drastically change compositional variation.

2 Introduction

Field observations show several trend of compositional variation; there is mainly vertical compositional variation of the hydrocarbon components in some reservoirs [1]. Some other reservoirs show pronounced horizontal compositional variation [2]. In some reservoirs, there is very little compositional variation with depth [3]. One may even observe a decrease of heavy components such as C_{7+} with depth [4]. It is believed that multicomponent diffusions and convection effect the distribution of various components in hydrocarbon reservoirs [5, 6]. In a multicomponent hydrocarbon fluid, the total mass flux of a given component consists of two parts: 1) the convective flux from the velocity of the bulk fluid, and 2) the diffusive flux as a result of the difference between component velocity and bulk velocity. The molecular diffusive flux of a given component depends not only on its composition gradient (mutual diffusion), but also on the composition gradient of all the other components in the mixture (cross-molecular diffusion). The diffusive flux also depends on pressure and thermal gradients– the so-called thermal diffusion (Soret effect) and pressure diffusion (gravitational segregation), respectively [7]. All these effects can be modeled using thermodynamics of irreversible processes.

The compositional variation of a component in multicomponent mixtures (more than two components) in a porous medium may radically differ from that in binary mixtures. The cross effects (cross-molecular diffusion and thermal diffusion) are the main processes

for a radical variation. The primary goal of this work is to model the compositional variation of multicomponent mixtures in porous media, taking various cross-effects into account, and to show that all the trends in field data (from Refs. [1] to [4]) can be predicted.

Methane in binary mixtures of C_1/C_2, C_1/C_3 and C_1/nC_4, where experimental data are available, segregates to the hot side [8, 9, 10]. On the other hand, in hydrocarbon reservoirs, there is generally more methane on the cold side (top of the reservoir) [4, 5]. Those facts imply that one may not use effective thermal diffusion factors to study the segregation of methane in mixtures with more than two components in a non-isothermal medium. Cross-molecular diffusion has also been shown to be important in some ternary and higher mixtures. There is no claim in the literature for having studied the combined effect of thermal diffusion, molecular diffusion and convection in ternary and higher mixtures. Larre *et al.* [11] investigated the stability of a horizontal layer heated from below filled with a water-isopropanol-ethanol mixture. The authors neglected the cross-molecular diffusion coefficients and assumed that the thermal diffusion factor of a component could be expressed as the sum of the thermal diffusion factors of the binaries consisting of the given component and the two others, respectively. The model results do not, however, agree with the experimental data. A similar conclusion has been reported by Krupiczka and Rotkegel [12] who investigated mass transfer in ternary mixtures of isopropanol-water-air and isopropanol-water-helium. Considerable discrepancies between experimental data and theoretical predictions were observed when cross-diffusion terms were neglected [12].

There is a vast body of literature on molecular diffusion coefficients in binary systems [13, 14, 15, 16, 17, 18, 19, 20]. A sizable amount of binary data on hydrocarbons is also available [13, 16, 17]. However, molecular diffusion data for mixtures consisting of three or more components, especially for hydrocarbon mixtures at reservoir conditions, are scarce. Reviews of the available data in ternary mixtures with summaries of the measurement methods are presented by Cussler [21] and Tyrrell and Harris [22]. Kooijman and Taylor [23] summarized the existing models for predicting the molecular diffusion coefficients in multicomponent mixtures and presented a correlation based on the Vignes correlation [24] for binary systems. Compared with experimental data for ternary systems, Kooijman and Taylor's correlation [23] provides better results than do the other available correlations. In this work, we adopted Kooijman and Taylor's correlation to calculate the molecular diffusion coefficients.

Surprisingly, no experimental data for ternary and higher mixtures exists in the literature for thermal diffusion factors, a necessary requirement for the calculation of thermal diffusion in a multicomponent mixture. Firoozabadi *et al.* [25] have recently developed a theoretical model to estimate thermal diffusion factors for ternary and higher mixtures. The new model accurately predicts the thermal diffusion factors of binary mixtures. Furthermore, using the thermal diffusion factors obtained by this model, we where able to successfully simulate the compositional variation in a thermogravitational porous column containing a ternary mixture as reported by El Maâtaoui [26]; that was an indirect validation, and the only source of verification, of the model in multicomponent mixtures. In this work, we use the thermal diffusion factors from the work of Firoozabadi *et al.* [25] (see appendix C).

Several attempts have been made in the last 20 years to model compositional variation in hydrocarbon reservoirs. The earlier studies considered the gravitational effect on compositional variation in a 1D convection-free system [27, 28, 29, 30]. The main conclusion from those studies is that gravitational effect causes the heavier components to segregate towards the bottom of the reservoir. Thermal diffusion in a 1D convection-free system has been accounted for in both binary and multicomponent mixtures in some studies [31, 5, 32]. From those studies one can mainly observe that thermal diffusion may have the same order of magnitude and may have an opposite effect than pressure diffusion. The above studies neglect the effect of convection on compositional variation (although it may be very important) and have been performed in a 1D vertical system; they do not, therefore, allow for investigating areal compositional variation. Furthermore, no appropriate model for thermal diffusion has been considered in the studies which considered thermal diffusion effect in compositional variation [5]. For multicomponent systems, Belery and da Silva [5] investigated the compositional variation in the Ekofisk field using a one dimensional model. They took into account molecular, pressure and thermal diffusion and assumed a convection-free system. Their model is based on effective molecular diffusion coefficients and effective thermal diffusion factors. The results from the work of Belery and da Silva show roughly the same qualitative trend of compositional variation of methane as in the field data; methane is more concentrated at the top of the reservoir. However, significant discrepancies between field data and predictions exist. This may be due to the fact that the authors neglected: 1) convection, and 2) certain cross-effects. The combined effect of convection and pressure diffusion has been considered by Jacqmin [6]. This study shows the mixing effect of convection; the more convection occurs in the reservoir, the more homogeneous is the composition. However, neglecting thermal diffusion may mask an inverse role that convection may play on compositional variation in hydrocarbon reservoirs in some range of permeability as it has been shown in recent studies [33, 34].

Compositional variation of methane in a C_1/nC_4 single-phase binary mixture has been studied by Riley and Firoozabadi [33] and Ghorayeb and Firoozabadi [34] in the same range of thermophysical and geometrical conditions as in this study. For a particular example, it has been shown that, at low permeabilities ($k < 1$ md), methane goes towards the hot side (the bottom of the reservoir). When the permeability increases, due to convection, there is only horizontal compositional variation. For high permeabilities ($k > 10$ md), convective mass transfer overrides both thermal and pressure diffusion; it is the main phenomenon effecting compositional variation within the porous medium for this specific binary mixture. The increase of permeability reduces the compositional variation. In a typical hydrocarbon binary mixture, for low permeabilities, compositional variation is mainly effected by the ratio $(D^T T_z)/(D^p p_z)$ where D^p, D^T, p_z and T_z are the pressure and thermal diffusion coefficients (see Riley and Firoozabadi [33]) and the vertical pressure and thermal gradients, respectively. When this ratio is > 1, the horizontal compositional variation is more pronounced than the vertical variation. The horizontal compositional gradient reaches a maximum value for $k \approx 1$ md and then decays as $1/k$ [33]. A small amount of convection can cause the horizontal compositional gradient to increase. A similar phenomenon has been experimentally and numerically observed in vertical columns (separation by thermogravitational effect) where there exists an optimal

value of k leading to the maximal separation [26, 35]. For $(D^T T_z)/(D^p p_z) < 1$, compositional variation is effected mostly by pressure diffusion; the vertical compositional variation is more pronounced than the horizontal variation.

The main goal of this paper is to provide a sound basis for the study of compositional variation in hydrocarbon reservoirs; both multicomponent diffusions and convection are taken into account. The results for a ternary system are presented in detail to show the effect of cross-molecular diffusion and thermal diffusion on the compositional variation of methane, and to explain the discrepancies occurring between field observations and results in binary systems. Furthermore, the modeling of compositional variation in a field case is presented. The paper is organized as follows; first we briefly present the mathematical formulation of the problem. Then, an overview of the numerical method is presented. Results obtained under several conditions of composition, temperature and pressure are discussed together with a comparison with previous results obtained in the binary mixture C_1/nC_4.

3 Mathematical Formulation

We consider a two-dimensional porous medium with width W and height H (Fig. 1) saturated by a single-phase mixture of n components. We assume that the Oberbeck-Boussinesq approximation is valid; the density ρ is assumed to be constant, except in the buoyancy term $(\rho g z)$, where it varies linearly with the temperature T and the mole fractions x_i, $i = 1, \ldots, n-1$:

$$\rho = \rho_0 \left[1 - \beta_T (T - T_0) - \sum_{i=1}^{n-1} \beta_{x_i} (x_i - x_{i0}) \right], \tag{1}$$

where

$$\beta_T = -\frac{1}{\rho_0} \left. \frac{\partial \rho}{\partial T} \right|_{x_i,\ i=1,\ \ldots,\ n-1},$$

and

$$\beta_{x_i} = -\frac{1}{\rho_0} \left. \frac{\partial \rho}{\partial x_i} \right|_{T, x_j,\ j=1,\ n-1,\ j \neq i}, \quad i = 1, \ \ldots, \ n-1$$

are the thermal expansion coefficient and the compositional coefficients of component i, respectively; ρ_0 is the density at temperature T_0 and mole fractions x_{i0}. The validity of the Oberbeck-Boussinesq approximation has been demonstrated by Ghorayeb and Firoozabadi [36]. The coefficients β_T and β_{x_i} are calculated using the Peng-Robinson equation of state (PR EOS) [37].

The unsteady state conservation equations of mass and species are:

$$\vec{\nabla}.\vec{v} = 0, \tag{2}$$

$$c \left[\frac{\partial x_i}{\partial t} + \vec{\nabla} (x_i \vec{v}) \right] + \vec{\nabla}.\vec{J}_i = 0, \quad i = 1, \ \ldots, \ n-1, \tag{3}$$

where c, $\vec{v}$, and $\vec{J}_i$ are the total molar density, the bulk velocity, and the molar diffusive flux relative to molar average velocity for component i ($i = 1, \ \ldots, \ n-1$), respectively.

The bulk velocity, $\vec{v}$, is given by Darcy's law:

$$\vec{v} = -\frac{k}{\phi\mu}\left(\vec{\nabla}p + \rho g \mathbf{z}\right), \tag{4}$$

where p, g, k, μ, and ϕ are the pressure, the acceleration due to gravity, the permeability, the viscosity, and the porosity, respectively. The unit vector $\mathbf{z}$ points upwards. Substitution of Eq. 4 into Eq. 2 and the assumption that $(k/\phi\mu)$ is constant lead to the pressure equation:

$$\vec{\nabla}^2 p = \rho_0 g \left(\beta_T \frac{\partial T}{\partial z} + \sum_{i=1}^{n-1} \beta_{x_i} \frac{\partial x_i}{\partial z}\right). \tag{5}$$

The above equation will be used later in the numerical solution to the problem. The reservoir is assumed to be bounded by an impervious rock that has constant temperature gradients T_x and T_y in horizontal and vertical directions, respectively. In the following, the temperature field is assumed to be a linear function of x and z: $T = T_x x + T_z z + a$, where a is a constant. Field data support this form of the temperature expression. If we set the temperature at $x = W/2$ and $z = H/2$ equal to T_0, then,

$$T = T_x\,(x - W/2) + T_z\,(z - H/2) + T_0. \tag{6}$$

The diffusive fluxes are given by the expression (see Appendix A):

$$\vec{J}_i = -c\left(\sum_{j=1}^{n-1} D_{ij}^M \vec{\nabla} x_j + D_i^p \vec{\nabla} p + D_i^T \vec{\nabla} T\right),\ i = 1,\ ...,\ n-1 \tag{7}$$

where D_{ij}^M, D_i^p and D_i^T are the coefficients of molecular diffusion, pressure diffusion and thermal diffusion, respectively. The diffusive flux, $\vec{J}_i$, results from the deviation in the velocity of component i from the velocity of the bulk fluid. Since, for an n-component mixture, the diffusive flux of the nth component is equal to $-\sum_{i=1}^{n-1} \vec{J}_i$ and the mole fraction of the nth component is equal to $1 - \sum_{i=1}^{n-1} x_i$, the equation expressing conservation of mass for component n will be a linear combination of Eqs. 2 and 3.

3.1 Boundary conditions

The boundary conditions for Eqs. 2, 3 and 4 are based on no-fluid fluxes across the outer boundaries (Fig. 1):

$$\vec{J}_i.\vec{n} = 0,\ \ i = 1,\ ...,\ n-1,\quad x = 0,\ W \ \text{ and } \quad z = 0,\ H, \tag{8}$$

$$\vec{v}.\vec{n} = 0,\qquad\qquad x = 0,\ W \ \text{ and } \quad z = 0,\ H, \tag{9}$$

where $\vec{n}$ is the unit normal vector. Eqs. 8 and 9 imply that:

$$\sum_{j=1}^{n-1} D_{ij}^M \frac{\partial x_j}{\partial x} + D_i^p \frac{\partial p}{\partial x} + D_i^T \frac{\partial T}{\partial x} = 0,\ \ i = 1,\ ...,\ n-1,$$

$$\text{and } v_x = 0 \qquad x = 0, W, \tag{10}$$

$$\sum_{j=1}^{n-1} D_{ij}^M \frac{\partial x_j}{\partial z} + D_i^p \frac{\partial p}{\partial z} + D_i^T \frac{\partial T}{\partial z} = 0,\ \ i = 1,\ ...,\ n-1,$$

$$\text{and } v_z = 0 \qquad z = 0, H. \tag{11}$$

From Eq. 4, we obtain the boundary conditions that are required for the integration of Eq. 5:

$$\frac{\partial p}{\partial x} = 0 \quad x = 0, W, \tag{12}$$

$$\frac{\partial p}{\partial z} = -\rho_0 \left[1 - \beta_T (T - T_0) - \sum_{i=1}^{n-1} \beta_{x_i} (x_i - x_{i0})\right] \qquad z = 0, H. \tag{13}$$

With the above Neumann boundary conditions, mole fractions and pressure must be assigned at one point in the medium. In this work we set $x_i(W/2, H/2) = x_{i0}$, $i = 1, \ldots, n-1$ and $p(W/2, H/2) = p_0$.

4 Numerical Scheme

Eqs. 3, 4 and 5, together with the boundary conditions given by Eqs. 10 to 13, are integrated numerically using the finite volume method (see Patankar [38]) with a nonuniform rectangular grid system. The spatial discretization is performed using a second-order centered scheme. A semi-implicit first-order scheme is used for the temporal integration. We seek the steady state solution and iterate on the unsteady state until the steady state is reached. In this work, convergence to the steady state is assumed when the absolute relative error of mole fractions is less than 10^{-7} between the two successive iterations at each grid point.

5 Model Validation

In a previous work (Ref. [34]), the spatial variation of C_1/nC_4 with the measured molecular diffusion coefficient and thermal diffusion coefficient was calculated for a given condition. In this work these coefficients are estimated from the procedures outlines in Appendix B and C. The results are very similar; provided the non-idealities are properly accounted for (see Ref. [39]).

El Maâtaoui [26] measured species separation by thermogravitational effect in n-alkane mixtures (see Furry *et al.* [40] and Lorenz and Emery [41] for details about the thermogravitational effect). He mainly investigated the binary mixture nC_{24}/nC_{12}. He also reported results for the ternary mixture $nC_{24}/nC_{16}/nC_{12}$. We simulated, using our numerical model, some of those experiments with the same thermophysical parameters. The main difference occurring between the experiment parameters and those used in our numerical simulations is that, in the former, a cylindrical column was used (two concentric cylinders, the inner one heated and the outer one cooled), though, in the latter, a rectangular column is used (which has the same height as the cylindrical column and a width equal to the difference of the radii of the two cylinders). Since the difference of the radii is small compared with either radius, we may proceed as if the convection were taking place in a thin flat slab as we assume in this study [40].

Table 1 presents, for different values of permeability, nC_{24} composition in the bottom and the top of the column (both experimental [26] and numerical results) and the separation factor $q = (x_{nC_{24}}/x_{nC_{12}})_{bottom} / (x_{nC_{24}}/x_{nC_{12}})_{top}$ as well; q is also depicted vs. k in Figure 2. The comparison between experimental data and numerical results shows good agreement. The maximal relative error is less that 20%. With regard to the optimal value of the permeability, k_{opt}, leading to a maximal segregation, experimental data and numerical results show $2.9 \times 10^{-11} < k_{opt} < 4.9 \times 10^{-11}\text{m}^2$ and $k_{opt} \approx 2.5 \times 10^{-11}\text{m}^2$, respectively. There is excellent agreement between measured and predicted value of the Soret coefficient $S_T = D_1^T / \left(D_{11}^M \, x_{10}(1 - x_{10})\right)$; El Maâtaoui [26] reported $S_T = 0.90\ \text{K}^{-1}$; from our model [25] we obtain $S_T = 0.85\ \text{K}^{-1}$.

For the ternary system $nC_{24}/nC_{16}/nC_{12}$ which is an ideal mixture for the given composition, the experimental data reported by El Maâtaoui [26] show that no qualitative change occurs between the ternary and binary systems for the compositional variation of nC_{24}; nC_{24} segregates towards the bottom of the column. The cross-diffusion coefficients are very small in comparison with the mutual diffusion coefficients and that D_1^T has, in this example, the same order of magnitude in both binary and ternary systems. Furthermore, no significant composition variation is observed for nC_{16} which is mainly due to the fact that the thermal diffusion coefficients D_2^T is much smaller that D_1^T; molecular diffusion prohibits any significant segregation of nC_{12}. Table 2 shows the measured and predicted results; the maximal relative error between numerical and experimental values is less than 10%.

6 Results

6.1 Ternary systems

In this study we focus on a non-ideal ternary mixture of $C_1/C_2/nC_4$. Two set of calculations were performed; the compositions at the center of the reservoir were fixed at (1) $x_{10} = 0.25$, $x_{20} = 0.25$, $x_{30} = 0.50$, and (2) $x_{10} = 0.35$, $x_{20} = 0.35$, $x_{30} = 0.30$. Several conditions of temperature and pressure were considered. The mixture in all investigations is in single phase. Table 3 presents the data used for this ternary mixture. To study the effect of grid size, numerical runs were performed with different mesh grids; we found that using finer grids than those mentioned in Table 3 did not significantly improve the accuracy of the results.

Figs. 3 and 4 show the $p-T$ plots for those mixtures, as well as the temperatures and pressures at which the calculations were performed. For every mixture, at each composition, three combinations (T, p) were selected. Tables 4 and 5 present, in detail, the data used in this work. The molecular diffusion coefficients are obtained using Kooijman and Taylor's correlation (see Appendix B). Appendix B also shows how the pressure diffusion coefficients are obtained using the molecular diffusion coefficients and the thermodynamic properties of the mixture. The thermal diffusion factors are from Firoozabadi *et al.* [25]. The cross-molecular diffusion coefficients D_{12}^M and D_{21}^M may be < 0 or > 0. As temperature increases, D_{12}^M and D_{21}^M become significant in comparison to D_{11}^M and D_{22}^M. Thermal diffusion coefficients and pressure diffusion coefficients show a similar trend. Figs. 5

to 10 show composition contour plots for C_1 and C_2 for permeabilities in the range of 0 (convection-free) to 100 md. Let us first discuss, according to those figures, compositional variation for the convection-free cases, and then proceed with the effect of convection as permeability increases.

First, from Figs. 5 to 10 it can be seen that, in almost all the cases we studied, component 2 (C_2) is more concentrated at the top of the reservoir. Therefore, the sign of the thermal diffusion factor in a non-ideal mixture with more than two components does not imply the segregation to the hot or cold side. Let us now discuss the compositional variation of methane (component 1). At high temperatures (the point denoted by "3" in Figs. 3 and 4), there is more methane at the top of the reservoir. This can be seen in Figs. 9 and 10. The behavior is reversed at low temperatures for the same range of pressure (the point denoted by "1" in Figs. 3 and 4); there is more methane at the bottom of the reservoir. Figs. 5 to 6 clearly show this behavior, which is similar to the compositional variation of methane observed in the binary mixture of C_1/nC_4 [33, 34]. In most cases we studied, there is no significant vertical compositional variation of C_1 for intermediate values of temperature at higher pressures. This can be seen in Figs. 7 and 8.

The methane mole fraction contour lines have a slope > 0 for low temperatures. The slope increases when one increases temperature. For some combinations of (T, p) (in the neighborhood of the point "2"), the mole fraction contour lines becomes almost vertical; there is no vertical compositional variation of methane in the reservoir. When one keeps increasing temperature, the slope of the mole fraction contour lines becomes < 0; methane in this case is more concentrated at the top of the reservoir.

Points "1", "2" and "3" differ also in terms of the effect of permeability on compositional variation. The same trend as reported by Riley and Firoozabadi [33] is observed for C_1/nC_4 when the permeability increases at point "1". The horizontal gradient of mole fraction of methane is almost constant; it reaches a maximum value for $k = 1$ md then decays with the increase of permeability so that, at $k = 100$ md, no significant compositional variation is observed. For point "3", the composition in the reservoir changes drastically when the permeability increases from $k = 0$ to $k = 1$ md. Fig. 11 shows the mole fraction contour lines of methane and ethane in this range of permeability. At $k = 0$ (that is, convection-free), methane is more concentrated in the top left corner of the reservoir. The slope of the mole fraction contour lines is < 0. At some permeability between 0.05 and 0.1 md, those contour lines become horizontal and then, their slope becomes > 0. When one increases k, there is always more methane at the top of the reservoir. For permeabilities > 1 md and up to 100 md (the end of our computational domain), there is almost no effect of permeability on compositional variation. At point "2", for $k > 10$ md, the whole reservoir has a homogeneous composition. The ternary mixture encompasses the features of compositional variation in Refs. [1, 2, 3, 4].

6.2 Field example

Recently, Lee *et al.* [3] presented data from a gas condensate reservoir with some unexpected behavior. We adopted this field example. The temperature data are not provided by the authors. Therefore, we assign them arbitrarily. Tables 6 and 7 present the data used in this field example and the composition at the center of the reservoir.

Figs. 12, 13 and 14 show the mole fraction contour lines of all the components in the mixture for three values of permeability: $k = 0$, $k = 1$ and $k = 10$ md. At convection-free conditions ($k = 0$ md), one can see from Fig. 12 that C_1, C_2, CO_2, N_2 segregate toward the top of the reservoir; the inverse trend is shown by the other components. One can also observe that the maximum segregation occurs for C_1, $C_7 - C_{19}$, and C_{20+}. However, no significant compositional variation is observed for the hydrocarbon components in between: C_2 and $C_3 - C_4$. Figure 12 also reveals that there is no significant compositional variation for CO_2.

When the permeability changes from $k = 0$ to $k = 1$ md, one observes by comparing Figs. 12 and 13 that there is less compositional variation for all the components at $k = 1$ than $k = 0$ md. Furthermore, methane, which was more concentrated in the right top corner of the reservoir for $k = 0$ md is more concentrated in the left top corner for $k = 1$ md. The compositional variation changes between $k = 0$ and $k = 1$ md are similar to that for the ternary mixture $C_1/C_2/nC_4$ depicted in Fig. 11.

As the permeability increases, the compositional segregation becomes less pronounced. For $k = 10$ md (average value for the field), for example, no significant compositional variation occurs for most of the components. The maximum compositional variation occurs for C_1 and C_{20+}; even though, compositional variation for these components at $k = 10$ md is insignificant comparing with that occurring at $k = 0$ md. The results are in agreement with the field data.

7 Remark and Conclusions

The use of general expressions for molecular, pressure, and thermal diffusion in multicomponent non-ideal hydrocarbon mixtures combined with natural convection allow the calculation of species distribution in hydrocarbon reservoirs. Since steady state convection is governed by horizontal temperature gradient, the measurement of horizontal temperature variation is a key factor. Without horizontal temperature variation, there is no convection at steady state. Specific conclusions from this study are drawn in the following.

Compositional variation in a single-phase ternary system of $C_1/C_2/nC_4$ under a wide range of pressure, temperature and composition and for a reservoir fluid have been numerically studied. For the ternary mixture at low permeabilities ($k < 1$ md), the calculations show that, in the same range of pressure, methane is more concentrated at the bottom of the reservoir for low temperatures. However, when the temperature increases, this trend is reversed; more methane segregates towards the top of the reservoir. For intermediate temperatures, no significant vertical compositional gradient is observed. When the permeability increases (up to $k = 100$ md), one may either have a reservoir with a homogeneous composition or very little convection effect on compositional variation. For some cases, at low permeabilities, the permeability increase results in a reversal of the compositional gradient of methane. The field example reconfirms the effect of convection on spatial variation of various species.

Nomenclature

c	total molar density
D_{ij}^M	molecular diffusion coefficient
$\hat{D}_{ij}$	Maxwell-Stefan diffusion coefficient
D_{ij}^0	infinite dilution diffusion coefficient
D_i^p	pressure diffusion coefficient
D_i^T	thermal diffusion coefficient
f_i	fugacity of component i
g	acceleration of gravity
H	reservoir height
$\vec{J}_i$	diffusive mass flux of component i
k	permeability
k_{Ti}	thermal diffusion ratio of component i
M	total molecular weight
M_i	molecular weight of component i
n	number of components
$\vec{n}$	normal vector
p	pressure
p_0	pressure at the reservoir center
T	temperature
T_0	temperature at the reservoir center
T_x	horizontal thermal gradient
T_z	vertical thermal gradient
t	time
v_x	horizontal velocity
v_z	vertical velocity
$\vec{v}$	velocity vector
W	reservoir width
x_i	mole fraction of component i
x_{i0}	mole fraction of component i at the reservoir center
z	upward vertical unit vector

Greek symbols

α_{Ti}	thermal diffusion factor of component i
β_{x_i}	compositional coefficient of component i
β_T	thermal expansion coefficient
ϕ	porosity
μ	viscosity
ρ	density
ρ_0	density at x_{i0} and T_0

References

[1] R.S. Metcalfe, J.L. Vogel and R.W. Morris, Compositional gradients in the Anschutz Ranch East field, SPE Res. Eng., pp. 1025-1032, August 1988.

[2] A.N. Hamoodi, A.F. Abed and A. Firoozabadi Compositional modeling of two-phase hydrocarbon reservoirs, SPE 36244 presented at the 7th Abu Dhabi International Petroleum Exhibition and Conference, Abu-Dhabi, UAE, 13-16 October 1996.

[3] S.T. Lee and M. Chaverra, Modeling and interpretation of condensate banking for the near critical Cupiagua Field, SPE 49265 prepared for presentation at the 1998 SPE Annual Technical Conference and Exhibition, New Orleans, Louisiana, September 27-30, 1998.

[4] K.O. Temeng, M.J. Al-Sadeg and A. Al-Mulhim, Compositional grading in the Ghawar Khuff Reservoirs, SPE 49270 prepared for presentation at the 1998 SPE Annual Technical Conference and Exhibition, New Orleans, Louisiana, September 27-30, 1998.

[5] P. Belery and F. V. da Silva, Gravity and thermal diffusion in hydrocarbon reservoirs, Third North Sea Chalk Research Symposium, Copenhagen, June 11-12, 1990.

[6] A. N. Jacqmin, Interaction of natural convection and gravity segregation in oil/gaz reservoirs, SPE Res. Eng., pp. 233-238, May 1990.

[7] K. Ghorayeb and A. Firoozabadi, Molecular, pressure, and thermal diffusion flux in non-ideal multicomponent mixtures, Part I, Chap IV.

[8] E. P. Sakonidou, H. R. van der Berg, C. A. Ten Seldam and J. V. Sengers, The thermal conductivity of an equimolar methane-ethane mixture in the critical region, J. Chem. Phys., Vol. 109, pp. 717-736, 1998.

[9] R. Haase, H. W. Borgmann, K. H. Duker and W. L. Lee, Thermodiffusion im kritischen vardampfungsgebiet ninarer systeme, Z. Naturforsch, Teil A., vol. 26, p. 1224, 1971.

[10] W. M. Rutherford and J. G. Roof, Thermal diffusion in methane n-butane mixtures in the critical region, J. Phys. Chem., vol. 63, p. 1506, 1959.

[11] J. P. Larre, K. K. Platten and G. Chavepeyer, Soret effects in ternary systems heated from below, Int. J. Heat Mass Transfer, Vol. 40, pp. 545-555, 1997.

[12] R. Krupiczka and A. Rotkegel, An experimental study of diffusional cross-effects in multicomponent mass transfer, Chemical Engineering Science, Vol. 52, pp. 1007-1017, 1997.

[13] P. M. Sigmund, Prediction of molecular diffusion at reservoir conditions. Part I – Measurement and prediction of binary dense gas diffusion coefficients, JCPT, April-June, pp. 48-57, 1976.

[14] M. R. Riazi and C. H. Whitson, Estimating diffusion coefficients of dense fluids, Ind. Eng. Chem. Res., Vol. 32, pp. 3081-3088, 1993.

[15] M. R. Riazi, A new method for experimental measurement of diffusion coefficients in reservoir fluids, J. Pet. Sci. Eng., Vol. 14, pp. 235-250, 1996.

[16] W. Hayduk and S. Loakimidos, Liquid Diffusivities in normal paraffin solutions, J. Chem. Eng. Data, Vol. 21, pp. 255-259, 1976.

[17] D. K. Dysthe and B. Hafskjold, Inter- and Intradiffusion in liquid mixtures of methane and n-decane, Int. J. Thermo., Vol. 16, pp. 1213-1224, 1995.

[18] W. Hayduk and B. S. Minhas, Correlations for predictions of molecular diffusivities in liquids, Can. J. Chem. Eng., Vol. 60, pp. 295-299, 1982.

[19] M. T. Tyn and W. F. Calus, Diffusion coefficients in dilute binary liquid mixtures, J. Chem. Eng. Data, Vol. 20, pp. 106-109, 1975.

[20] M. A. Siddiki and K. Lucas, Correlations for prediction of diffusion in liquids, Can. J. Chem. Eng., Vol. 64, pp. 839-843, 1986.

[21] E. L. Cussler, Multicomponent Diffusion, Elsevier Sci. Pub. Co., 1976.

[22] H. J. V. Tyrell and K. R. Harris, Diffusion in Liquids, a theoretical and experimental study, Butterworths, 1984.

[23] H. A. Kooijman and R. Taylor, Estimation of diffusion coefficients in multicomponent liquid system, Ind. Eng. Chem. Res. Vol. 30, pp. 1217-1222, 1991.

[24] A. Vignes, Diffusion in Binary Solutions, Ind. Eng. Chem. Fundamentals, Vol. 5, pp. 189-199, 1966.

[25] A. Firoozabadi, K. Ghorayeb and K. Shukla, Theoretical modeling of multicomponent thermal diffusion factors, Part II, Chapter IV.

[26] M. El Maâtaoui, Conséquences de la thermodiffusion en milieu poreux sur l'hydrolyse des solutions de chlorures ferriques et sur les migrations d'hydrocarbures dans les mélanges de n-alcanes et dans un pétrole brut: implications géochimiques, PhD thesis, Université Paul Sabatier, Toulouse, France, 1986.

[27] A.M. Schulte, Compositional variation whitin a hydrocarbon column due to gravity, SPE 9235 prepared for presentation at the 1980 SPE Annual Technical Conference and Exhibition, Dallas, Texas, September 21-24, 1980.

[28] F. Montel and P.L. Gouel, Prediction of compositional grading in a reservoir fluid column, SPE 14410 prepared for presentation at the 1985 SPE Annual Technical Conference and Exhibition, Las Vegas, Nevada, September 22-25, 1985.

[29] A. Hirscberg, Role of asphaltenes in compositional grading of a reservoirs's fluid column, J. Pet. Tech., pp. 89-94, January 1988.

[30] R.J. Wheaton, Treatement of variations of compostion in gaz-condensate reservoirs, SPE Res. Eng., pp. 239-244, May 1991.

[31] T. Holt, E. Lindeberg, and S.K. Ratkje The effect of gravity and temperature gradients on methane distribution in oil reservoirs, SPE 11761, 1983.

[32] C.H. Curtis and P. Belery, Compositional Gradients in Petroleum Reservoirs, SPE 28000 prepared for presentation at the University of Tulsa Centennial Petroleum Engineering Symposium, Tulsa, Oklahoma, August 29-31, 1994.

[33] M. F. Riley and A. Firoozabadi, Compositional variation in hydrocarbon reservoirs with natural convection and diffusion, AIChE J., Vol. 44, pp. 452-464, 1998.

[34] K. Ghorayeb and A. Firoozabadi, Features of convection and diffusion in porous media for binary systems, Part IV, Chapter IV.

[35] Ph. Jamet, D. Fargue, P. Costesèque, G. De. Marsily and A. Cernes, The thermogravitational effect in porous media: a modelling approach, Transport in Porous Media, Vol. 9, pp. 223-240, 1992.

[36] K. Ghorayeb and A. Firoozabadi, Natural convection and diffusion in fractured porous media, Part III, Chapter IV.

[37] D. Y. Peng and D. B. Robinson, A new two-constant equation of state, Ind. Eng. Chem. Fund., Vol. 15, pp. 59-64, 1976.

[38] S. V. Patankar, Numerical Heat Transfer and Fluid Flow, Hemisphere, Washington, 1980.

[39] A. Firoozabadi, Thermodynamics of Hydrocarbon Reservoirs, Mc Graw-Hill, New York, 1998.

[40] W. H. Furry, R. C. Jones and L. Onsager, On the theory of isotope separation by thermal diffusion, Phys. Rev., Vol. 55, pp. 1083-1095, 1939.

[41] M. Lorenz and A. H. J. R. Emery, The packed thermal diffusion column, Chem. Eng. Sci., Vol. 11., pp. 16-23, 1959.

[42] S. R. de Groot and P. Mazur, Non-Equilibrium Thermodynamics, North-Holland Pub. Co., Amsterdam, 1962.

[43] L. Onsager, Reciprocal relations in irreversible processes. I, Phys. Rev., Vol. 37, pp. 405-426, 1931.

[44] L. Onsager, Reciprocal relations in irreversible processes. II, Phys. Rev., Vol. 38, pp. 2265-2279, 1931.

[45] R. Krishna, Ternary mass transfer in a wetted wall column. Significance of diffusional interaction. Part II: equimolar diffusion, Trans. Inst. Chem. Eng., Vol. 59, pp. 44-53, 1981.

[46] J. A. Wesselingh and R. Krishna, Elements of Mass Transfer, Ellis Hoorwood, Chichester, U.K., 1990.

[47] C. R. Wilke and P. Chang, Correlation of diffusion coefficients in dilute solutions, AIChE J., Vol. 1, pp. 264-270, 1955.

[48] J. Bandrowski and A. Kubaczka, On the prediction of diffusivities in multicomponent liquid systems, Chemical Engineering Science, Vol. 37, pp. 1309-1313, 1982.

[49] R. C. Reid, J. M. Prausnitz and B. Poling, The Properties of Gases and Liquids, 4th ed., McGraw-Hill, New York, 1987; Chapter 11, pp. 577-631.

[50] B. A. Younglove and J. F. Ely, Thermophysical properties of fluids. II- Methane, Ethane, Propane, iso-Butane and normal-Butane, J. Phy. Chem. Ref. Data, Vol. 16, pp. 577-798, 1987.

[51] C. M. B. P. Oliveira and W. Wakeham, The viscosity of five liquid hydrocarbons at pressure up to 250 MPa, Int. J. Termo., Vol. 13, pp. 773-790, 1992.

[52] M. J. Assael, J. H. Dymond, S. K. Polmatidou and E. Vogel, measurements of the viscosity of n-Heptane, n-Nonane, and n-Undecane at pressure up to 70 MPa, Int. J. Termo., Vol. 12, pp. 801-810, 1991.

[53] A. Fenghour, W. A Wakeham and V. Vesovic, The viscosity of carbon dioxide, J. Phy. Chem. Ref. Data, Vol. 27, pp. 31-44, 1998.

[54] B. A. Younglove, Thermophysical properties of fluids. 1. Argon, Ethylene, para-Hydrogen, Nitrogen, Nitrogen Triluoride and Oxygen, J. Phy. Chem. Ref. Data, Vol. 11, pp. 1-353, 1982.

[55] K. E. Starling, Fluid Thermodynamics Properties for Light Petroleum Systems, Gulf Pub. Co., Houston, 1973.

[56] K. Shukla, and A. Firoozabadi, A new model of thermal diffusion coefficients in binary hydrocarbon mixtures, Ind. Eng. Chem. Res. Vol. 37, pp. 3331-3342, 1998.

[57] S. Glasstone, K. J. Laidler and H. Eyring, The theory of Rate Processes, McGraw-Hill, 1941.

Appendix A–Diffusion mass flux

Ghorayeb and Firoozabadi [7] have used: 1) the entropy production expression [42]; 2) phenomenological laws of the thermodynamics of the irreversible processes; 3) Onsager's reciprocal relations [43, 44]; and 4) equilibrium thermodynamics at a local level to derive the diffusive flux vector $\mathbf{J} = \left(\vec{J}_1, \ ..., \ \vec{J}_{n-1}\right)$ in a non-ideal fluid mixture of n components. The flux reads

$$\mathbf{J} \ = \ -c\left(\mathbf{D}^{\mathbf{M}}.\nabla \mathbf{x} + \mathbf{D}^{\mathbf{T}}.\vec{\nabla} T + \mathbf{D}^{\mathbf{P}}.\vec{\nabla} p\right). \qquad \text{(A-1)}$$

The molecular diffusion coefficients, thermal diffusion coefficients and pressure diffusion coefficients D_{ij}^M, D_i^T and D_i^p, $i,j = 1,\ ...,\ n-1$, are expressed by

$$D_{ij}^M = a_{in} D_{in} \frac{M_i x_i}{L_{ii}} \sum_{k=1}^{n-1} L_{ik} \sum_{l=1}^{n-1} \frac{M_l x_l + M_n x_n \delta_{lk}}{M_l} \left. \frac{\partial \ln f_l}{\partial x_j} \right|_{x_j, T, P}, \quad i,j = 1,\ ...,\ n-1,, \tag{A-2}$$

$$D_i^T = a_{in} D_{in} M \frac{k_{Ti}}{T}, \quad i = 1,\ ...,\ n-1, \tag{A-3}$$

$$D_i^P = a_{iN} D_{iN} \frac{M_i x_i}{RTL_{ii}} \sum_{k=1}^{n-1} L_{ik} \left[\sum_{j=1}^{n-1} x_j \bar{V}_j + \frac{M_N x_N}{M_k} \bar{V}_k - \frac{M}{\rho} \right] \quad i = 1,\ ...,\ n-1, \tag{A-4}$$

respectively, where M_i, f_i and $\bar{V}_i$ are the molecular weight, the fugacity, and the partial molar volume of component i, respectively. In the above equations, L_{ij}, $i,j = 1,\ 2$ are the phenomenological coefficients ($L_{ij} = L_{ji}$) [42]. $\bar{V}_i$ and f_i can be obtained using an equation of state [39]. The coefficients a_{in}, D_{in} and k_{Ti} (thermal diffusion ratio of component i) are given by

$$a_{in} = \frac{M_i M_n}{M^2}, \quad i = 1,\ ...,\ n-1, \tag{A-5}$$

$$D_{in} = \frac{M^3 R L_{ii}}{\rho M_i^2 M_n^2 x_i x_n} \quad i = 1,\ ...,\ n-1, \tag{A-6}$$

$$k_{Ti} = \frac{M_i x_i M_n x_n L'_{iq}}{MRTL_{ii}} = \alpha_{Ti} x_i x_n, \quad i = 1,\ ...,\ n-1; \tag{A-7}$$

α_{Ti} is the thermal diffusion factor of component i. Let

$$c_1 = \frac{M_1 x_1 + M_3 x_3}{M_1} \left. \frac{\partial \ln f_1}{\partial x_2} \right|_{P,\ T,\ x_1} + x_2 \left. \frac{\partial \ln f_2}{\partial x_2} \right|_{P,\ T,\ x_1},$$

$$c_2 = x_1 \left. \frac{\partial \ln f_1}{\partial x_2} \right|_{P,\ T,\ x_1} + \frac{M_2 x_2 + M_3 x_3}{M_2} \left. \frac{\partial \ln f_2}{\partial x_2} \right|_{P,\ T,\ x_1},$$

$$c_3 = \frac{M_1 x_1 + M_3 x_3}{M_1} \left. \frac{\partial \ln f_1}{\partial x_1} \right|_{P,\ T,\ x_2} + x_2 \left. \frac{\partial \ln f_2}{\partial x_1} \right|_{P,\ T,\ x_2},$$

$$c_4 = x_1 \left. \frac{\partial \ln f_1}{\partial x_1} \right|_{P,\ T,\ x_2} + \frac{M_2 x_2 + M_3 x_3}{M_2} \left. \frac{\partial \ln f_2}{\partial x_1} \right|_{P,\ T,\ x_2}.$$

For a ternary mixture, Eqs. A-2-A-4 then read

$$D_{11}^M = a_{13} D_{13} M_1 x_1 \left(c_3 + c_4 \frac{L_{12}}{L_{11}} \right), \tag{A-8}$$

$$D_{12}^M = a_{13} D_{13} M_1 x_1 \left(c_1 + c_2 \frac{L_{12}}{L_{11}} \right), \tag{A-9}$$

$$D_{21}^{M} = a_{23}D_{23}M_2x_2\left(c_4 + c_3\frac{L_{21}}{L_{22}}\right), \tag{A-10}$$

$$D_{22}^{M} = a_{23}D_{23}M_2x_2\left(c_2 + c_1\frac{L_{21}}{L_{22}}\right), \tag{A-11}$$

$$D_1^p = a_{13}D_{13}\frac{M_1x_1}{RT}\left[\frac{M_1x_1 + M_3x_3}{M_1}\bar{V}_1 + x_2\bar{V}_2 - \frac{M}{\rho} + \left(\frac{M_2x_2 + M_3x_3}{M_2}\bar{V}_2 + x_1\bar{V}_1 - \frac{M}{\rho}\right)\frac{L_{12}}{L_{11}}\right], \tag{A-12}$$

$$D_2^p = a_{23}D_{23}\frac{M_2x_2}{RT}\left[\frac{M_2x_2 + M_3x_3}{M_2}\bar{V}_2 + x_1\bar{V}_1 - \frac{M}{\rho} + \left(\frac{M_1x_1 + M_3x_3}{M_1}\bar{V}_1 + x_2\bar{V}_2 - \frac{M}{\rho}\right)\frac{L_{21}}{L_{22}}\right]. \tag{A-13}$$

$$D_1^T = a_{13}D_{13}Mk_{T1}, \tag{A-14}$$

$$D_2^T = a_{23}D_{23}Mk_{T2}, \tag{A-15}$$

From Eqs. A-8-A-11 the phenomenological coefficients read (provided that $c_2c_3 - c_1c_4 \neq 0$)

$$L_{11} = \frac{cM_3x_3}{R\ (c_2c_3 - c_1c_4)}\left(c_2D_{11}^{M} - c_4D_{12}^{M}\right), \tag{A-16}$$

$$L_{12} = \frac{-cM_3x_3}{R\ (c_2c_3 - c_1c_4)}\left(c_1D_{11}^{M} - c_3D_{12}^{M}\right), \tag{A-17}$$

$$L_{21} = \frac{cM_3x_3}{R\ (c_2c_3 - c_1c_4)}\left(c_2D_{21}^{M} - c_4D_{22}^{M}\right), \tag{A-18}$$

$$L_{22} = \frac{-cM_3x_3}{R\ (c_2c_3 - c_1c_4)}\left(c_1D_{21}^{M} - c_3D_{22}^{M}\right). \tag{A-19}$$

Suppose the molecular diffusion coefficients are known say by experimental measurements or from a correlation (see Appendix B for the correlation we used in this work); the phenomenological coefficients can be obtained using Eqs. A-16-A-19. Note that $c_2c_3 - c_1c_4$ (appearing in Eqs. A-16 to A-19) vanishes at the critical point because of the criticality condition [39]. Once the phenomenological coefficients are calculated, the pressure diffusion coefficients are readily obtained from Eqs. A-12 and A-13.

Appendix B–Molecular diffusion coefficients

There are a number of attempts in the literature to predict multicomponent molecular diffusion coefficients for liquid systems (Krishna [45], Wesselingh and Krishna [46]). Kooijman and Taylor [23] summarized the existing equations and proposed a correlation for the Maxwell-Stefan diffusion coefficients $\hat{D}_{ij}$ for multicomponent mixtures based on a generalization of the Vignes [24] equation for binary systems. For a mixture of n components,

this correlation reads [23]

$$\hat{D}_{ij} = \left(\hat{D}^0_{ij}\right)^{x_j} \left(\hat{D}^0_{ji}\right)^{x_i} \prod_{\substack{k=1 \\ k \neq i,\ j}}^{n} \left(\hat{D}^0_{ik}\hat{D}^0_{jk}\right)^{x_k/2}. \tag{B-1}$$

where $\hat{D}^0_{ij}$ are the coefficients at infinite dilution. The Maxwell-Stefan and the Fickian expressions for the molar diffusive fluxes for non-ideal mixtures are

$$\mathbf{J} = -c\,\mathbf{B}^{-1}.\mathbf{\Gamma}.\vec{\nabla}x \tag{B-2}$$

and

$$\mathbf{J} = -c\,\mathbf{D}^{\mathrm{M}}.\vec{\nabla}x, \tag{B-3}$$

respectively [23]. In the above equations $\mathbf{D}^{\mathrm{M}}$ denotes the Fickian diffusion coefficients matrix, $\mathbf{B}$ is a square matrix (order $n-1$) with elements given by

$$B_{ii} = \frac{x_i}{\hat{D}_{in}} + \sum_{\substack{k=1 \\ i \neq k}}^{n} \frac{x_k}{\hat{D}_{ik}}, \tag{B-4}$$

$$B_{ij} = -x_i\left(\frac{1}{\hat{D}_{ij}} - \frac{1}{\hat{D}_{in}}\right), \tag{B-5}$$

and, $\mathbf{\Gamma}$ is the matrix with elements given by

$$\Gamma_{ij} = x_i \left.\frac{\partial \ln f_i}{\partial x_j}\right|_{\mathbf{x_j},T,P}, \tag{B-6}$$

where $\mathbf{x_j}$ denotes $\mathbf{x_j} \equiv (x_1, ..., x_{j-1}, x_{j+1}, ..., x_{n-1})$. Thus, the Maxwell-Stefan diffusion coefficients are related to the Fickian diffusion coefficients by the following relationship

$$\mathbf{D}^{\mathrm{M}} = \mathbf{B}^{-1}.\mathbf{\Gamma}. \tag{B-7}$$

Several attempts have been made to estimate the infinite dilution diffusion coefficients (Wilke and Chang [47], Tyn and Calus [19], Bandrowski and Kubaczka [48], and Hayduk and Minhas [18]). Review and evaluation of those correlations have been made by Siddiki and Lucas [20], and Reid *et al.* [49]. After comparing the results obtained by those correlations, Siddiki and Lucas [20]recommended using the correlation proposed by Hayduk and Minhas [18] for liquid mixtures of normal paraffins

$$\hat{D}^0_{ij} = 13.3\left(10^{-8}\right) T^{1.47} \eta_j^{(10.2/V_i - 0.791)} V_i^{-0.71}, \tag{B-8}$$

where η_j and V_i are the viscosity and the molar volume at the normal boiling point of component i, respectively.

Eqs. B-1 and B-8 allow us to predict the Maxwell-Stefan diffusion coefficients. Following this calculation, the Fickian diffusion coefficients can be obtained using Eq. B-7. The fugacities f_i are calculated using the PR EOS [37]. We used the viscosity and the normal boiling point data reported in Refs. [50, 52, 53, 54] and [55], respectively. We have also performed an independent evaluation of the above correlation for some new binary diffusion coefficients such as the C_1/nC_{10} mixture at high pressures and temperatures [17], which yielded satisfactory results.

Appendix C–Thermal diffusion coefficients

Thermal diffusion coefficients in multicomponent mixtures has been studied by Firoozabadi *et al.* [25]. Here, we summarize the model reported by the authors for the sake of completeness. The diffusion flux $\vec{J}_i$ of the *ith* component in a mixture of n components can be written in the two following forms

$$\vec{J}_i = -L'_{iq}\frac{\vec{\nabla}T}{T^2} - \frac{1}{T}\sum_{k=1}^{n-1} L_{ik}\vec{\nabla}_T\left(\frac{\mu_k}{M_k} - \frac{\mu_n}{M_n}\right), \quad i = 1, \ ..., \ n-1, \tag{C-1}$$

$$\vec{J}_i = -\frac{1}{T}\sum_{k=1}^{n-1} L_{ik}\left[\left(\frac{Q_k^*}{M_k} - \frac{Q_n^*}{M_n}\right)\frac{\vec{\nabla}T}{T} + \vec{\nabla}_T\left(\frac{\mu_k}{M_k} - \frac{\mu_n}{M_n}\right)\right], \quad i = 1, \ ..., \ n-1, \tag{C-2}$$

where Q_k^* is the net heat of transport, and L'_{iq} and L_{ik} are the phenomenological coefficients. Eqs. C-1 and C-2 imply

$$L'_{iq} = \sum_{k=1}^{n-1} L_{ik}\left(\frac{Q_k^*}{M_k} - \frac{Q_n^*}{M_n}\right), \qquad i = 1, \ ..., \ n-1. \tag{C-3}$$

Let

$$\begin{aligned}
\mathbf{L} &\equiv [L_{ij}] \equiv L_{ij} \quad i,j = 1, \ ..., \ n-1, \\
\mathbf{L_q} &\equiv \left[L'_{iq}\right] \quad i = 1, \ ..., \ n-1, \\
\mathbf{Q} &\equiv \left[\frac{Q_k^*}{M_k} - \frac{Q_n^*}{M_n}\right] \quad i = 1, \ ..., \ n-1.
\end{aligned}$$

Eq. C-3 can be then written in a compact form as

$$\mathbf{L_q} = \mathbf{L.Q}. \tag{C-4}$$

Let

$$\begin{aligned}
\mathbf{D} &\equiv [\mathbf{D}_{ij}] \equiv a_{in}D_{in}\delta_{ij} \quad i,j = 1, \ ..., \ n-1, \\
\mathbf{M} &\equiv [\mathbf{M}_{ij}] \equiv \frac{M_i x_i}{L_{ii}}\delta_{ij} \quad i,j = 1, \ ..., \ n-1, \\
\mathbf{W} &\equiv [\mathbf{W}_{ij}] \equiv \frac{M_j x_j + M_n x_n \delta_{ij}}{M_j} \quad i,j = 1, \ ..., \ n-1, \\
\mathbf{K_T} &\equiv [\mathbf{K}_{\mathbf{T}i}] \equiv k_{Ti} = x_i x_n \alpha_{Ti} \quad i = 1, \ ..., \ n-1;
\end{aligned}$$

Using Eqs. A-1–A-4 $\mathbf{D^M}$ and $\mathbf{L_q}$ read

$$\mathbf{D^M} = \mathbf{D.M.L.W.F}, \tag{C-5}$$

and

$$\mathbf{L_q} = \frac{MRT}{M_n x_n}\mathbf{M}^{-1}.\mathbf{K_T}, \tag{C-6}$$

respectively. Eq. C-6 can be written as

$$k_{Ti} = \frac{M_i x_i M_n x_n}{MRTL_{ii}} \sum_{j=1}^{n-1} L_{ij}\left(\frac{Q_j^*}{M_j} - \frac{Q_n^*}{M_n}\right). \quad i = 1, \ ..., \ n-1 \tag{C-7}$$

The net heat of transport for the *ith* component in an n component mixture has been determined by generalizing, for n components, the expression used by Shukla an Firoozabadi [56]

$$Q_i^* = -\frac{\Delta\bar{U}_i}{\tau_i} + \left[\sum_{j=1}^{n} \frac{x_j \Delta\bar{U}_j}{\tau_j}\right] \frac{\bar{V}_i}{\sum_{j=1}^{n} x_j \bar{V}_j} \quad i = 1, \ ..., \ n, \tag{C-8}$$

where $\Delta\bar{U}_i$ is the partial molar internal energy departure of component i, $\tau_i = \Delta U_i^{vap}/\Delta U_i^{vis}$; ΔU_i^{vap} and ΔU_i^{vis} are the energy of vaporization and the energy of viscous flow, respectively [57].

From Eq. C-5, one obtains the expression relating the phenomenological coefficients matrix $\mathbf{L}$ to the molecular diffusion coefficients matrix $\mathbf{D^M}$ [7]

$$\mathbf{L} = (\mathbf{D.M})^{-1}.\mathbf{D^M}.(\mathbf{W.F})^{-1}; \tag{C-9}$$

which can be written as [7]

$$\sum_{l=1}^{n-1}\sum_{k=1}^{n-1} \frac{M_k x_k + M_n x_n \delta_{lk}}{M_k} \left.\frac{\partial \ln f_k}{\partial x_j}\right|_{x_j,T,P} L_{li} = \frac{\rho M_n x_n}{R} D_{ij}^M,$$
$$i, j = 1, \ ..., \ n-1. \tag{C-10}$$

Thus, having $\mathbf{D^M}$ and $\mathbf{Q}$, the calculation of $\mathbf{D^T}$ becomes straightforward from Eq. A-3.

Table 1: Predicted and experimental composition in a thermogravitational column for a binary mixture of nC_{14}/nC_{12}. Initial composition: 8.15% nC_{24}; 91.85% nC_{12}. $T_0 = 321.5$ K, $\Delta T = 25$. Column height = 40 cm.

	Data of El Maâtaoui [26]			Model Results		
$k(m^2)$	$(nC_{24})_{bottom}$	$(nC_{24})_{top}$	q	$(nC_{24})_{bottom}$	$(nC_{24})_{top}$	q
2.90×10^{-11}	0.200	0.095	2.38	0.202	0.094	2.44
4.90×10^{-11}	0.230	0.109	2.44	0.193	0.105	2.03
6.10×10^{-11}	0.205	0.116	1.96	0.187	0.111	1.83
1.18×10^{-10}	0.188	0.133	1.51	0.171	0.128	1.41
1.79×10^{-10}	0.169	0.140	1.25	0.164	0.135	1.26
2.69×10^{-10}	0.151	0.136	1.13	0.160	0.140	1.17
4.75×10^{-10}	0.165	0.148	1.13	0.156	0.144	1.09

Table 2: Predicted and experimental composition in a thermogravitational column for a ternary mixture of $nC_{24}/nC_{16}/n_C12$; initial composition 12.67% nC_{24}; 37.41% nC_{16}; 49.92% nC_{12} . $T_0 = 321.5$ K, $\Delta T = 25$. Column height = 120 cm. $k = 6.1 \times 10^{-11}$ m^2.

	$(nC_{24})_{bottom}$	$(nC_{24})_{top}$	$(nC_{16})_{bottom}$	$(nC_{16})_{top}$
Measured data (Ref. [26])	0.240	0.140	0.415	0.380
Model results	0.265	0.135	0.408	0.389

Table 3: Relevant reservoir and fluid property data for the ternary mixture.

Reservoir Width	1500 m
Reservoir Height	150 m
Porosity	0.25
Viscosity	0.2 cp
Permeability	0–100 md
Vertical thermal gradient	3.5 K / 100 m
Horizontal thermal gradient	1.8K / 1000 m
Mesh	301×41

Table 4: Physical and transport properties for the $C_1/C_2/nC_4$ mixture: $x_{10} = 0.25$, $x_{20} = 0.25$ and $x_{30} = 0.50$.

Physical and transport properties	$P_0 = 7.0 \times 10^6$ Pa $T_0 = 315$ K	$P_0 = 7.8 \times 10^6$ Pa $T_0 = 345$ K	$P_0 = 7.4 \times 10^6$ Pa $T_0 = 395$ K
ρ_0 Kg/m^3	450.35	374.41	175.36
β_T K^{-1}	-0.52×10^{-2}	-0.86×10^{-2}	-1.43×10^{-2}
β_{x1}	−1.25	−2.17	−3.98
β_{x2}	−0.72	−1.25	−2.44
$D_{11} \times 10^{+9}$ m^2/s	+3.14	+3.52	+3.96
$D_{12} \times 10^{+9}$ m^2/s	−0.77	−1.68	−3.24
$D_{21} \times 10^{+9}$ m^2/s	−0.32	−0.83	−1.87
$D_{22} \times 10^{+9}$ m^2/s	+4.68	+6.43	+8.76
$D_1^P \times 10^{+16}$ m^2.Pa	+0.32	+0.87	+4.54
$D_2^P \times 10^{+16}$ m^2.Pa	+0.14	+0.47	+2.86
$D_1^T \times 10^{+12}$ m^2/s K	−5.13	−8.94	−11.8
$D_2^T \times 10^{+12}$ m^2/s K	−1.35	−2.71	−4.36

Table 5: Physical and transport properties for the $C_1/C_2/nC_4$ mixture: $x_{10} = 0.35$, $x_{20} = 0.35$ and $x_{30} = 0.30$.

Physical and transport properties	$P_0 = 8.5 \times 10^6$ Pa $T_0 = 290$ K	$P_0 = 9.3 \times 10^6$ Pa $T_0 = 315$ K	$P_0 = 8.8 \times 10^6$ Pa $T_0 = 365$ K
ρ_0 Kg/m^3	423.20	358.66	178.58
β_T K^{-1}	-0.51×10^{-2}	-0.86×10^{-2}	-1.26×10^{-2}
β_{x1}	−1.71	−2.48	−3.98
β_{x2}	−0.97	−1.44	−2.44
$D_{11} \times 10^{+9}$ m^2/s	+2.51	+2.26	+3.11
$D_{12} \times 10^{+9}$ m^2/s	−1.14	−2.03	−3.89
$D_{21} \times 10^{+9}$ m^2/s	+0.06	−0.74	−0.56
$D_{22} \times 10^{+9}$ m^2/s	+4.87	+6.10	+9.67
$D_1^P \times 10^{+16}$ m^2.Pa	+0.43	+0.98	+4.87
$D_2^P \times 10^{+16}$ m^2.Pa	+0.12	+0.43	+2.75
$D_1^T \times 10^{+12}$ m^2/s K	−6.94	−10.0	−13.2
$D_2^T \times 10^{+12}$ m^2/s K	+0.32	+0.11	−0.76

Table 6: Relevant reservoir and fluid property data for the field example.

Reservoir Width	10 km
Reservoir Height	1.5 km
Porosity	0.20
Viscosity	0.05 cp
Permeability	10 md
Vertical thermal gradient	2.0 K/ 100 m
Horizontal thermal gradient	1.5 K / 1000 m
Mesh	501×81

Table 7: Composition at the center of the reservoir for the field example.

Component	mole %	Component	mole %
CO_2	4.230	$C_3 - C_4$	9.120
N_2	5.000	$C_5 - C_6$	3.630
C_1	53.40	$C_7 - C_{19}$	6.345
C_2	10.95	C_{20+}	7.325

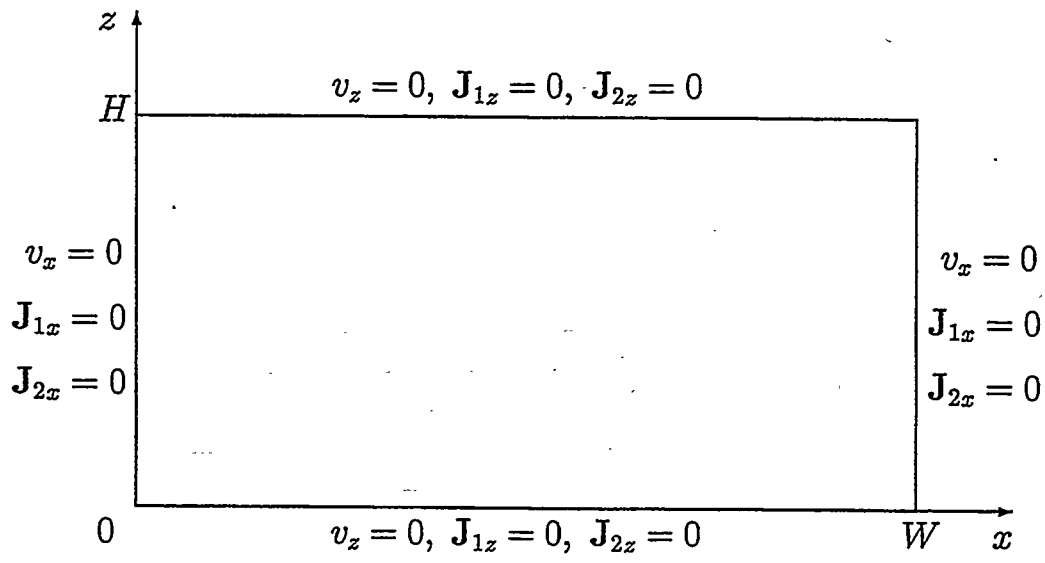

Figure 1: Geometry and boundary conditions.

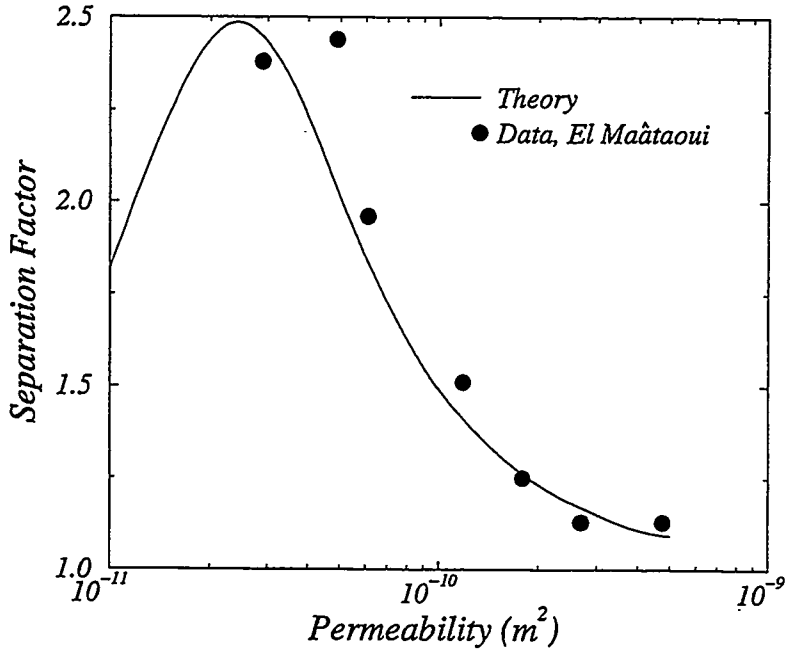

Figure 2: Predicted and measured separation factor $q = (x_{nC_{24}}/x_{nC_{12}})_{bottom} / (x_{nC_{24}}/x_{nC_{12}})_{top}$. Initial composition: 8.15% nC_{24}; 91.85% nC_{12}. $T_0 = 321.5$ K, $\Delta T = 25$. Column height = 40 cm.

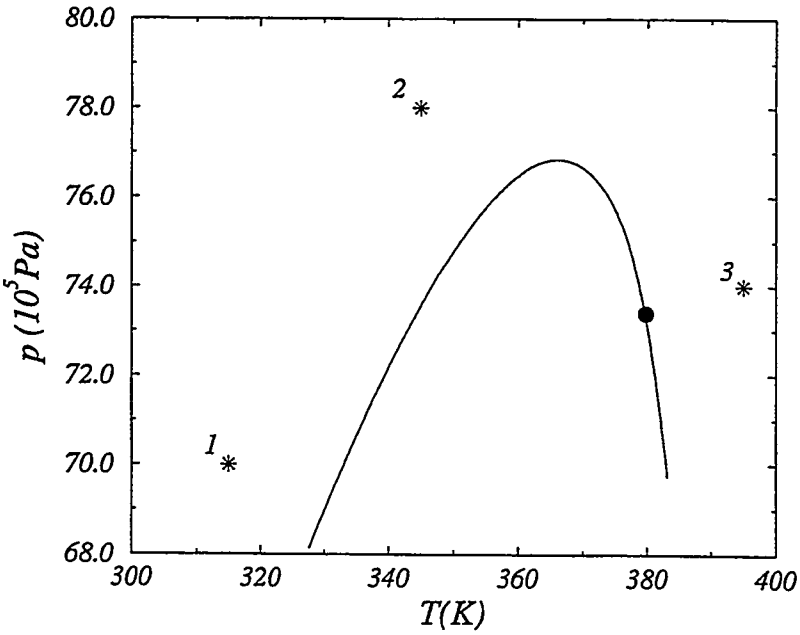

Figure 3: $p - T$ diagram for the ternary mixture $C_1/C_2/nC_4$: $x_{10} = 0.25$, $x_{20} = 0.25$ and $x_{30} = 0.50$. • denotes the critical point.

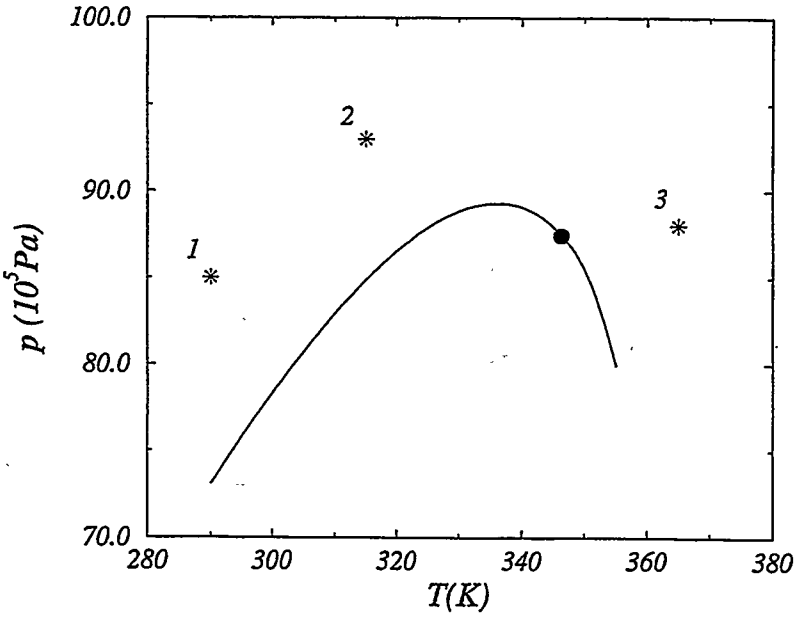

Figure 4: $p-T$ diagram for the ternary mixture $C_1/C_2/nC_4$: $x_{10} = 0.35$, $x_{20} = 0.35$ and $x_{30} = 0.30$. • denotes the critical point.

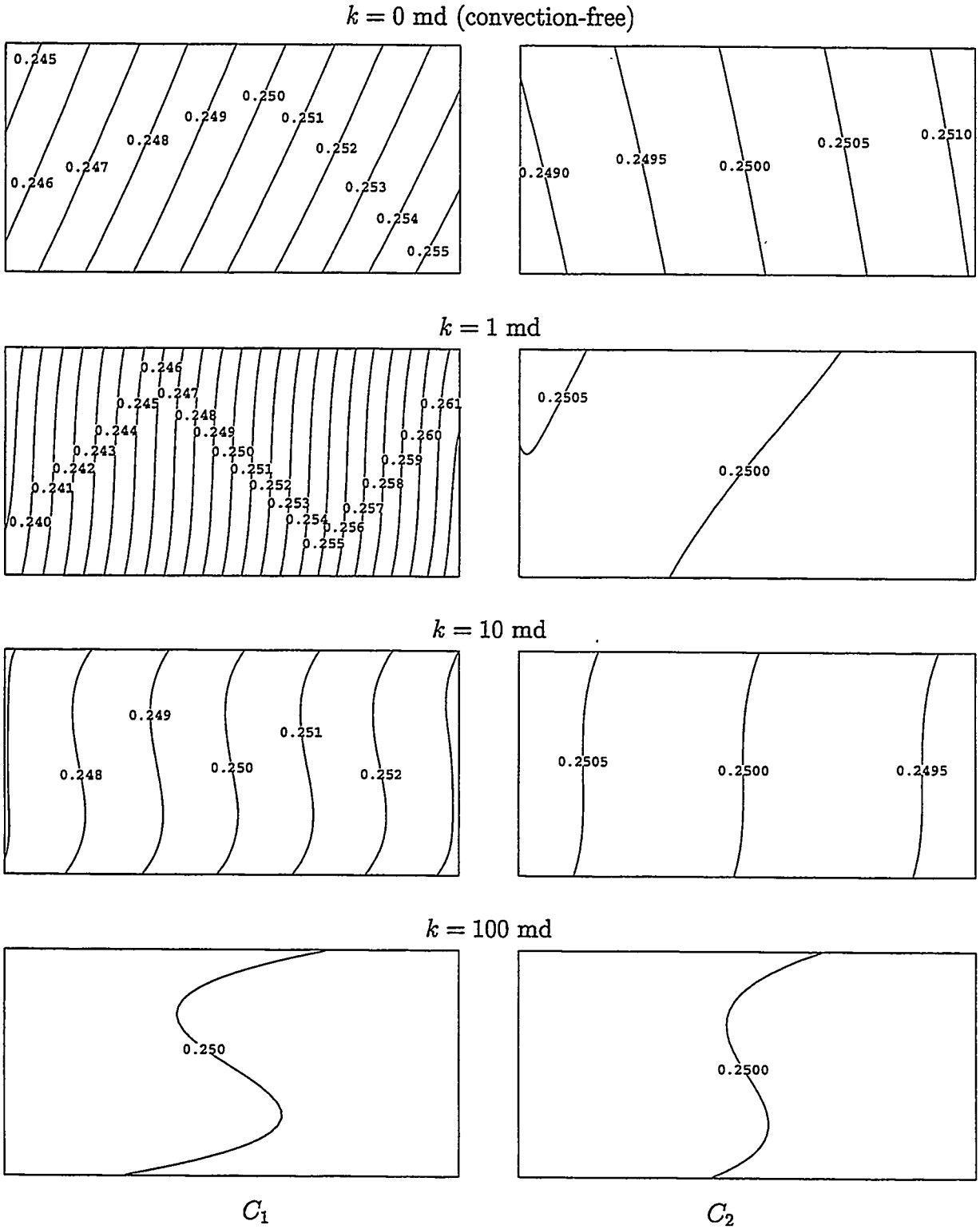

Figure 5: Composition contour plots for the $C_1/C_2/nC_4$ mixture: $P = 7.0 \times 10^6$ Pa, $T = 315$ K. $x_{10} = 0.25$, $x_{20} = 0.25$, $x_{30} = 0.50$.

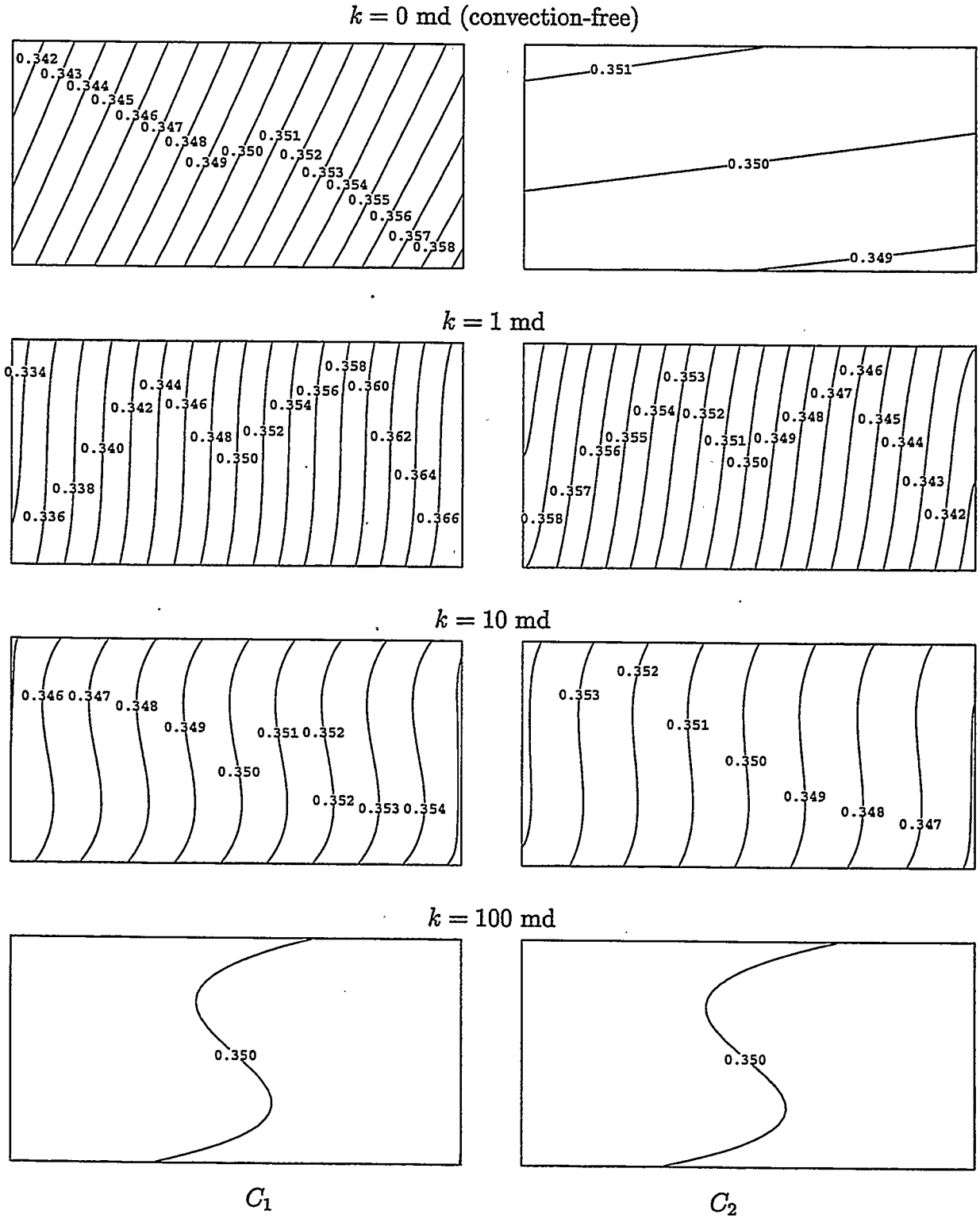

Figure 6: Composition contour plots for the $C_1/C_2/nC_4$ mixture: $P = 8.5 \times 10^6$ Pa, $T = 290$ K. $x_{10} = 0.35$, $x_{20} = 0.35$, $x_{30} = 0.30$.

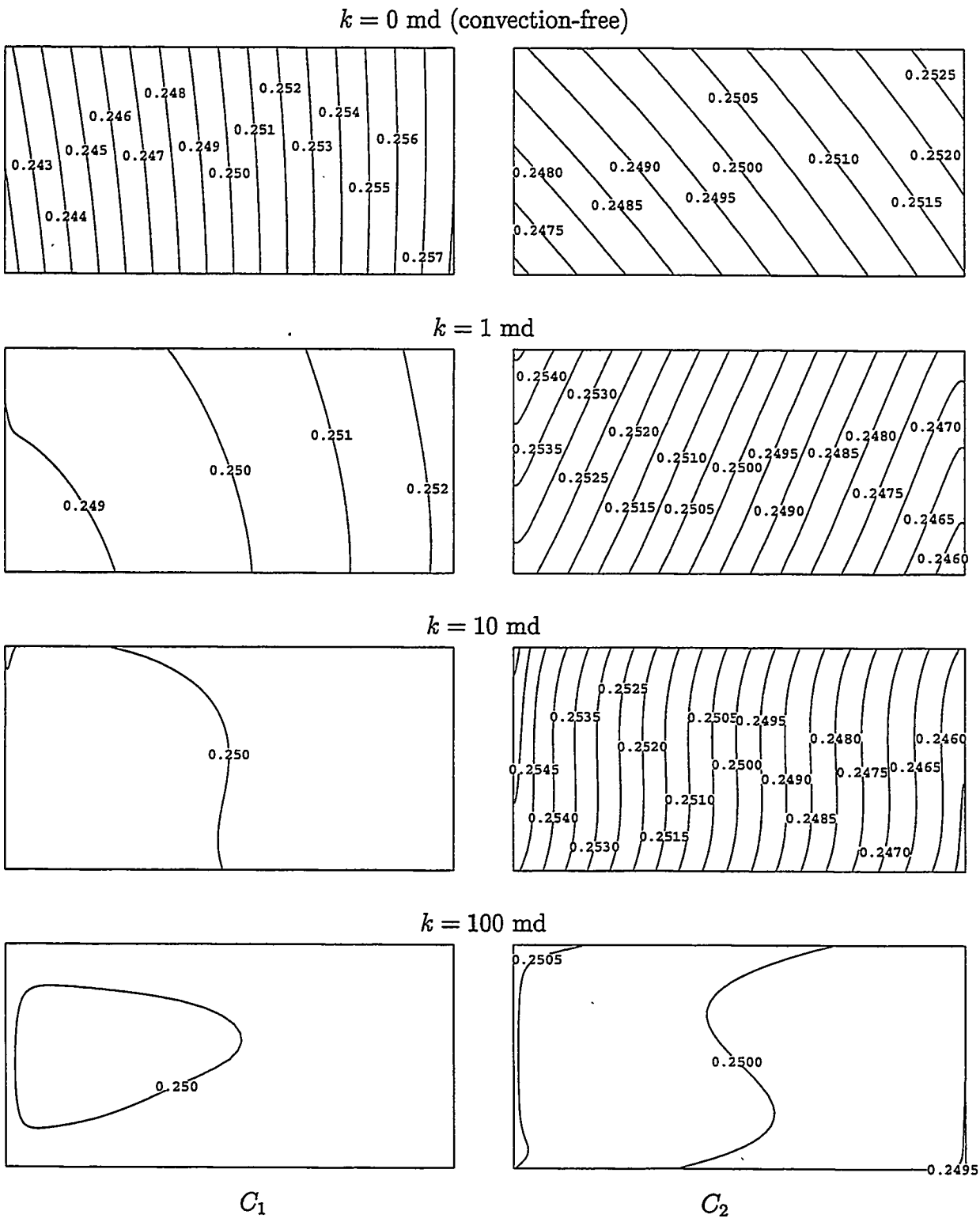

Figure 7: Composition contour plots for the $C_1/C_2/nC_4$ mixture: $P = 7.8 \times 10^6$ Pa, $T = 345$ K. $x_{10} = 0.25$, $x_{20} = 0.25$, $x_{30} = 0.50$.

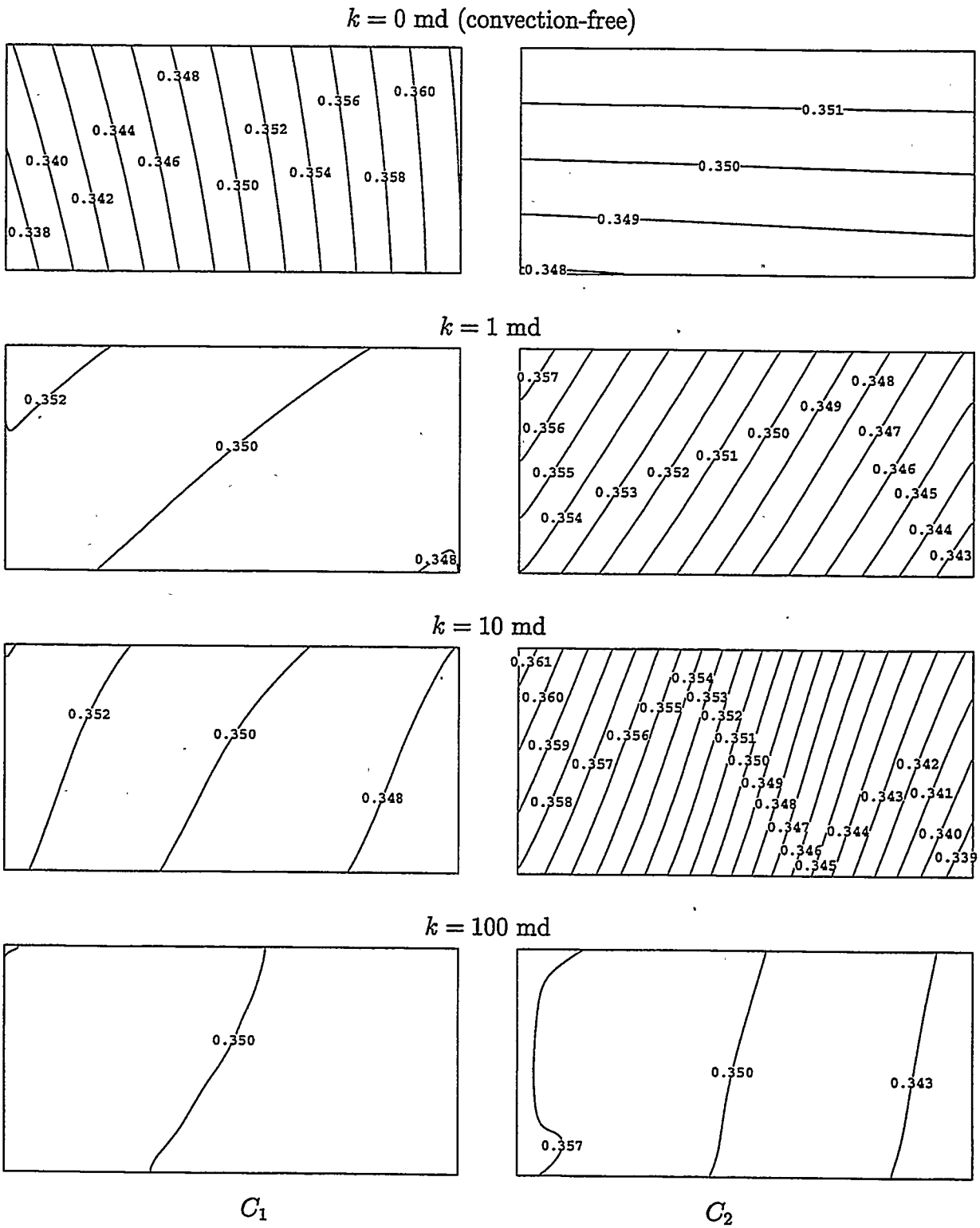

Figure 8: Composition contour plots for the $C_1/C_2/nC_4$ mixture: $P = 9.4 \times 10^6$ Pa, $T = 320$ K. $x_{10} = 0.35$, $x_{20} = 0.35$, $x_{30} = 0.30$.

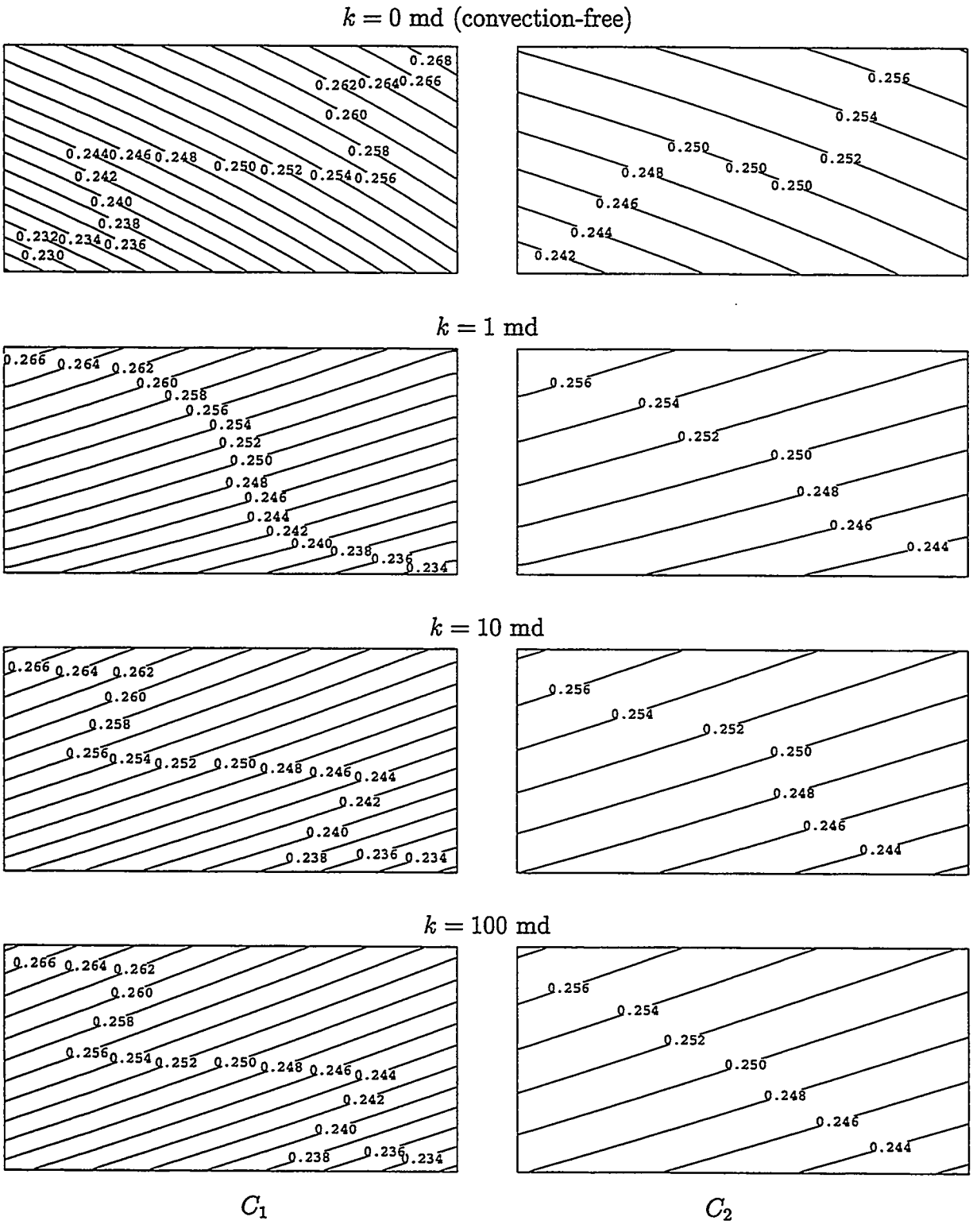

Figure 9: Composition contour plots for the $C_1/C_2/nC_4$ mixture: $P = 7.4 \times 10^6$ Pa, $T = 395$ K. $x_{10} = 0.25$, $x_{20} = 0.25$, $x_{30} = 0.50$.

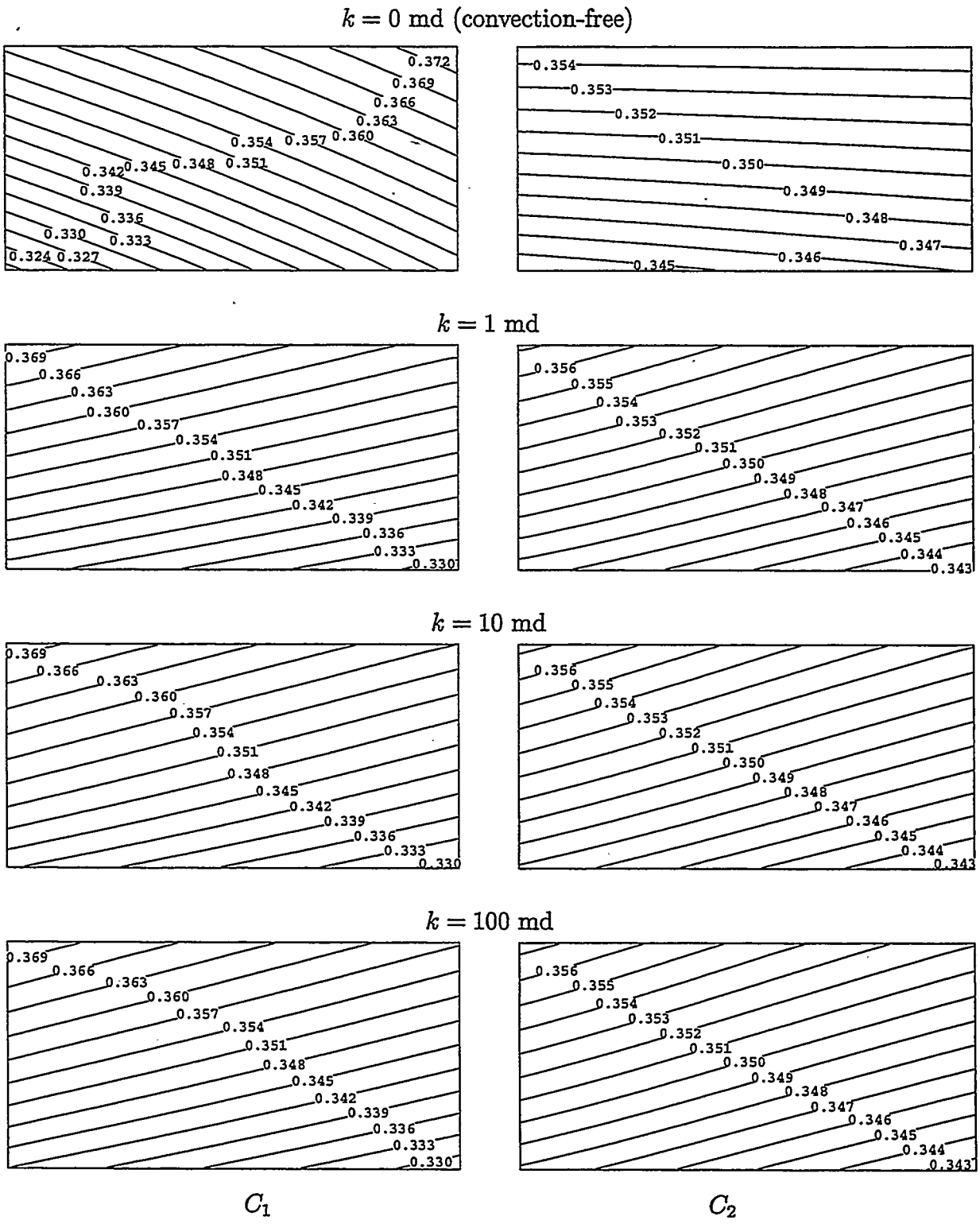

Figure 10: Composition contour plots for the $C_1/C_2/nC_4$ mixture: $P = 8.8 \times 10^6$ Pa, $T = 365$ K. $x_{10} = 0.35$, $x_{20} = 0.35$, $x_{30} = 0.30$.

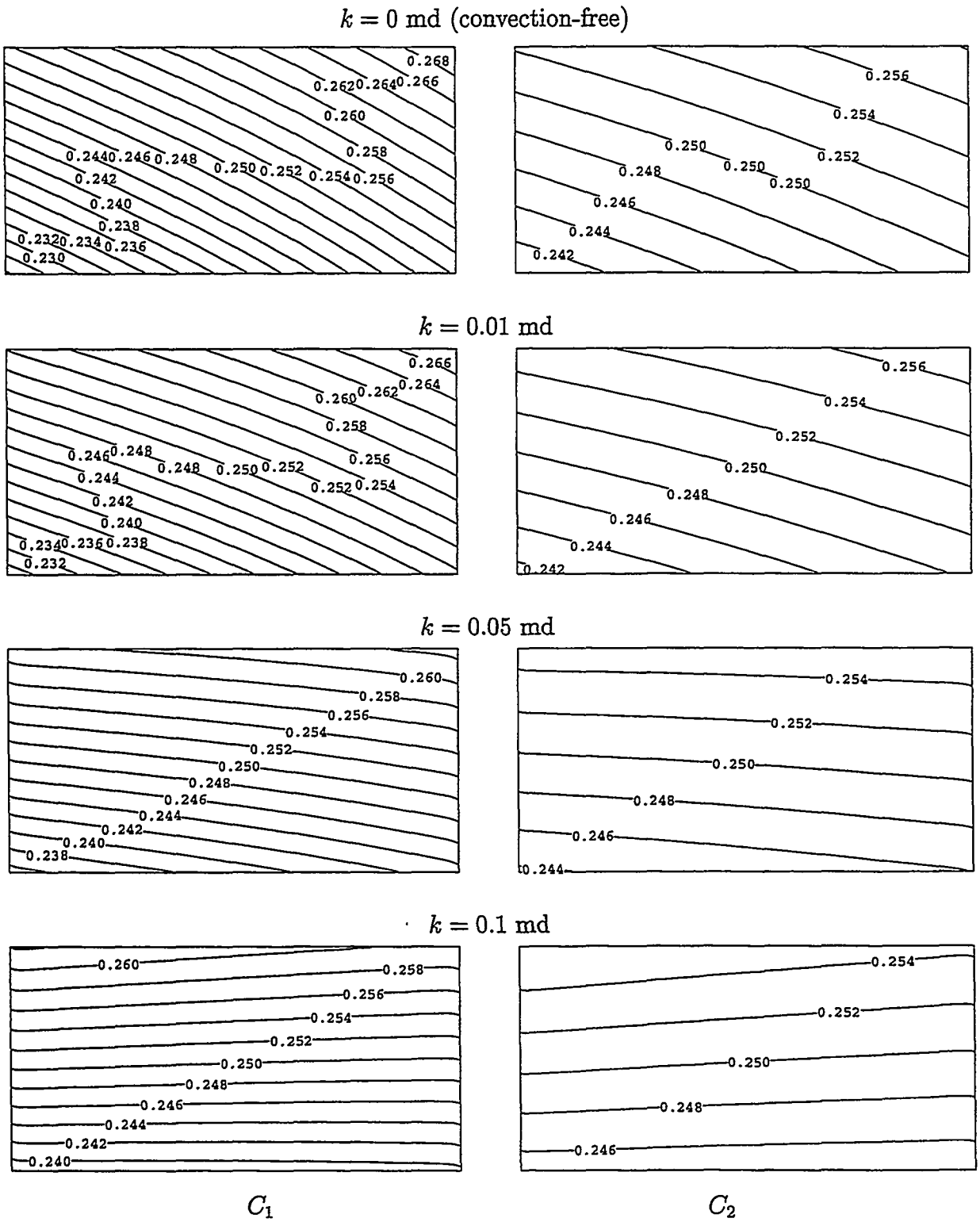

Figure 11: Composition contour plots for the $C_1/C_2/nC_4$ mixture: $P = 7.4 \times 10^6$ Pa, $T = 395$ K. $x_{10} = 0.25$, $x_{20} = 0.25$, $x_{30} = 0.50$.

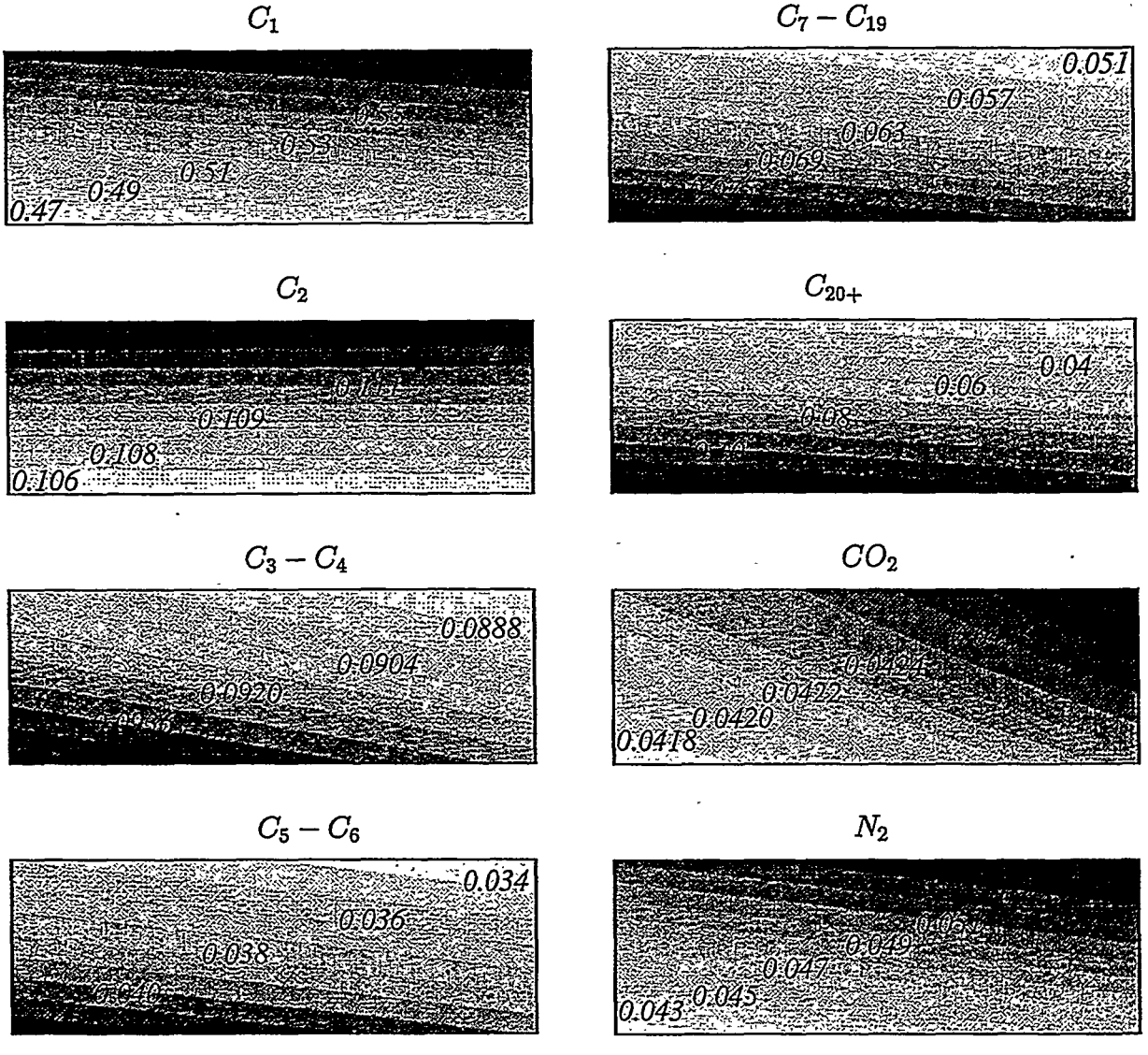

Figure 12: Composition contour plots for the field example: $k = 0$ md (convection-free)

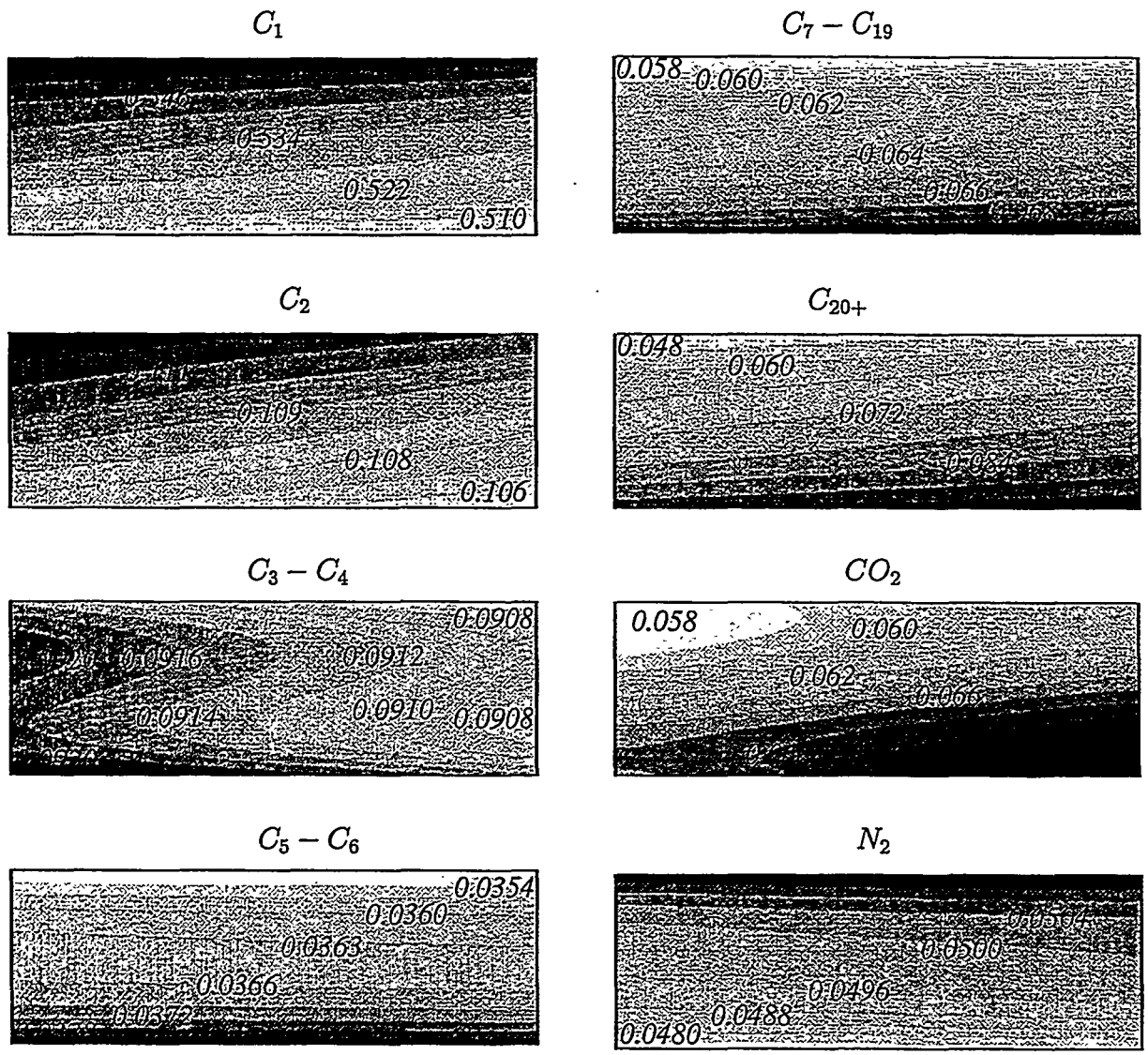

Figure 13: Composition contour plots for the field example: $k = 1$ md

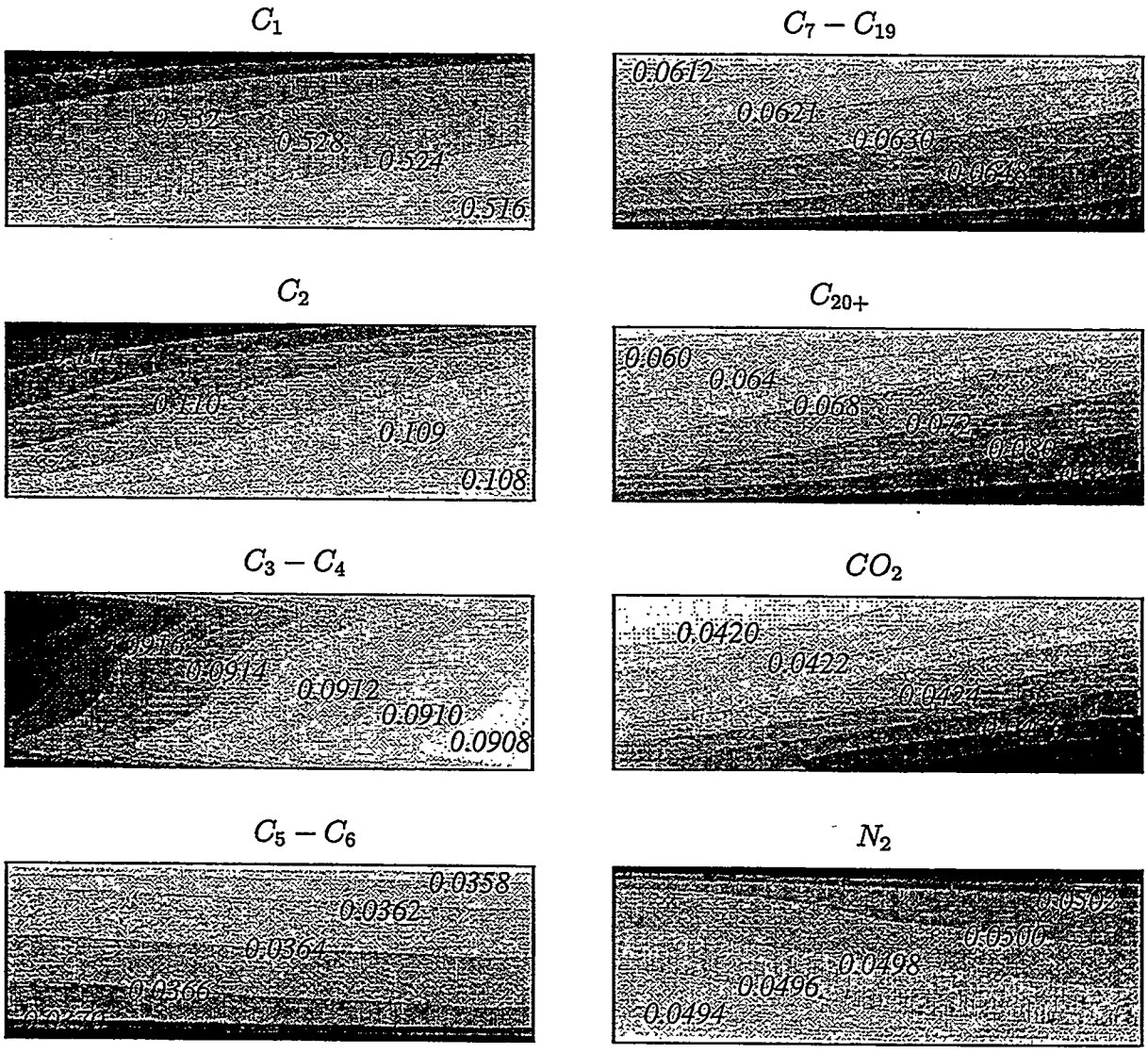

Figure 14: Composition contour plots for the field example: $k = 10$ md